Volume 55
Number 1
12 January 2026
Pages 1–558

Chem Soc Rev

Chemical Society Reviews

rsc.li/chem-soc-rev

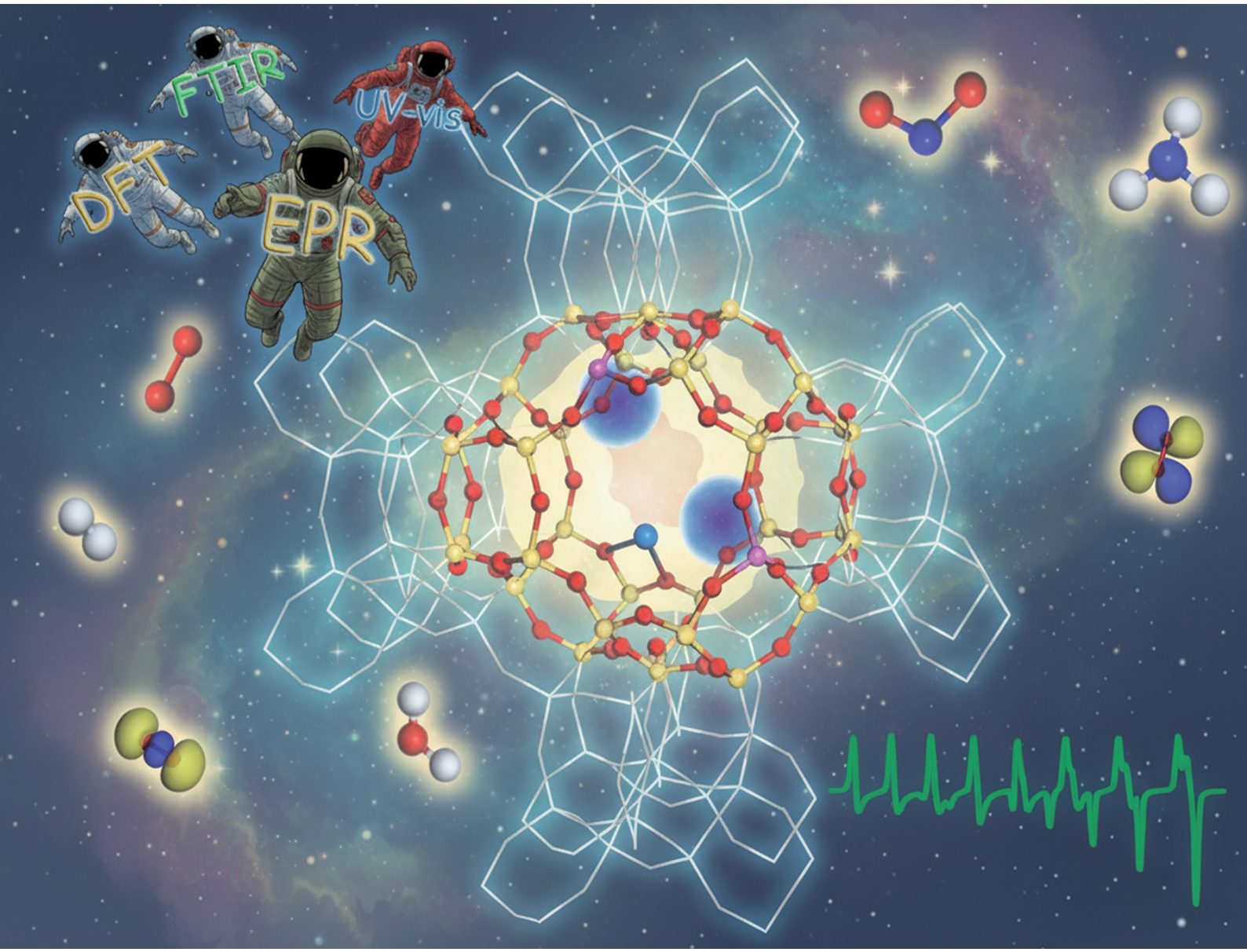

ISSN 0306-0012

ROYAL SOCIETY OF CHEMISTRY

REVIEW ARTICLE

Zbigniew Sojka *et al.*

Mechanistic and thermodynamic insights into binding and activation of small molecules on metallozeolites – relevance for adsorption and catalysis

Chem Soc Rev

REVIEW ARTICLE

View Article Online
View Journal | View Issue

Cite this: *Chem. Soc. Rev.*, 2026, **55**, 144

Mechanistic and thermodynamic insights into binding and activation of small molecules on metallozeolites – relevance for adsorption and catalysis

Filip Zasada, Piotr Pietrzyk, Mariusz Radoń and Zbigniew Sojka *

Metallozeolites exchanged with 3d transition metal ions (TMI) are versatile catalytic materials due to their well-defined framework structures, redox flexibility, and remarkable adsorption and catalytic properties. These features make them invaluable for both fundamental and applied research, underpinning numerous catalytic technologies. The binding and activation of small reactant molecules is governed by the complex mechanistic interplay of involved intrazeolite reactions, whose course is influenced by the flexible valence, spin, and coordination states of the encaged metal ions and the metal–oxo entities. Despite significant advances, the nature of active sites, confinement effects, and the complex activation mechanisms of reactant molecules, which act as both innocent and non-innocent ligands, remain subjects of ongoing debate. This has driven extensive research into the thermodynamic constraints and molecular-level insights into activation processes with orbital and spin resolution. This review critically examines the thermodynamic and molecular aspects of intrazeolite speciation of transition-metal ions and metal–oxo active sites, their structural dynamics, and reactivity toward catalytically relevant small molecules, including NH_3, H_2O, CO, N_2, O_2, NO, N_2O. Particular emphasis is placed on ligand coordination, redox activation, and the role of electronic and spin states in dictating the catalytic behaviour of metallozeolites. The discussion integrates insights from site-selective spectroscopies and computational methods to elucidate the structural, thermodynamic, and molecular aspects of metal–ligand interactions and activation pathways, with an emphasis on the role of spin states in binding and reactivity. We hope that this review can serve as a relevant and valuable reference for researchers working with zeolite catalysts, providing new insights and inspiration.

Received 31st March 2025

DOI: 10.1039/d5cs00346f

rsc.li/chem-soc-rev

Faculty of Chemistry Jagiellonian University, ul. Gronostajowa 2, 30-387 Krakow, Poland. E-mail: sojka@chemia.uj.edu.pl

Filip Zasada

Filip Zasada, born 1981, received his PhD in Chemistry from Jagiellonian University in 2009, where he currently serves as Associate Professor in Inorganic Chemistry Department. He completed two research internships in the Heterogeneous Catalysis Department at the University of Lille, where he combined DFT modelling and first principles thermodynamics for applications in redox catalysis. His current research interests focus on the molecular pathways of reactions involving small molecules in contact with redox catalytic centers on oxide surfaces and within zeolite frameworks.

Piotr Pietrzyk

Piotr Pietrzyk has been a Professor at the Faculty of Chemistry, Jagiellonian University (JU) since 2019. He holds an MSc (2001) and a PhD in chemistry from JU (2005). He completed research stays at the University of Lille, France, and the University of Turin, Italy. He was awarded by the Prime Minister of Poland, the Ministry of Science and Higher Education, and the Foundation for Polish Science. Since 2024, he has been elected Dean of the Faculty of Chemistry at Jagiellonian University. His research focuses on characterizing catalysts and investigating reaction mechanisms in heterogeneous catalysis (activation of small molecules, SCR, AOP) through spectroscopic and quantum chemical studies. He has co-authored over 80 scientific publications.

1. Introduction – context, theoretical and experimental background

Shortly after the development of synthetic zeolite materials, they were ion-exchanged with various transition-metal ions (TMI)[1,2] to acquire new, and often unique functionalities and reactivities, providing a solid foundation for their widespread applications in adsorption and redox catalysis.[3–6] In this context, the numerous zeolite frameworks[7] have provided a large variety of molecular architectures with the degree of perfection required for sensible molecular-level studies of the fundamental events in chemisorption and catalytic chemistry.[8] Due to their unique structural features, metallozeolite catalysts provide an opportunity to investigate the transition from simple (molecular ligation *via* lone pair donation with spin conservation) to complex (dissociative redox processes with a change in spin state) adsorption events, as well as from single-site to multiple-site chemistry. They also made it possible to explore the intermediate reaction steps both stoichiometrically and structurally, using spectroscopic methods in combination with theoretical modelling at various levels of sophistication.[1,2,8–11]

As a result, a large variety of promising research areas has emerged over the past few decades, including specific issues related to the substitution of TMI for the framework Al^{3+} or Si^{4+} ions, extra-framework accommodation of TMI, as well as capture, redox activation, and catalytic transformations of reactant molecules into desired products.[6,8,12–14] The coupled redox and acid–base chemistries, as well as space-confined effects, significantly impact the latter processes. In this context, the unique properties of the encaged bare transition-metal ions and the metal–oxo active centres result from their flexible valence, spin, and coordination states, which, in conjunction with the space confinement effects, lead to specific catalytic performance not encountered in the counterpart homogeneous catalysis.[12,13] Among the catalytic processes involving small-molecule gas-phase reactants, NH_3-SCR,[14,15] HC-SCR,[16,17] CH_4 oxidation,[18,19] and N_2O decomposition[20,21] are the most notable.

The zeolite framework type, the Si/Al ratio, and the distribution of Al atoms within the cavities and channels (constrained by the Löwenstein rule[22]), essentially govern the intrazeolite speciation of TMI. It is manifested in the simultaneous presence of exchanged cations in various valence and coordination states. The mutually related intrazeolite hydrolysis, olation, and oxolation processes lead to the formation of oligomeric metal–oxo entities, particularly for the high valent cations. Besides the framework and extra-framework oxygen ligands (oxo-centers), reactant molecules (such as NO, NO_2, O_2, H_2O, and NH_3) can also be captured in the coordination sphere of encaged transition-metal ions in various modes of hapticity and stoichiometries. Therefore, the successful delineation of TMI speciation in metallozeolite catalysts requires the application of a broad suite of spectroscopic techniques. Nevertheless, due to common speciation effects, single spectroscopic techniques rarely provide a thorough insight into the complex structure of the intrazeolite TMI species in their particular framework locus, including valence and oxidation states. Thus, a combination of dedicated techniques is typically required for the successful resolution of the geometric, electronic, and magnetic structures of the active sites.[17–20]

The chemical states of transition-metal ions and their agglomeration can be monitored with several conventional and commonly available spectroscopic techniques such as UV-vis/UV-vis-NIR,[23,29,30] EPR,[1,3,17] MAS-NMR,[24] IR,[25,26] Raman (RS) and resonance Raman (rR),[27] and luminescence (PL),[28] applied directly or with using suitable probe molecules.[31,32]

Mariusz Radoń

Mariusz Radoń, born 1982, received PhD (2011) and habilitation (2019) in Chemistry and is currently an Associate Professor at the Faculty of Chemistry, Jagiellonian University, Kraków. He has completed internships in KU Leuven, HPC Centre Cyfronet AGH (Kraków), and visited Max-Planck-Institut für Kohlenforschung (Mülheim). His research interests are focused on computational (bio)inorganic chemistry using quantum chemistry methods. He received the 2024 Award of the Quantum Bio-Inorganic Chemistry Society for his contributions to the accurate prediction of energetics in transition metal complexes.

Zbigniew Sojka

Zbigniew Sojka is a full professor at the Faculty of Chemistry of the Jagiellonian University (Poland), a corresponding member of the Polish Academy of Science, and Head of the Catalysis and Solid State Chemistry Group. He earned his PhD in Chemistry from Jagiellonian University in 1984 and subsequently completed postdoctoral fellowships at Pierre and Marie Curie University (France), and then at Lehigh University (USA). His research is focused on experimental and computational catalysis, materials chemistry, molecular modelling, spectroscopy, and electron microscopy. He published over 230 papers and holds more than 25 patents. Professor Zbigniew Sojka received several awards from the Minister of Science and Higher Education of Poland, the Polish Chemical Society, and a Jagiellonian Laurel for achievements in science.

More advanced methods include correlation 2D IR,[33] pulse EPR (HYSCORE,[34] ESEEM,[35] ENDOR[36]), and high-field EPR,[37] as well as a toolbox of powerful synchrotron X-ray absorption techniques (XAFS, XANES, EXAFS[38]), which have been of growing importance, recently.[39] In addition to the wide-ranging applications of these methods, various techniques have been developed to study zeolites in *operando*/*in situ* modes, providing valuable insights into intrazeolite coordination chemistry and elucidating the catalytic reaction mechanisms based on the establishment of functional structure–property–performance relationships. *Operando* characterization techniques enable monitoring of the adsorption and desorption of reactants, as well as the identification of surface intermediates and their dynamics. Additionally, they aid in understanding how and why zeolite catalysts behave differently under working conditions in real-life applications in comparison to static experiments.[18–20] However, the actual capacity of *operando* techniques to deliver definitive mechanistic insights is often limited by a compromise between the optimal circumstances for recording the high-quality spectra and the reaction conditions. The imposed constraints are particularly due to the temperature dependence of peak positions, line broadening effects, loss of the signal-to-noise ratio, and accumulation of spectator species. As a result, static and often low-temperature spectroscopic techniques still play a crucial role in providing high-quality reference spectra and reliable spectroscopic fingerprints, which can be used not only to guide the interpretation of *operando* results but also as crucial experimental constraints for *ab initio* molecular modelling.

Experimental studies on metallozeolites and their adsorption properties, as well as their catalytic chemistry, are consistently corroborated by theoretical modelling for the advanced interpretation of their intrinsic catalytic performance at both molecular (DFT, post-HF calculations) and phenomenological (*ab initio* thermodynamics) levels. Various quantum-chemical methods have been productively applied to characterise catalytically-relevant TMI systems, starting from commonly used and well-grounded density functional theory, progressing to more involved post-Hartree–Fock (post HF) methods, such as complete active space (CAS)[40] or coupled cluster (CC)[41,42] for proper treatment of correlated electron systems. Due to its overall good compromise between accuracy and computational cost, DFT remains the method of choice in computational catalysis. However, one should be aware of the limitations in currently available density functionals, which are approximated in their accuracy.[43–45] Examples of particularly challenging problems in computational catalysis, where DFT methods may not be sufficiently precise, include the prediction of chemically accurate adsorption energies and barrier heights in extended systems,[46–48] binding of noninnocent ligands to TMI,[49–51] and the spin-state splittings in mononuclear[52,53] and polynuclear complexes.[54,55] In such cases, a critical evaluation of the DFT results may be necessary, including cross-checking with the results of post-HF wave function calculations and comparing them with experimental spectroscopic or thermodynamic quantities, wherever available. When properly used, quantum-chemical calculations have been of crucial importance in developing a comprehensive molecular description of the coordination chemistry of TMI in zeolites, explaining their structure, dynamics, reactivity, and spectroscopic features, which are not directly accessible by experimental techniques. Supplemented by molecular simulation methods including molecular dynamics (MD) at various sophistication levels,[56–59] first-principles thermodynamics (FPT),[60,61] advanced methods of electronic structure analysis, including natural orbitals for chemical valence combined with extended-transition-state method (ETS-NOCV),[62–64] crystal orbital Hamiltonian population COHP,[65,66] and machine learning (ML) approaches,[67,68] they define a robust panoply of modern computational chemistry of zeolites.

In this review, we focus on the interfacial coordination chemistry of 3d transition-metal cations encaged in zeolites and its relevance for adsorption and catalysis, with the following topics that are covered: (1) accommodation and spectroscopic characterization of intrazeolite transition metal (TMI) centres (bare single, dual, and polynuclear metal–oxo), (2) survey of their structure and spectroscopic fingerprints, (3) first principles thermodynamic account of TMI speciation and stability at various p_{O_2} and p_{H_2O} conditions, (4) coordination of extra-framework non-redox (H_2O, NH_3, N_2, CO) and redox (NO, O_2, N_2O) molecules and their activation with the specific accent on the role of electronic and spin state of the active sites and (5) thermodynamic and molecular orbital interpretation of the binding and activation processes. The emphasis is placed on the utility and diagnostic capacity of selected molecular spectroscopies, particularly CW-EPR and related pulsed variants, UV-vis, Raman/resonance Raman, and IR techniques commonly applied in such investigations, and on *ab initio* thermodynamic and molecular modelling, supplemented by spin-resolved analysis of the nature of metal–ligand bonds using natural orbitals for chemical valence (NOCV).

The examples discussed herein demonstrate the capacity of these spectroscopies to probe the interaction of the reactant molecules with intrazeolite first-row 3d transition metal ions, and unravel various ways of their activation, particularly when the spin of TMI plays a crucial role. In selected cases of special relevance, this review is expanded to include non-transition metal ions (such as Zn) dispersed in zeolites. However, the framework cations obtained by isomorphous substitution, which form corner-sharing MO_4 tetrahedra fully integrated with the zeolite structure through covalent framework M–O–Si bonds, are only scarcely considered. Lastly, we do not aim to provide a comprehensive review herein, but rather present illustrative examples that demonstrate the value of advanced concepts in establishing the rational basis of redox catalysis on metallozeolites, which complements the previous notable reviews devoted essentially to copper and iron.[5,14,29,69–73]

2. Localisation, structure, and speciation of cationic metallic active sites

The unique structural and topological features of zeolites, such as 3D and 2D channel networks, accessible void space, space

confinement, the presence of ion-exchange sites, and Brønsted acidity, make them versatile catalysts of enormous importance for both fundamental investigations and wide-ranging practical applications, particularly when functionalized with transition metal ions.[13,74–76]

The introduction of transition-metal ions to zeolite matrices gives rise to four broad types of accommodation scenarios: (1) substitution of alien cations for the framework Al or Si ions, (2) formation of charge balancing ionic pairs with the framework O–Al$^-$–O centres, (3) encapsulation of metal species and entities within the channels and cages, (4) support of nanoparticles on the external zeolite surface. Depending on the Si/Al and M/Al ratio, zeolite topology, Al distribution, and the preparation method used, a variety of confined species of various site topologies, structures, and nuclearity, such as single and dual bare cations, and a diversity of polynuclear metal–oxo species, can appear (Fig. 1).

2.1. Isolated TMI centres

Hydrated metallozeolites are usually catalytically inert, but elevated temperature (prevailing during catalyst pretreatment and reaction conditions) drives off the labile ligands and generates coordinatively unsaturated active 3d metal (and/or metal-hydroxo and -oxo) centres. The resultant charge-balancing extra-framework cations hosted in the zeolites exhibit diverse low coordination states depending on their electronic configuration, charge, and spin (Fig. 2a). The topology of the sitting sites, size of the rings (Fig. 2b$_1$), Si/Al ratio, and Al spatial distribution (Fig. 2b$_2$ and b$_3$) play a decisive role in the accommodation mode of these cations.[82] This issue is illustrated by various coordination patterns of the bare 3d^n cations in the MFI matrix, as well as for selected single and dimeric Cu and Fe cations hosted in the CHA and FER frameworks, which are derived from DFT structure optimization (Fig. 2b–d).[83] Generally, ligation to more basic Al–O–Si oxygen atoms is preferred over Si–O–Si.[5] Furthermore, the Al pairs (*i.e.*, Al atoms arranged in the Al–O–(Si–O)$_2$–Al sequences) are capable of stabilising M^{2+} cations, whereas the single Al atoms (present in the Al–O–(Si–O)$_n$ sequence, $n > 2$) can charge-balance only the monovalent ions or hydroxylated divalent cations, M^{2+}–OH$^-$, and any other oxo species of an effective charge $q = 1$.[84] As a result, zeolite hosts with abundant Al–O–(Si–O)$_2$–Al sequences are needed to obtain catalysts with an enhanced content of the divalent redox sites. Accommodation of TMI cations leads to significant deformation of the rings where the alien cations are sited, and the associated lowering of the local site symmetry. In this way, the flexible zeolite framework acting as a polydentate ligand tends to maximize the coordination number (M$_{nc}$, n = 1, 2, 3 ...) of TMI, yet at the expense of forming appreciably strained bonds.

The resultant structural deformations are well reflected in the IR spectra of the T–O–T asymmetric skeletal vibrations (T = Si or Al).[85] The extent of this perturbation and the ensuing shift of the perturbed asymmetric T–O–T vibration varies with the valence state, size, particular exchangeable position the hosted ion occupies in the zeolite framework, and the presence of co-ligands as well.[86] The corresponding IR bands appear between two strong bands of antisymmetric and symmetric T–O–T

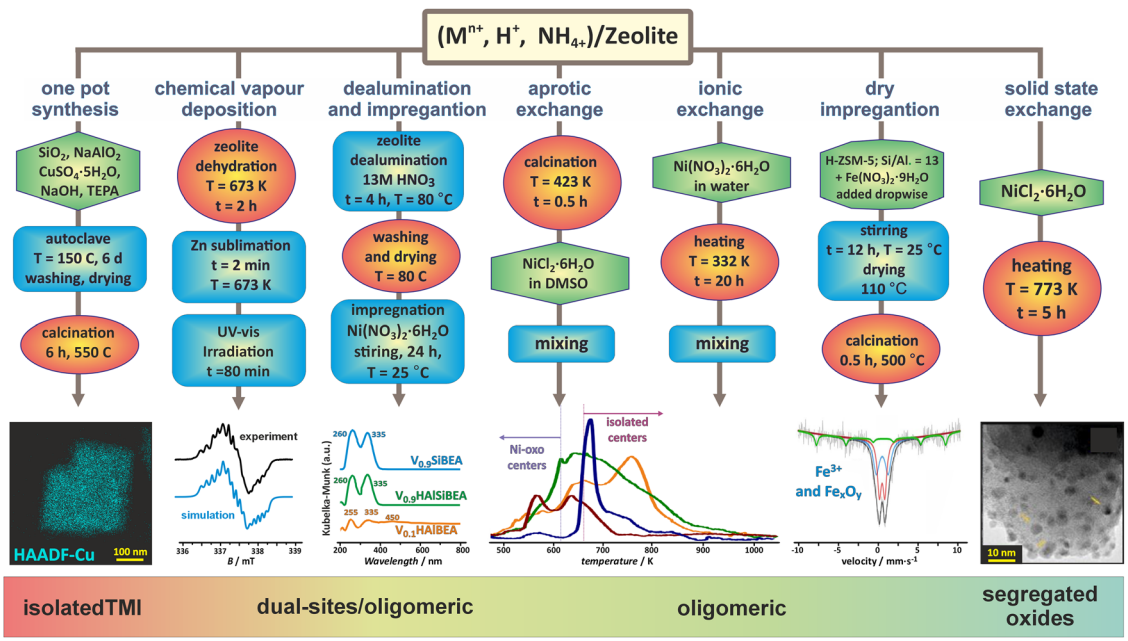

Fig. 1 Selected preparation methods applied for synthesizing the metallozeolites, including one-pot synthesis (illustrated with TEM/EDX imaging of Cu in SSZ-13),[33,77] chemical vapour deposition (with EPR spectrum of Zn$^+$ cations dispersed in ZSM-5),[78] dealumination and impregnation (with UV-vis of VO$_2^+$ species incorporated in Si-BEA),[79] aprotic and ionic exchange (with H$_2$-TPR profiles of Ni/BEA),[80] dry impregnation (with Mössbauer spectra of iron in ZSM-5),[81] and solid state exchange[33] (with TEM image of segregated oxide nanocrystals). The figure was drawn based on data published in the quoted references. The microscopic images were adapted from ref. 33 with permission from Elsevier, Copyrights 2023.

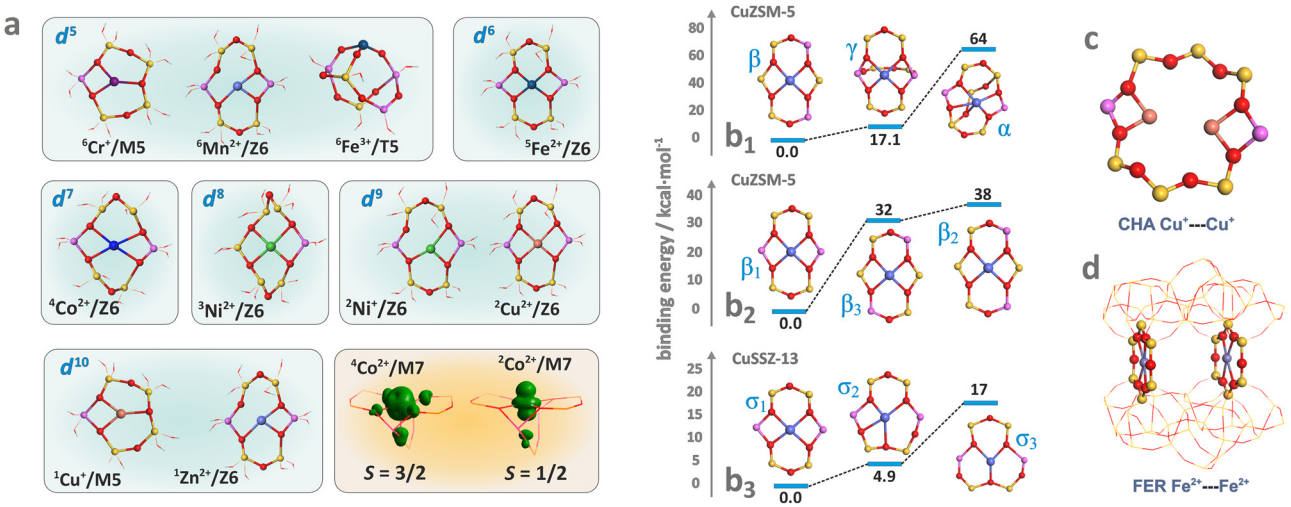

Fig. 2 Exemplary (DFT optimized) coordination patterns of selected isolated TMI hosted in MFI frameworks with the illustrative spin density distribution for Co^{2+} cation in the high (S = 3/2) and low (S = 1/2) spin states (a). Coordination environments of single Cu^{2+} cations showing the effect of site topology (b_1), and Al distribution (b_2) and (b_3) on the TMI relative stability (based on data published in the ref. 82). Dimer Cu–Cu sites in CHA (c) and Fe–Fe sites in FER (d).

vibrations, and are shifted from 1020–1100 cm^{-1} to about 800–1000 cm^{-1} upon accommodation of the alien cations. This effect can be exemplified by the Cu^{2+}, Ni^{2+}, and Mn^{2+} hosted in the FER matrix (Fig. 3a), and Cu^{2+}, Cu^{2+}–OH^- and Cu^+ in ZSM-5 (Fig. 3b) and SSZ-13 (Fig. 3c).[86–88] In the case of small charge cations (Cu^+, Cu^{2+}–OH^- or Zn^+), these deformations and the associated T–O–T frequency shifts are less pronounced (Table 1). The perturbed T–O–T vibrations can be used, for instance, to differentiate between the single Cu^{2+} species located in 6MR (900 cm^{-1}) and the Cu^{2+}–OH^- centres in 8MR (~950 cm^{-1}) rings present in the CHA zeolite.[88]

Direct insight into the ligation of TMI in zeolites can be derived using classic continuous wave CW-EPR[91–94] or advanced pulse and high-field techniques (HYSCORE, ESEEM, ENDOR).[95,96] For the series of Ti^{3+} ($3d^1$), V^{3+} ($3d^2$), Cr^{3+} ($3d^3$), Cr^{2+} ($3d^4$), Mn^{2+}, Fe^{3+} ($3d^5$), Fe^{2+} ($3d^6$), Co^{2+} ($3d^7$), Ni^{2+} ($3d^8$) Cu^{2+}, Ni^+ ($3d^9$) and Zn^+ ($3d^{10}4s^1$) ions of the first row, which can be hosted in zeolites, all tend to assume the high-spin configuration, noting the position of the zeolite oxygen (O_z) ligands in the spectrochemical series (AlO) < (O_z) < (SiO) ~ (H_2O) proposed by elswhere.[97] Among them, those with S = 1/2 are amenable to straightforward investigations using the commonly available X-band CW-EPR technique.

The hyperfine coupling $\boldsymbol{A}$- and the $\boldsymbol{g}$-tensor values obtained from the EPR spectra are strongly affected by the local environment of the encaged TMI. Apart from the $3d^n$ configuration, the $\boldsymbol{g}$- and $\boldsymbol{A}$-tensor anisotropies are sensitive to the local symmetry and the covalency of the M–O_z bonds with the zeolite

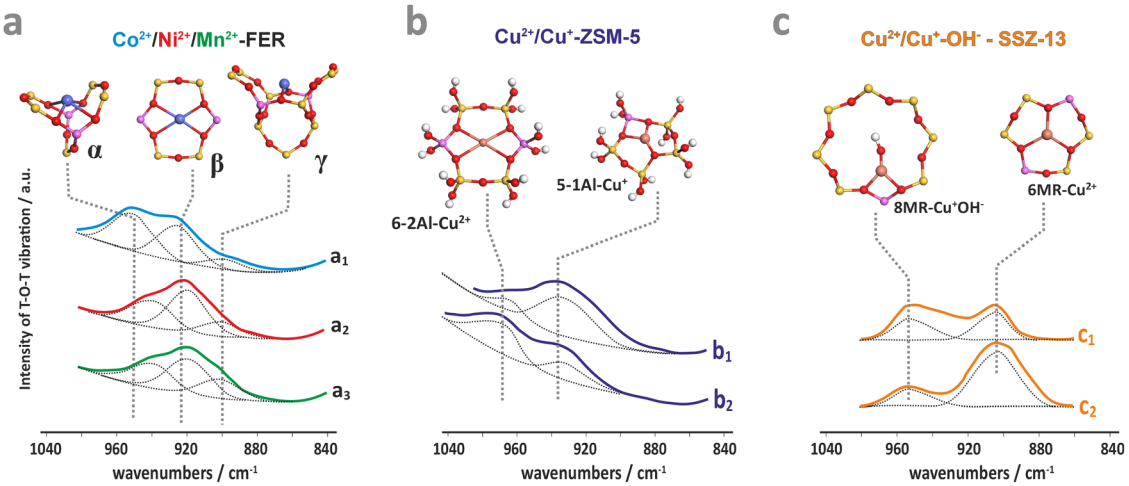

Fig. 3 IR spectra of the perturbed T–O–T antisymmetric mode for dehydrated ferrierite substituted with Co (a_1), Ni (a_2), and Mn (a_3),[87] for ZSM-5 zeolite loaded with Cu^{2+} (b_1) and Cu^{2+}/Cu^+ (b_2),[86] and for Cu-SSZ-13 with the Si/Al ratio of 6 (c_1) and 30 (c_2).[88] The figure was drawn based on data published in the quoted references.

Table 1 Antisymmetric T–O–T vibrations (cm^{-1}) for selected cations accommodated in the FER, CHA, and MFI zeolites

Zeolite framework	FER		MFI		CHA		
Cation	α-site	β-site	α-site	β-site	σ-site	τ-site	Ref.
Fe^{2+}	935–940	913–915		927			89 and 90
Co^{2+}	942–945	918–920	970	931–935	895	924, 948(τ^{3Si})	23, 87 and 89
Mn^{2+}	953	928					89
Ni^{2+}	940	918		930			89
Zn^{2+}	935	915–917					84
Cu^{+}				977			86 and 89
Cu^{2+}				937	900–892		86 and 89
Cu^{2+}–OH^{-}						950	88

framework oxygens. Simple perturbation theory treatment within the crystal field approximation allows for a straightforward (yet coarse) molecular interpretation of the ***g***-tensor (g_{ij}) values of the $S = 1/2$ TMI hosted in zeolites, based on eqn (1):[98]

$$g_{ij} = g_e\delta_{ij} + 2\lambda\sum_n \frac{\langle \mathrm{SOMO}|L_i|n\rangle\langle|L_j|\mathrm{SOMO}\rangle}{E_{\mathrm{SOMO}} - E_n} \qquad (1)$$

For further discussion, upon a rudimentary account for the M–O_z bond covalency, gauged succinctly by the α coefficient (it accounts for the extent of delocalisation of the unpaired electron from the metal core into the ligands (Fig. 4d), for more details see ref. 99), this equation may be reframed in a simplified handy form as; $g = g_e \pm m\lambda\alpha^2/(E_{\mathrm{SOMO}} - E_n)$, where m = 2, 6, 8 (depending on the 3d orbital involved in SOMO – singly-occupied molecular orbital), g_e = 2.0023, λ is the one-electron spin–orbit coupling constant, and L_i, L_j are the orbital angular momentum operators that couple SOMO ≈ $\alpha|3d\rangle$, with the $|n\rangle$ states of E_n energy. The requisite energy differences ($E_{\mathrm{SOMO}} - E_n$) can be derived from the d–d transitions observed in the complementary UV-vis spectra, as illustrated in Fig. 4a and b. Their relation with the corresponding EPR spectrum is shown in Fig. 4c.

The ligand field symmetry around the intrazeolite TMI in the hosting site imposes distinct constraints on the *g*-values. Axial signals with $g_\parallel = g_{zz} \neq g_\perp = g_x = g_y$ are expected for the local D_{4h}, C_{4v}, D_{3h}, C_{3v}, D_{2d} symmetries, whereas for lower symmetries (D_{2h}, C_{2v}, C_{2h}, C_s) orthorhombic (or monoclinic) signals with $g_{zz} \neq g_{xx} \neq g_{yy}$ are anticipated. As a result, for a $3d^1$ (Ti^{3+}) cation with the d_{xy} SOMO in an exemplary tetragonal C_{4v} environment, $g_\perp < g_\parallel < g_e$ is expected, and indeed experimentally observed, whereas for a $3d^9$ cation (Ni^{+}), $g_\parallel > g_\perp > g_e$ for $d_{x^2-y^2}$ SOMO (Fig. 5a and b) and $g_\perp > g_\parallel \sim g_e$ for d_{z^2} SOMO are typical. The hyperfine (hf) coupling constants for the unhybridized $d_{x^2-y^2}$ SOMO can be expressed as $A_{zz} = A_s + P[-4/7\alpha^2 + \Delta g_{zz}]$ and $A_{yy} = A_s + P[-4/7\alpha^2 + \Delta g_{yy}]$, $A_{xx} = A_s + P[-4/7\alpha^2 + \Delta g_{xx}]$, where the α coefficient accounts again for the M–O_z bond covalency, $P = g_e g_N \mu_B \mu_N \langle r^{-3}\rangle$, neglecting smaller terms.[101] Thus, the value of the α coefficient can be assessed from the analysis of the ***A***-tensor, using the calculated atomic values of the *P* parameters, which are tabulated for a given TMI elsewhere.[99]

More ionic bonds of the encaged TMI with the framework O_z (small spin density delocalisation) increase the hyperfine A_{Metal} values on the metal core and decrease the superhyperfine splitting on the ligands with magnetic nuclei (A_{Ligand}), such as ^{17}O (I = 5/2) labelled O_z framework oxygen atoms, and *vice versa* (see Fig. 4d). In the latter case, the superhyperfine patter due to $^{17}O_z$ can be used to ascertain the coordination environment of intrazeolite TMI (see below, Fig. 6).

A comprehensive listing of the equations that can be used for molecular interpretation of the ***g*** and ***A*** tensors of TMI in

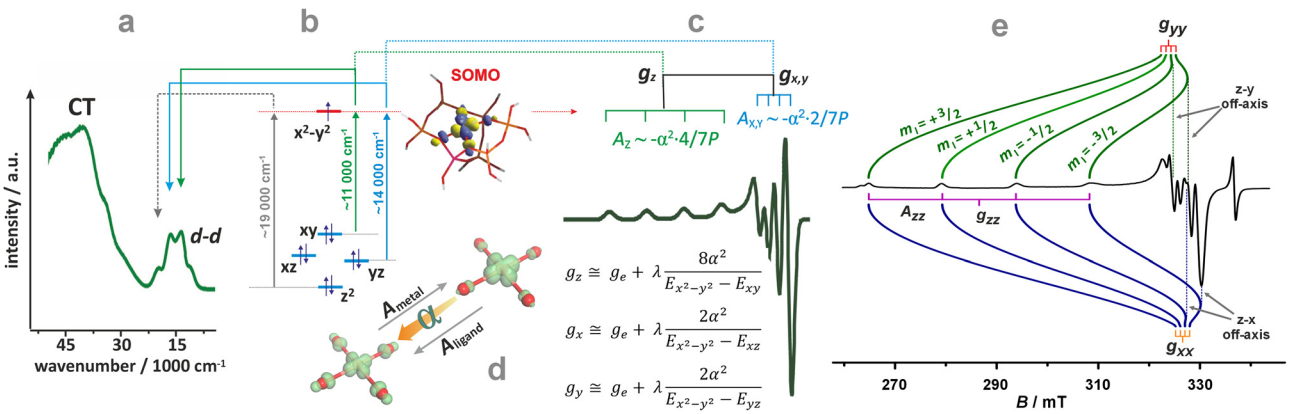

Fig. 4 UV-Vis-NIR spectrum of dehydrated Cu-SSZ-13 (a), together with the 3d energy levels (b) and the corresponding simulated EPR spectrum (c) (panels a, b, and c inspired by ref. 100). Structural model showing influence of a shift of spin density between Cu- and ligand-based states on the magnitude of hyperfine coupling gauged by α coefficient (d). The road map showing the origin of the off-axis features in the EPR spectrum of Cu^{2+} hosted in the CHA matrix (e), based on ref. 83.

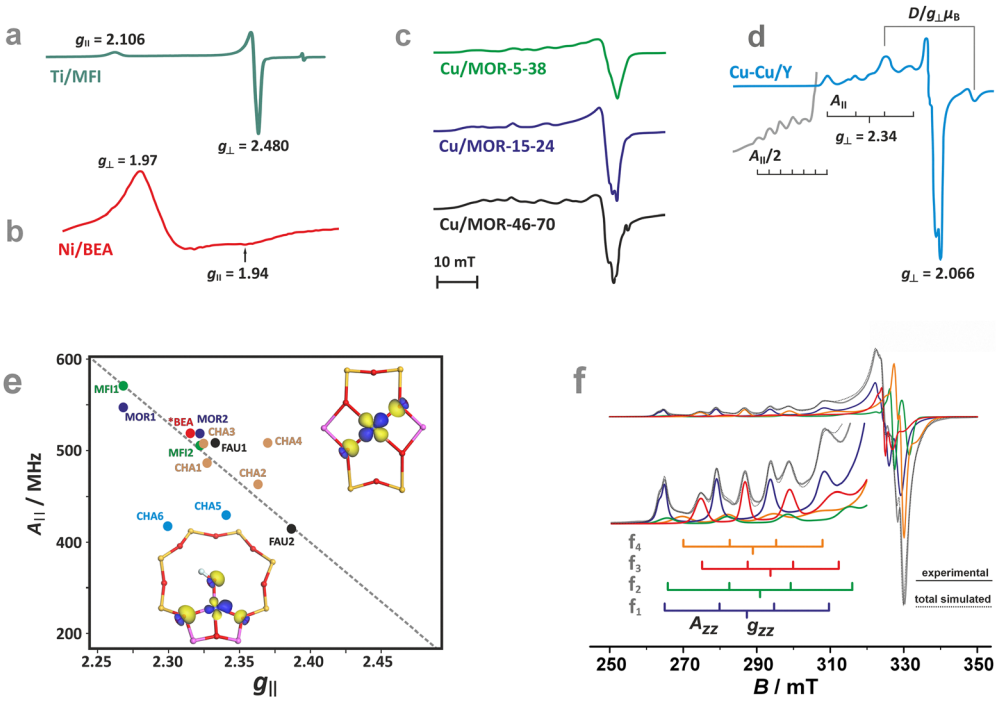

Fig. 5 EPR spectra of Ti/MFI (a) Ni/BEA (b). EPR spectra of the dehydrated Cu-mordenite samples of various Si/Al ratios (Si/Al = 5, 15, 46) and Cu exchange levels (2Cu/Al = 38, 24, 70) (c). Room temperature EPR spectra of Cu···Cu pairs in CuCe/Y zeolite oxidized at 450 °C and evacuated at 600 °C (d). Blumberg–Peisach-type (P–B) plot for the EPR active Cu^{2+} species stabilized within different zeolite environments (e), (colours indicate various bare Cu^{2+} species hosted in different zeolite matrices. In the case of CHA, yellow and blue colours correspond to various Cu^{2+} and Cu^{2+}–OH^- species). The corresponding spin density contours are provided for exemplary Cu^{2+}/6MR and Cu^{2+}–OH^-/8MR structures. EPR spectrum of Cu-SSZ-13 zeolite activated at 250 °C *in vacuo* (f), resolved into the contributing signals. The $A_{||}$ and $g_{||}$ values for the species identified in (f), labelled as (f_{1-4}), are shown in the P–B plot as CHA1–4. The figure was drawn based on data from ref. 80, 83, 91, 92, 104 and 105 respectively.

ligand fields of various symmetries can be found elsewhere.[102] It should be noted, however, that except for the regular features along the z and x, y directions, shown in Fig. 4c, additional off-axis lines may appear in the powder EPR spectra when

$$2A_i^2 - h\nu A_i/m_I < (g_i^2A_i^2 - g_j^2A_j^2)/(g_i^2 - g_j^2) < 2A_j^2 - h\nu A_j/m_I \quad (2)$$

where ν is the microwave frequency and m_I is the nuclear magnetic spin number (Fig. 4e).[103] These extra features, which correspond to additional extrema in the angular dependence of the magnetic resonant field ($\partial B/\partial\theta = 0$ and $\partial B/\partial\varphi = 0$), may exhibit significant intensity in the copper EPR spectra and should not be confused with the speciation of copper.

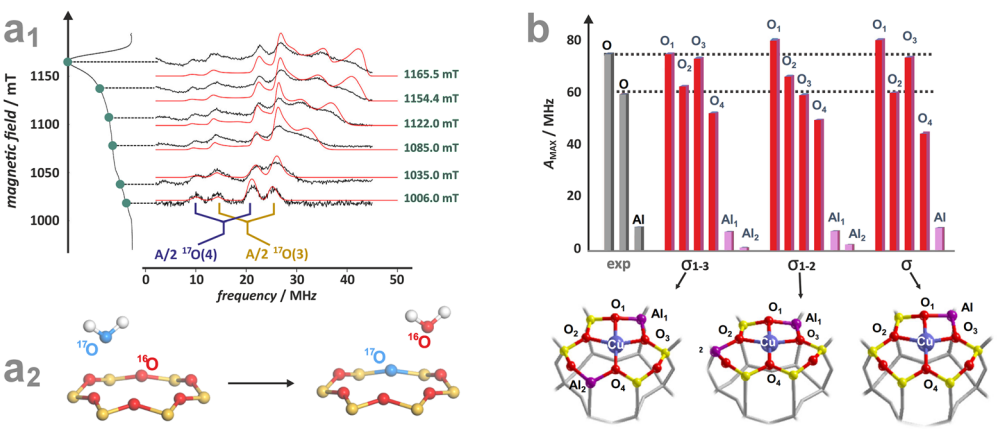

Fig. 6 Experimental (black) and simulated (red) Q-band ^{17}O ENDOR spectra, recorded at different magnetic field settings, of ^{17}O isotopically enriched and fully dehydrated Cu-CHA (a_1), together with the schematic representation of the isotopic enrichment of the zeolite framework (a_2). Comparison of experimental (grey) and computed (red) maximum hyperfine coupling values (A_{max}) for ^{17}O and ^{27}Al nuclei for the three different Al distributions: 2Al-3NN, 2Al-3NN, and 1Al (b) (the black dashed lines represent the experimental range of A_{max} for ^{17}O nuclei). Adapted from ref. 95 under the terms of the CC-BY 4.0 license, copyright 2021, published by Springer Nature.

Broadening of the EPR signals caused by local strain (structural inhomogeneity of the siting environment) and the presence of abundant magnetic ^{27}Al (I = 5/2) atoms for zeolites of low Si/Al ratio, along with the high TMI loading, lead to loss of the hyperfine structure $\boldsymbol{A}$ and $\boldsymbol{g}$-anisotropy, which can be illustrated by the EPR spectra of copper hosted in mordenite of various Si/Al (5, 15, 46) ratios, and copper exchange (2Cu/Al × 100% = 38, 24, 70) levels (Fig. 5c), where the perpendicular hyperfine structure of copper remains unresolved, and the parallel hyperfine structure becomes barely visible.[91] Furthermore, at higher loadings, the decreased distance between the copper cations may result in Cu^{2+} pairs formation, which is manifested in the EPR spectrum by the appearance of additional fine structure features on both sides of the perpendicular component of the single-ion signal of Cu^{2+}, separated by $D/g_{\perp}\mu_B$.[104] They can be used for assessment of the distance between the two adjacent copper ions (D/cm^{-1} $\cong$ $0.433g^2/r^3$ for r in Å) when the direct exchange interactions ($\sim J$) are small. The presence of a half-field signal due to the forbidden ΔM_s = 2 transition and the appearance of $2I$ + 1 = 7 lines of the hyperfine structure with half-splitting are other important characteristics of the Cu dimer formation (Fig. 5d).

The M–O_z covalency depends primarily on the presence of Al in the coordination environment of the encaged TMI. The framework oxygen atoms in the Si–O_z–Al entities are more negatively charged than those in the Si–O_z–Si motives. These factors make g and A values structure sensitive, which can be illustrated concisely in the form of Blumberg–Peisach-type diagrams[106] for Cu^{2+} in various zeolite frameworks and different Si/Al ratios.[92,107] Although the application of such a diagram to zeolites, due to the absence of suitable model compounds, requires some caution, it demonstrates its usefulness for the preliminary sorting of the intrazeolite copper species based on their EPR fingerprints.

Overall, copper ions in the more positively charged environments are found in the lower right part (smaller $A_{\parallel}$ and bigger $g_{\parallel}$), whereas Cu^{2+} species in the more negative coordination environments are located in the upper left end (bigger $A_{\parallel}$ and smaller $g_{\parallel}$) of the trend line in the Blumberg–Peisach-type diagram (Fig. 5e). This is well exemplified by the different positions in the plot of two types of the Cu-MFI zeolites, with two Al atoms in a MR6 ring generating a higher charge (MFI2) and with only one Al atom in the MR6 ring with the resultant lower charge (MFI1).[92] For the particular case of Cu-CHA, the EPR parameters for the MR6 ring (σ-site) fall in the middle of the trend line. The scattering of the positions in the plot reflects the sensitivity to the local symmetry of copper ligation ($A_{\parallel}(C_{2v})$ > $A_{\parallel}(C_1)$), yet the position of the Al atoms within the 6MR appears to be of less importance. The presence of a hydroxy OH^- co-ligand in the coordination sphere of Cu^{2+} located in the MR8 (τ-sites, see CHA5 in Fig. 5e) considerably lowers the value of the hyperfine structure, providing a straightforward means for the distinction between the bare Cu^{2+} and hydroxylated Cu^{2+}–OH^- species.

As a result, the structural sensitivity of the g and A values can not only reveal the speciation of the TMI hosted in zeolites, but also provide a rational basis for unambiguous site-specific assignment, particularly using the benchmarking parameters calculated by DFT or post-HF methods. This is well illustrated for the most extensively investigated Cu^{2+} hosted in CHA, MFI, and BEA zeolites, as shown in Table 2.

As an example, the diagnostic $A_{\parallel}$ region of the EPR spectra of CuSSZ-13 shows pronounced speciation of copper (Fig. 5f)[83], which has been resolved into two tetracoordinate Cu^{2+} cations of the local C_1 and C_{2v} symmetry in the σ-rings (marked as CHA-3 and CHA-4 in Fig. 5e, respectively), and two types of the $Cu^{2+}OH^-$ species hosted in the τ-sites of the CHA matrix (CHA-5 and CHA-6 in (Fig. 5e).

The local structure of single-site TMI cations hosted in zeolitic structures, and quantification of the covalency of the Cu–O_z bonds with an accuracy unattainable for other site-sensitive methods, can be ascertained using advanced EPR techniques combined with the ^{17}O isotopic labelling of the zeolite framework.[95] Of particular note here is the study of the CuSSZ-13 zeolite using ^{17}O, ^{27}Al ENDOR spectroscopy (Fig. 6a$_1$), supported by DFT modelling.[95,117] The requisite 17-O labelling of the zeolite framework can be achieved quite readily using isotopic exchange with $H_2{}^{17}O$ (Fig. 6a$_2$).

In contrast to the metal A values, the ^{17}O superhyperfine couplings depend significantly on the Al distribution in the 6MR ring, allowing for unambiguous discrimination between various Al tetrahedra locations. Their presence and number can be directly probed by ^{27}Al HYSCORE or ENDOR spectroscopies. In particular, the σ-rings characterized by 2 Al atoms separated by two Si (2Al-3NN) or one Si atom (2Al-2NN), as well as the rings with one Al atom only, exhibit characteristic patterns of the ^{17}O and ^{27}Al superhyperfine coupling constants (Fig. 6b), providing the basis for the Al-resolved identification of hosting sites. The exquisite sensitivity of such couplings enables, therefore, the univocal identification of the Cu^{2+} coordination environments. This approach has also been used to examine the location of VO^{2+} (ref. 95) and Zn^+ in ZSM-5,[117] demonstrating that it is possible to ascertain the specific location of paramagnetic TMI active centres in zeolite matrices with the level of detail needed for the rational establishment of structure–reactivity relationships. It is worth mentioning here that anomalous X-ray powder diffraction at the K-edge, which probes the long-range order of aluminium atoms within the zeolite frameworks, can also be used to determine isolated Al atoms and pairs (*i.e.*, the Al(–O–Si–O–)$_x$Al sequences). Using this approach in combination with ^{27}Al and ^{29}Si MAS-NMR, the spatial distribution of Al atoms in ZSM-5 has recently been resolved.[118]

The TMI species with S > 1/2 (with more than one unpaired electron) exhibit zero-field splitting of the ground state gauged by the axial D and rhombic E parameters. The high-spin TMI can be divided into Kramers ions of half-integer spin numbers (S = 3/2, Co^{2+} and S = 5/2, Fe^{3+}) and non-Kramers ions with integer spins (S = 1, Ni^{2+} and S = 2, Fe^{2+}, Mn^{3+}). The zero-field splitting can make the intrazeolite non-Kramers TMI ''EPR-silent'' using conventional X-band ($\sim$0.3 cm^{-1}) or Q-band ($\sim$1.2 cm^{-1}) EPR, or detectable, particularly for the Kramers ions, when the ZFS leads to a well-separated M_s = ±1/2 state as

Table 2 Experimental and calculated EPR spin-Hamiltonian parameters for selected TMI in zeolites

TMI–zeolite	Notes[a]	g tensor	A tensor/MHz	Ref.
$Ti^{3+}(3d^1)$/TS-1	Experimental	1.922; 1.939; 1.9897 1.981; 1.960; 1.91		108
$Ti^{+}/(3d^1)$/ZSM-5	Experimental	1.94; 1.97		109
$VO^{2+}(3d^1)$/ZSM-5	Experimental	1.9843; 1.9843; 1.931	214; 214; 542	37
$VO^{2+}(3d^1)$/BEA	Experimental	1.987; 1.983; 1.927	234; 214; 558	110
	B3LYP calculated, 6MR	1.987; 1.984; 1.952	156; 139; 440	
$VO_2(3d^1)$/SiBEA	Experimental	1.803; 1.942; 1.968	676; 892; 876	110
	B3LYP calculated, 6MR	1.853; 1.992; 1.998	838; 1124; 1043	
$Cr^{5+}(3d^1)$/Na-Y	Experimental, supercage site II	1.98; 1.98; 1.92		111
	Small cage site I or II	1.98; 1.98; 1.92		
$Cr^{5+}(3d^1)$/Na-MOR	Experimental	1.99; 1.98; 1.93		111
$Fe^{3+}(3d^5)$/ZSM-5 (Fe^{3+}OH/ZSM-5)	Experimental	g_{eff} = 4.3 g_{eff} = 6.3; 5.7		112
$Fe^{3+}(3d^5)$/BEA (Fe^{3+}OH/BEA)	Experimental	g_{eff} = 4.3 g_{eff} = 6.1		112
$Co^{2+}(3d^7)$/MFI	Experimental, S = 3/2	g_{eff} = 5.1		113
$Co^{2+}(3d^7)$/AlPO		g_{eff} = 5.80–5.44; 2.0		119 and 120
$Ni^{+}/(3d^9)$/ZSM-5	Experimental	2.49; 2.072; 2.072		64
$Ni^{+}(d^9)$/ZSM-5	B3LYP calculated, 6MR	2.337; 2.112; 2.159		114
$Cu^{2+}(3d^9)$/ZSM-5	Experimental	2.323[d]	471[d]	115
$Cu^{2+}(3d^9)$/ZSM-5	Experimental	2.276[d]	545[d]	115
	Calculated, 6MR (α site)	2.230[d]	479[d]	
	6MR (β site)	2.192[d]	497[d]	
	6MR (γ site)	2.206[d]	531[d]	
$Cu^{2+}(3d^9)$/CHA	Experimental	2.352; 2.075; 2.075	470; 35; 35	116
	Experimental	2.347[d]	493[d]	115
$Cu^{2+}(3d^9)$/CHA	Experimental	2.325; 2.072; 2.072	490; 35; 35	116
	B2PLYP calculated, 6MR	2.282[c]	455[c]	
$Cu^{2+}OH(3d^9)$/CHA	Experimental	2.290; 2.072; 2.072	410; 45; 45	116
	B2PLYP calculated, 8MR[b]	2.275, 2.135, 2029	388[c]	
$Cu^{2+}OH^{-}$ $(3d^9)$/CHA	Calculated, 8MR[b], B3LYP	2.194[d]	203[d]	115
	6MR[b], B3LYP	2.200[d]	401[d]	
	6MR[b], B3LYP	2.242[d]	492[d]	
	D6R, B3LYP	2.243[d]	368[d]	
$Zn^{+}/(3d^{10}4s^1)$ZSM-5	Experimental	1.9951; 1.9984; 2.0015	1520, 1520, 1535	78
	B3LYP calculated for:			
	T7 site	1.992, 1.9963, 2.0023	1321, 1325, 1347	
	T8 site	1.9946, 1.9975, 2.0023	1458, 1460, 1480	
	T10 site	1.9921, 1.9965, 2.0023	1331, 1335, 1357	

[a] Calculated when the quantum chemical method is provided; otherwise, the g and A tensors are the experimental values. [b] Cluster models with different arrangements of Al sites. [c] Only one value (g_{zz}, A_{zz}) reported. [d] $g_{x,y}$ ($g_\perp$) and $A_{x,y}$ ($A_\perp$) are not reported (for zeolites typical values of $g_\perp \sim 2.07$ and $A_\perp \sim 30$–40 MHz are structurally less informative than the $g_\parallel$, $A_\parallel$ values).

the lowest one (Fig. 7a and b_1).[119,120] Such systems can be treated simply as exhibiting effective $S' = 1/2$ states, but due to closely lying energy states that promote fast relaxation, registration of the EPR spectra usually requires liquid helium

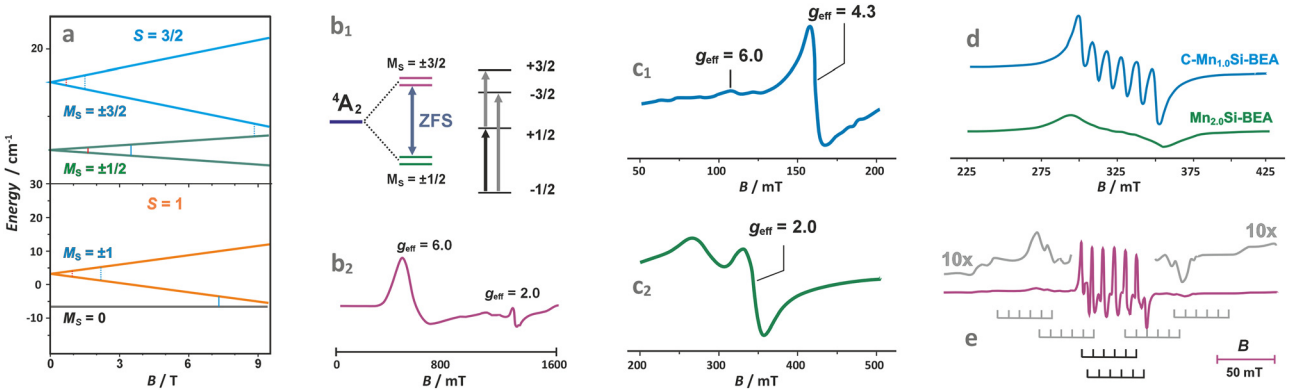

Fig. 7 Splitting of the energy levels in the magnetic field for exemplary S = 3/2 and S = 1 states of TMI (a), zero-field splitting (ZFS) for the $^4A_2$ state of Co^{2+} (d^7) with $D > 0$ (b_1), with the corresponding Q-band EPR spectrum of Co/AlPO (b_2).[119,120] X-band spectra of Fe/ZSM-5 (c_1 – low field, c_2 – high field component),[122] Mn/BEA of different loading (d),[123] and Q-band spectrum of Mn^{2+} in A zeolite matrix (e).[124] The figure was drawn based on data published in the quoted references.

temperatures.[120,121] The zero-field splitting depends on the anisotropy of the local ligand field and is mediated by spin–orbit coupling (SOC). The magnitude of the latter increases as one passes from early to late 3d TMI across the periodic table. As a result, ZFS may vary from small values (of the order of 10^{-2} cm^{-1}) for Mn(II) in symmetric environments to large values of the order of even 10^2 cm^{-1} for Co(II).[119] Notable examples can be provided by liquid helium X/Q-band EPR studies of CoZSM-5 (Fig. 7b$_2$)[121] or CoAPO zeotypes with the Kramers $M_s = \pm 1/2$ ground state, which exhibit effective g-values of $g_{\perp,\mathrm{eff}} \approx 5.80$–$5.44$ and $g_{\parallel,\mathrm{eff}} \approx 2.00$, and the zero-field splitting of 7 cm^{-1}. Another example of a Kramers high-spin system is provided by FeZSM-5 zeolites.[122] The EPR signal at $g_{\parallel,\mathrm{eff}} \approx 2$ with small ZFS has been associated with the highly symmetric α sites. In contrast, the signal at $g_{\perp,\mathrm{eff}} = g_{\perp}(S + 1/2) \approx 6$ and $g_{\parallel,\mathrm{eff}} \approx 2$ to β sites of local axial symmetry ($D \gg h\nu$, $E \approx 0$), whereas the $g_{\mathrm{eff}} \approx 4.3$ signal to γ sites with rhombic ZFS ($D \gg h\nu$, and $D/E \approx 1/3$) (Fig. 7c$_1$ and c$_2$). It is more likely, however, that the trivalent ions are actually encaged in the ZSM-5 host in the form of hydroxo or oxo species, which can be more readily charge balanced by 2 Al and 1 Al atoms, respectively, since the configurations of 3 Al atoms per ring/cage are available in zeolites of low Si/Al ratio, such as X faujasite, only. A broad signal appearing at $g_{\mathrm{eff}} \approx 2.3$ corresponds, in turn, to small Fe_xO_y clusters. The extension of the low-field signal to $g_{\mathrm{eff}} \approx 9.6$ can mainly be attributed to the rhombicity D/E parameter, which characterizes the Fe^{3+} cations in highly anisotropic (low-symmetry) environments. A signal at $g \sim 3.3$ may also appear for Fe^{3+} in the sites of trigonal symmetry, but some spectral features can be smeared out due to the strong dependence of their resonance magnetic fields on the spatial orientation of the paramagnets, or distribution of the ZFS values caused by local strain.

In the case of Mn^{2+} ions exchanged into zeolite hosts, the EPR spectra show gradual smearing of the 6-line hyperfine structure due to $I = 5/2$ with an increasing Mn content due to dipolar broadening effects caused by the adjacent Mn^{2+} ions (Fig. 7d).[123] The observed spectrum results from transitions within the $M_s = \pm 1/2$ doublet produced by the combined action of the ligand field and the spin–orbit coupling.

In fact, in powder spectra only the central line due to the $M_s = -1/2 \leftrightarrow +1/2$ transitions of the least angular dependence on the magnetic field is strong, whereas the other allowed inter-doublet transitions (such as $M_s = -\pm 3/2 \leftrightarrow \pm 1/2$ or $-\pm 3/2 \leftrightarrow \pm 5/2$, marked with the grey stick diagrams in Fig. 7e) are smeared to large extent, and barely observed as mere wings flanking the central hyperfine sexted. A relevant example is provided by Mn^{2+} exchanged in A zeolites.[124]

2.2. Terminal and bridging metal oxo centres

Besides the bare state (Co^{2+}, Ni^{2+}/Ni^{+}, Cu^{2+}/Cu^{+}), extraframework cations, particularly those of $z \geq 3$ (V^{5+}, Ti^{4+} or Fe^{3+}) hosted in zeolites of moderate Si/Al ratio, can be stabilised in the form of hydroxo and terminal or bridging oxo TMI centres of various nuclearity. Their appearance results from hydrolysis when the local pH during the catalysts preparation is too high ($[M(H_2O)_n]^{z+}_{(cage)} + hH_2O_{(cage)} \rightarrow [M(OH)_h(H_2O)_{n-h}]^{(z-h)+}_{(cage)} + hH_3O^{+}/Z$), launching the intrazeolite olation/oxolation reactions that lead to the formation of M=O or O=M=O oxo-species (for instance, $[V(H_2O)_6]^{5+} \rightarrow [V(OH)_4(H_2O)_2]^{+} \rightarrow [VO_2(H_2O)_4]^{+} + 4H_3O^{+}$ (ref. 125)). The relevant thermodynamic background of these processes is provided in Chapter 3. Notable examples of the intrazeolite terminal oxo-systems of high valent metals include mono-oxo ($[V{=}O]^{2+}$/BEA, $[W{=}O]^{3+}$/ZSM-5[126] or $[Fe{=}O]^{2+}$/MOR,[26] $[Fe{=}O]^{2+}$/CHA, $[Fe{=}O]^{2+}$/BEA,[19] and di-oxo species ($[MoO_2]^{2+}$/ZSM-5-[127] and VO_2/BEA zeolites[110]). Alternatively, metal–oxo species can also be formed during the redox-type interactions of bare (single and adjacent) TMI cations with O_2 or N_2O, and this chemistry is described in detail in Chapters 4.3.1 and 4.3.3.

Generally, the metal–oxo bonding of TMI can be described in terms of σ- and π-type overlap between the 2p orbitals of the O_t moiety with the corresponding 3d orbitals of the M^{z+} core. A tetragonal environment (for clarity, with enhanced C_{4v} symmetry) with the M–O_t bond placed along the z-axis can be used as a basic, semiquantitative model for the TMI situated in the 6MR rings. In such case, the d_{z^2} orbital is involved in the σ-overlap with the $2p_z$(O) in the M–O_t bond, the d_{zx}, d_{zy} orbitals participate in the π-overlap, whereas the $d_{x^2-y^2}$ orbital is primarily engaged in the σ-bonding to the framework O_z ligands (assuming the x- and y-axes intersecting O_z ligand positions), and in a considerably weaker δ-type interaction with the terminal oxygen, as well. The d_{xy} orbital remains essentially nonbonding. The resultant general scheme of the energy levels is shown in Fig. 8 (note, it may be altered by changes in the local site symmetry and oxidation state of the cations). All bonding oxo orbitals are occupied by the 6 electrons provided by the terminal O_t moiety. In contrast, the nonbonding d_{xy} and the antibonding $\pi^*_{x,y}$, δ* and σ* orbitals are occupied by the electrons derived from the metal d^n centres. Thus, for the d^0–d^1 TMI (exemplified by $[VO_2]^{+}$ and $[VO]^{2+}$ hosted in BEA[24] VO_2^{+}/MCM-22[128] or $[VO]^{2+}$ in ZSM-5[37]), the M–O_t bonds acquire a distinct triple bond character (1σ and 2π), and are the strongest among the 3d series. For $[VO]^{+}$/ZSM-5,[129] the bond order decreases to 2.5, as in the high-spin d^2 configuration, the antibonding π^*_x becomes occupied.

Distinction between the diamagnetic $[VO_2]^{+}$ ($3d^0$) and paramagnetic VO_2 and VO^{2+} ($3d^1$) cations, accommodated, *e.g.*, in the BEA zeolite, can be performed by MAS-NMR (Fig. 9a) in combination with photoluminescence techniques (Fig. 9b$_1$ and b$_2$),[130] and EPR spectroscopy (Fig. 9c1–c3),[24,110] respectively. The resolved fine structure in the PL spectra of $[VO_2]^{+}$/BEA reveals directly not only the V=O bonds, but also speciation of the vanadium(V)-oxo species (Fig. 9b2).

The superimposed EPR spectra of the paramagnetic VO^{2+} and VO_2 species observed in the dealuminated BEA zeolite are shown in Fig. 9c1 and the component signals in Fig. 9c2 and c3, whereas the associated structures with spin density contours are shown in Fig. 9c4.[24] Different SOMO nature of both species ($d_{x^2-y^2}$ for VO^{2+} and $3d_{z^2}/4s$ hybrid for VO_2) is well reflected in the dramatically different EPR parameters:

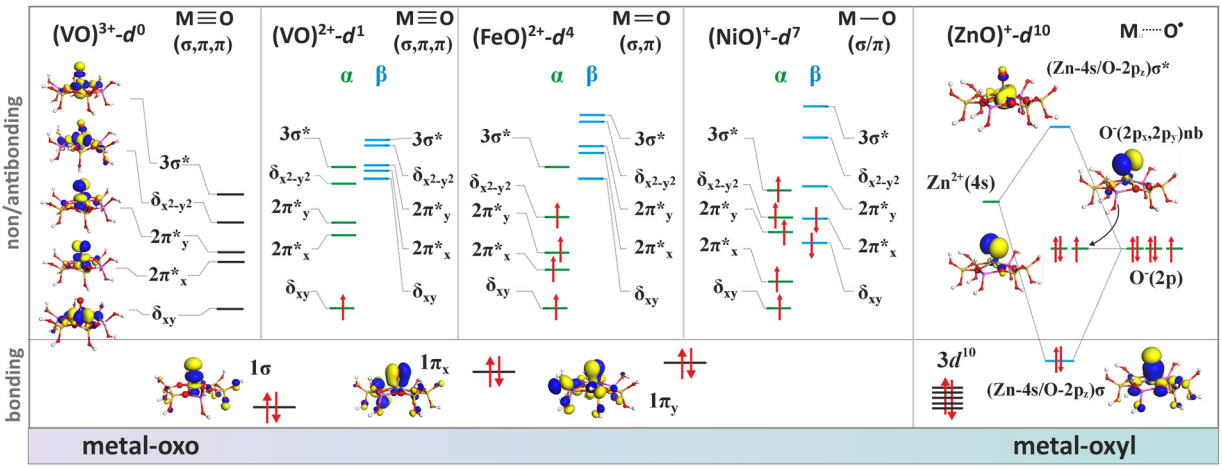

Fig. 8 Qualitative energy level diagrams for 3d $[MO]^{n+}$ cores hosted in a 6M ring containing two $[AlO_4]^-$ sites representing the evolution of the metal–oxygen bond nature with the increasing number of d electrons.

g_{xx} = 1.987, g_{yy} = 1.983, g_{zz} = 1.927, $|A_{xx}|$ = 8.4, $|A_{yy}|$ = 7.7, and $|A_{zz}|$ = 20.7 mT for VO^{2+}, and VO_2: g_{xx} = 1.803, g_{yy} = 1.942, g_{zz} = 1.968, $|A_{xx}|$ = 26.8, $|A_{yy}|$ = 32.8, and $|A_{zz}|$ = 31.8 mT. The isotropic hyperfine constant is extremely sensitive to the number of oxo-ligands, and therefore, can be used as a simple diagnostic for resolving the oxo *vs.* dioxo dichotomy of the vanadium(IV) species. Application of multifrequency EPR illustrates, in turn, a possibility of separation of the spectral $A_{\parallel}(A_{zz})$ and $A_{x,y}(A_{\perp})$ features of the VO^{2+} entities exchanged in the ZSM-5 zeolites, and may be helpful to reveal their possible speciation (Fig. 9d1–d3).[37]

With an increasing electron count, the antibonding $\pi^*_{x,y}$ orbitals become progressively populated (Fig. 8), decreasing the M–O bond order and weakening its strength. In the particular case of $3d^4$ cations, the bond order drops to 2. The resultant double bond in the M═O_t unit can be represented by a quintet $[Fe{=}O]^{2+}$ ferryl species $(d_{xy}{}^1d_{xz}{}^1d_{yz}{}^1(d_{z^2-y^2})^1\ \sigma^2$, S = 2, Fig. 8) stabilized in various zeolite matrices,[90,131,132] which is featured by the presence of a low-lying ferric-oxyl septet $(d_{xy}{}^1d_{xz}{}^1d_{yz}{}^1(d_{z^2-y^2})^1(d_{z^2})^1$, σ^1, S = 3),[20] or by isoelectronic $[MnO]^+$ units hosted in ZSM-5 and SSZ-39 (AEI) modelled by DFT.[133] Yet, both $[Fe{=}O]^{2+}$ and $[MnO]^+$ species hosted in the MFI and AEI topologies exhibit different sitting locus, the structure and stability of which depends considerably on the distribution of Al atoms within the rings. The most stable $[Fe{=}O]^{2+}$ species in ZSM-5 exhibit a square pyramidal (coordination number CN = 5) structure located in δ-sites of the 6MR(T11/T11) rings with the Al atoms in the *para*-position,

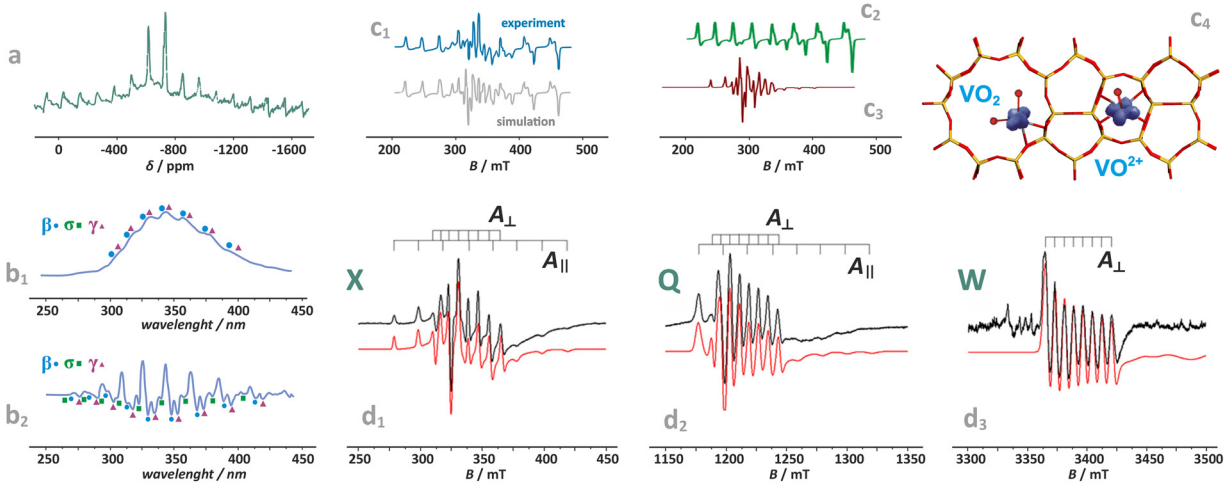

Fig. 9 Exemplary NMR (a) and photoluminescence spectra of vanadium(V)-oxo species in BEA zeolite (b_1) and (b_2), (β, σ, γ indicate three vanadium species of various structures), based on data published in the ref. 130 redrawn and modified for clarity. Simulated and experimental EPR spectra of vanadium in the dealuminated BEA zeolite (c_1) and the component signals of VO^{2+} (c_2) and VO_2 (c_3) species, together with spin density contours calculated for the VO_2 and VO^{2+} species (c_4), adapted from ref. 110 with permission from American Chemical Society, Copyright 2007. Experimental (black) and simulated (red) EPR spectra of the VO^{2+}/ZSM-5 sample registered at (d_1) X-band, (d_2) Q-band, and (d_3) W-band, adapted from ref. 37 with permission from Elsevier Inc., Copyright 2020.

whereas $[MnO]^+$ species are most stable in the 10MR (T12) rings, assuming a trigonal structure of CN = 3,[134] characteristic for intrazeolite monovalent species such as $[CuO]^+$ or $[ZnO]^+$.

The $[Fe{=}O]^{2+}$ entity is known as α-oxygen and exhibits unique reactivity toward C–H bond cleavage, which is addressed in Section 4.3.3. Particularly, for the BEA topology, the spin Hamiltonian parameters (S = 2 and the sign and magnitude of D = 13 ± 1 cm^{-1}) confirm the $[^5Fe(IV){=}O]^{2+}$ formulation of this species, definitely.[135]

In the case of the late intrazeolite transition metal cations (Co, Ni, Cu), the high-valent states ($z \geq 3$) become more hardly accessible. With an increasing electron number, the corresponding M–O_t bonds gradually lose their oxo character. For the transition $[Fe–O]^+$ $(d_{xy}{}^1d_{xz}{}^1d_{yz}{}^1(d_{z^2-y^2})^1(d_{z^2})^1\ \sigma^2$, S = 5/2) and $[Co–O]^+$ $(d_{xy}{}^2d_{xz}{}^1d_{yz}{}^1(d_{z^2-y^2})^1(d_{z^2})^1\ \sigma^2$, S = 2) species, the bond order (bo) drops to 1.5, decreasing further upon passing to Ni^{2+}–O (bo = 1) and Cu^{2+}–O (bo = 1/2). Since the $\pi(3d_{zx,yz}–2p_{x,y})$ overlap is significantly decreased, such entities acquire a distinct metal–oxyl (M–$O^\bullet$) character with the high-spin metal core magnetically coupled to the oxyl-moiety.[136] Elongation of the M–O_t bond, *e.g.*, in the transition state while interacting with reactants, weakens the $3d_\pi$–$2p_\pi$ overlap, favouring the highly reactive oxyl state.[137] Finally, in the case of the closed $3d^{10}$ shell the 3d–2p bond order ceases entirely, and, *e.g.*, a $[Zn^{II}–O]^+$ bonding is realized essentially *via* the 4s–2p overlap,[134] exhibiting a distinct zinc–oxyl nature $((3d)^{10}(\sigma)^2(O2p_x)^2(O2p_y)^1(\sigma^*)^0)$, with the nearly degenerate non-bonding $2p_x$ (HOMO) and $2p_y$ orbitals (SOMO), see Fig. 8.

Summarizing, vanadium, chromium, or molybdenum terminal oxo-species are relatively rigid and disposed to protonation[138] or an electro-protic activity ($M^{z+}{=}O + HR \rightarrow M^{(z-1)+}–OH + R$), which is mainly observed in the photocatalytic reactions, where the reactive excited oxyl state, $M^{z+}{=}O \rightarrow M^{(z-1)+}–O^{\bullet-}$, becomes accessible by photon ($h\nu$) absorption[139–141] or at elevated temperatures (typically 400–500 °C) for thermal catalytic processes.[142,143] In the case of Fe, Co, Ni, and Cu, the terminal oxygen functionalities are more chemically labile (unstable), and featured by the co-existence (or close lying and thermally available) electromeric $M^{z+}–O^{2-} \leftrightarrow M^{(z-1)+}–O^{\bullet-}$ forms.[137] They may appear as important intermediates, particularly involved in low-temperature catalytic redox reactions (150–350 °C), entailing hydrogen or oxygen atom transfer processes, exemplified by CH_4 hydroxylation[135,144] or appear during N_2O decomposition that requires somewhat higher temperatures,[145] see Chapter 4.3.3 for more details.

A brief survey of typical spectroscopic Raman, IR, PL, and UV-vis techniques used for the characterization of terminal Cr-, Mn-, Fe-, Co-, Ni-, Cu–oxo, and Zn–oxyl species encaged in various zeolitic matrices is shown in Fig. 10a–g.

Apart from providing the spectroscopic fingerprints for identification and monitoring of the investigated species during catalytic reactions, these examples also illustrate the structure sensitivity of the particular signals associated with the mono-oxo and di-oxo states (Fig. 10a–f). It includes the effect related with the Al content in the rings (Fig. 10a), local symmetry distortion of the 6MR rings in the CHA *vs.* BEA topologies (Fig. 10b), perturbation of T–O–T vibrations by various mono-oxo Mn, Fe, Ni species (Fig. 10c), and the unique structure features of the Zn–oxo entities (Fig. 10d). In the case of bridging-oxo species (*vide infra*) the effect of the Si/Fe (Fig. 10e), and influence of the Al atoms distribution within the 6MR rings of the CHA framework on the Raman features are shown in Fig. 10f. Formation of the trinuclear coper-oxo clusters, $[\mu\text{-}CuO]_3{}^{2+}$ accommodated in mordenite can be monitored, in turn, by UV-vis spectroscopy (Fig. 10g). However, it is important to critically evaluate many of the structural assignments of such species reported in the literature.

As already mentioned above, a nucleophilic character (negative partial charge) of the TMI–OH ligands triggers interazeolite olation and oxolation processes, which lead to the appearance of various di- and tri- and even tetranuclear species containing the bridging oxygen moieties (see Chapter 3). The structures of homo-metallic bridging μ-oxo, and bis(μ-oxo) species of various nuclearity for selected cations (Fe, Ni, Co, Cu, Zn) are shown in Fig. 11a–c. Examples of heterometallic M_1–(μ-O)–M_2 analogues (predicted by DFT) include $[Cu(\mu\text{-}O)Zn]^{2+}$ in MFI and FAU zeolites[152] or $[Cu(\mu\text{-}O)Ag]^{2+}$ entities hosted in ZSM-5.[153] The nearest environment (sitting topology) exhibits a noticeable effect on their stability, as illustrated by the μ-oxo $[Fe(\mu\text{-}O)Fe]^{2+}$ species, and even more markedly by the bis(μ-oxo) $[Fe(\mu\text{-}O)_2Fe]^{2+}$ species accommodated in the α, β, γ, δ positions of the ZSM-5 zeolite (Fig. 11d1 and d2).[154]

It should be emphasized that univocal spectroscopic identification of the particular oxo-entities in the presence of speciation, which is a typical case, is a challenging endeavour. Overlapping of signals, insufficient structure sensitivity, and poor resolution are typical impediments. These can be exemplified by Fe/ZSM-5 zeolites, which may exhibit UV-vis bands virtually identical to those of isolated and dimeric oxo iron sites when the antiferromagnetic coupling is weak.[160] Therefore, the application of site-selective spectroscopies such as variable-temperature and variable-field magnetic circular dichroism (VTVH-MCD), resonance Raman, EXAFS, or advanced multi-frequency EPR techniques, especially when combined with isotopic labelling, provides the most reliable information on metallozeolites regarding the actual nature of the active sites.[5]

Apart from the electronic structure, magnetic interactions may also exert an appreciable influence on the catalytic activity of the oxo-species. Therefore, their spin state and the structural and orbital factors that determine the magnetic exchange coupling between the TMI should also be examined for a thorough understanding of the structure–reactivity relationship. This issue has been recently addressed in the case of bridging $[Cu(\mu\text{-}O)Cu]^{2+}$ cores hosted in CHA and MFI zeolites.[161] The dissimilar spin states, antiferromagnetic in MFI and ferromagnetic in CHA, revealed by variable-temperature/variable-field magnetic circular dichroism spectroscopy, exhibit different reactivities in CH_4 hydroxylation. Coupling between both Cu^{2+} (S = 1/2) cations of the intrazeolite $[Cu(\mu\text{-}O)Cu]^{2+}$ species leads to an antiferromagnetic (S = 0) state in Cu-MFI (Fig. 12a) and ferromagnetic (S = 1) ground state in

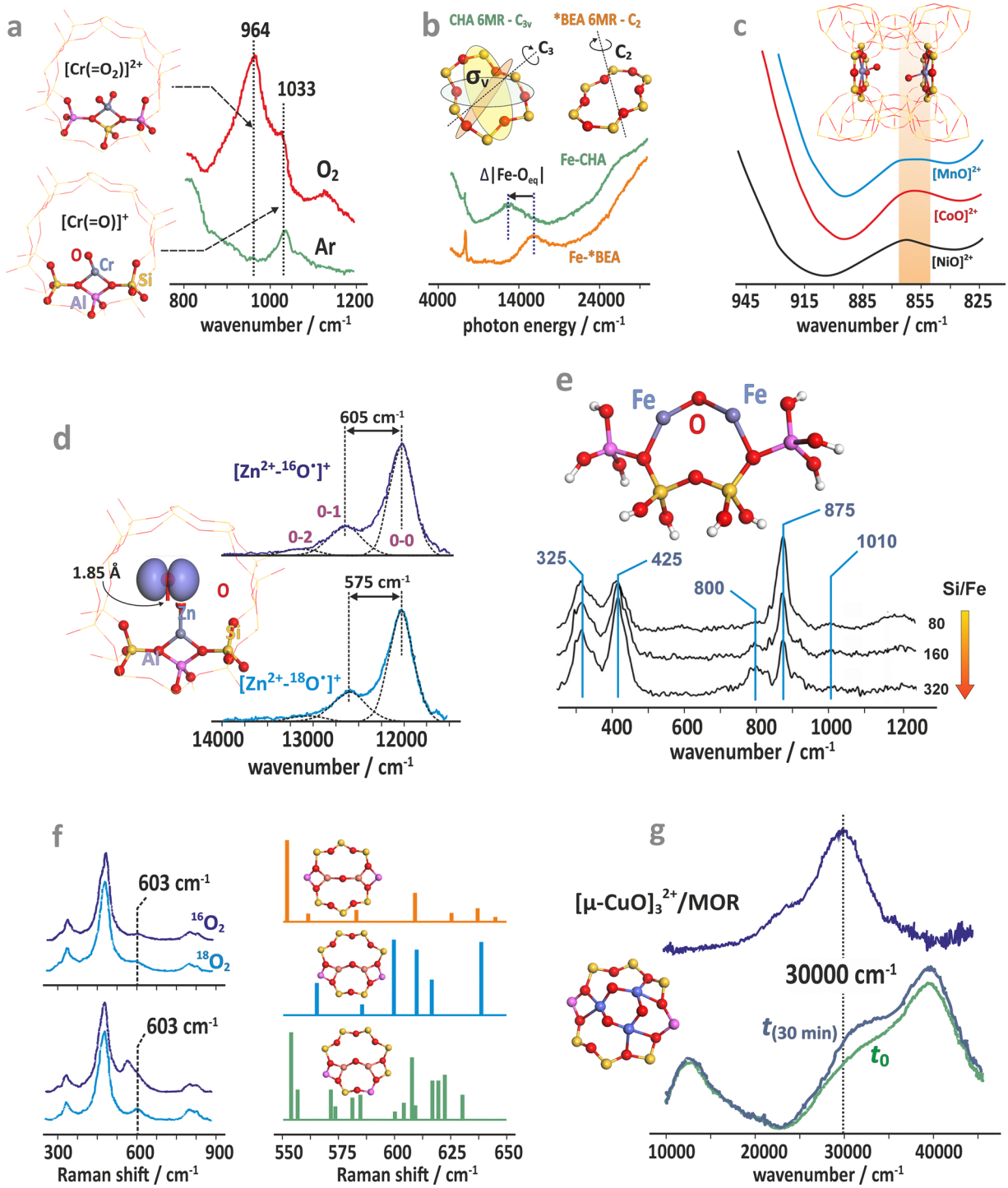

Fig. 10 Survey of spectroscopic techniques used for probing the intrazeolite metal–oxo species. Raman spectra for the Cr/ZSM-5 (Si/Al = 15) catalyst (a).[146] UV-Vis spectra of iron in CHA and BEA (b),[147] FTIR spectra of Ni-, Mn-, and Co-ferrierite samples showing perturbation of the region of T–O–T vibrations by the corresponding oxo-species (α-oxygen), illustrated here by distant binuclear centers (c),[148] UV-vis-NIR vibronic absorption spectra of the isotopically labelled Zn^{II}–$O^{\bullet-}$ complex formed in the MFI-type zeolite framework (d).[137] *In situ* UV resonance Raman spectra of the high-temperature-treated Fe/ZSM-35 samples with different Si/Fe ratios (e).[149] *In situ* steady-state Raman spectra of Cu/CHA-I (top) and Cu/CHA-M (bottom) after activation with $^{16}O_2$ and $^{18}O_2$ and the corresponding structures along with the simulated Raman spectra (f).[150] *In situ* UV-vis spectra of Cu/MOR during activation in O_2 at 200 °C and the corresponding difference spectra (blue) obtained by subtracting the initial spectrum (g).[151] The figure was based on data from the quoted references.

Cu-CHA (Fig. 12b). Surprisingly, it does not dependent on the Cu–O–Cu angle (as it usually is observed in homogeneous complexes), but is governed by the mutual arrangement of the bidentate (π-type ligation) moieties linked to the two copper

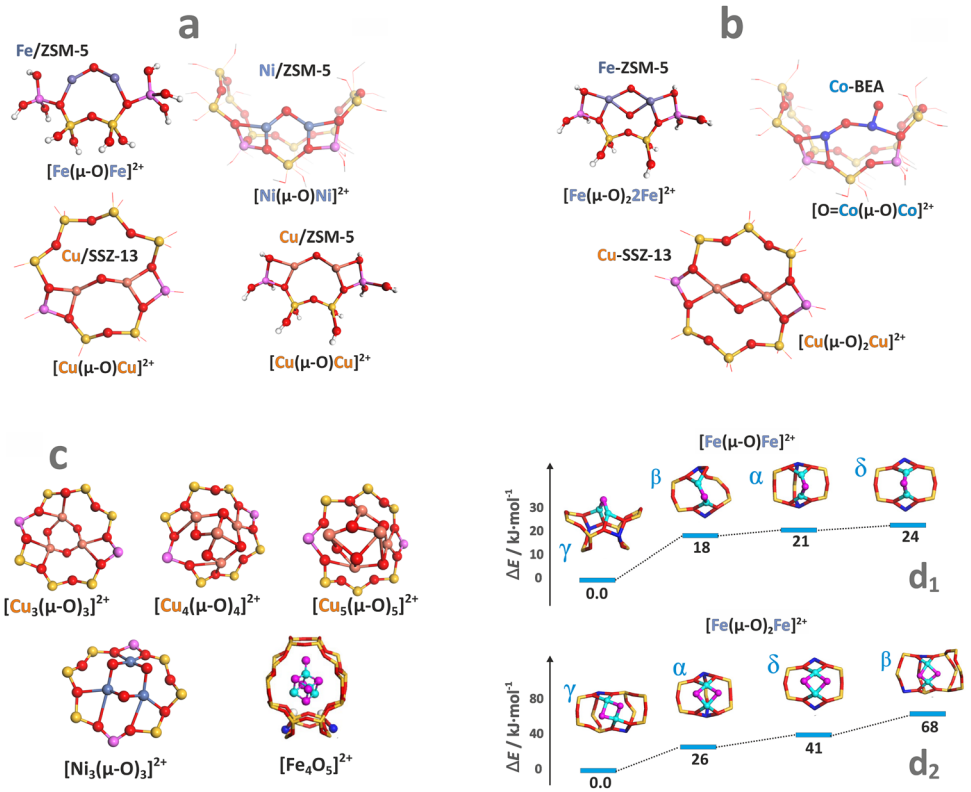

Fig. 11 Structure of selected oligomeric oxo-species (derived from DFT optimisation). Mono-oxo species (a), dual oxygen species (b), and oligomeric M_xO_y species with $x \geq 3$ (c).[18,149,155–159] Relative stability of the μ-oxo $[Fe(\mu\text{-}O)Fe]^{4+}$ (d_1), and the bis(μ-oxo) $[Fe(\mu\text{-}O)_2Fe]^{2+}$ (d_2) entities accommodated at the α, β, γ, δ positions of ZSM-5 zeolite.[154] The figure was based on data from the quoted references.

cations (AlO–Cu–OAl). Therefore, the zeolite framework topology imposes unique spin patterns in the $[Cu(\mu\text{-}O)Cu]^{2+}$ cores, resulting in a distinctly different magnetic structure and reactivity through the rigid, stereo-specific bidentate ligation effect.[161]

Molecular orbital interpretation of the magnetic structure of the exchange-coupled oxygen-bridging cores can be analysed with the DFT broken symmetry (BS) calculations, taking as an example the $[Fe(\mu\text{-}O)_2Fe]^{2+}$ species hosted in ZSM-5 zeolite.[162] The relevant magnetic orbitals are visualized in Fig. 12c. The α/β pairs of magnetic orbitals shown in Fig. 12c constitute symmetric magnetic exchange pathways between the 3d Fe states *via* the in-plane σ–π overlap (orbitals 1, 2, 4), and the out-of-plane π–π overlap (orbitals 3 and 5) mediated by the 2p oxo orbitals. Such pathways indicate that the antiferromagnetic coupling is realized by the superexchange interactions *via* both μ-oxo bridges.[163] The spin coupling parameter J can be calculated within the broken-symmetry approach using, for example, the $E_{HS} - E_{BS} = -(2S_1S_2 + S_2)J$ equation, which has been demonstrated to provide more accurate coupling constants for DFT calculations.[164] The J values for several dinuclear oxo and hydroxo species hosted in the 6MR and 8MR rings of SSZ-13 and in ZSM-5 zeolites can be found elsewhere, along with the impact of the magnetic interactions on N_2O decomposition.[164,165] These points are discussed in Chapter 4.3.3.

3. Thermodynamic factors influencing the speciation of metal centres in zeolites

The chemistry of TMI in zeolites is complex because of speciation into isolated bare cations (of different valence state M^{n+}), isolated oxygen-containing species (metal–oxo and metal–oxyl complexes), dinuclear oxo-cations, larger oligomeric metal–oxo species, and segregated M_xO_y oxide particles that often coexist within the same zeolite catalyst. They may undergo distinct transformations evolving significantly under different conditions, ranging from catalyst pretreatment and activation to actual reaction conditions.[71,166]

The most important chemical processes during activation of metallozeolites include hydration, hydroxylation, olation, oxolation, auto-reduction (*in vacuo*) or oxidation in the presence of O_2.[33,167,168] The interrelation of these processes for zeolite TMI centers (M^{n+}) associated with single (z_1) and double (z_2) aluminum sites (isolated and dual exchange centers, respectively), which bear a formal negative charge of −1 and −2, is schematically illustrated in Fig. 13, and the corresponding reactions are summarized in Table 3. The possibility of further transformations of dual metallic centers into polynuclear metal–oxo species is discussed below (Fig. 16). First-principles thermodynamic modelling is often used to provide a clear background

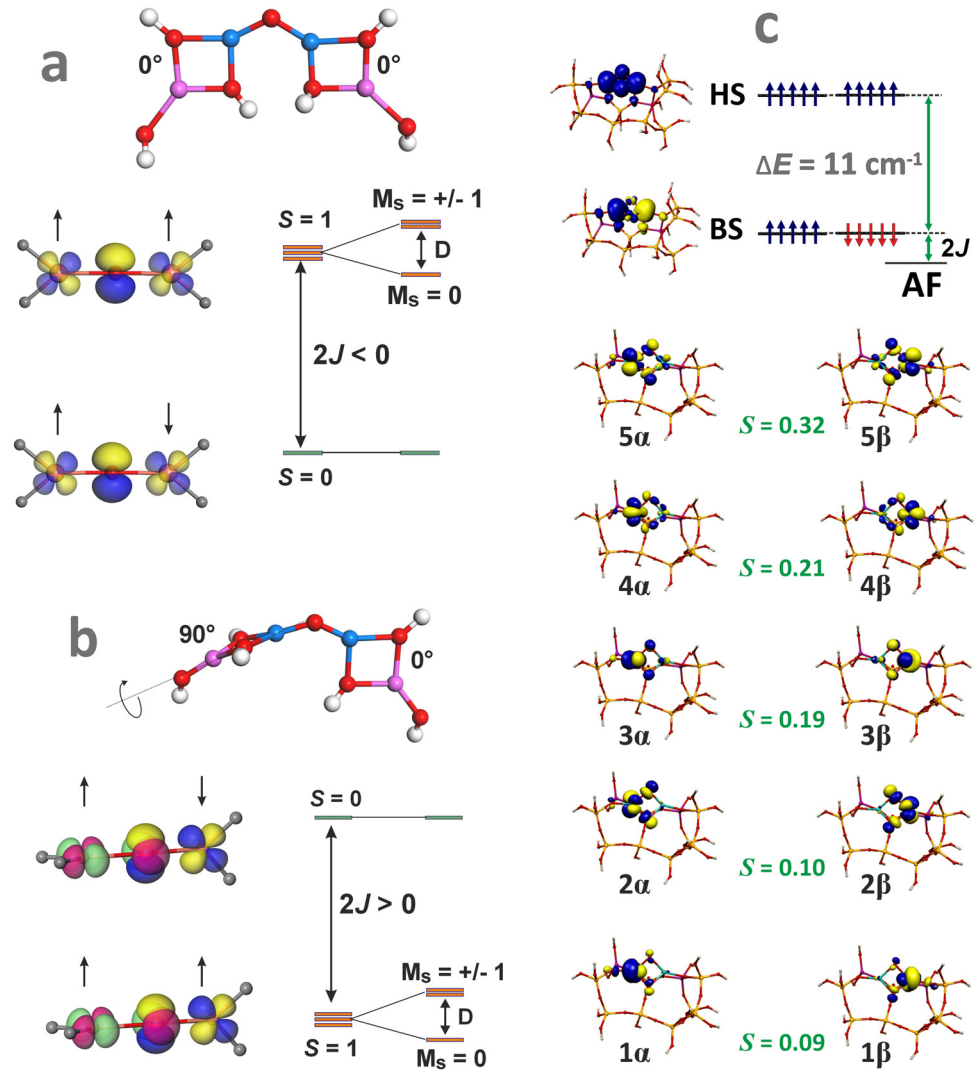

Fig. 12 Structural features of the Cu–O–Cu entities that lead to an antiferromagnetic coupling in MFI (a) and a ferromagnetic coupling in CHA (b), based on data from ref. 161. Broken symmetry picture (UKS B3LYP/SOMF TZV/CP(PPP) calculations) of the magnetic structure of the $[Fe(\mu\text{-}O)_2Fe]^{2+}$ species hosted in ZSM-5 zeolite matrix (c).

for relating the feasibility of these processes to their energetics and various T,p conditions.

3.1. First-principles thermodynamics of metallozeolites

One of the most useful computational techniques applied for the modelling of metallozeolite catalysts beyond the basic "0 K/UHV model"[169] is the first principles thermodynamics (FPT). It integrates density functional theory (DFT) with statistical physics to describe the stability, possible transformations, and reactivity of the investigated system at the atomic level, as a function of the temperature and pressure of reactants.[170,171] After appropriate adaptation, FPT is now routinely applied in modelling of the zeolite catalytic materials and their adsorption properties.[15,165,172] Typically, (i) a parent zeolite network distinct by the amount and distribution of Al atoms, where formal negative charge generated by z $AlOH_4$ units is counterballanced by z protons (zeolite (zH)), (ii) a bulk metal ($M_{(bulk)}$ – serving as the source of the metallic centers), and (iii) relevant gaseous reagents that may interact with the zeolite centers (*e.g.*, $H_2O_{(gas)}$ and $O_{2(gas)}$ in case of catalyst pretreatment) are used as convenient reservoirs of the involved species. Such an assembly is shown in Fig. 16a$_1$, where gas phase, bulk metal, and zeolite parts (b_1, b_2, and b_3, respectively) are used to build a specific model of metal-exchanged zeolite interacting with exemplary $O_{2(g)}$ and $H_2O_{(g)}$ molecules. In this case, general equilibrium reaction (eqn (3)) of the zeolitic system ($M_xH_nO_m$) formation may be formulated as:[154]

$$\text{zeolite(zH)} + x\text{M}_{(\text{bulk})} + \frac{n-z}{2}\text{H}_2\text{O} + \frac{2m-n+z}{4}\text{O}_2 \leftrightarrow \text{zeolite(M}_x\text{H}_n\text{O}_m) \quad (3)$$

with the reaction energy defined by eqn (4).

$$\Delta E = E_{\text{zeolite(M}_x\text{H}_n\text{O}_m)} - E_{\text{zeolite(zH)}} - xE_{\text{M}} - \frac{n-z}{2}E_{\text{H}_2\text{O}} - \frac{2m-n+z}{4}E_{\text{O}_2} \quad (4)$$

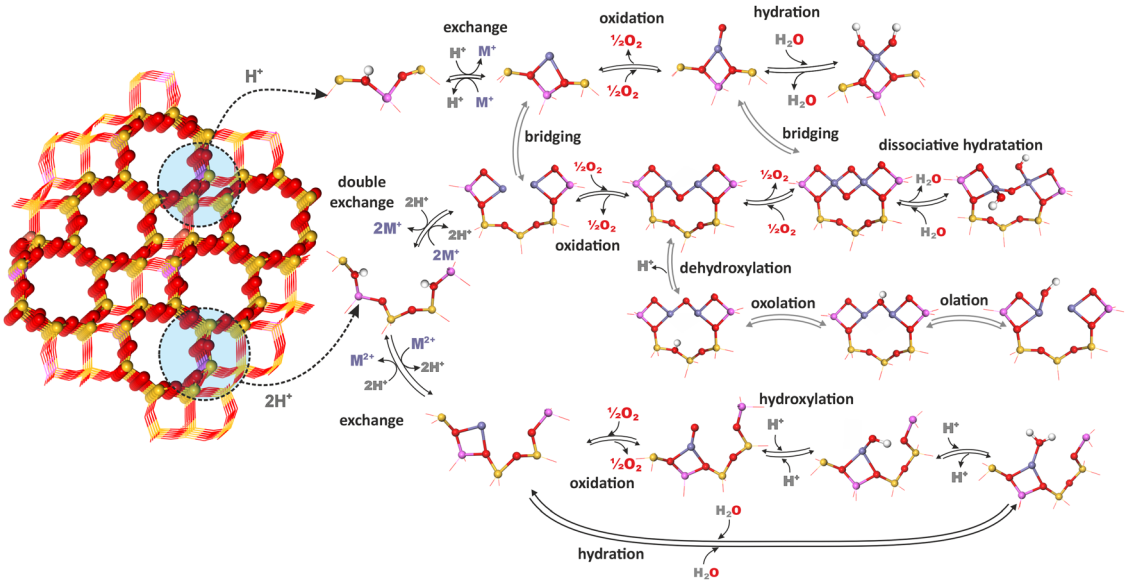

Fig. 13 Typical transformations of metal-containing zeolite centers controlled by thermodynamic conditions (temperature and O_2/H_2O pressures) associated with single (z_1) and double (z_2) exchange sites (tetrahedral AlO_4^- units). Atom color coding: O – red; Si – yellow; Al – pink; H – light grey; TMI (M^{n+}) – pale blue.

Table 3 The most important chemical processes taking place during the synthesis and activation of metallozeolites. The formal negative charge of the zeolite framework associated with tetrahedral $(AlO_4)^-$ units is denoted z

Autoreduction of oxo-species	$2[M^{n+}\text{–}O^{2-}](z) \rightleftharpoons 2M^{(n-2)+}(z) + O_2$
Direct oxidation to metal–oxo species	$M^{n+}(z) + 1/2O_{2(g)} \rightleftharpoons [M\text{–}O]^{n+}(z)$
Intrazeolite hydrolysis	
Associative hydration	$M^{n+}(z) + mH_2O_{(g)} \rightleftharpoons (z)M^{n+}\text{–}(H_2O)_m$
Dissociative hydration (hydroxylation)	$M^{n+}(z) + H_2O_{(g)} \rightleftharpoons M(OH)^{(n-1)+}(z) + H^+$
Agglomeration into oligomeric metal–oxo entities	
Olation	$M(OH)^{(n-1)+}(z) + M^{n+}(z) \rightarrow (M\text{–}OH\text{–}M)^{(2n-1)+}(z_2)$
Oxolation	$(M\text{–}OH\text{–}M)^{(2n-1)+}(z_2) \rightarrow (M\text{–}O\text{–}M)^{(2n-2)+}(z) + H^+(z)$
Oxidative oxolation	$3[(z)M^{2+}\text{–}OH^-)] + 1/2O_2 \rightarrow (z_2)[M_3(\mu\text{-}O)_3]^{2+} + H_2O + H^+(z)$
Merging of metal–oxo species	$2[MO]^{n+}(z) \rightarrow [M(\mu\text{-}O)_2M]^{2n+}(z_2)$

where $E_{\text{zeolite}(M_xH_nO_m)}$ is the total energy of the metal containing zeolite with active sites covered by water/oxygen, $E_{\text{zeolite}(zH)}$ is the energy of the initial H-form of the zeolite with z Al sites and z protons, whereas E_M, E_{H_2O} and E_{O_2} correspond to the computed total energies of bulk metal M, gaseous water, and gaseous dioxygen, respectively. The ΔE values are obtained from periodic DFT calculations, which assure fairly good accuracy in combination with good computational efficiency. Geometries and energetics computed using hybrid functionals (*e.g.*, B3LYP, B3PW91,[173] and PBE0[174]), complemented by inclusion of the semiempirical treatment of the dispersion interactions,[175,176] generally align well with experimental results, and high-level post-HF calculations, as well.[177,178] However, benchmark calculations comparing different levels of the DFT methods are highly valuable, allowing for sensible selection of the required computational scheme.[172,179–181]

The change in the free energy ΔG due to intrazeolite chemical processes is given by:

$$\Delta G(T,p) = \Delta E + \frac{2m - n + z}{4}\Delta\mu_{O_2} + \frac{n - z}{2}\Delta\mu_{H_2O} \qquad (5)$$

where the chemical potential differences of gaseous reactants (herein $\Delta\mu_{O_2}$ and $\Delta\mu_{H_2O}$) are obtained applying standard statistical thermodynamics.[182] Using gas-phase molecules as a reference state for interaction with the active sites, the changes in chemical potential correspond to the external equilibria with reactants located outside the zeolite channels (Fig. 14a$_1$ with the reference states taken from (Fig. 14b$_1$–b$_3$)). For modelling the internal equilibria, the intrazeolite molecules (molecule$_{(IC)}$) are used as a reference state (Fig. 14a$_2$ with the reference states taken from Fig. 14b$_2$–b$_4$). The entropy correction for the in-cage molecule can be calculated using molecular dynamics methods[183–185] or estimated by scaling, for instance, to the

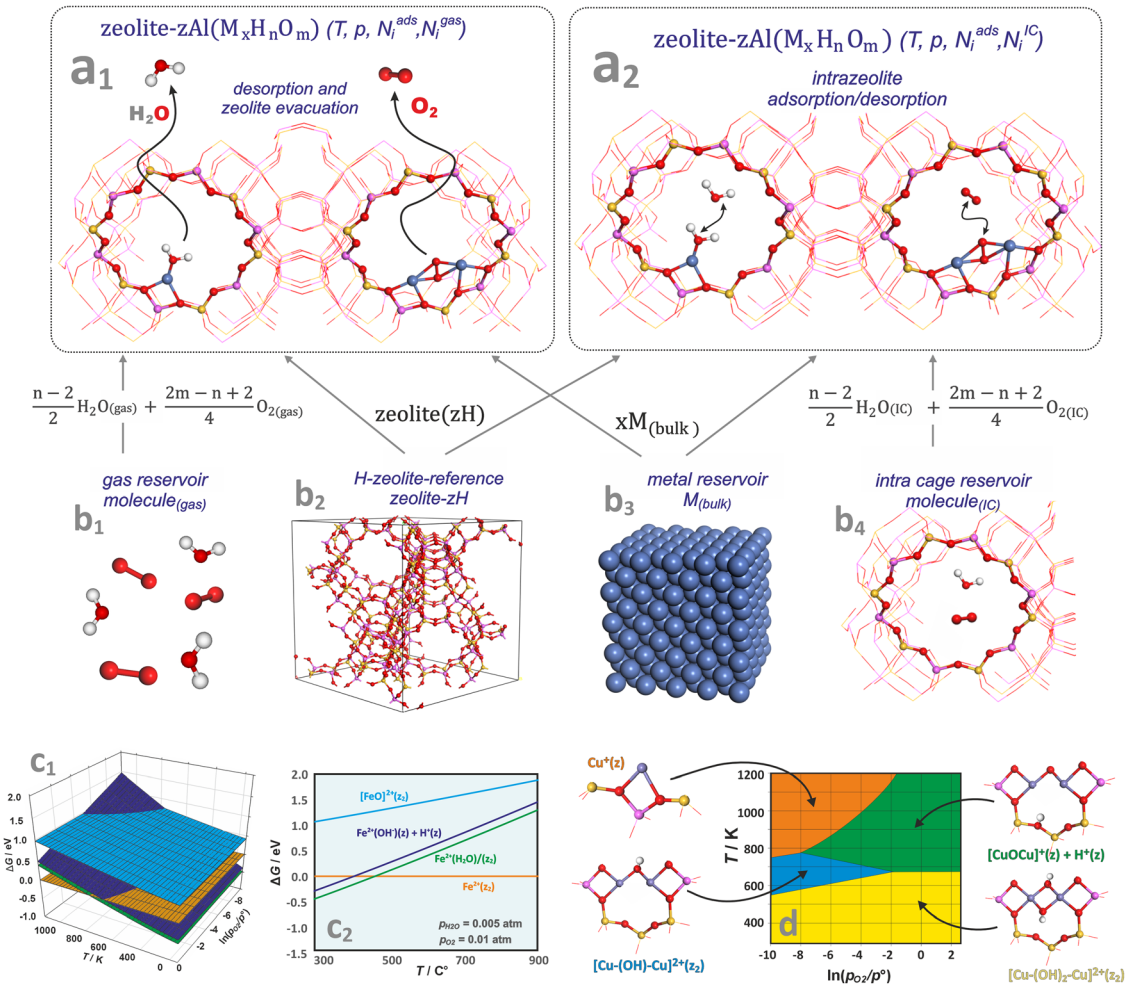

Fig. 14 A molecular model of zeolite in equilibrium with free-standing molecules (a_1), and molecules trapped inside zeolite cages (a_2) together with molecular and bulk-phase reservoirs used in FTP modelling to assemble the zeolite catalyst in equilibrium with the reactants (b_1)–(b_4). The 3D (c_1) and 2D (c_2) representations of the thermodynamic diagrams representing the stability of iron species in the Fe/SSZ-13 zeolite as a function of (T,p_{O_2}) and (T), respectively. Bottom envelope of 3D FPT diagram representing stability regions (T,p_{O_2}) of dual copper sites in the Cu/CHA zeolite (d), based on ref. 181.

NH_3-TPD peaks for catalysts with well-defined active sites.[172] It is noteworthy to recognize that the Al configuration may not be constant under experimental conditions.[186] As a practical solution, several stoichiometric or configurational models of the zeolite catalyst can be evaluated comparatively.

Thermodynamic phase diagrams, constructed using first-principles data, provide insight into the various aspects of metal–zeolite chemistry within the widespread operational limits of pressure, temperature, and composition. They are typically presented in the form of 3D (see Fig. 14c_1) and 2D (Fig. 14c_2) plots, where the Gibbs energy is plotted as a function of temperature and the pressures (or chemical potentials) of the reactants. Due to the constraints imposed by the 2D/3D representation, thermodynamic properties are often presented assuming variable temperature and the partial pressure of one gas reactant, with the other variables fixed or constrained by the reaction stoichiometry (*e.g.*, $NO/NH_3 = 1$ in SCR reaction).

As an example, the stabilities of different iron species present in the Fe/SSZ-13 zeolite are compared in Fig. 14c_2 as a function of temperature, with the oxygen and water partial pressures fixed at $p_{O_2} = 0.01$ atm, and $p_{H_2O} = 0.005$ atm. At low temperatures, the most stable form is the hydrated $Fe^{2+}(H_2O)(z_2)$ center, which releases a water molecule at around 250 °C. The hydroxylated forms, $Fe^{2+}(OH)(z) + H^+(z)$, are slightly less stable than the hydrated Fe cations across the entire temperature range (thus, both forms may coexist). In contrast, the terminal iron-oxo species, $[FeO]^{2+}(z_2)$, of the highest free energy, are not expected to appear in the whole temperature range.

To present the results more explicitly, often only the lower envelope of the FPT diagrams (defining the most stable species) is shown (Fig. 14d). Such a 2D diagram, for instance, reveals the thermodynamic conditions of copper auto-reduction in the Cu/SSZ-13 zeolite.[181] For low water vapor pressure ($p_{H_2O} = 10^{-6}$), three stable dual-, and one mono-copper sites are expected depending on the (T,p) conditions. At lower temperatures ($T < \sim 500$ K), regardless of the oxygen pressure, the Cu–$(OH)_2$–Cu(z_2) dimer dominates, whereas at higher temperatures it transforms into an oxygen-bridged entities, Cu–O–Cu(z) +

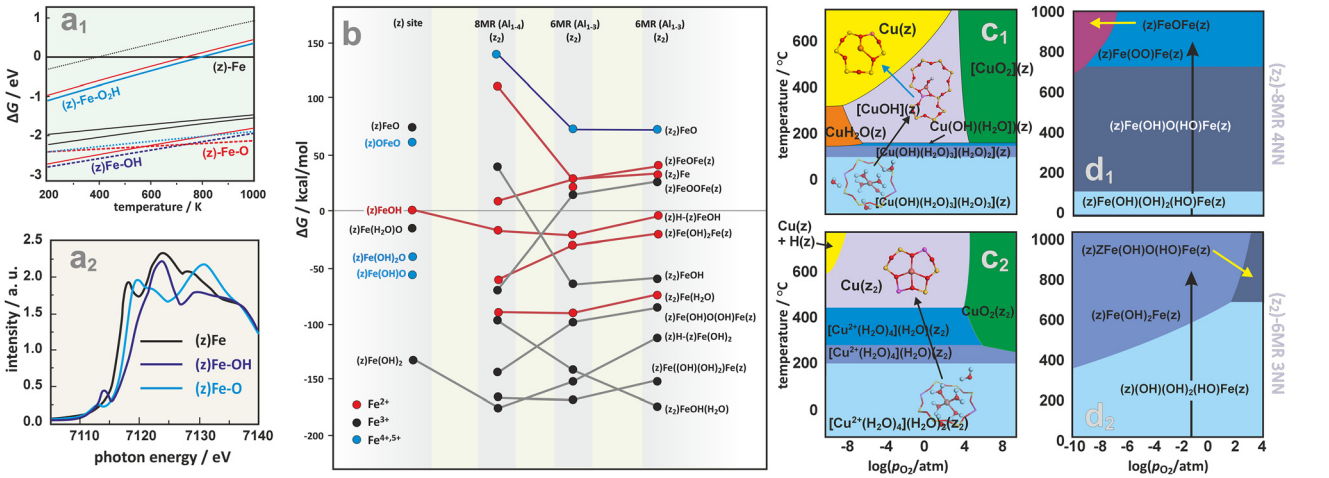

Fig. 15 2D thermodynamic diagram representing stability of iron active centers formed within the six- or eight-membered rings (6MR or 8MR) of Fe/SSZ-13 (a_1), together with the associated XANES spectra simulated for the most important species (a_2).[187] The expanded diagram (b) comparing the stability of Fe species on isolated (z_1) and dual (z_2) exchange centers positioned in 8MR and 6MR rings of CHA zeolite with different Al distribution (Al_{1-3} *vs.* Al_{1-4}).[165] Calculated (HSE06-TSvdw) copper speciation phase diagrams for 1Al (c_1) and 2Al (c_2) exchange sites of Cu/SSZ-13.[188] Phase diagrams for iron speciation in Fe/SSZ-13 zeolite as a function of relative O_2 pressure and temperature with $p(H_2O)$ set at 0.02 atm, constructed for sites stabilized within the z_2-8MR (d_1) and z_2-6MR (d_2) rings.[165] The figure was based on data from the quoted references.

H(z), with desorption of a water molecule, or into a Cu–(OH)–Cu(z_2) dimer upon losing the OH group. These transformations are controlled by the oxygen pressure with a threshold value of ~0.01 atm. Under the most reducing conditions (highest T and lowest p_{O_2}, orange area), copper bridges are expected to decompose, leading to the formation of two adjacent highly reactive monomeric copper(I) centres (Cu(z)) (Chapters 4.3.1 and 4.3.3).

FPT modeling is also a convenient tool that enables comparison of the stability and evolution of intrazeolite active sites such as (z)FeOH, (z_2)FeOH, (z)FeO, (z_2)[FeO]$^{2+}$, (z)Fe-OH$_2$ in the six- or eight-membered rings (6MR or 8MR) of Fe/SSZ-13.[187] The corresponding phase diagram (Fig. 15a_1) implies that H_2O prefers to adsorb on a Fe^+ cation in a wide range of temperatures. However, the hydrated sites are much less stable than the hydroxylated (z)FeOH and (z)FeO species, which dominate at low and high temperatures, respectively. The most energetically favourable sites for iron accommodation are 6MR rings (Fe in 8MR are less stable by 0.5 eV). Still, upon ligation of water, hydroxyl, and oxygen species, the energy gap between Fe located in the 8MR and 6MR sites becomes negligible. The K-edge of XANES spectra (see the simulated spectra in Fig. 15a_2) is diagnostic for the presence of those ligands in the coordination sphere of the Fe cations.[187]

A more advanced analysis of the stability of different iron forms in the isolated (z) and dual (z_2) exchange centers in the chabazite-type zeolite is illustrated in Fig. 15b, where ring multiplicity (8MR *vs.* 6MR), internal aluminum distribution (Al_{1-3} *vs.* Al_{1-4}), formation of bridged species and the possibility of iron existing in higher oxidation states are taken into account as well.[165] This diagram can be used to track the evolution of Fe sites under various pretreatment conditions, showing that autoreduction temperatures and water desorption conditions are highly dependent on the proximity of aluminum atoms and the nuclearity of iron.

In the case of Cu/SSZ-13 zeolite, the akin phase diagrams representing evolution of CuOH(z) and Cu(Z_2) as a function of temperature and O_2 pressure at fixed H_2O pressure,[188] are shown in Fig. 15c_1 and c_2, respectively. Both Cu sites are hydrated under ambient conditions (where solvated Cu^{2+}–H_2O and $[CuOH]^+$ dominate), and become dehydrated at elevated temperatures in an O_2 environment. However, only CuOH(z) species undergo autoreduction to monovalent copper (Cu(z)) in the inert environment (Fig. 15c_1). The preference of populating the Cu(z_2) sites over CuOH(z) sites is independent of the extent of hydration.[15]

A comparison of the Fe ions' stability in the 8MR (Fig. 15d_1) and 6MR (Fig. 15d_2) rings of the Fe/SSZ-13 zeolite as a function of T, p_{O_2}, and p_{H_2O}[165] revealed a dramatic impact of the ring multiplicity on the distribution of dimeric iron centers. At room temperature, the most stable species are the iron-dimers ligated by water (without their detachment from the framework). They are initially in the most stable trivalent state, and as the temperature rises, all sites transform into partially dehydrated entities at T = 100 °C and 450 °C for 8MR and 6MR, respectively. An additional difference of even greater significance for the catalytic activity arises from the fact that the dimers in the 8MR ring transform into (z)Fe–(μ-O)$_2$–Fe(z) bridging species, while the 6MR dimers are stabilized as (z)Fe–(OH)$_2$–Fe(z). The latter sites contain divalent iron and may be treated as "autoreduced" (similarly to the monocopper sites in Cu-/SSZ-13[61,188]). The autor-eduction temperatures vary widely from site to site, and the high-temperature activated zeolites are expected to contain a mixture of Fe^{2+} and Fe^{3+}. The validity of such prediction has been proven for Fe/ZSM-5 and Fe/Y zeolites heated in helium (or in vacuum) using the X-ray absorption and Mössbauer spectroscopies.[189,190]

Going beyond the charged mono- and dimeric centres requires a sensible postulation of proper chemical processes

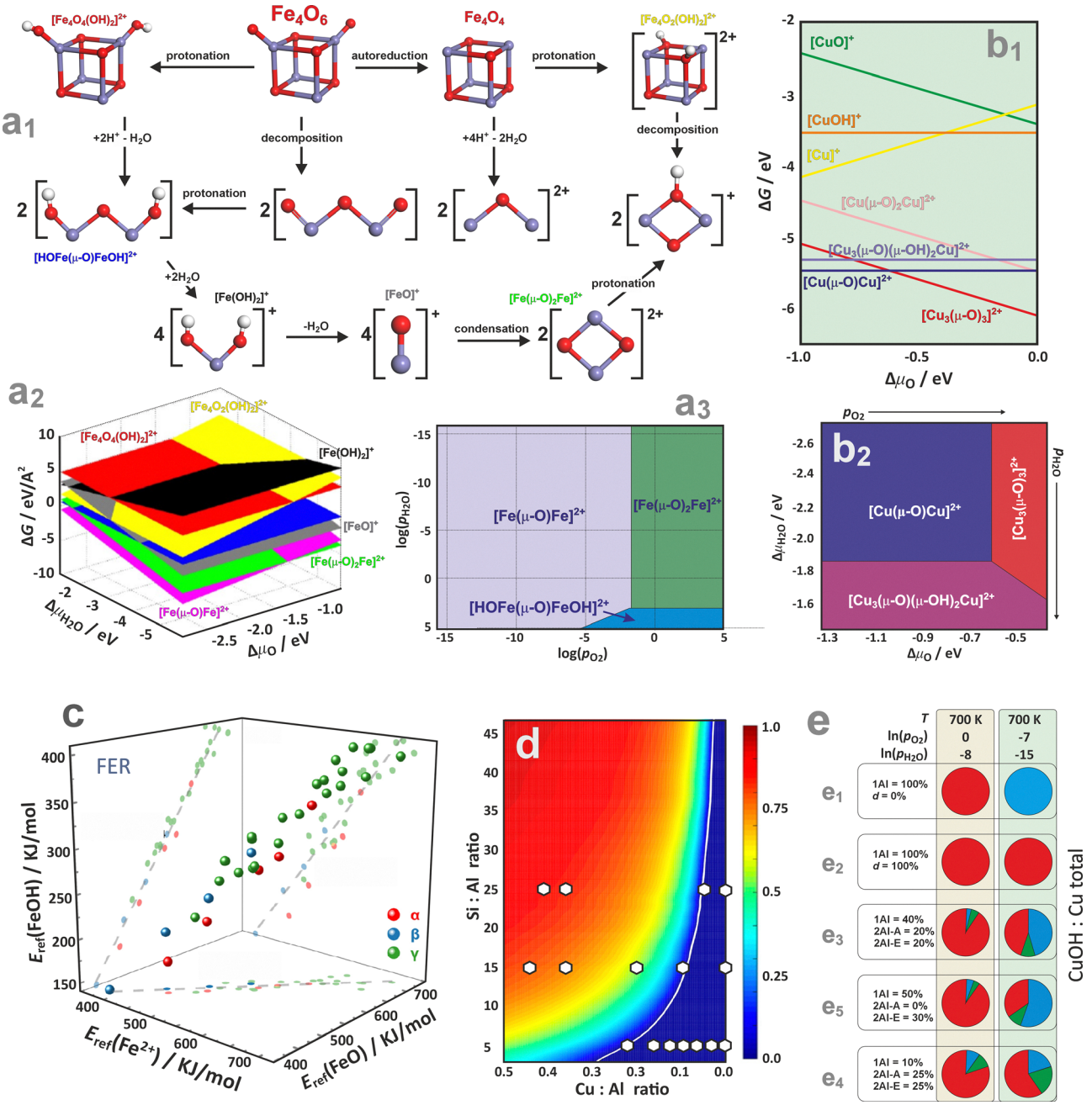

Fig. 16 Possible transformations of a cubic Fe_4O_6 cluster (a_1), together with the FPT diagram representing the stability of the most important iron forms in the 3D (a_2) and 2D (a_3) representation, based on data from ref. 154. The relative stabilities of multi-nuclear copper species hosted in the ZSM-5 zeolite, as a function of $\Delta\mu_O$ (b_1) and (T,p_{O_2}) (b_2), based on data from ref. 191. The stability correlations of the Fe^{2+}, $[FeO]^{2+}$, and $[FeO]^{2+}$ species accommodated in the ferrierite α, β, and γ sites (c), adapted from ref. 195 with permission from Wiley, Copyright 2025. The CuOH/Cu fraction plotted as a function of the Si : Al and Cu : Al, revealing regions representing a composition space where Cu^{2+} species dominate (below white line), and a space where gradual increase in the $[ZCuOH]^+$ fraction is expected (above the white line), white circles denotes experimental results (d), adapted from ref. 188 with permission from American Chemical Society, Copyright 2016. Distribution of Cu^{2+}, Cu^+, $[Cu_2OH]^{2+}$ species (coded with blue, red, and green, respectively), presented as pie charts for Cu/SSZ-13 zeolite hypothetical samples (e) based on data from ref. 61. Samples (e_1)–(e_5) differ in the distribution of the monomeric and dimeric exchangeable 1Al and 2Al centres, in Al pair arrangements, and in defect concentrations (d) and are studied under different conditions (top and bottom row).

interconnecting the dispersed and oligomeric metal species in the presence of H_2O, O_2, and the zeolitic protons as well. An exemplary diagram representing possible transformations of a bulky Fe_4O_6 cluster hosted in the Fe/ZSM-5 zeolite is shown in Fig. 16a_1.[154] Its decomposition into binuclear species (*via* protonation at Brønsted acid sites) proceeds either through hydrolysis, leading to isolated oxygenated or hydroxylated mononuclear species, or through dehydration, forming oxo-

bridged $[Fe(\mu\text{-}O)Fe]^{2+}$ species. Thermodynamic diagrams confirm that the intrazeolite $[Fe(\mu\text{-}O)Fe]^{2+}$ and $[Fe(\mu\text{-}O)_2Fe]^{2+}$ binuclear complexes represent the most stable species under typical reaction conditions (Fig. 16a2–a3). They preferentially occupy the γ site (8MR), but other iron varieties of comparable stability can also lodge at the α, δ, and β sites (6MR). Oxygen pressure controls the thermodynamically preferred mixing between the $[Fe(\mu\text{-}O)Fe]^{2+}$ and $[Fe(\mu\text{-}O)_2Fe]^{2+}$ binuclear clusters. The formation of Fe^{2+} ions and binuclear complexes occurs only at high temperatures, aligning well with experimental observations.[154]

Comprehension of thermodynamic conditions is crucial when analysing multinuclear copper species in ZSM-5 zeolites, as the stability of the extra-framework complexes involved is strongly influenced by temperature and the composition of the gas phase (Fig. 16b1 and b2).[191] The binuclear Cu sites correspond to the lowest-energy structures, yet under the O_2-rich conditions, typically employed for the activation of Cu/ZSM-5 catalysts, when *T*- and *p*-related effects are taken into account, the $[Cu_3(\mu\text{-}O)_3]^{2+}$ trinuclear complex turns out to be more stable than the mono- and binuclear species. The intrazeolite mononuclear oxo- and hydroxo-complexes are generally less stable than the oligonuclear species.[192–194]

The thermodynamic analysis can also be used to draw more general conclusions than the relative stability of TMI within the given zeolite network structure. For example, a noteworthy analysis of the FTP data on iron species stabilized in the 6MR, 8MR sites of chabazite, and α, β and γ sites of ferrierite zeolites (Fig. 16c), allowed for the demonstration that there is a distinct linear correlation ($R^2 \sim 0.9$) between the stabilities of the Fe^{2+}, [FeO], and $[FeOH]^+$ species.[195] This implies that the stability trends of the related Fe^{2+}, [FeO], and $[FeOH]^+$ species with the varying framework type and the Al distribution remain consistent, regardless of thermodynamic conditions, and are, therefore, of a more general character.

The impact of Al arrangements on the monomer and dimer configuration of Cu cations and their oxidation state, concerning the auto-reduction of Cu in SSZ-13,[188] is illustrated in Fig. 16d. Within the assumption that the exchanged copper ions initially populate all available dual sites as Cu^{2+}/z_2, before occupying 1Al sites in the form of $Cu^{2+}OH/z$, the CuOH/Cu fraction can be assessed as a function of the Si : Al and Cu : Al ratios.[196,197] Two distinct regions, where Cu^{2+} species associated with 2Al are expected to dominate (below the white line), and where a gradual increase in the $Cu^{2+}OH/z$ fraction is predicted (above the white line), can be distinguished. This diagram helps to rationalize the speciation of copper in real catalysts (white circles) depending on the Al/Si and Cu/Al ratios. Furthermore, the pie charts can be used for concise illustration of the relative contributions of key copper species in CHA[61] (Cu^+ – blue, Cu^{2+} – red, $[Cu_2OH]^{2+}$ – green), depending on the zeolite composition (Si/Al, Al pair arrangements, defect concentrations) and thermodynamic (oxidizing or reducing) conditions (Fig. 16e).

4. Interfacial coordination chemistry – principal pathways of ligation

4.1. Molecular picture of ligation

Most simply, the binding of reactants to encaged metal c entres can be rationalized in terms of the molecular orbital diagrams, which can be categorized into normal (NEL), mixed (MEL), and inverted (IEL) energy level schemes (Fig. 17a_1, a_2, and a_3, respectively).[198] In the case of open-shell cations such as Fe^{2+} ($S = 2$), Co^{2+} ($S = 3/2$) Ni^{2+} ($S = 1$) or Cu^{2+} ($S = 1/2$), typically involved in important catalytic reactions with zeolite materials,[13,18,199] for sensible interpretation the corresponding energy level diagrams should be constructed for the α and β channels separately, including the exchange splitting (see Fig. 8). In the normal scheme (Fig. 17a_1), the 3d

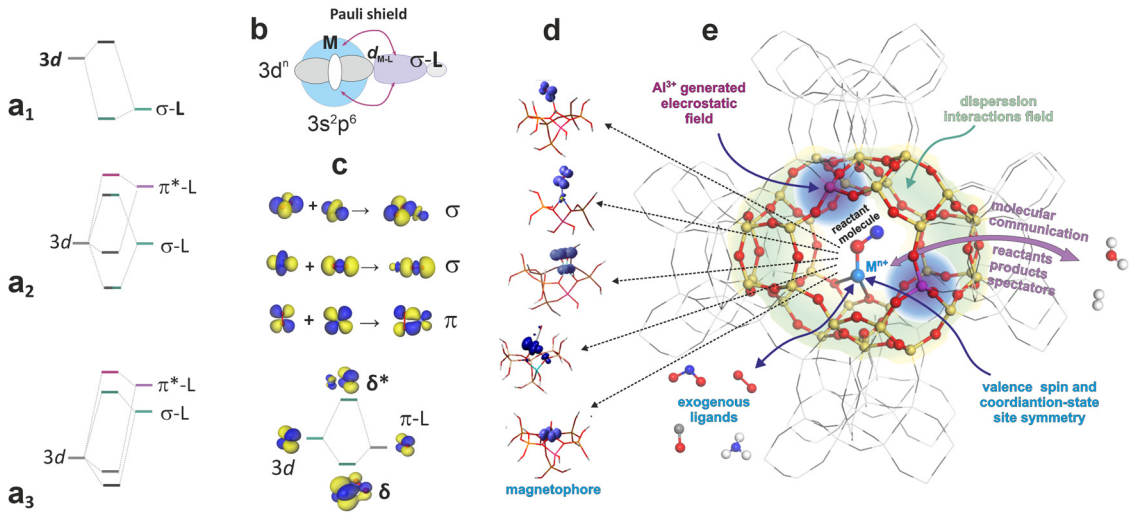

Fig. 17 Schematic representation of the metal–ligand energy levels (a_1)–(a_3), epitomic representation of the Pauli shield (b),[198] and principal types of the molecular orbital overlap sorted by symmetry (c). Five categories of the spin density distributions defining a magnetophore of the open-shell intrazeolite adducts (d), and an exemplary illustration of a zeolite nano-cage reactor with the associated signifiers (e).

levels of the metal centre lie above the occupied levels of the ligands. Since the filled $3s^2p^6$ sub-shell shields the inner 3d orbitals, the resultant Pauli repulsion leads to 'stretched' M–L bonds, which secures the integrity of the $3d^n$ configuration upon ligation.[198] This classic Werner-type scheme is characteristic of the intrazeolite 3d cations, typically in the 2+ oxidation states interacting with the innocent σ-donor ligands such as NH_3 or H_2O (see Chapter 4.2). Intrazeolite adducts with more extensive metal–ligand covalency may lead to the mixed (MEL) pattern (Fig. 17a_2). In the most extreme situations, when 3d levels are situated below those of the ligand, which may be caused by enhanced oxidation state and/or exchange interactions (in the case of open-shell systems), an inverted scheme (IEL) shown in (Fig. 17a_3) is appropriate. Two mechanisms can be distinguished by which the Pauli shield (Fig. 17b) can be breached, and the $3d^n$ integrity of the metal core perturbed. When the cation oxidation state becomes too positive, the 3d orbitals are shifted down in energy so far that the Pauli shield can be broken (from 'outside') by the redox ligands. Analogically, when the 3d orbitals become sufficiently electron-rich, they may overcome the Pauli shield from 'inside' and transfer electron density onto ligands (such as O_2), altering the $3d^n$ configuration of the metal core.[198] These binding modes are discussed in detail in Chapter 4.3.

Attachment of molecules to the caged transition-metal cations *via* σ, π, and δ type overlap (Fig. 17c) may occur in an isodesmic (with conservation of the number of bonds) or an alterdesmic (with a change in the total number of bonds) way. In the former case, new covalent bonds with the coordinated reactants are formed at the expense of the strained bonds between the metal center and the zeolite O_z ligands. The simplest behaviour of intrazeolite transition metal complexes of NEL character in the catalytic redox process consists of oxidation or reduction of the metal centre only, leaving the redox state of the ligands unaffected. Yet, the ligands control indirectly the redox properties of the metal core by modifying the energy levels of the 3d orbitals (see Chapter 4.2.4). In some cases, however, ligands can also participate in the redox process. Then, such ligands are referred to as non-innocent or redox ligands (see Chapters 4.3.1 and 4.3.2).

As a result, the four leading roles the ligated molecules can play in the catalytic reactions are as follows. (i) Tuning of the metal catalytic properties through reduction/oxidation, which strongly influences the affinity to capture reactants, and the mechanistic course of ensuing follow-up reactions. (ii) Acting as an ''electron-reservoir'' in the case of redox active ligand, which allows the metal to store and release electrons on the ligand moiety (anionic redox) in the elementary steps unavailable on the metal core only. (iii) The formation of reactive ligand-radicals that actively participate in the making and breaking of chemical bonds during catalysis. (iv) The modification of the substrate reactivity in cases where the substrate itself acts as a redox non-innocent ligand.[200]

The redox reactivity of the open-shell species, in particular, is governed by the spin density distribution between the metal core and the ligated molecule that both constitute a common magnetophore. The latter notion, analogous to the chromophore in optical spectroscopy, refers to the molecular fragment of a paramagnetic adduct where the bulk of the spin density is confined, thereby determining the magnetic properties of the entire system essentially. Three main magnetophore patterns are categorized as ligand-centred, mixed, and metal-centred (Fig. 17d). The locus of the highest spin density defines the centre of the preferential attack of paramagnetic reactants such as NO, O_2, or NO_2 (see Chapter 4.3.2). The zeolite aperture controls, in turn, the accessibility of these centres to the reactant molecules. In contrast, the speciation and reactivity of the active sites are significantly influenced by the framework topology and the associated confinement effects, as well as the Si/Al and M/Al ratios, and the spatial distribution of the Al atoms. Those aspects are epitomized in the form of a zeolite nanoreactor in Fig. 17e.

4.1.1. Orbital interaction analysis. Metal centres embedded within the zeolite framework exhibit complex interactions with the zeolite framework, and the conventional bonding descriptors (total energy, bond length, bond order) cannot sensibly characterize the reactant molecules. Thus, natural orbital for chemical valence (NOCV) analysis[201] becomes an insightful tool for probing orbital interactions within metal–zeolite systems, offering an advanced understanding of bonding, charge transfer, and electron distribution in these materials. NOCV analysis enables the separation and quantification of electron and spin density transfer channels, such as π-backdonation or σ-donation, between virtually delineated interacting fragments. The pairs of the natural orbitals for chemical valence (Ψ_{-k}, Ψ_k) allow for decomposition of the differential charge density, $\Delta\rho$, into the particular NOCV contributions ($\Delta\rho_k$):[201]

$$\Delta\rho(r) = \sum_{k=1}^{M/2} \nu_k \left[-\psi_{-k}^2(r) + \psi_k^2(r)\right] = \sum_{k=1}^{M/2} \Delta\rho_k(r) \qquad (6)$$

The ν_k stands for the NOCV eigenvalues, and M for the number of basis functions. The eigenvalue expresses a fractional electron population transfer in each electron flow channel. For open-shell systems, the decomposition is carried out separately for the α and β electron densities (spin-resolved NOCV). Afterwards, the contributions of similar orbital character appearing in both spin densities can be treated jointly. The NOCV analysis, combined with the Ziegler–Rauk extended transition state energy decomposition scheme (ETS-NOCV),[202] allows for the partitioning of the total orbital interaction energy into particular NOCV channels (k,$-k$):

$$\Delta E_{\mathrm{orb}} = \sum_{k=1}^{M/2} \nu_k \left[-F_{-k,-k}^{\mathrm{TS}} + F_{k,k}^{\mathrm{TS}}\right] = \sum_{k=1}^{M/2} \Delta E_k^{\mathrm{orb}} \qquad (7)$$

The integrals $F_{ij}^{\mathrm{TS}} = \langle i|\nabla^2/2 + V_{\mathrm{ne}} + V_{\mathrm{C}}[\rho^{\mathrm{TS}}] + V_{\mathrm{xc}}[\rho^{\mathrm{TS}}]|j\rangle$ are matrix elements of the Kohn–Sham operator evaluated for the electron density at the ''TS'' state, which is given by $\rho^{\mathrm{TS}} = 1/2\rho + 1/2\rho^0$ (ρ and ρ^0 represents the electron density of interacting

and non-interacting fragments, respectively).[202] The NOCV method has enabled a deeper understanding of the origin of the IR red shift of the stretching C–C frequencies due to metal–ligand bonding on the Cu and Ni centres of ZSM-5 zeolite,[203] and it has also provided a reliable description of various non-covalent interactions.[204,205] The ETS-NOCV analysis has also been used to unravel the binding mechanism of dinitrogen, carbonyl (Chapters 4.2.3 and 4.2.4), superoxide (Chapter 4.3.1), and nitrosyl adducts (Chapter 4.3.2) of nickel, copper, and cobalt ions in the exchangeable positions of various zeolites.

4.2. Ligation of innocent molecules

Innocent molecules such as H_2O, NH_3 are the non-redox ligands that interact with metal centres in metallozeolites primarily through sigma-donation (Fig. 17a1). The strength and nature of sigma-donation depend on several factors, among them, the most important are electronegativity and hardness/softness of the metal centres (according to the HSAB principle, where Cu^{2+}, Ni^{2+}, Fe^{3+}, *etc.*, exhibit different affinities towards innocent ligands), availability of coordination sites on the metal ion within the zeolite framework, and the intracage solvation effects that may modulate metal–ligand interactions.[206–208] Moreover, the ability of innocent molecules to form multiple coordination σ-bonds (poly-molecular adsorption) with metal ions is controlled by the oxidation state and the electronic structure of metal ions, and the cage size of the zeolite framework.[209,210] It is well established that the interaction of H_2O and NH_3 with metallozeolites can also lead to partial or complete detachment of the metal ion from the zeolite framework.[211] This occurs through ligand-induced solvation, where strong coordination of ligands stabilizes the metal ion inside the cage. This effect plays a vital role in modulating the catalytic activity within the zeolite pores. In light of these facts, although such reagents are considered innocent, their impact on the catalytic and adsorption properties of metallozeolites is significant. Other innocent ligands, often used to probe the valence and coordination states of the intrazeolite TMI by IR, are CO and N_2 molecules. Although their adsorption energy has a pronounced dispersion component, a minute electron exchange between the ligated N_2 or CO and the metal is responsible for the observed site sensitivity (see Chapters 4.2.3 and 4.2.4).

4.2.1. Intrazeolite hydration of TMI. Water and hydroxyl groups serve as the primary ligands in metal-exchanged zeolites immediately after synthesis and catalyst activation (Chapter 3.1). Another common source of water is its autogenic production during catalytic reactions such as oxidation of hydrocarbons, NH_3 or NH_3-SCR, where water molecules are either final or intermediate products.[33,212]

While water is often considered a co-reagent in catalytic processes and implicated in specific reaction steps,[152,213,214] more general studies aiming to identify general trends in its interaction with metal centres are relatively scarce. In this context, B3LYP-DFT cluster calculations of water adsorption on various divalent metal centres (Zn^{2+}, Cu^{2+}, Ni^{2+}) stabilized at exchange positions I and II in zeolite Y (Fig. 18a) can be invoked as a suitable example.[215] The oxidation state and type of the cation have a greater impact on the adsorption than the specific exchange position. An ALMO (absolutely localized molecular orbitals) analysis,[216,217] allowed for the decomposition of the adsorption energy into none-CT (non-charge transfer), ligand to metal charge transfer (CT(X → MY)), metal to ligand charge transfer (CT(MY → X)), and CT(HO) terms. This reveals that the electronic H_2O-TMI interactions are primarily governed by the non-CT and CT(X → MY) contributions, in contrast to those previously studied for alkali metal sites.

Comparison of water adsorption on divalent cations (Cu^{2+}, Zn^{2+}, Fe^{2+}) incorporated in FAU zeolite (see Fig. 18b_1–b_3) shows that Zn^{2+} and Cu^{2+} exhibit the strongest interactions with water, with the adsorption energies of −105.3 kJ mol^{-1} and −81.6 kJ mol^{-1}, respectively.[218] These values, comparable to those of alkaline earth metal cations, may be attributed to their significant HSAB hardness. This is further supported by the iso-surface electron density contours (Fig. 18b_3, insert), which agree well with theoretical studies on mordenite, where the influence of high (HC) and low (LC) coverage is illustrated (Fig. 18c).[219]

A more thorough approach to studying water ligation involves a set of copper multi-aqua complexes in different configurations (Fig. 18d_1–d_5)[83] to construct 2D thermodynamic stability diagrams for the 8MR (Fig. 18e_1) and 6MR (Fig. 18e_2) exchangeable sites of CHA zeolite. This analysis reveals the level of ligation at which a copper cation is pulled out from the zeolite rings, gradually acquiring considerable mobility within the cages. Regardless of the site, this occurs when four H_2O ligands are bound to a Cu cation. When the charge of the cation is reduced, a smaller number of solvent molecules is needed for the detachment, as illustrated by $Cu^+(H_2O)_2$ species entrapped in mordenite.[161] Then, the polyaqua-complexes exhibit sufficient mobility to migrate between the zeolite channels. For selected H_2O pressure of 10^{-4} (typical for the NH_3-SCR reaction, marked with a dashed line), this condition is met below 125 °C (8MR) and below 75 °C (6MR).

4.2.2. Coordination of NH_3 and interpretation of NH_3-TPD profiles. Essentially, NH_3 exhibits stronger binding to TMI than H_2O due to its higher electron-donating ability, resulting in the formation of more pronounced σ-bonds.[211] In the metal–zeolite catalysis, the adsorption and desorption kinetics of NH_3, and the associated modification of the coordination state and redox properties of the intrazeolite TMI play an essential role, particularly in NH_3-SCR[33,77,93] and AMO[33] reactions. These processes are chiefly studied for Cu in the small-pore zeolites, and both mononuclear and binuclear copper species serve as the primary adsorption sites.[220,221] Much less attention has been paid to other transition metal ions.[40,222] Brønsted acid sites also contribute to NH_3 capture, leading to the formation of $NH_4^+ \cdot nNH_3$ associations, which can complicate the interpretation of experimental NH_3 uptakes,[223] whereas extra-framework Al species play a minor role.[224] In addition to spectroscopic techniques (mainly IR), temperature-programmed desorption (TPD) of NH_3 is widely used for coarse characterisation of both metal Lewis (LAS) and Brønsted (BAS)

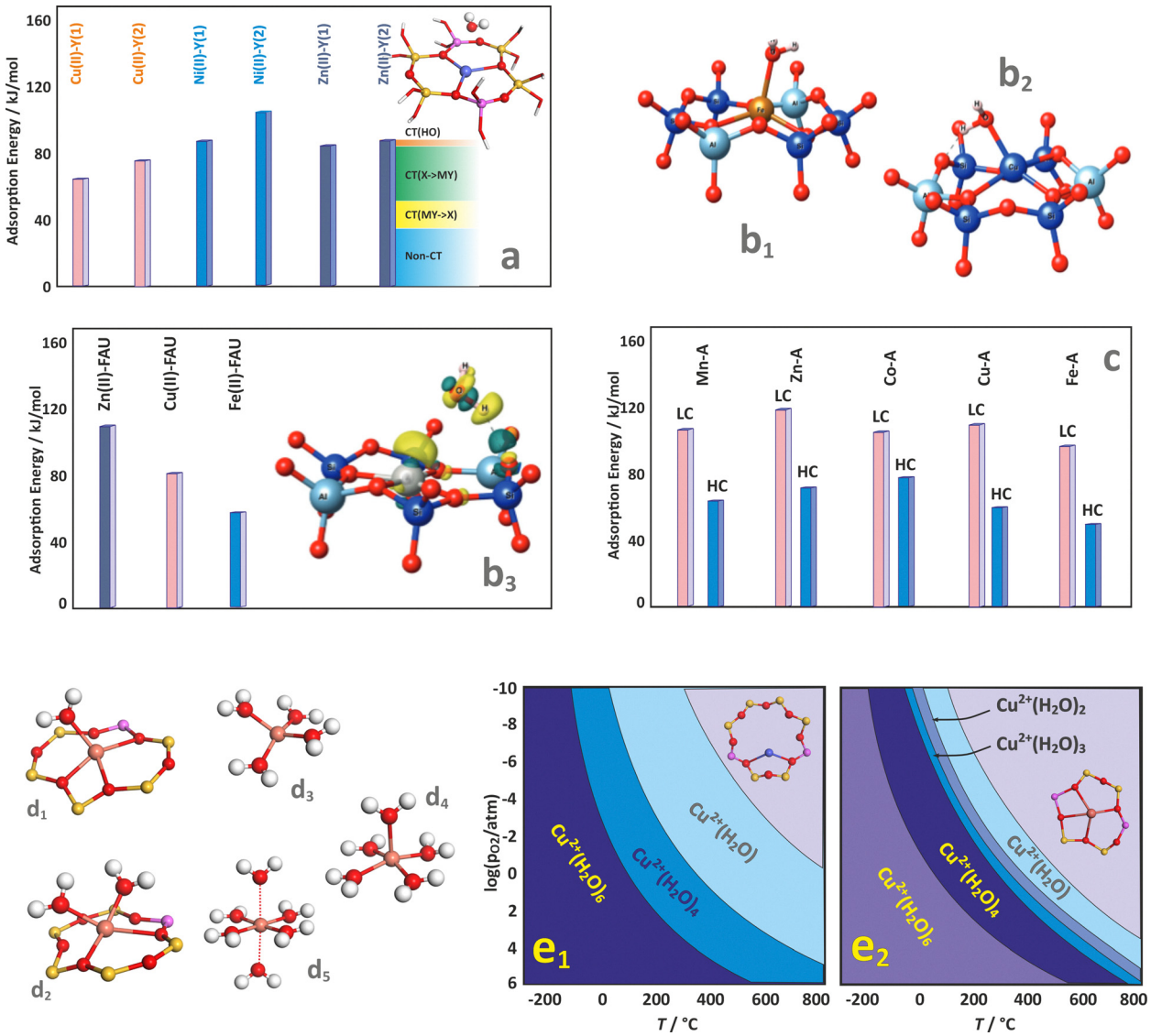

Fig. 18 Adsorption of water on divalent metal centres (Zn^{2+}, Cu^{2+}, Ni^{2+}) located at the exchange positions I and II in zeolite Y, together with ALMO EDA analysis for Zn^{2+} in II site of Y zeolite (a), based on data from ref. 215. Cluster models (b_1) and (b_2) and water adsorption energies on Cu^{2+}, Zn^{2+}, and Fe^{2+} incorporated in FAU (b_3), together with the iso-surface electron density contour for Fe^{2+}–H_2O (b_3, insert), adapted from ref. 218 with permission from Royal Society of Chemistry, copyright 2022. Adsorption energy of water on various TMI centres incorporated in MOR framework in the high (HC) and low coverage (LC) limits (c), based on data from ref. 219. Optimised geometries of the copper poly-aqua complexes (d_1)–(d_5), together with the corresponding 2D thermodynamic stability diagrams constructed for the 8MR (e_1) and 6MR (e_2) exchangeable sites of CHA. The panels (a)–(d) were based on data from the respective references. Panels (e_1) and (e_2) were based on data from ref. 83.

acid sites in zeolite catalysts.[196,225,226] This technique provides valuable insights into the thermodynamic stability of various intrazeolite metal–ammonia complexes across different temperatures. It can serve as an essential experimental benchmark for validating the FTP modelling of NH_3 interactions with TMI present in zeolites. The combination of TPD and FTP methods can be applied for in-depth investigations into NH_3 adsorption, *e.g.*, on various monomeric and dimeric copper centres, and BAS sites present simultaneously in Cu/SSZ-zeolite catalysts, differing in Si/Al ratios and aluminium distribution within the zeolite framework.[172,227] For each adsorption site, the energies of multiple NH_3 adsorption (see Fig. 19a for the exemplary 6MR site) can be used for the construction of the 3-dimensional FPT diagram (Fig. 19b_1), and its recasting into variation of Θ_{NH_3} (site coverage) as a function of temperature and partial pressure of NH_3 (Fig. 19b2). The cross-sections at p_{NH_3} set to the experimental value (10^{-4} atm) allow for a straightforward determination of the temperature windows in which NH_3 desorption peaks are expected due to ammonia release from the particular centres (Fig. 19b_3 and b_4). The overall theoretical desorption profile results from adding the contributions of all involved adsorption sites (Fig. 19c_1). They can be compared with the experimental TPD-profile obtained for Cu/SSZ-13 catalysts differing in the Si/Al ratio (Fig. 19c_2). The

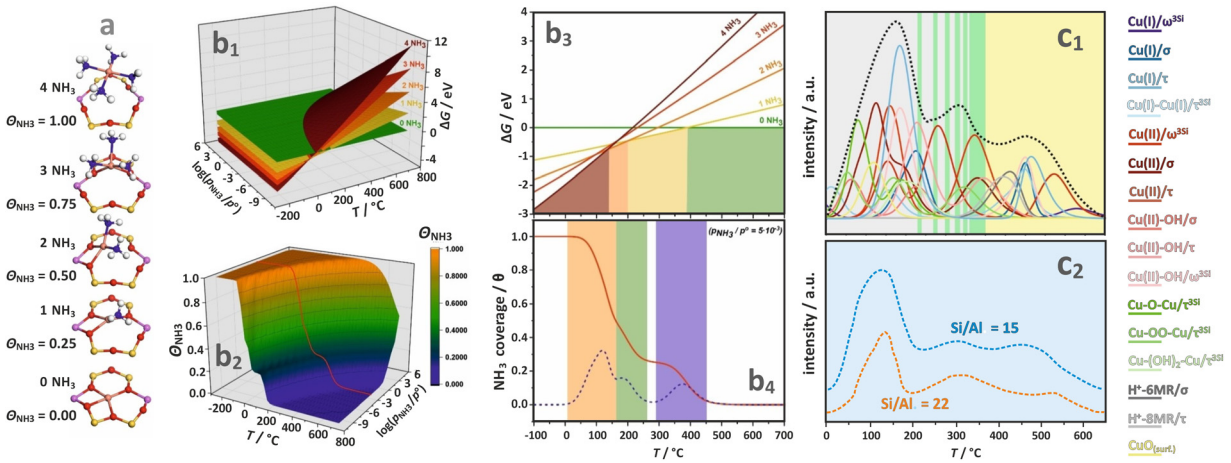

Fig. 19 Optimized geometries of the Cu^{2+}–$(NH_3)_n$ adducts located in the 6MR site of CHA (a). The 3-dimensional diagrams of ΔG *vs.* T, p_{NH_3} (b_1) and Θ_{NH_3} *vs.* T, p_{NH_3} (b_2), together with the corresponding cross-sections for p_{NH_3} set to 10^{-4} atm (b_3) and (b_4). The overall calculated TPD profile with all component bands (c_1). The experimental NH_3-TPD profile obtained for samples differing in Si/Al ratio (c_2). Adapted from ref. 227 with permission from John Wiley and Sons, Copyright 2021.

comparison implies that the desorption peaks resolved in TPD cannot be univocally assigned to NH_3 release from specific Cu centres or Brønsted acid sites. The experimentally observed low-, medium-, and high-temperature desorption bands arise from multiple copper species whose speciation and redox states evolve dynamically throughout the NH_3-TPD process. This behaviour is driven by copper migration, its reduction, and condensation within the zeolite framework, as revealed by complementary *in situ* EPR and IR investigations.[172]

At lower temperatures, when higher coordination numbers of TMI to ammonia are expected ($n > 2$), detachment and mobilisation of the metal cations from the zeolite framework is typically observed (analogous to the water ligation case). This phenomenon has been extensively investigated due to its crucial role in the low-temperature NH_3-SCR process.[179,229] A combination of computational (DFT-HSE06) and experimental (XANES, XAS) studies has been applied to thoroughly examine different Cu–$(NH_3)_n$ complexes under *in situ*, *ex situ*, and *operando* SCR conditions, considering variations in the catalyst composition.[228] The copper speciation, mobility, and its actual siting are primarily dictated by environmental factors, rather than the initial location of the Cu cations or the type of zeolite framework. As an example, the mobility of $[Cu(NH_3)_2]^+$ within the CHA framework, as revealed by *ab initio* meta-dynamic simulations, is shown in Fig. 20a1. The Cu ion migration through the 8-MR rings between two cages requires an activation energy $\sim$55 kJ mol^{-1}, confirming that the CHA framework provides sufficiently large windows for efficient intrazeolite diffusion of the $[Cu(NH_3)_2]^+$ species, triggering the oxidation half cycle (OHC) of the SCR reaction.[15,179,229]

The role of Cu ion mobility in Cu/SSZ-13 has also been explored using large-scale simulations, employing an interatomic potential obtained from machine learning that accurately replicates the *ab initio* results.[229,230] A combination of biased and unbiased simulations enabled an in-depth analysis of the $[Cu(NH_3)_2]^+$ mobility in Cu-CHA catalysts, revealing that the Al pairing within the 8-MR rings facilitates local hopping, whereas higher NH_3 concentrations enhance long-range diffusion. The $[Cu(NH_3)_2]^+$ migration under NH_3–SCR–NO_x conditions obtained from AIMD simulations is illustrated in Fig. 20b_1–b_3. The diffusion is hindered when additional NO/O_2 molecules are present in the zeolite cavity (Fig. 20b_2). Furthermore, a decrease in the number of BAS sites leads to an increase in the diffusion barrier of $[Cu(NH_3)_2]^+$. The van der Waals interactions between $[Cu(NH_3)_2]^+$ and the zeolite framework (Fig. 20c_1–c_3) are significantly influenced by the BAS distribution, inhibiting the low-temperature NH_3-SCR activity.[231] For zeolites of uneven Al distribution, variations in the interaction energy between $[Cu(NH_3)_2]^+$ and the zeolite framework are mainly responsible for the inter-cage diffusion. The migration of $[Cu(NH_3)_2]^+$ from an Al-poor cage to an Al-rich cage exhibits a lower diffusion barrier, favouring the formation of active dimer-Cu species and enhancing the SCR reaction.

The oxidation of mobile diamino copper complexes (Fig. 20d) monitored by XANES and EXAFS techniques shows consistently that the Si/Al ratio of the zeolite hosts influences the structure of the mobile μ-η^2,η^2-peroxo diamino dicopper(II) adducts, which are formed during the oxidation of $[Cu(NH_3)_2]^+$ complexes by O_2 (OHC).[232]

4.2.3. Adsorption of N_2 and the probe molecule characteristics. A non-polar N_2 molecule with no lone pairs interacts primarily through non-specific van der Waals forces when adsorbed onto metal centres within zeolite frameworks. Despite its chemical inertness, weak residual covalent interactions can also be formed, which are notably sensitive to the chemical state of the metal center. The nature of this sensitivity to the metal oxidation and coordination environment within the zeolite matrix can be better understood through computational NOCV analysis. It enables a deeper understanding of these interactions, as it identifies the regions of electron and spin density flow between the metal center and the N_2 ligand. These fluxes are indicative of weak but significant covalent

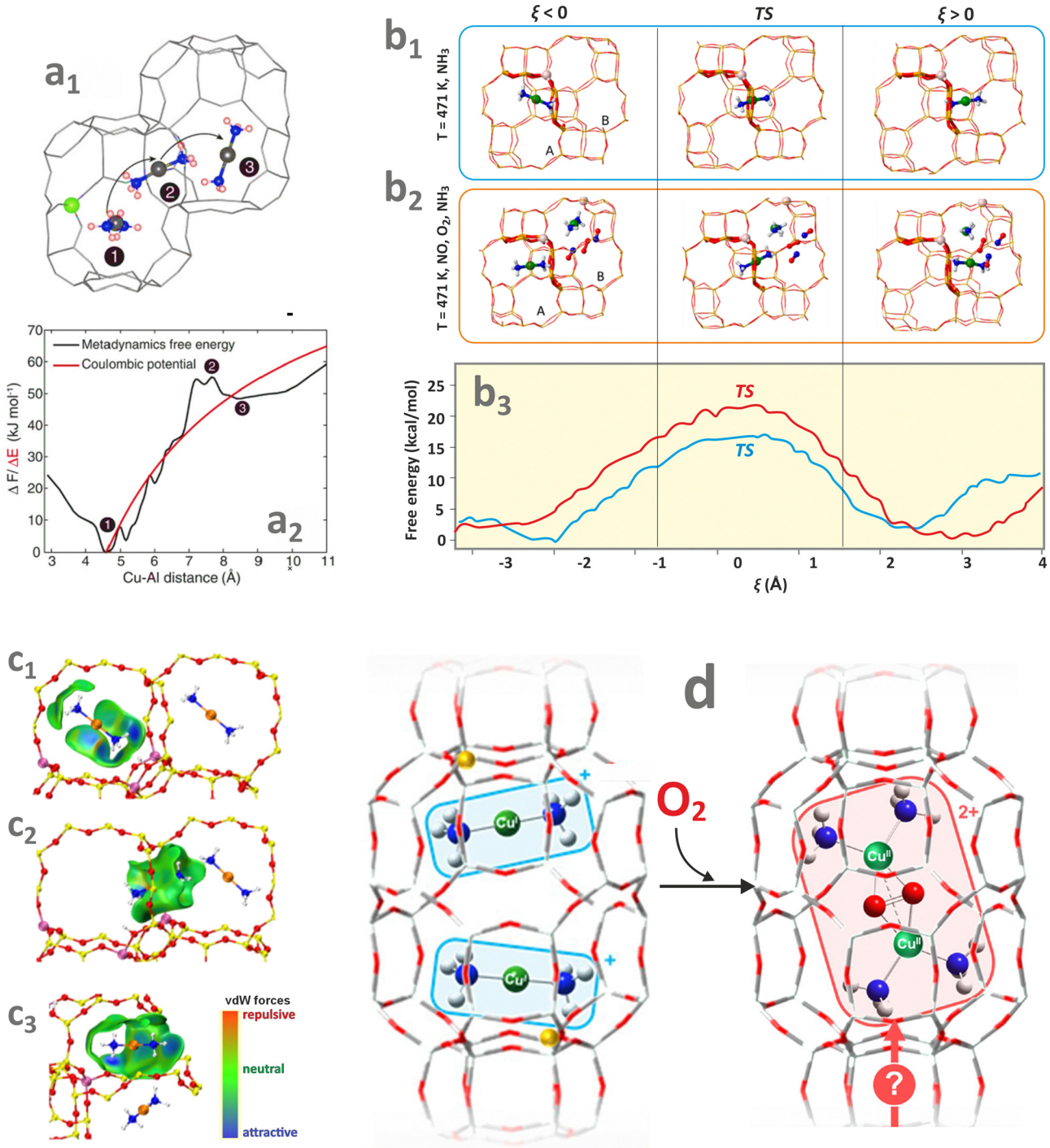

Fig. 20 The migration pathway of $[Cu(NH_3)_2]^+$ species presented inside the channels of CHA zeolite (a_1), together with the corresponding free energy profile plotted against Cu–Al distance (a_2), adapted from ref. 228 with permission from the American Association for the Advancement of Science, Copyright 2017. Representative configurations of $[Cu(NH_3)_2]^+$ in the initial state ($\xi < 0$), transition state (TS, $\xi = 0$), and final state ($\xi > 0$) during the diffusion through the 8-membered ring windows of Cu-CHA without co-adsorbed molecules (b_1) and in the presence of O_2 and NO (b_2), together with the corresponding free energy profiles as a function of the reaction progress ξ (b_3) at 423 K, adapted from ref. 229 with permissions from American Chemical Society and The Authors, Copyright 2021. The initial (c_1), transition (c_2), and final state (c_3) structures of the $[Cu(NH_3)_2]^+$ complex migrating from 6MR rings with a single Al to 6MR with a pair of Al, adapted from ref. 231 with permission from American Chemical Society, Copyright 2024. Postulated route of formation of mobile μ-η^2,η^2-peroxo diamino dicopper(II) complexes upon oxidation of the $[Cu(NH_3)_2]^+$ species (c), adapted from ref. 232 under the terms of the CC BY 4.0 license, Copyright 2022, published by American Chemical Society.

interactions, even though N_2 itself remains largely non-polar upon the ligation.

The interest in dinitrogen coordination chemistry is mainly associated with gas separation, such as N_2/O_2, CO_2/N_2, or

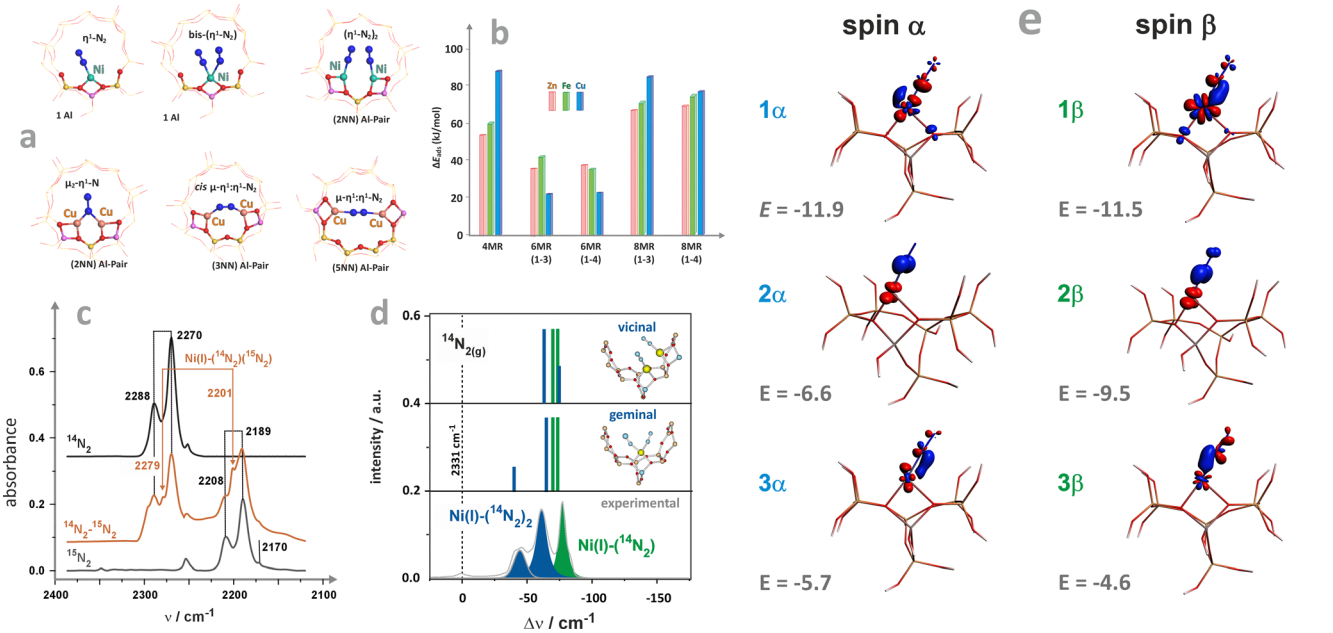

Fig. 21 Stable binding modes of N_2 to Ni^+ and Cu^+ in ZSM-5 (a). Adsorption energies of N_2 on selected metallozeolites (b). IR spectrum of $^{14}N_2$ and $^{15}N_2$ adsorption on Ni^+/ZSM-5 zeolite (c), together with the calculated IR bands for two possible conformations of di-N_2 adducts (d). The NOCV analysis of the σ- and π-type bonds in $\{(\eta^1\text{-}N_2)_2Ni^+\}$/ZSM-5 complex (e). Panels a, b, and c were based on the data from ref. 234 and 240. Panels d and e adapted from ref. 80 with permission from Elsevier, Copyright 2020.

CH_4/N_2[233] and the challenging activation of the highly inert N_2 molecule. Catalytic nitrogen fixation, as well as air separation, begins with the coordination of N_2 to the transition metal centres. As a ligand, N_2 exhibits certain similarity to the isoelectronic CO, since both molecules are diatomic, having a strong triple bond (σ,2π) and empty antibonding 2π* orbitals. Dinitrogen usually coordinates to metal cations in an end-on (η^1) mode. In contrast to CO, which often forms polycarbonyl complexes (see Chapter 4.2.4), both experimental and theoretical results show that the dinitrogen complexes with the intrazeolite TMI ions usually contain one or two (at low temperatures) N_2 ligands only.[80,234] Typical examples include Cu^+ and Cu^{2+} centers in ZSM-5[235,236] MOR,[237] and BEA,[238] as well as Ni^+ and Ni^{2+} hosted in ZSM-5[80,239] or Fe^{2+}, Cu^{2+}, Zn^{2+} in CHA.[233] Apart from the most common η^1-attachment, stable *trans* and *cis* $\mu\text{-}\eta^1\text{:}\eta^1$ and μ-1,2 adducts of N_2 with Cu^+ in ZSM-5 (computationally optimized) have also been reported, see Fig. 21a.[240] Dinitrogen interacts relatively strongly with the intrazeolite TMI with energies varying from −100 to −20 kcal mol^{-1}, depending on the framework type and accommodation site (see Fig. 21b).[234,240]

While forming intrazeolite adducts, N_2 is coordinated by σ- and π-type bonds. The TMI–N_2 bonding depends on the overlap between the available 3d-orbital with the σ (HOMO) and 2π* (LUMO) orbitals of the dinitrogen molecule. Such an overlap pattern implies a synergy of the σ-donation and π-backdonation interactions.[236] Therefore, the resultant electron density redistribution between the metal and N_2 ligand leads to a decrease in the N–N bond order. As a result, the N–N stretching frequency is lower than the corresponding frequency of a gas-phase molecule (2331 cm^{-1}), see, *e.g.*, IR spectra of N_2 with Ni^I/ZSM-5 in Fig. 21c. Apart from orbital contributions, the N–N vibration frequencies also have an electrostatic component, $\Delta\nu_{tot} = \Delta\nu_{(\sigma+\pi)} + \Delta\nu_{el}$, which makes them particularly sensitive to the oxidation state of the metal centre.[236] These features make the N_2/IR method a convenient spectroscopic probe for measuring the electron donor/acceptor properties of the intrazeolite TMI. The N–N stretching frequency of the Cu^I–$^{14}N_2$ species is observed in the region of 2300–2285 cm^{-1},[236] for Ni^I–N_2 at 2254–2252 cm^{-1}.[80] In contrast, for Ni^{II}–N_2 it increases to 2324 cm^{-1},[239] revealing the different extent of back π-donation and the diverse oxidation states of the TMI centres as well.

The Ni^+ ions hosted in Ni–ZSM-5, in contrast to Cu^+/ZSM-5,[241] can coordinate two N_2 molecules simultaneously, and the ensuing $\{(\eta^1\text{-}N_2)_2Ni^+\}^9$ adducts are characterized by ν_s at 2288 cm^{-1} and ν_{as} at 2270 cm^{-1}.[234] The coupling between the two N_2 ligands is usually confirmed by co-adsorption of $^{14}N_2$ and $^{15}N_2$ isotopic mixtures. Because of the presence of mixed ligands ($^{14}N_2$ $^{15}N_2$), the resultant structural dichotomy of possible formation of the geminal $(\eta^1\text{-}N_2)_2Ni^+$/ZSM-5 and two coupled vicinal $(\eta^1\text{-}N_2)Ni^+\cdots(\eta^1\text{-}N_2)Ni^+$ adducts can be resolved by complementary DFT modelling, see Fig. 21a.[80] The calculated spectroscopic IR signatures of both types of dinitrogen adducts, shown in Fig. 21d, allow for a straightforward distinction between the types of complexes. In particular, the coupling through bonds in the geminal adducts is stronger (25 cm^{-1}) than the coupling through space in the vicinal ones (12 cm^{-1}).

The intimate mechanism of N_2 bonding and the delicate balance between the σ-donation and the back-donation effects, which are responsible for the IR shifts, can be unravelled and quantified by NOCV analysis. The main orbital contributions to

the α and β electron density flows are shown in Fig. 21e, together with the corresponding energy values. The α-polarized σ-donation from the N_2 ligand (1α) is accompanied by electron relaxation of the β-3d manifold of the Ni^I centre, consisting of depopulation of $3d_{x^2-z^2}$ and population of $3d_{xz}$ (1β), and both flow channels exhibit similar energy contribution to the binding. Such deep electronic relaxation is typical of the TMI that undergoes anisodesmic changes in its structure upon binding (CN = 4 for bare Ni^+/ZSM-5 centre changes into CN = 3 in the case of dinitrogen adduct), see also Chapters 4.2.4, 4.3.1, and 4.3.2. The π channel of the back-donation is constituted by the 2α + 2β spinorbitals, and involves the out-of-plane $2\pi^*_\perp$ orbitals of N_2 and $3d_{yz}$ of Ni. The resultant electron density flow is primarily responsible for the lessening of the N–N stretching frequency. The second (3α + 3β) channel of the π-symmetry is formed by the overlap between $2\pi^*_\parallel$ and $3d_{xz}$ orbitals. The resultant flow of electron density along this channel leads to the accumulation of the electron density within the Ni–N bond at the expense of the π and 3d states. Therefore, it can be designated as a dative coordinative contribution. Overall, the π donation/back-donation effects account for 53% of the orbital interactions, whereas the σ channel is in charge of 24% of the binding strength. This allows for unravelling the intimate nature of the Ni^+–N_2 bonding and the observed bathochromic shift of the stretching vibrations.[80]

4.2.4. Coordination of CO molecules

Structure of carbonyls and formation of TMI–CO bond. Transition-metal cations hosted in zeolites upon contact with CO form carbonyl adducts rapidly. The CO molecule prefers to bind *via* a metal–carbon bond, despite carbon being less electronegative than the oxygen atom. The HOMO of CO exhibits an essentially non-bonding character, and this orbital is primarily localized at the carbon moiety. Since the π and π* orbitals are relatively close in energy to the HOMO, they can also be involved in the bonding of carbonyls.

Bonding of CO to TMI in zeolites can be described by the classical synergistic effect of σ-donor and π-acceptor interactions (Fig. 22a), commonly referred to in textbooks as the Dewar–Chatt–Duncanson model. It serves as the basis for more advanced analysis based on quantum chemical calculations.[242] Briefly, the σ-donor interaction relies on donating the electron density from the lone pair at the carbon into the empty metal 3d-orbitals, and in this way, a dative bond is formed. The donated electron density raises the energy levels of the 3d electrons due to an increased electron–electron repulsion. As a result, the 3d electrons are more easily accepted by the CO ligand through the π-acceptor interaction. The two lobes of the π* orbitals overlap with the lobes of a metal 3d orbitals of proper symmetry. This type of binding is highly efficient for low-valent metal centers, as the energy of the 3d electron manifold approaches the π* level. The efficiency of the π*

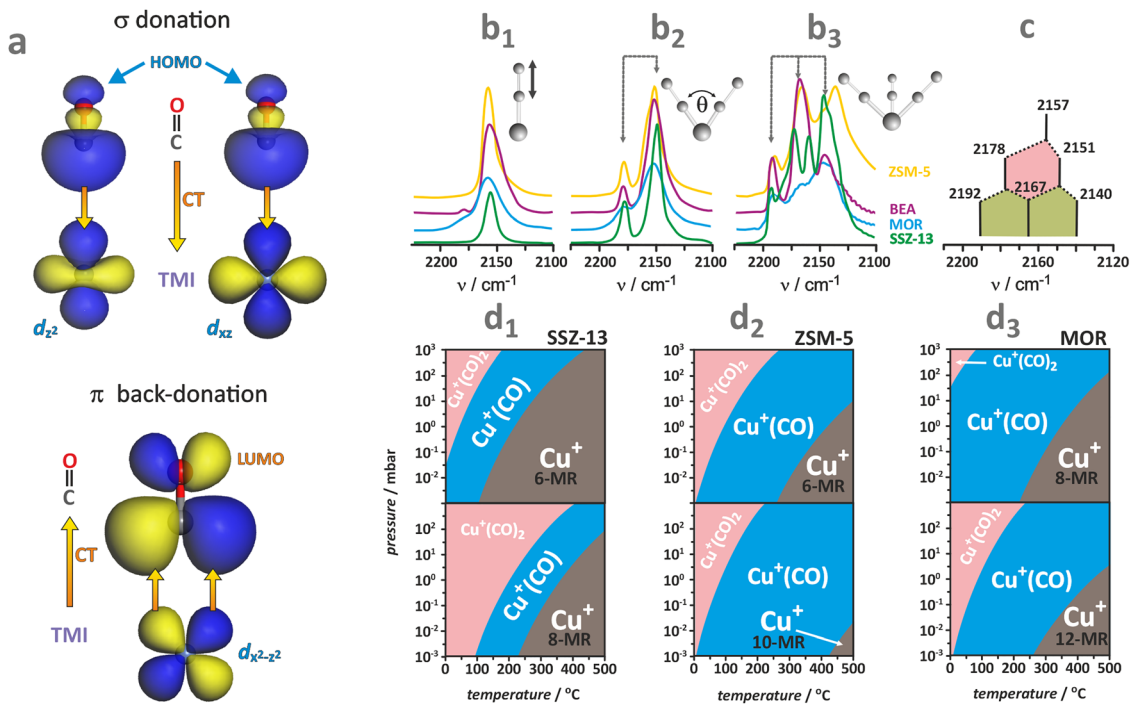

Fig. 22 Schematic representation of the σ-donation and π-back-donation effects during binding of CO to a transition-metal cation (a). IR spectra of CO adsorption on reduced Cu^+-exchanged ZSM5, BEA, MOR, and SSZ-13 zeolites. The consecutive sets of spectra correspond to increasing doses of CO, which lead to predominant formation of mono- (b_1), di- (b_2), and tricarbonyl species (b_3) adapted from ref. 257 with permission from the Royal Society of Chemistry, Copyright 2015. A schematic diagram showing the splitting of the C–O vibration IR bands due to the coupling of two and three CO molecules in CuZSM-5 zeolite (c). The ΔG *vs.* T and p_{CO} phase diagrams of the isolated Cu^+, $Cu^+(CO)$, and $Cu^+(CO)_2$ species hosted within SSZ-13, ZSM-5, and MOR zeolites, adapted from ref. 244 under the terms of the CC BY 4.0 license, Copyright 2023, published by Elsevier B.V.

back-bonding reflects the stability of the resulting carbonyls. Generally, the more nucleophilic the CO moiety upon bonding, the higher the stability of the adduct. Positive charges destabilize TMI–CO complexes. The stability of neutral carbonyls, which often appear in the zeolite systems, is intermediate. Apart from this short-range electron interaction, specific long-range electrostatic effects imposed by the zeolite lattice, such as polarization and dispersion forces, must be included when analysing the chemical state of intrazeolite carbonyl adducts.[243,244]

Cu–zeolites are well-suited for studying the coordinative unsaturation of the Cu^+ cations and binding of carbon monoxide. Exemplary IR spectra of CO sorption at increasing pressure for Cu^+–zeolites (ZSM-5, BEA, MOR, and SSZ-13) are shown in Fig. 22b. Depending on the CO pressure and temperature, various copper carbonyl adducts are formed. At room temperature and low p_{CO}, $Cu^+(CO)$ monocarbonyls are characterized by a single band observed at 2154–2159 cm^{-1}, Fig. 22b$_1$. Upon introducing more doses of CO, the formation of dicarbonyls $Cu^+(CO)_2$ is observed (see Fig. 22b$_2$), as indicated by splitting of the monocarbonyl band into two peaks corresponding to the asymmetric (ν_{asym}, 2150–2152 cm^{-1}) and symmetric (ν_{sym}, 2178–2180 cm^{-1}) vibrations of the two coupled CO oscillators. In such a case, the I_{asym}/I_{sym} ratio can be used to estimate the angle the geminal ligands form in the $\{TMI(CO)_2\}^n$ adducts, using the $I_{asym}/I_{sym} = tg^2(\theta/2)$ equation proposed by Cotton.[245] The presence of two bands is indicative of a C_{2v} local symmetry of the dicarbonyl species.

A further increase in p_{CO} (Fig. 22b3) leads to the transformation of dicarbonyls into $Cu^+(CO)_3$ species, and the appearance of a new triplet of the IR bands with approximate positions at 2135, 2168, and 2192 cm^{-1}. The scheme of splitting of the carbonyl bands upon increasing the number of CO ligands coordinated by Cu^+–zeolite centers is shown in Fig. 22c. This triplet is indicative of a local symmetry lower than C_{3v}. The presence of individual species or the joint occurrence of the mono-, di-, or tricarbonyls is linked to the accessibility of the copper centres and the size of the intrazeolite channels and pockets. The IR spectra shown in Fig. 22b1–b3 reveal that ZSM-5 and BEA zeolites are more apt for the formation of well-defined polycarbonyls $Cu^+(CO)_n$ ($n = 1, 2, 3$) than MOR or SSZ-13 zeolites, suggesting CO sensitivity to the speciation of the copper active centres.

The stability of the carbonyl species can be predicted with first-principles thermodynamic calculations (see Chapter 3.1) and compared with spectroscopic observations. The calculated phase diagrams (ΔG *vs.* T and p_{CO}) shown in Fig. 22d1–d3 delineate the stability regions of $[Cu(CO)]^+$ and $[Cu(CO)_2]^+$ adducts and the bare Cu^+ centres located in various sites of the SSZ-13, ZSM-5, and MOR zeolites.[244] In all cases, formation of the carbonyl adducts is thermodynamically favoured. The ZSM-5 topology exhibits the highest propensity among the described zeolite series for the formation of $[Cu(CO)]^+$ adducts. In contrast, the SSZ-13 framework exhibits the lowest energy difference between the mono- and dicarbonyl species.

The phase diagrams can be used for elucidating the critical conditions for the decomposition of the involved adducts at either a fixed temperature or CO pressure. For instance, at room temperature, transformation between di- and monocarbonyls is irreversible only for the 8-MR sites of the SSZ-13 framework. The decomposition temperature of $[Cu(CO)]^+$ to bare Cu^+ species at 10^{-3} mbar (corresponding to a negligible amount of CO in typical catalytic conditions) in the case of SSZ-13 is much lower (162 °C) than that for the other two frameworks (275 °C and 340 °C for MOR and ZSM-5, respectively), especially for the Cu^+ cations located in the 6-MR. This influence of the framework topology was observed experimentally during the TPD experiments for the SSZ-13, ZSM-5, and MOR samples, corroborating the FPT results.[244]

Similar behaviour was observed for Ni^+-exchanged zeolites subjected to CO adsorption. However, since Ni^+ centres are paramagnetic, EPR spectroscopy can also be used to elucidate the structure and properties of the resulting carbonyls.[80,114,247,248] Yet, the primary identification of the adducts formed is provided by IR spectroscopy.[31,239,249] Typical IR spectra are shown in Fig. 23a. The spectral region of the CO vibrations can be separated into two parts, imposed by a band located at 2175 cm^{-1}, which is attributed to the CO molecule interacting with the Brønsted centres. The IR bands located at higher frequencies originate from CO interacting with the oxidized nickel centres (Ni^{2+}, Ni^{2+}-oxo species). In contrast, those of lower frequencies are associated with CO adsorbed on the reduced intrazeolite Ni^+ cations.

Briefly, the adsorption of CO at room temperature leads to a band at 2214 cm^{-1} due to the Ni^{2+}–CO adducts in ZSM-5. At low temperatures, this band reveals a shoulder at 2198 cm^{-1} associated with the Ni^{2+}-oxo species. After reduction of NiZSM-5 with CO (400 °C), this new band disappears, indicating a reactive character of the adsorption of CO associated with the redox transformation of Ni-oxo species to Ni^+. This is accompanied by the development of a new doublet signal characteristic of nickel(I) geminal dicarbonyl adducts, with symmetric (2136 cm^{-1}) and antisymmetric (2092 cm^{-1}) vibrations. Desorption of CO at progressively increasing temperatures (Fig. 23a, spectra (2) and (3)) results in transformation of the $Ni^+(CO)_2$ dicarbonyl into the Ni^+CO monocarbonyl adducts (see the band at 2109 cm^{-1}). On the other hand, upon increasing the number of CO doses, a set of bands at 2124, 2118, and 2112 cm^{-1} appears between the symmetric and antisymmetric dicarbonyl bands, which are attributed to the tricarbonyl $Ni^+(CO)_3$ species. The corresponding vibrational splitting scheme is similar to that of $Cu^+(CO)_3$ (Fig. 22c), although the positions of the bands are different. Therefore, both Cu- and Ni-containing zeolites provide easily accessible, reduced Cu^+ and Ni^+ centres, capable of forming several polycarbonyl adducts, whose stoichiometry and structure depend on CO pressure and temperature. More accurate measurements of the CO frequencies, and the definite confirmation of the polycarbonyl structures (ligation stoichiometry), can be ascertained using isotopically labelled gas mixtures $^{12}C^{16}O/^{12}C^{18}O/^{13}C^{16}O/^{12}C^{18}O$.[249,250]

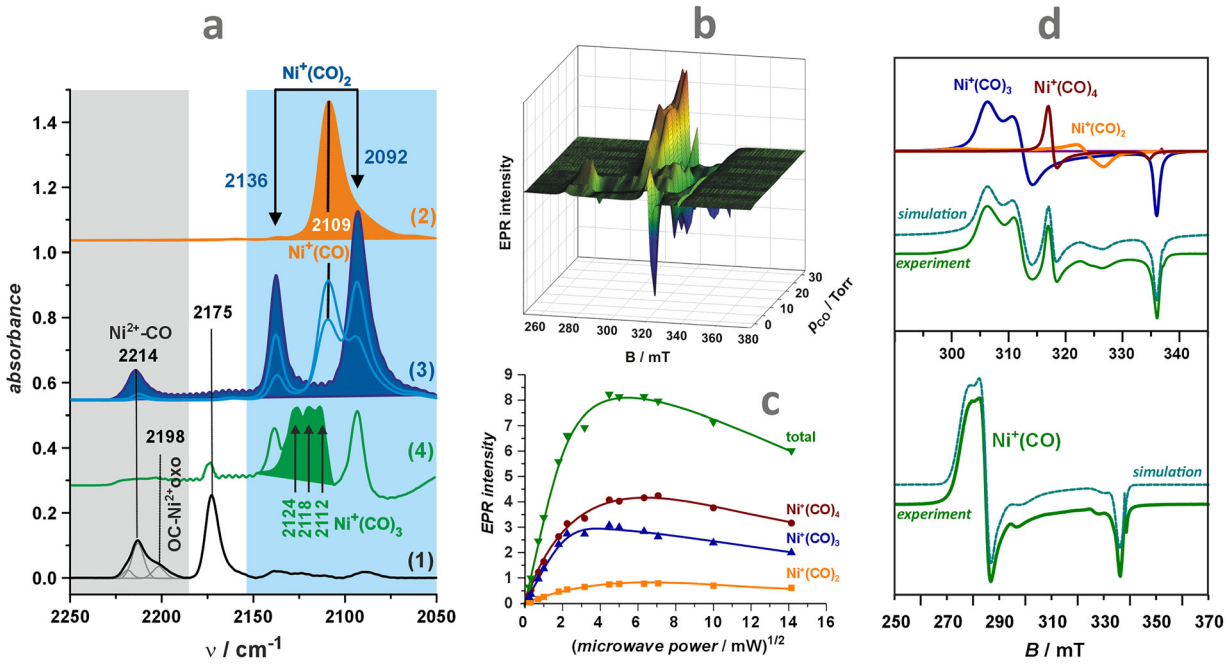

Fig. 23 IR and EPR fingerprints for the formation of nickel(I) polycarbonyls in the reduced NiZSM-5. The IR spectra of CO adsorption (a) on thermally activated NiZSM-5 (1), sample reduced in CO and evacuated at 150 °C (2), sorption–desorption equilibrium showing conversion of mono- and dicarbonyls (3), sorption of CO excess (4), adapted from ref. 247 with permission from the American Chemical Society, Copyright 2011. The set of CW-EPR spectra obtained after variable pressure CO sorption (up to 30 Torr) (b). Changes in the intensity of the mono-, di-, tri-, and tetracarbonyl EPR spectra recorded during microwave power saturation experiments (c). Decomposition of the experimental EPR spectra into individual carbonyl signals (d). Panels b, c, and d adapted from ref. 246 with the author's permission.

Magnetic properties of carbonyl adducts and the binding mechanism. The CO adsorption process can be followed successfully by *in situ* EPR measurements.[80,114,239,248] The advantage of EPR over IR spectroscopy stems from the lack of limitations imposed on the CO pressure, as the high pressures lead to the appearance of excessive CO in the gas phase, obscuring the IR spectra of the surface species. The EPR spectra of Ni^+/ZSM-5 (and Ni^+/BEA) zeolites, pre-reduced with CO, show dramatic changes upon increasing the pressure of CO (Fig. 23b). CW-EPR measurements at liquid helium temperature with an increasing microwave power allowed to saturate successively the component signals of the individual carbonyl species coexisting upon CO adsorption. Then, using computer simulation, the individual EPR spectra of the adducts $[Ni^+(CO)_n]$ZSM-5 with n = 1, 2, 3, 4 (mono-, di-, tri-, and tetracarbonyl nickel(I)) can be obtained (see Fig. 23c and d). Their magnetic properties have been examined using the DFT calculations of spin-Hamiltonian parameters for model complexes $[Ni^+(CO)_nL_m]$ (n = 1–4, L = H_2O, OH^-), which can be regarded as discrete, well-defined molecular analogues of the intrazeolite polycarbonyls.[251] The molecular nature of the calculated $\boldsymbol{g}$ and ^{13}C hyperfine tensors, when using ^{13}CO, can be interpreted in terms of the nickel coordination state and its local symmetry, providing clear guidelines for justifying their assignment.

Although the DFT calculations of the $\boldsymbol{g}$ and ^{13}C tensors has been restricted to the rudimentary $[Ni^+(CO)_nL_m]$ models, despite missing of the relevant EPR data for such discrete systems, generic categories of the $\boldsymbol{g}$ tensor structure–relationship can be delineated, and associated with the particular magnetophore $[Ni^+(CO)_n]$ that is embedded in the zeolite matrices. Additionally, the calculated data can be confronted with the available EPR parameters for nickel(I) polycarbonyls that are produced in ZSM-5 zeolites or supported on silica,[252,253] as the surface functional groups ($\equiv SiO^-$, –OH, $\equiv Si–O–Si(Al)\equiv$) play the role of mere ligands and can be inserted into the spectrochemical series close to aqua and hydroxyl ligands.[254] Additionally, it has been shown that the $[Ni^+(CO)_n]$ core acts as the proper magnetophore, whose spectroscopic properties are primarily controlled by the spatial arrangement of the CO ligands, being only slightly perturbed by the number and position of the H_2O, OH^-, or $\equiv SiO^-$ co-ligands.

The comparison of results obtained from DFT calculations reveals that the polycarbonyl complexes can be divided into two classes with distinct ground states, characterized by distinctive EPR spectra. They are schematically illustrated in Fig. 24a_1 and a_2 and accompanied by the simulated EPR spectra using the DFT-calculated parameters and typical experimental linewidths. The class of the $|3d_{z^2}\rangle$ ground state (*e.g.*, T-shaped monocarbonyl, tri- and tetracarbonyls) is characterized by a rhombic EPR spectrum with the g_{xx}, g_{yy} components varying between 2.4 and 2.1 (the actual shift depends on the number of CO ligands), and the smaller g_{zz} value close to g_e = 2.023. In the case of the $|3d_{x^2-y^2}\rangle$ ground state, observed for the dicarbonyl complexes, the reversed $\boldsymbol{g}$-tensor values are expected with one component being larger (2.2–2.13) and two components lying closer to the g_e value (2.07–2.01).

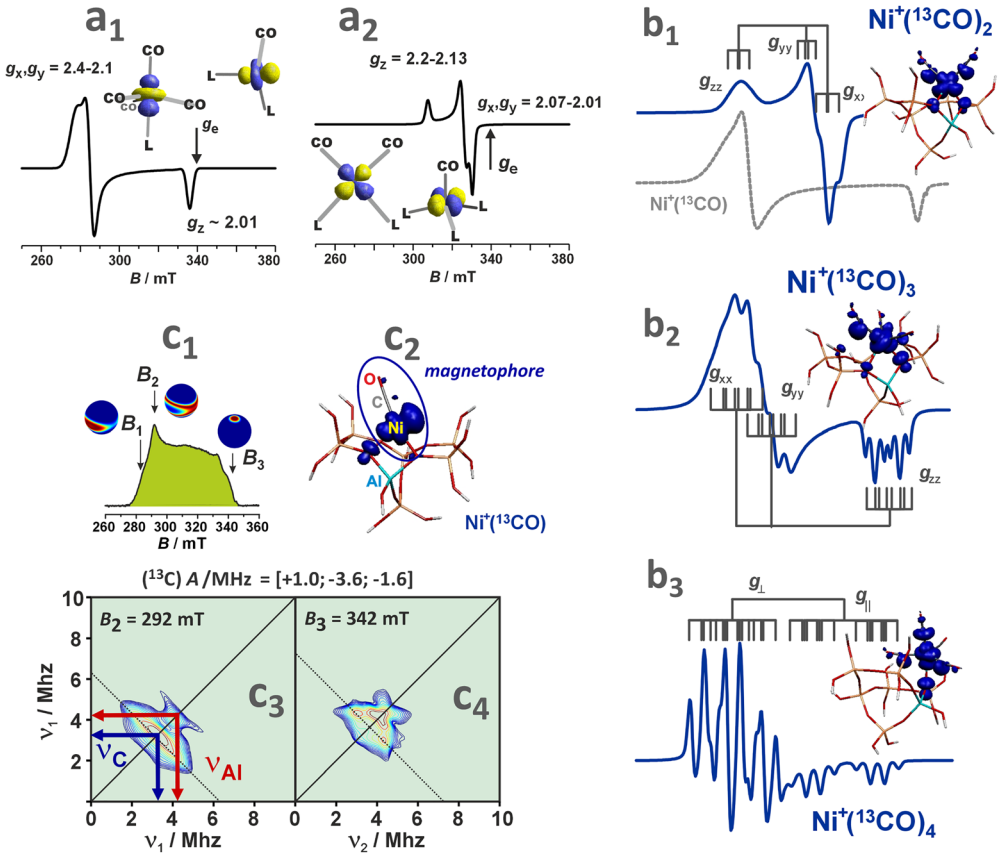

Fig. 24 EPR spectra of nickel(I) carbonyls in ZSM-5. Simulated X-band EPR spectra for the generic structural models of Ni^+ carbonyl adducts with dominant $3d_{z^2}$ (a_1) or $3d_{x^2-y^2}$ (a_2) ground state of the nickel core (depicted structures show SOMO contours, derived from DFT calculations). Experimental X-band EPR spectra of the isotopically labelled carbonyl species, showing hyperfine structures due to the ^{13}CO ligands (hyperfine splitting is shown with stick diagrams) (b_1), (b_2), (b_3). For better comparison of the hyperfine splittings, the spectra are recalculated to the common magnetic field axis and supplemented with the corresponding spin density contours calculated for the identified carbonyl structures. HYSCORE spectra of the monocarbonyl species, including echo-detected EPR spectrum (c_1), where the arrows indicate the observer positions at which HYSCORE spectra were recorded, whereas the unit spheres show orientation selectivity connected with the observer positions. Spin density contour of the Ni^+CO magnetophore (c_2), and HYSCORE spectra recorded at B_2 (c_3) and B_3 (c_4) positions in the magnetic field. Adapted from ref. 248 and 251 with permissions from the American Chemical Society, Copyrights 2008 and 2013.

It was found that increasing the number n of CO ligands resulted in smaller Δg_{ii} shifts as the energy separation between occupied and virtual spinorbitals increases from 0.8 (n = 1) to 1.6 eV (n = 4). The other reason stems from the fact that the corresponding matrix elements of the g-tensor (see Chapter 2.2) are dominated by the spin–orbit couplings (SOC) of the metal centre and the ligands. Noting the substantial difference in the SOC constants, $\lambda_{Ni^+} = 565\ cm^{-1}$ and $\lambda_C = 30\ cm^{-1}$, the resulting g tensor shifts become reduced considerably in magnitude, upon passing from the mono- to the tetracarbonyl adducts.[251]

Direct confirmation of the structure of the $[Ni^+(CO)_n]$ adducts formed within the channels of ZSM-5 zeolite can be achieved using EPR measurements with an isotopically labelled ^{13}CO. Due to the nuclear spin $I = 1/2$ of ^{13}C, the labelled carbon monoxide can be used for counting the number of the CO ligands and their possible equivalence, as the EPR spectrum acquires an informative superhyperfine structure (Fig. 24b_{1-3}). Additionally, molecular models of the individual polycarbonyl species, along with the corresponding spin density contours, are also shown in these figures. The ^{13}CO EPR measurements eventually prove the presence of the tri- and tetracarbonyls. In the latter case, almost complete solvation of the Ni^+ adsorption centres takes place, leaving a residual attachment of the adduct to the zeolite backbone with one Ni–O_z bond only. Notably, it has been previously observed that nickel undergoes significant migration upon formation of $Ni^+(CO)_n$ adducts in NiCaX zeolite.[255]

The EPR measurements are usually performed at cryogenic temperatures. Only mono- and dicarbonyls were observed in the IR spectra at room temperature. Higher polycarbonyls ($n > 2$) are possibly formed only at cryogenic conditions. Indeed, a comparison of the energies of the successive adsorption steps for the mono- (−42.9 kcal mol^{-1}), di- (−20.2 kcal mol^{-1}), and tricarbonyl species (−5.7 kcal mol^{-1}) with the $T\Delta S$ term of $CO_{(g)}$ reveals that already above 140 °C, the dicarbonyls are unstable. Therefore, for simple thermodynamic reasons, in most cases, only the monocarbonyl species can be expected at actual catalytic conditions. Thus, their structure and properties have been studied in more detail so far.

The expected hyperfine doublet is not resolved in the [Ni$^+$CO]–ZSM-5 adduct. This issue has been explained elsewhere,[251] based on the composition of SOMO and its structural misalignment with the Ni–C bond direction (see Fig. 24c$_2$). To describe the mechanism of CO–Ni$^+$ bond formation, pulse EPR measurements (HYSCORE) are of particular relevance. They allow for the successful determination of the small ^{13}C hyperfine couplings.[248] The corresponding echo-detected EPR spectrum and HYSCORE spectra are collated in Fig. 24c$_1$, c$_3$ and c$_4$. The interaction of ^{13}CO with Ni$^+$ZSM-5 under low p_{CO} pressures gives rise to the formation of a monocarbonyl adduct of the trigonal Ni$^+$ with $g_{zz} > g_{yy} \gg g_{xx} > g_e$, $|A_{yy}| > |A_{zz}| > |A_{xx}|$, which is characteristic of the T-shaped conformation (Fig. 24a$_1$). The binding of CO is accompanied by an intrinsic d–d relaxation of the nickel 3d manifold, due to the allied charge and β-spin density relocation between the 3d$_{xz}$ and 3d$_{x^2-y^2}$ orbitals, which stabilizes energetically the carbonyl adduct. The resolved spectroscopic parameters (g_{xx} = 2.018, g_{yy} = 2.380, g_{zz} = 2.436, A_{xx} = +1.0 MHz, A_{yy} = −3.6 MHz, A_{zz} = −1.6 MHz for ^{13}C hyperfine interaction, and e^2Qq/h = −13 MHz, η = 0.8 for ^{27}Al quadrupole interaction), reinforced by DFT calculations within the SOMF/B3LYP calculation scheme, provide a suitable background for validation of the T-shaped structure of the Ni^I–CO intrazeolite adduct.[248]

Electronic details on the CO bonding mechanism can be deduced from the frontier molecular orbital (FMO) interaction diagram, and NOCV analysis of the interacting CO and Ni$^+$–zeolite model fragments (see Chapter 4.1.1). The resultant orbital overlap correlation diagram of the π(2p) and σ states of the CO ligand with the 3d states of the zeolite [Ni$^+_{2c}$M7]$_{frag}$ fragment is shown in Fig. 25a. The ligation of CO results primarily from the sizable π overlap between low-lying π(2p) CO states with the symmetry-adopted 3d$_{xz}$ and 3d$_{yz}$ orbitals of the nickel core. It is enhanced by a slight contribution owing to the σ-type overlap of σ(2p + 2s) with one of the lobes of the in-plane 3d$_{xz}$ orbital, made possible by an unusual T-shape geometry of the CO–Ni–zeolite entity.

The energy levels of the bonding and antibonding π(2p) CO orbitals define the low and high-energy boundaries encompassing the 3d nickel-based states of the [Ni$^I_{2c}$M7] fragment. The interaction of 3d orbitals with the corresponding π^*_x and π^*_y MO of the CO ligand gives rise to strong spin polarization, reflected by the pronounced shift of the α and β spin manifolds of the carbonyl adduct. The singly-occupied α-orbital (SOMO) exhibits small delocalization on the CO moiety, which accounts well for the lack of the ^{13}C hyperfine splitting in the CW-EPR spectra. Yet, the residual spin density on the ligand is responsible for a very weak ^{13}C hyperfine interaction, as detected with the HYSCORE technique.

The delicate balance between the donation and back-donation effects can be quantified using the ETS-NOCV analysis, which enabled the identification and visualization of specific charge and spin flow channels. The main orbital

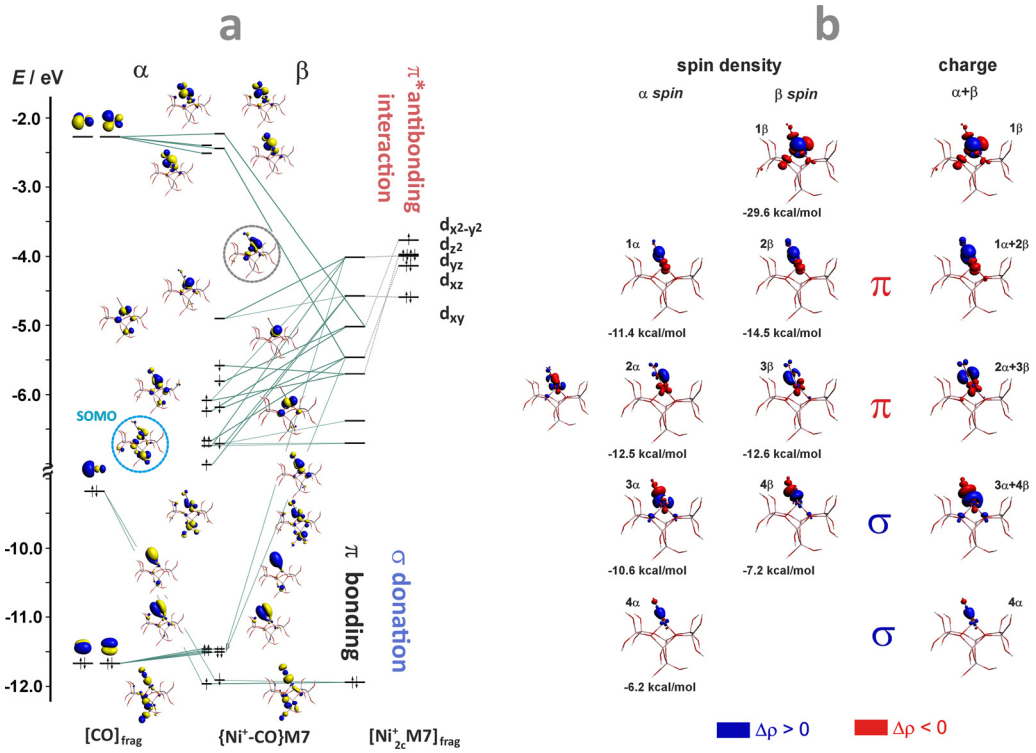

Fig. 25 The molecular energy diagram and electronic structure of the Ni$^+$–CO adduct in ZSM-5 (a) with the corresponding Kohn–Sham frontier orbital interaction diagram, and NOCV deformation density contours (b). For the charge density (α + β) and the spin density (α − β) contours, the corresponding values indicate the interaction energies associated with the individual channels of the orbital σ and π symmetries. Adapted from ref. 248 with permission from the American Chemical Society, Copyright 2013.

contributions to the α and β electron and spin density flows constituting those channels are shown in Fig. 25b, along with the corresponding energy values. As a result, the analysis enabled the disentanglement of the cooperative σ donation and π back-donation effects involved in the ligation of a CO molecule to Ni^+ ions hosted in zeolites.[248] The dominant effect is the back-donation along the π channel of a spinless charge transfer. This explains the position of the carbonyl band in the IR spectrum and its bathochromic frequency shift. The spin density redistribution within the CO moiety primarily operates *via* the 4α and (3α + 4β)σ channels. Due to the substantially uneven contributions of the 3α and 4β components, the ensuing unbalanced spin flow leads to a spin polarization of the carbon sp-hybrid. On the contrary, the 4α channel allows for a direct delocalization onto the carbon 2s orbital. Since the polarization effect prevails, this explains the negative sign of the isotropic constant $a_{iso}(^{13}C)$.[248] These two effects virtually cancel each other, resulting in a minute net spin density flow within the σ channel. Because upon the CO attachment the unpaired electron relaxation (1β) is restricted to the 3d-based orbitals of nickel, and the main channels (one σ and two π) of the electron density flow within the Ni^+–CO unit involve both α and β spins in a similar manner, the magnetophore of the monocarbonyl adduct is essentially constituted by the metal core. All the discussed effects provide a rational basis for an in-depth molecular interpretation of the IR and EPR parameters in terms of charge and spin flows along the σ and π channels.

Quantification of TMI with CO as an IR molecular probe. The IR spectra of adsorbed CO can be used to explore the nature and content of TMI in zeolites, which primarily relies on the formation and quantification of C-bonded carbonyls. The small kinetic size of the CO and its high affinity to ligation make this molecule well-suited as an effective probe for investigating Lewis and redox sites present inside the channels of zeolites. The vibrational spectrum of the diatomic CO molecule is relatively simple and strongly depends on the nature of the adsorption site. The advantage of CO as a probe molecule lies in its sensitivity to the speciation of TMI due to the subtle balance of electrostatic effects, σ-donation and π-back-donation as well as the static and dynamic interactions between the adsorbed molecules.[256,257] As a result, the CO-IR technique can inspect various valence states of TMI and their speciation (bare TMI, isolated TMI–oxo species, oxide nanoclusters). Additionally, it is often possible to selectively detect cations in different valence and coordination states, even when present simultaneously.[258] Yet, although CO can serve as a probe for analysing the coordination vacancies of exchangeable cations within zeolites, in some cases, the adsorption of CO is isodesmic, *i.e.*, formation of new TMI–CO bonds occurs at the expense of the TMI–O_z bonds with the zeolite framework, keeping the overall coordination number intact.[248] Spectroscopic fingerprints for commonly studied intrazeolite carbonyl adducts of Co, Cu, Fe, and Ni are presented in Table 4.

There are certain limitations to using CO as a probe, primarily when reactive CO adsorption occurs, resulting in chemical modification of the TMI centre by the adsorbed species. The typical products of reactive CO adsorption include carbonates, bicarbonates, carboxylates, and even formates. In some instances, CO can also be oxidised to carbon dioxide.[263] The undesired reactive CO adsorption can often be mitigated by using low-temperature experiments. These issues should be considered when aiming for a more accurate determination of the oxidation states of TMI ions in zeolites. A more general account of the application of IR spectroscopy in zeolite research can be found in previous works.[256,257]

Table 4 Spectoscopic fingerprints for commonly studied intrazeolite carbonyl adducts of Co, Cu, Fe, and Ni

Intrazeolite	TMI–CO adduct	Frequency/cm^{-1}	Ref.
Co/MFI	Co^{2+}–CO	2204	32
	$(CoO)_n$–CO	2194	
Ni/ZSM-5	Ni^{2+}–CO	2220–2180	31, 80, 249 and 259
	Ni^{+}–CO	2109	
Cu/ZSM5	Cu^{+}–CO	2157	260
	Cu^{0}–CO	2124	
	Cu^{2+}–CO	2206	
Fe/MFI	Fe^{2+}–CO	2196	261 and 262
	Fe^{2+}–$(CO)_2$	2188	

After establishing the experimental conditions for generating the monocarbonyl adducts (see the $\Delta G(p,T)$ diagrams), IR absorption coefficients can be obtained through careful CO titration under controlled conditions (CO pressure and temperature). The most convenient situation occurs when the specific probe molecule reacts selectively with only one type of adsorption center, and the stoichiometry of this process is well understood. It can be inferred, for instance, from the FPT phase diagrams (Fig. $22d_1$–d_3), which also reveal differences in the formation of monocrbonyls between the zeolite frameworks and TMI localisation within the particular channels.[243] In most cases, it is reported that the value of the absorption coefficient for the respective carbonyls is independent of the zeolite structure, despite the observed various CO stretching frequencies.

In the case of cobalt cations accommodated in the pentasil zeolites (*e.g.*, MFI, FER), the CO band at 2204 cm^{-1} is attributed to Co^{2+}–CO adducts formed with the exchanged Co^{2+} cations, whereas the bands at 2194 cm^{-1} and 2179 cm^{-1} are associated with Co^{2+} in oxide clusters and segregated CoO, respectively.[32] The plot of the intensity of the characteristic monocarbonyl IR band as a function of the amount of CO sorbed is used to determine the absorption coefficient. For the 2204 cm^{-1} band, the absorption coefficient is equal to 0.123 ± 0.002 cm^2 μmol^{-1}, and its value is independent of the zeolite type and the adsorption temperature.[32] For the 2194 cm^{-1} band, a value of 0.129 ± 0.004 cm^2 μmol^{-1} has been reported, based on the intensity (height) of the corresponding IR signal. In addition, the absorption coefficient of the CO–OH band at 2175 cm^{-1} due to adsorption of CO on Brønsted centres is equal to 0.120 ± 0.003 cm^2 μmol^{-1} (determined for FER zeolite). All these coefficients can be used to evaluate the complete balance of cationic sites in pentasil zeolites from a single IR adsorption measurement.

Coordination of CO to Ni^{2+} cations leads to the formation of Ni^{2+}–CO monocarbonyl adducts with the IR bands located in two spectral regions: 2220–2180 cm^{-1} and 2170–2130 cm^{-1}.[80,249,259] The low-energy region is characteristic of carbonyls formed on nanosized NiO and mixed oxides. The high-energy band is characteristic of isolated Ni^{2+} cations present in the exchangeable positions. The absorption coefficient for this band in NiZSM-5 zeolite (2212 cm^{-1}) equals 0.143 ± 0.003 cm^2 μmol^{-1}.[31] The same value was obtained for NiY, despite slight differences in the CO stretching frequencies of the Ni^{2+}–CO monocarbonyls (2212 and 2220 cm^{-1} for NiZSM-5 and NiY, respectively). During the reactive adsorption of CO on nickel–oxo compounds, CO acts simultaneously as a reducing agent and as a probe for the generated Ni^+ cations.[247] The characteristic band of the Ni^+–CO adduct is located at 2109 cm^{-1}, and the absorption coefficient is equal to 1.104 ± 0.018 cm^2 μmol^{-1}.[31] A strong increase in the absorption coefficient of Ni^+–CO compared to Ni^{2+}–CO originates from more efficient transfer of the 3d electron density from the Ni^+ cation onto the π^* antibonding orbital of CO (π-back-donation effect) due to the better energy matching of the overlapping orbitals.[249]

The interaction of CO with copper sites in thermally treated ZSM-5 zeolite results in the formation of a strong band at 2157 cm^{-1} due to Cu^+–CO monocarbonyls at low CO doses. In contrast, the band at 2130 cm^{-1} produced when CO was sorbed in higher amounts was attributed to Cu^+ ions present in an oxide form.[260] Treatment of CuZSM-5 zeolite with H_2 results in the appearance of a band at 2124 cm^{-1}, attributed to the monocarbonyls of metallic copper (Cu^0–CO). When oxidised with O_2, some of the Cu^+ cations in exchange positions are transformed into Cu^{2+} species, which is recognised by the development of a band at 2206 cm^{-1} due to the Cu^{2+}–CO monocarbonyls. By measuring the intensity (height) of the 2157 cm^{-1} band corresponding to the sorbed CO, the slope of the resulting linear correlation defines the extinction coefficient, yielding a value of 1.30 cm^2 μmol^{-1}. The extinction coefficient of CO interacting with Cu^{2+} species in zeolite CuZSM-5 was obtained after treatment with oxygen. The intensity of a relatively weak Cu^{2+}–CO band at 2206 cm^{-1} can be used to calculate the absorption coefficient, which equals 0.11 cm^2 μmol^{-1}. Note that this value is similar to other divalent cations hosted in ZSM-5 (see above). The experimental and calculation details can be found elsewhere.[260]

Iron speciation in zeolites is also extensively studied using IR spectroscopy with a CO probe. For instance, the corresponding carbonyl bands appear at 2200–2194 cm^{-1} for the zeolites BEA,[264] FER,[265] and MFI.[261] In general, iron species in zeolites prepared from a ferrous solution were found to be mainly in the Fe^{2+} form. Fe^{2+}–CO monocarbonyls (with the band at 2195 cm^{-1}) convert easily into $Fe^{2+}(CO)_2$ dicarbonyls (2188 cm^{-1}) at low temperatures, but the reaction progress depends on the exchangeable sites within the zeolite. Other identified Fe^{2+} ions in FER produced exclusively monocarbonyls (band at 2189 cm^{-1}), and in comparison to the previous hosting site, they were easily oxidised to Fe^{3+} ions in the presence of oxygen (or air). Sorption of CO on FeZSM-5 zeolite resulted in monocarbonyl bands at 2188 and 2200 cm^{-1}, which were attributed to the Fe^{2+}(CO) based on the results of oxidation/reduction reactions with O_2 and H_2.[262] The calculated extinction coefficient based on the integral absorption is equal to 2.52 ± 0.07 cm μmol^{-1}, while the value obtained from the band height measurement drops to 0.11 ± 0.01 cm^2 μmol^{-1}.

4.3. Non-innocent molecules – ligation pathways

Non-innocent (ambivalent) ligands such as $O_2/O_2^-/O_2^{2-}$, NO/NO^+/NO^-, NO_2/NO_2^- play an essential role in a large variety of catalytic reactions involving metallozeolite catalysts, including HC (hydrocarbons) oxidation and HC-SCR,[17,156,157,266] NH_3-SCR,[156,188,267,268] deNO_x[269,270] or oxidation of CH_4[271–275] and NO[172,276,277] in particular. Their ambiguous electronic and magnetic structures, as well as their electronic flexibility upon binding to intrazeolite TMI, pose challenges for the clear assignment of the metal and ligand oxidation states, and therefore, for establishing their distinct roles in the redox mechanisms of the investigated reaction. In contrast to the innocent H_2O or NH_3 ligands (which are characterised by a well-defined charge that is usually preserved upon ligation, see Chapter 4.2), the non-innocent ligands can change their redox states due to breaching of the Pauli shield, and participate in electron transfer to or from the TMI centres. As a result, the valence and coordination states of non-innocent ligands can change to facilitate the mechanistic redox steps during a catalytic reaction. The non-innocent ligands can play an auxiliary role, meaning that they do not interact directly with the reactants, but alter the redox state of the metal centre (redox functionality tuning), or participate explicitly in the reaction by making and breaking covalent bonds with the captured reactant molecules.[172] For instance, the appearance of an unusual $3d^9$ state of cobalt is made possible upon the coordination of redox-active NO ligands to Co^{2+} hosted in ZSM-5, which triggers the subsequent capture of olefin molecules by the Co^0 centres for driving the HC-SCR reaction efficiently with the involvement of the Co^{2+}/Co^0 redox couple.[17] An intricate network of NO oxidation[172] and NO reduction with ammonia over Cu/CHA and Cu/MFI catalysts[199,278,279] or with ethylene over NiSZM-5[156] can also be invoked here as illustrations.

To circumvent the ambiguity of oxidation state assignments and dichotomy of the electrons division, the Enemark–Feltham notation $\{XYM\}^{d+\pi}$ can be used, where XY indicates a diatomic ligand, M – metal, and d + π is the sum of the electrons on d orbitals of M and π orbitals of XY.[280] Two alternative coordination situations between a transition metal cation, $M^{p/p\pm1}/z$, and an attached non-innocent ligand, $L^{q/q\pm1}$, involve resonance structures, $XY^qM^p/z \rightleftharpoons XY^{q-\delta}M^{p+\delta}/z$ (redox counterparts[281]), with the delocalized electrons in a single or double energy minimum. In this notation, p and q represent the charges of the TMI and XY ligand, respectively, whereas δ corresponds to the partial charge shifts. This ambivalence is particularly amplified in the case where the 3d levels of the intrazeolite transition metal cations, such as Co, Ni, or Cu, are intermingled with the $2\pi^*$ levels of the non-innocent XY ligands (Fig. 26a). The classic

ligation dichotomy involves here spin pairing and electron transfer categories.

The alignments of the energy levels shown in Fig. 26a favour electron transfer from Cu^{+} and Ni^{+} to O_2 and spin-pairing for NO. In the case of Cu^{2+} and Co^{2+}, since the β-3d manifold is located below the $2\pi^*$ level, coordination of the donor co-ligands (*e.g.*, NH_3) is needed to trigger the MLET (see Chapter 4.3.1). Ligation of open-shell non-innocent XY molecules leads to changes in the overall spin state of the $\{XYM\}^{d+\pi}$ unit. Exemplary scenarios collated in Fig. 26b illustrate computational isodesmic pathways of spin addition, spin pairing, and spin crossing coupled with spin pairing upon NO molecule coordination to selected transition metal ions of different spin multiplicity hosted in the MFI matrix (see Chapter 4.3.2. for more details).

4.3.1. Binding and activation of O_2. The interaction of O_2 molecules with intrazeolite transition metal ions yields a variety of mono- and bidentate M–O_2 and bridging M–O_2–M adducts (Fig. 27a), which are capable of the O–O bond scission or direct attack on an organic substrate, exhibiting an intricate combination of interfacial coordination and redox chemistries. It involves the partial reduction of the ligated O_2 *via* one- ($1e^-$) or two-electron ($2e^-$) transfers from the TMI active sites, producing superoxide and peroxide 1 : 1 and 1 : 2 species. The deep four-electron dissociative reduction of O_2 on single sites occurs at electron-rich TMI. However, attainment of elevated oxidation states ($z \geq 4$) is hindered by high energy costs, particularly for those TMI that are positioned after Mn in the periodic table. Actually, it takes place in a more complex manner, favourably on dimeric centres (1 : 2), and can be promoted by coupling with proton relocation (electroprotic route), leading to more stable hydroperoxo M–OOH and hydroxyl M–OH intermediates. Various combinations of these processes, involving the removal of the inert triplet ground state of molecular oxygen ($^3\Sigma_g^-$) and an apposite stabilisation of the resultant species by coordination to the metal centres, make the activation thermodynamically more favourable and kinetically accessible. Isotopic labelling is widely explored in the elucidation of the O_2 binding and activation processes, being particularly useful for identifying activated oxygen species and studying the activation mechanisms, using ^{18}O (IR, RS) and ^{17}O (EPR) labelled dioxygen.

The variety of ways in which single and two adjacent TMI cations (M∪M) can bind an O_2 molecule includes a considerable diversity of the resultant structural motifs.[282–285] End-on η^1-O_2 superoxide (Pauling structure), the side-on η^2-O_2 superoxide or peroxide (Griffith structure), the *cis* μ-η^1:η^1 (Yeager structure) and *trans* μ-η^1:η^1, side-on μ-η^2:η^2, μ-η^2:η^1, as well as the bis(μ-oxo) or η^2-ozonide molecular adducts with Fe, Co, Ni, Cu or Zn are the most common in the case of metallozeolites. Their energetic, structural, and spectroscopic characteristics depend on Al location within the rings (Fig. 27b), accommodation locus in the given zeolite framework (Fig. 27c and d), and the framework type (Fig. 27d).[285–287] The bridging peroxo species, upon further reductive dissociation, can be converted into highly reactive terminal (such as Fe=O) or bridging (*e.g.*, Cu–O–Cu), mono-oxo species, accomplishing the complete $4e^-$ reduction and splitting of O_2, discussed below.

Dioxygen attachment and activation on single TMI centres. The reductive monodentate (η^1) and bidentate (η^2) attachment of O_2 to single intrazeolite TMI centres can occur through the σ, π and δ-overlap (see Fig. 17c) between the metal donor 3d (or 4s for Zn) and the $2\pi^*$ acceptor orbitals of dioxygen leading to the formation of paramagnetic superoxide ($1e^-$ transfer) or diamagnetic peroxide ($2e^-$ transfer) 1 : 1 species. However, due to the simultaneous operation of bonding and back-bonding interactions, fractional changes in the charge and spin transfers between the metal and ligand are actually observed. Reasonably, the adducts with the O–O bond length of 1.4–1.5 Å and ν_{O-O} 750–930 cm^{-1} are designated as peroxides, whereas those with 1.2–1.3 Å bond length and ν_{O-O} lying in the range of 1050–1200 cm^{-1} are classified as superoxides.[289] Their dinuclear nature can be deduced from the $\Delta^{18}O$ shifts (~50–60 cm^{-1}) in IR spectra, and from the character of ^{17}O hf pattern in the EPR spectra of the paramagnetic superoxide complexes (11 equidistant lines are diagnostic for η^2 and up to 36 lines for η^1 attachment).[290] The correlation between the

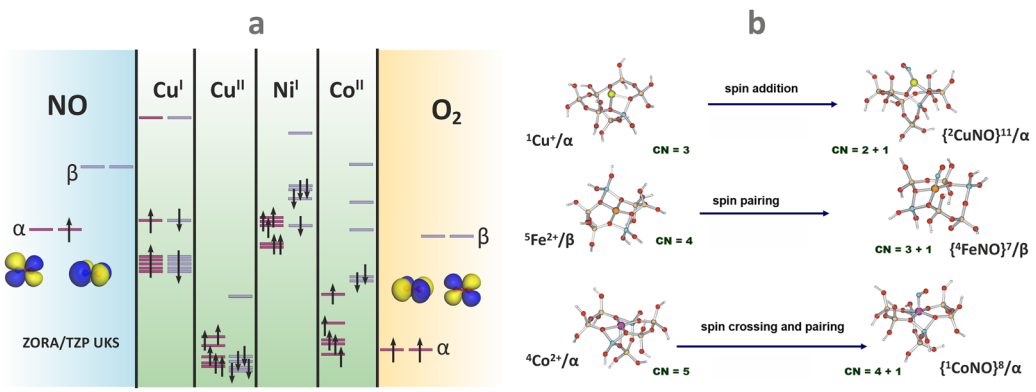

Fig. 26 Alignment of the $2\pi^*$ levels of the non-innocent NO and O_2 molecules to the 3d levels of Co, Ni, and Cu cations hosted in the exemplary ZSM-5 zeolite (a). Isodesmic routes of the intrazeolite coordination *via* spin addition, spin pairing, and spin crossing coupled with pairing mechanisms (b), calculated at the ZORA/TPZ UKS level.

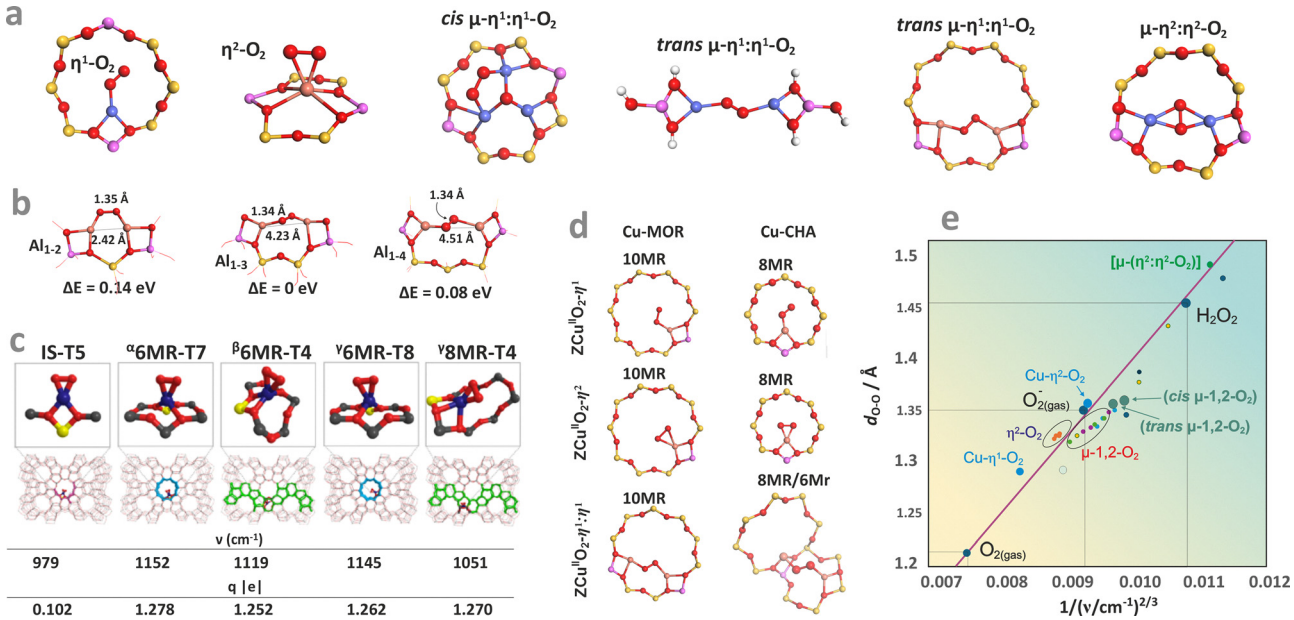

Fig. 27 Typical binding modes of oxygen to mono- and dinuclear metal centres hosted in zeolites (a). The influence of Al distribution on the stability of the *cis* μ-η¹:η¹-O_2 di-copper adducts presented in TON zeolite (b).[285] The effect of the zeolite framework on the structure of η²-O_2–Co in various sites of the distinct topology of MFI (c), and on the structure of η¹-O_2–Cu, η²-O_2–Cu, and *trans* μ-η¹:η¹-O_2 di-copper adducts in MOR and CHA zeolites (d).[287] The d-O–O *vs.* $1/(\nu_{O-O})^{2/3}$ 2D correlation diagram for classification of oxygen adducts with the intrazeolite transition metal ions (e). The calculated positions of the reference O_2, O_2^-, H_2O_2, and bare η¹-O_2–Cu, η²-O_2–Cu and *cis*, *trans* μ-η¹:η¹-O_2, μ-η²:η²-O_2 species (terminated with –OH) are marked in large circles, whereas the positions of the corresponding adducts of Cu, Co, Fe, hosted in CHA, TON, MFI, MOR zeolites are marked with small circles.[286,288] Panels a, b, d, and e based on data from the quoted references. Panel c adapted from ref. 286 with permission from the American Chemical Society, Copyright 2020.

d_{O-O} bond length and the ν_{O-O} vibration frequencies based on empirical Badger relation ($d_{O-O} = C/(\nu_{O-O})^{2/3} + b$), established previously for homogeneous complexes,[289] shows that the vibration frequencies smoothly span the whole range from the superoxide-like to the peroxide-like species (Fig. 27e). As a result, assignment of the discrete (integer) oxidation states of oxygen species has a formal character only. Thus, the covalent communication between the metal centre and the O_2 ligand leads to the formation of intrazeolite adducts, which may be regarded as valence hybrids of the limiting superoxide and peroxide extremes.[289] In addition to assigning the formal oxidation states to metal and dioxygen moieties, the mode of binding and the orbital overlap responsible for bond formation, as well as the MLET pathway, are of key importance. Especially, recognising the impact of the O_2 activation type on the catalytic reactivity with reactant molecules.

The intrazeolite superoxide adducts can then be categorised into the σ, π and δ-type paramagnetic species, exemplified by the $[\eta^1\text{-}O_2^-\text{–}Zn^{II}]^+$/MFI,[291] $[\eta^1\text{-}O_2^-\text{–}Co]^{2+}Y^{292}$ and $[\eta^2\text{-}O_2^-\text{–}Ni]^+$ZSM-5[64] cage adducts identified univocally by EPR spectroscopy using ^{17}O-labelling.

The Zn^+/ZSM-5 (Si/Al = 11.9) species react with O_2 (5 mbar, 300 K) with the formation of $[O_2^{\bullet-}Zn]^+$/MFI adducts, as demonstrated by the EPR spectrum with $g_{zz} = 2.039$, $g_{yy} = 2.0108$, $g_{xx} = 2.0033$ (Fig. 28a).[78,291] Based on the internuclear bond distance of $d_{O-O} = 1.33$ Å and $\nu_{O-O} = 115$ cm^{-1} (see Fig. 27e) this adduct has been assigned to top-on $[^1\eta\text{-}O_2^{\bullet-}\text{–}Zn]^+$/ZSM-5, produced by transfer of the electron density (0.7–0.8) from $4s^1$ to the in-plane $2\pi_{\parallel}^*$ orbital, *via* the σ-donation channel that is favourable for the top on ligation (Fig. 28a_1). The $4s/3d_{zx} - 2\pi_{\parallel}^*$ HOMO is mainly responsible for the O_2 binding (−150 kJ mol^{-1}), whereas the out-of-plane $2\pi_{\perp}^* - 3d_{zy}$ SOMO is localized essentially on the oxygen moiety, interacting weakly with the Zn ion.

An alternative η²-attachment of dioxygen, distinct by a higher $g_{zz} = 2.061$ value (and similar $g_{yy} = 2.010$, $g_{xx} = 2.003$), is disclosed by the ^{17}O hyperfine structure with the resolved 11 equidistant lines that are separated by $A_{xx} = 7.68$ mT (Fig. 28b), observed in the EPR spectrum when $^{17}O_2$ is contacted with Zn^I/ZSM-5 (Si/Al = 140).[294] Such ^{17}O hf pattern confirms that both oxygen atoms are magnetically equivalent, which is tantamount to the side-on ligation of dioxygen with $\Delta E_{ads} = -110$ kJ mol^{-1}. The internuclear bond distance of $d_{O-O} = 1.24$ Å is indicative of the superoxide nature of the bound O_2. The NOCV analysis reveals that formation of the $O_2^{\bullet-}$ species results from the dominant flow of electron density from the $4s^1$ to 2π* orbital in the β-channel, which is accompanied by a small back-donation of the α-spin density towards the zinc core (Fig. 28b_1). The recognition of both the top-on $[\eta^1\text{-}O_2^{\bullet-}\text{–}Zn]^+$/MFI (Si/Al = 11.9) and the side-on $[\eta^2\text{-}O_2^{\bullet-}\text{–}Zn]^+$/MFI (Si/Al = 140) adducts illustrates a subtle role played by the intermolecular electrostatic interactions in supporting the particular binding mode of dioxygen. It is also plausible that the η² superoxide adduct is actually produced *via* the η¹ intermediate, since the nil overlap between the redox $4s^1$ to 2π* orbitals in the side-on mode impedes charge flow. In the case of $[Zn\text{–}O^{\bullet-}]$/MFI species where the spin density is mainly localized on the ligand (characterized

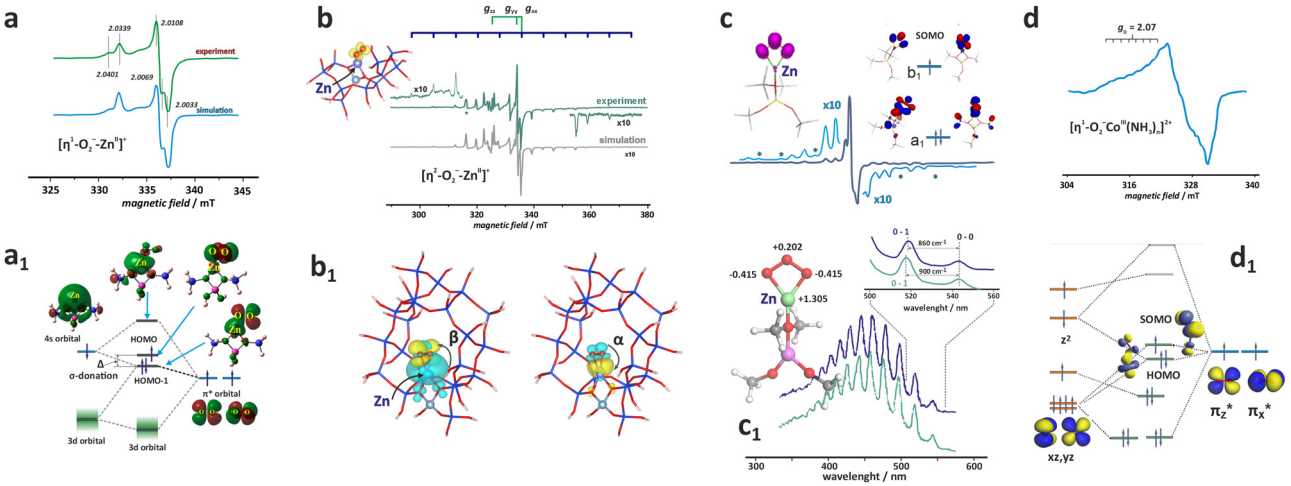

Fig. 28 X-band CW-EPR spectrum of the $[\eta^1\text{-}^{16}O_2^{-}\text{–}Zn]^+$/ZSM-5 adduct (a) with the corresponding MO energy diagram (a_1) (adapted from ref. 291 with permission from the American Chemical Society, Copyright 2013) and of $[\eta^2\text{-}^{17}O_2^{-}\text{–}Zn]^+$/ZSM-5 (b) with the corresponding NOCV analysis of the spin-polarized MLET along the β-channel and back donation along the α-channel (b_1). EPR spectrum (c),[293] and UV-vis spectrum (c_1) of the $[\eta^2\text{-}O_3^{-}\text{–}Ni]^+$/ZSM-5 adduct (adapted from ref. 294 with permission from the American Chemical Society, Copyright 2021). The EPR spectrum of the cage $[\eta^1\text{-}O_2^{-}\text{–}Co(NH_3)_n]^{2+}$/ZSM-5 adduct (d) together with the associated MO diagram of the energy levels (d_1).[113] Panels b, b_1, d, and d_1 are inspired by the quoted references.

by $g_{\parallel} = 2.37$ and $g_{\perp} = 1.98$ and the UV/vis band at 12 020 cm^{-1}), a room temperature interaction with O_2 ($p_{O_2} > 0.1$ Torr) leads to the reversible formation of a zinc–ozonide adduct, $[Zn\text{–}O^{\bullet -}]^+$/MFI + O_2 ↔ $[\eta^2\text{-}O_3^{\bullet -}Zn]^+$/MFI, produced by the attack of dioxygen at the $O^{\bullet -}$ moiety (see Chapter 4.1 and Fig. 17d). It is characterized by $g_{xx} = 2.0019$, $g_{yy} = 2.0106$, $g_{zz} = 2.0124$, $A_{xx} = -8.37$, $A_{yy} = 0.14$, $A_{zz} = 0.36$ (Fig. 28c), and the $n_b \rightarrow \pi^*(O\text{–}O\text{–}O)$ band centred at ∼450 nm, which is featured by a well resolved vibronic progression due to the stretching O–O–O oscillations with the 860 and 900 cm^{-1} splitting for $\eta^2\text{-}^{16}O_3^{\bullet -}Zn^{II}$ and $\eta^2\text{-}^{18}O_3^{\bullet -}Zn^{II}$ species, respectively (see Fig. 28c1).[294] The binding of O_2 occurs *via* an $[\eta^1\text{-}O_3^{\bullet -}Zn]^+$ intermediate,[293] and a rather small overall energy of this process (96 kJ mol^{-1}), together with low activation barriers (the highest is equal 68 kJ mol^{-1}), accounts well for the experimentally observed complete reversibility of this process. The a_1-bonding orbital (labelled in the local C_{2v} symmetry of the zinc–ozonide magnetophore) with the largest overlap between the Zn and O_3 counterparts, contributes mainly to the Zn–O_3 bond. In contrast, the b_1-SOMO is almost entirely localised on the bidentate ozonide moiety. The remaining orbital interactions (a_2, b_1, and b_2 MO) are less important for the strength of the Zn–O_3 interaction due to the small overlap. The distinct polarisation of two O–O bonds in the O_3 ligand lead to a unique pattern where both side oxygens that are directly bound to Zn^{2+} become more negatively charged (−0.415|*e*|). In contrast, the central oxygen acquires surprisingly a partially positive charge (0.202|*e*|), in comparison to the free ozonide anion (−0.167|*e*|). The zeolite framework plays a vital role in maintaining the effective charge of the zinc cation at approximately +2, stabilising the highly polarised $\eta^2\text{-}O_3^{-}\text{–}Zn^{2+}$ bond.

In the case of di-oxo vanadium ↑VO_2/BEA, a room temperature contact with dioxygen (2 Torr) leads to the formation of a bent (α = 16°) top-on $[\eta^1\text{-}O_2^{-}\ VO_2^{+}]$/BEA complex ($g_z = 2.0236$, $g_y = 2.113$, $g_x = 2.0054$, $A_z = 0.98$, $A_y = 0.68$, $A_x = 0.54$ mT) *via* the MLET, $d_{z^2} \rightarrow 2\pi^*$, pathway. The π*-type SOMO is essentially confined to the $\eta^1\text{-}O_2^{-}$ moiety.[295]

The π-type adducts are exemplified by superoxide species attached to cage $Co^{2+}(NH_3)_n$ complexes. The intrazeolite Co^{2+} ($S = 3/2$) cations cannot directly activate O_2 into the superoxide state due to the inverse energy levels (IEL) of the donor 3d and acceptor 2π* orbitals (see Fig. 26a). However, when boosted by the coordination of stronger σ-donor NH_3 co-ligands (which can be allied with an "orthosteric effect") the resultant $[Co(NH_3)_n]^{2+}$ adducts hosted in FAU(Y)[292] and ZSM-5 zeolites[113] upon exposure to O_2 form the corresponding $[\eta^1\text{-}O_2^{-}Co(NH_3)_n]^{2+}$ heteroleptic superoxide complexes identified readily by EPR spectroscopy (Fig. 28d). The reductive binding of O_2 is accompanied by a spin crossing in the 3d manifold of the cobalt core (↑↑O_2 ($S = 1$) + ↑↑↑Co^{2+} ($S = 3/2$) → ↑O_2^{-}–Co^{3+}↑↓ ($S = 1/2$)), giving rise to the observed doublet state of the superoxide adduct. In an alternative spin pairing process (↑↑O_2 ($S = 1$) + ↑↑↑Co^{2+} ($S = 3/2$) → ↑O_2^{-}↑↓Co^{3+}↑ ($S = 1$), the adduct should assume a triplet state. Yet, the ***g***-tensor anisotropy ($g_1 = 2.084$, $g_2 = 2.01$, $g_3 = 2.00$) is diagnostic for the formation of a superoxide species with $S = 1/2$. The superhyperfine structure ($^{Co}A_1 = 1.78$ mT, $^{Co}A_2 = 1.2$ mT and $^{Co}A_3 = 1.25$ mT)[292] can be interpreted in terms of the β-electron density transfer to $|SOMO\rangle = a_1|d_{xz}\rangle + b_1|\pi_x^*\rangle$ formed by the out of plane π-type overlap, and the spin polarization of the close-lying in-plane $|HOMO\rangle = a_2|d_{z^2}\rangle + c_2|d_{yz}\rangle + b_2|\pi_z^*\rangle$ of the mixed π/σ character, as discussed elsewhere.[296] Such in-plane d/π interactions impart a bent configuration of the Co–O–O moiety and local C_s symmetry of the ensuing magnetophore. A qualitative molecular energy diagram shown in Fig. 28d1 accounts for the reductive coordination of O_2 by $[Co(NH_3)_n]^{2+}$/ZSM-5 *via* the MLET mechanism associated with spin crossing.

The superoxide η^2-species can also be produced in the δ-type MO overlap. This relatively rare binding mode of O_2 results from an isodesmic $^2Ni^+_{4c}$/ZSM-5 + $^3O_2$ → $[\eta^2\text{-}O_2^-Ni_{2c}]^+$ZSM-5 process, where the initial coordination number of the nickel cation (Ni^+_{4c}) equalled 4, is preserved. The corresponding EPR spectrum obtained for ^{17}O-enriched dioxygen is shown in Fig. 29a. The 11-line pattern proves the side-on attachment of the dioxygen ligand. The diagnostic features of the heteroleptic $[\eta^2\text{-}O_2^-Ni_{4c}]^+$ZSM-5 adduct ($g_e < g_{xx(3)} = 2.0635 < g_{yy(2)} = 2.0884 < g_{zz(1)} = 2.1675$, $A_{yy(2)}$ (5.67 mT) ≫ $A_{xx(3)}$ (1.0 mT) ∼ $A_{zz(1)}$ (1.3 mT)) with the highest hf splitting along the $g_{yy(2)}$ mid value direction are distinctly different from those observed for the π-type O_2^- adducts ($g_e \approx g_{xx(3)} < g_{yy(2)} < g_{zz(1)}$, and $A_{zz(1)} > A_{xx(3)} \sim A_{yy(2)}$ with the maximum of hf splitting along the highest $g_{zz(1)}$ value). The $[\eta^2\text{-}O_2^-Ni]^+$ZSM-5 complex is best described as a mixed metalloradical with two supporting oxygen donor framework O_z ligands and nearly even spin density repartition between the superoxide moiety and the nickel centre (ρ_{Ni} = 0.36, $\rho_{O(1)}$ = 0.32, $\rho_{O(2)}$ = 0.30), as shown in Fig. 29a$_1$. The associated changes in the charge distribution upon O_2 attachment (Δq_{Ni} = 0.32, Δq_O = −0.09, Δq_O = −0.11) confirm the MLET mechanism of dioxygen activation with back donation playing a crucial role (see below). Notably, the observed triangle spin density and charge distribution resemble those observed for $\eta^2\text{-}O_3^{\bullet-}Zn^{2+}$ species, where the middle Ni cation and the middle oxygen are both positively charged.

The SOMO orbital is constituted by a δ overlap between the out-of-plane $2\pi^*_\perp$ MO of dioxygen and the $3d_{x^2-y^2}$ orbital of nickel, whereas LUMO results from the π-type overlap between d_{zy} and in-plane $2\pi^*_\parallel$ orbitals (see Fig. 30a), following the superoxide nature of the $[\eta^2\text{-}O_2^-Ni]^+$ZSM-5 species. The overall binding energy of dioxygen, equal to −16 kcal mol^{-1}, results from the molecular (−141 kcal mol^{-1}) and electrostatic (−87 kJ mol^{-1}) contributions that are attenuated by a sizable steric repulsion (+212 kJ mol^{-1}).

The intrazeolite $[\eta^2\text{-}O_2^-Ni_{4c}]^+$/ZSM-5 species exhibit significantly different electronic and magnetic structure than the akin dioxygen adducts with nickel in homogeneous complexes,[298,299] where the spin pairing mechanism prevails. The SOMO is then constituted mainly by the $3d_{z^2}$ orbital, giving rise to $g_{zz} \ll g_{xx}, g_{yy}$, and a small ^{17}O hf splitting (which usually remains unresolved). Thus, dissimilar magnetic structures of both types of adducts can be accounted for by the different mechanisms of dioxygen binding, which are based on coupled electron and spin transfer in the case of $[\eta^2\text{-}O_2^-Ni_{4c}]^+$ZSM-5, and a spin pairing model for the homogeneous complexes. The ETS-NOCV analysis of the $[\eta^2\text{-}O_2^-Ni_{4c}]^+$ZSM-5 electronic structure reveals three distinct orbital channels of the congruent and incongruent charge and spin density flows, associated with δ, π, and σ overlap, which contribute jointly to the attachment energy and the reductive activation of the dioxygen ligand (Fig. 30b1 and b2).

The unequal charge and spin density transfers along the π-channel result from the π-donation from $3d_{yz}$ to $2\pi^*_y$ (1β) and the π-backdonation (1α) processes, with highly uneven energetic contributions −83.2 and −5.0 kcal mol^{-1}, respectively. The δ-channel (2β) of a congruent but opposite spin and charge transfer $3d_{x^2-y^2} \rightarrow 2\pi^*_x$ MO contributes to −30.5 kcal mol^{-1} of the O_2–Ni interaction energy, whereas the spinless charge back-donation, $2\pi^*_y \rightarrow 3d_{yz}$, through the σ channel (2α + 3β) is associated with a relatively small energy gain of −14.2 kcal mol^{-1}. As a result, the β-spin polarised charge δ-donation, reinforced by the partly counterbalancing β-charge donation and α-polarised back-donation along the π-channel, together with a small charge-only σ-back-donation (Fig. 30b$_2$, and b$_3$) are mainly responsible for the formation of nickel-bound superoxide O_2^- radical of the

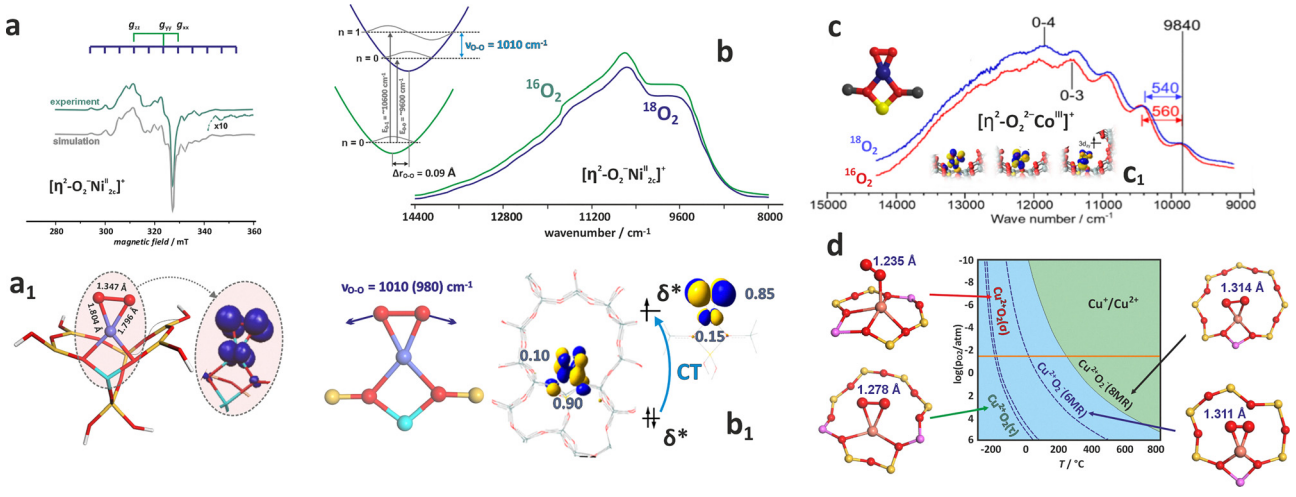

Fig. 29 X-band EPR spectrum of $[\eta^2\text{-}O_2^-Ni_{4c}]^+$/ZSM-5 adducts (a), and the structure of the η^2-O_2Ni moiety with the spin density distribution (a$_1$) adapted from ref. 64 with permission from the American Chemical Society, Copyright 2011. NIR spectra of η^2-$^{16}O_2$ and η^2-$^{18}O_2$ adducts of nickel (b), and cobalt (c) hosted in MFI zeolite, and the corresponding structures of these species (b$_1$) and (c$_1$), adapted from ref. 286 and 297, with permissions from the American Chemical Society (Copyrights 2020 and 2019, respectively). Thermodynamic stability diagram of η^1-O_2 and η^2-O_2 adducts of Cu^{2+} and Cu^+ hosted in CHA (d), based on data from ref. 83.

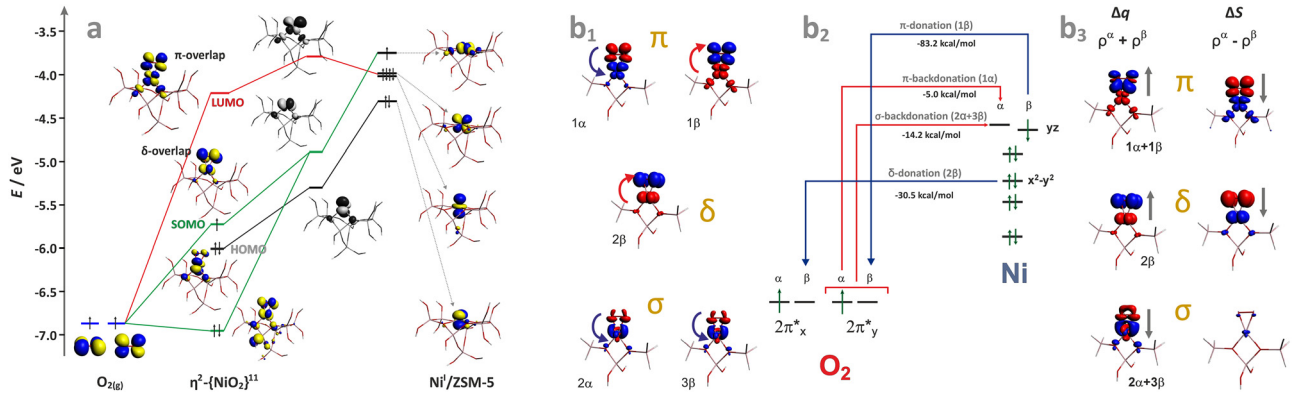

Fig. 30 Molecular orbital correlation diagram of O_2 binding to Ni^+/ZSM-5 (a). The NOCV contours that describe the bonding between the dioxygen and the intrazeolite Ni^+ cation (b_1), along with the corresponding diagram showing the charge and spin flow channels and the associated energies (b_2), together with the orbital channels of the overall charge (Δq) and spin (ΔS) flows (b_3). The red and blue contours correspond to loss and gain of the electron and spin density, respectively. Adapted from ref. 64 with permission from the American Chemical Society, Copyright 2011.

$(\pi)^2(\delta)^2(3d_{z^2})^2(3d_{x^2-y^2})^2(3d_{zy^2})^2(\delta^*)^1(\pi^*)^0$ configuration, and its $S = 1/2$ ground state. This illustrates the inherent complexity of what appears to be a simple process.[64]

The vibronic progression with the O–O stretching frequency of 1010 cm^{-1} and the isotopic shift, $\Delta^{18}O = 30$ cm^{-1}, associated with the $\delta \rightarrow \delta^*$ excitation seen in the NIR spectra (Fig. 29b) provides another argument that the δ channel interaction contributes to the formation of the superoxide species.[297] The bonding δ orbital is mainly localised on the Ni^{2+} centre, and the antibonding δ* orbital on the O_2^- moiety (Fig. 29b$_1$), hence the $\delta \rightarrow \delta^*$ transition lengthens the O–O bond from 1.308 to 1.405 Å, contributing additionally to dioxygen activation *via* MLCT. Furthermore, the ionicity of the δ bond has been linked to the abnormal electrophilic reactivity of the unoccupied β-2π* orbital of the superoxide moiety.[297]

In contrast to the superoxide species produced on Ni^+/ZSM-5, the side-on attachment of O_2 to Co^+ hosted in ZSM-5 leads, *via* $2e^-$ transfer, to the formation of a peroxo $[\eta^2\text{-}O_2^{2-}Co]^+$/ZSM-5 adduct (Fig. 29c).[286] Actually, this species is indirectly produced from a dicarbonyl precursor $[Co(CO)_2]^+ + 2Co^{2+} + O_2 \rightarrow [Co(O)_2]^+ + 2[Co(CO)]^{2+}$. The positioning of the Al atoms at the interface between the straight and sinusoidal channels of the MFI framework is essential for the successful implementation of this process. In the $[\eta^2\text{-}O_2^{2-}Co_{4c}]^+$/ZSM-5 adduct with $S = 1$, the Co^{3+} core is chelated by the peroxo ligand, and supported by two weak donor anionic lattice oxygen atoms, forming a square planar structure (similar to that observed for the superoxide adduct with the intrazeolite Ni^{2+}) with the ground state electronic configuration of $(\pi)^2(\delta)^2(d_{z^2})^2(d_{x^2-y^2})^2(d_{zy})^1(\delta^*)^1(\pi^*)^0$. This structure of the $[\eta^2\text{-}O_2^{2-}Co_{4c}]^+$/ZSM-5 adduct is ascertained by a distinct NIR absorption band around 9840 cm^{-1}, assigned to the $\delta \rightarrow \delta^*$ transition in the $[Co(O_2)]^+$ moiety (Fig. 29c). The interval between the first and second vibrational fine structure features equal to 560 cm^{-1} for the $^{16}O_2$, and the isotopic shift of $\Delta^{18}O \approx 20$ cm^{-1} are typical for the symmetric vibrational frequency of the peroxo side-on species (O_2^{2-}).

The coordination of O_2 to Cu^+ (d^{10}) cations hosted in zeolites of different topologies (AFI, CHA, TON, MOR, MFI) leads to the formation of stable magnetic, η^1, and non-magnetic, η^2, adducts with the side-on attachment being energetically more favourable by ~0.5 eV.[285] The η^2 adsorption energies are around -1.3 ± 0.1 eV for CHA(8MR), TON(10MR), MFI(10MR), AFI(12MR), dropping to -1.03 eV for MOR(12MR), indicating that the size of the zeolite cavities plays a secondary role in controlling the strength of the Cu–O_2 binding. The O–O stretching frequencies varying about 1172–1198 cm^{-1} are characteristic of superoxide species ($Cu^I/z + O_2 \rightarrow [\eta^2\text{-}O_2^-\text{–}Cu^{II}]^+/z$). The thermodynamic stability diagram of η^1-O_2 and η^2-O_2 adducts of the Cu^{2+} and Cu^+ cations hosted in the 6MR and 8MR sites of CHA at various temperatures and p_{O_2} pressures (Fig. 29d) shows that O_2 is only weakly bound to Cu^{2+} in both 6MR and 8MR positions, desorbing already below 0 °C under the O_2 pressure of 5% (horizontal orange line). This is consistent with a weak activation of dioxygen ($d_{O\text{–}O}$ of 1.235 Å is close to the free O_2 value of 1.21 Å), primarily due to the formation of inverted energy levels (IEL, see Chapter 4.1 and Fig. 17). The stability of the superoxide $[\eta^2\text{-}O_2^-\text{–}Cu]^+$ species hosted in the 6MR and 8MR extends to ~200 °C, following the sizable charge transfer stabilization of the ligated superoxide moiety. Interestingly, attachment of the ancillary NH_3 ligands of stronger donor properties makes the mononuclear $[O_2\text{–}Cu(NH_3)_2]^+$ adducts that are solvated in the zeolite cavities unstable (at the DFT calculation level of BEEF-vdW), regardless of the attachment mode.[300] Yet, the $[\eta^1\text{-}O_2\text{–}Cu(NH_3)_3]^+$ species, proposed to be formed upon NH_3-induced dissociation of the peroxo diamino dicopper(II) complexes, are apparently stable.[301]

Dioxygen attachment to dinuclear metal and metal–oxo centres. The binding of O_2 by two adjacent TMI cations typically leads to the formation of end-on *cis* μ-η^1:η^1, *trans* μ-η^1:η^1, the side-on μ-η^2:η^2, and the bis(μ-oxo)[282] species of predominantly peroxo and oxo character, mentioned above (Fig. 27). Notable examples are provided by the bridging oxygen species, produced upon O_2 attachment to dimeric $Cu^+ \cup Cu^+$ centres in MOR,[285,302] CHA,[285,303] BEA,[304] MFI[285,305,306] and $Fe^{2+} \cup Fe^{2+}$

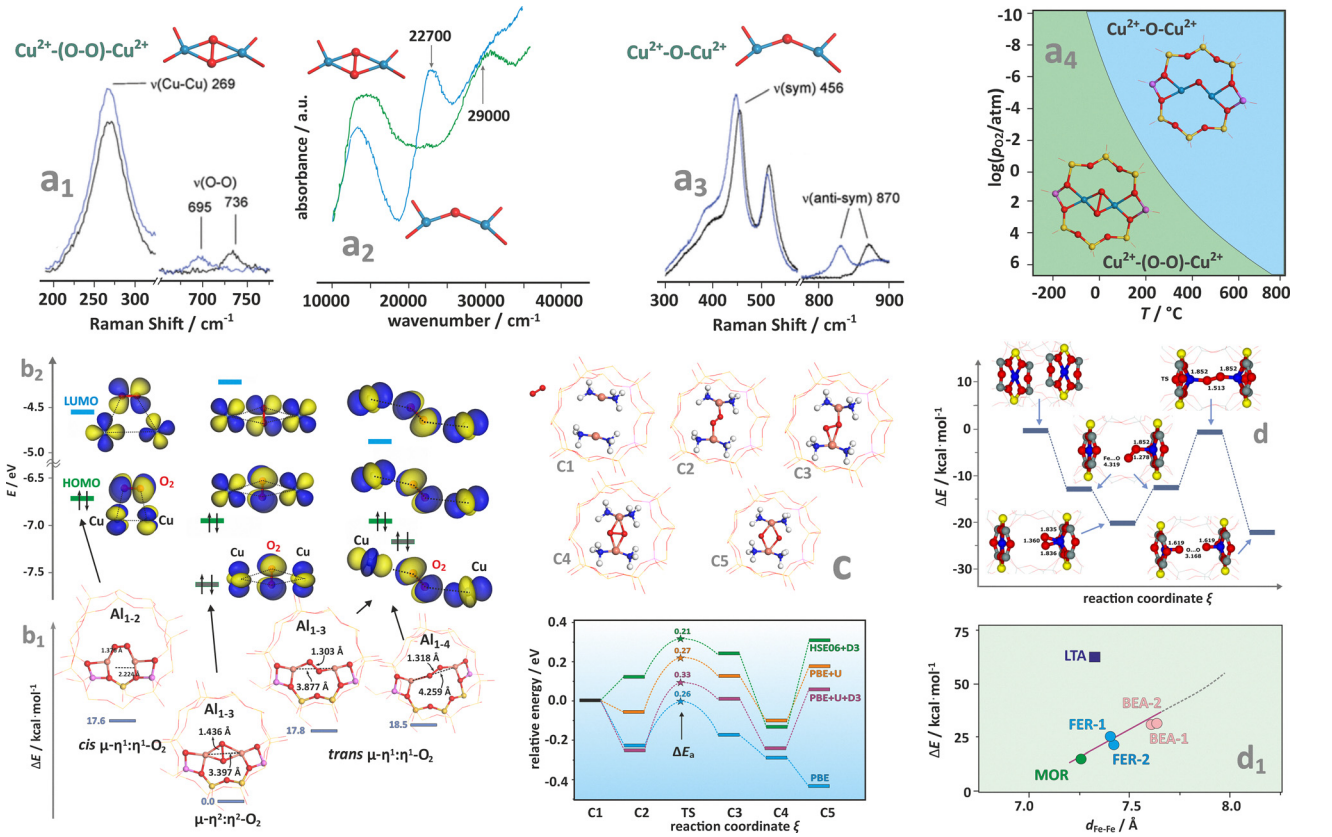

Fig. 31 Resonance Raman (a_1) and (a_3) and UV-vis-NIR (a_2) spectra of Cu^{2+}–(O–O)Cu^{2+} and Cu^{2+}–(O)–Cu^{2+} species hosted in CHA, together with corresponding FPT diagram (a_4).[83,311] Influence of copper distance on the nature of oxygen adducts, together with the associated key molecular orbitals responsible for O–O bonding (b_1) and (b_2).[306] Evolution of the dinuclear diamino adducts of O_2 with the corresponding energy profile (c).[310] Energy profile for dioxygen splitting on Fe/FER catalysts (d), and dependence of the activation energy of O_2 dissociation on the zeolite topology (d_1). Panels d and d_1 are adapted from ref. 308 with permission from the American Chemical Society, Copyright 2021. Panels a–c are based on data form quoted references.

centres in BEA,[307] MOR or FER.[308] Other less explored species include trimeric Cu_3O_3 centres in MOR[302] or $Co^{2+}\cup Ca$ in FAU(X) zeolites.[309] The metal–metal distance and the presence of ancillary ligands (such as common NH_3[310]) play a notable role in controlling the nature of the produced species, as well as the pathways of eventual splitting of the bound O_2 moiety.

When the auto-reduced Cu/ZSM-5 is contacted with O_2 at room temperature, side-on peroxo dicopper species ([Cu(μ-η^2:η^2-O_2^{2-}–Cu]$^{2+}$) are formed.[311] The resonance Raman ν(Cu^+,Cu^+) band at 269 cm^{-1}, the isotopically sensitive ν(O–O) vibrations at 736 cm^{-1} (for ^{16}O) and 695 cm^{-1} (^{18}O), respectively, and the UV-vis peak around 29 000 cm^{-1} (assigned to $\pi^*_\sigma \rightarrow Cu^{II}$ LMCT) are their typical diagnostic features (Fig. 31a1 and a2). The [Cu(μ-η^2:η^2-O_2^{2-}–Cu]$^{2+}$ adduct after heating at $T > 150$ °C transforms into mono-μ-oxo dicopper [Cu(μ-O^{2-})–Cu]$^{2+}$ characterized by the UV-vis band at 22 700 cm^{-1} and the rR lines at 237 cm^{-1} (ν_δ, $\Delta^{18}O$ = 3 cm^{-1}), 456 cm^{-1} (ν_s, $\Delta^{18}O$ = 8 cm^{-1}) and 870 cm^{-1}(ν_{as}, $\Delta^{18}O$ = 40 cm^{-1}), see Fig. 31a$_2$ and a$_3$. Although the splitting of the O–O bond is an uphill process, a relatively small barrier <0.4 eV (for the SSZ-13 zeolite) makes the subsequent transformation of the μ-η^2:η^2 peroxo adduct into the bis(μ)oxo descendant quite feasible. Indeed, this process becomes thermodynamically favourable above 200 °C at $\log(p_{O_2}/p_0) < 1$ (Fig. 31a4). The bis-μ-oxo species are the precursors for mono(μ-oxo)dicopper(II) species,[284] which exhibit high activity in C–H bond activation, and are recognised as the active sites for CH_4 or benzene hydroxylation.[304,311,312]

Molecular modelling studies show that the distribution of Al atoms within the cavities/channels and the resultant Cu–Cu distance control to a large extent the nature of the bridging oxygen species. For 2NNAl pairs configuration (d_{Cu-Cu} = 2.224 Å) a *cis* μ-η^1:η^1-O_2 binding mode is preferred, in the case of 3NNAl pairs a μ-η^2:η^2-O_2 (d_{Cu-Cu} = 3.397 Å) and a *trans* μ-η^1:$\eta^1$$O_2$ (d_{Cu-Cu} = 3.887 Å) adducts are formed, whereas at larger distances between the Al atoms (4NN) only a *trans* μ-η^1:$\eta^1$$O_2$ (d_{Cu-Cu} = 4.249 Å) can be produced.[282] The O–O bond activation gauged by lengthening of the interatomic distance, varies significantly between the adducts.[306] In the 2NN configuration, the end-on *trans* μ-η^1:$\eta^1$$O_2$ complex has the O–O bond of 1.376 Å, whereas for *trans* μ-η^1:$\eta^1$$O_2$ adducts in 3NN and 4NN environment this bond is shorter (~1.31 Å). The largest O–O bond length (1.436 Å) is observed for the side-on μ-η^2:η^2-O_2 peroxo species (Fig. 31b1). The corresponding MO energy diagram of these species, shown in Fig. 31b2, reveals a lucid molecular orbital rationale for different extents of dioxygen activation. The antibonding character of the

overlap in the HOMO and HOMO−1 orbitals of the O–O moiety for the side-on 3NN adduct is responsible for lengthening of the O–O bond in comparison to 2NN top-on species with only one antibonding HOMO in the frontier orbitals region.[282] In the case of the 4NN end-on adduct, HOMO exhibits in-phase overlap, whereas HOMO−1 exhibits out-of-phase overlap of the oxygen orbitals. The cancellation of both effects accounts for the shorter O–O bond in the *trans* μ-η^1:η^1O_2 4NN in comparison to *cis* μ-η^1:η^1O_2 2NN species.

The μ-dioxygen adducts are also formed upon reaction of O_2 with $[(NH_3)_2Cu]^+$ complexes, where the parent framework O_z ligands are entirely replaced by the NH_3 molecules, which are produced in the reduction half-cycle (RHC) of the SCR reaction.[310,313,314] DFT calculations show that the most probable products include *trans* μ-η^1:η^1-peroxo and μ-η^2:η^2-peroxo dicopper(II) adducts with a bidentate attachment of O_2, without complete dissociation of the O–O bond, or a bis-μ-oxo dicopper(III) adduct with the split O–O bond (Fig. 31c). Despite that, the corresponding energy profiles are quite sensitive to the calculation scheme, the μ-η^2:η^2-peroxo dicopper(II) species with the O–O bond retained is favoured.[310] It remains in agreement with the experimental UV-vis (a band at 13 850 cm^{-1}) and EXAFS (Cu–Cu distance of ∼3.4 Å) investigations, which show that the side-on μ-η^2:η^2 peroxo dicopper(II) complex predominates after O_2 interaction with a pair of the cage diamino copper(I) complexes hosted in CHA zeolites (Si/Al = 15, Cu/Al = 0.5) at 200 °C.[301]

The zeolite FER, MOR, and *BEA frameworks containing iron that exhibit high concentrations of Al atoms (Si/Al < ∼10) with a large part of the Al pairs of apposite spatial organisation are capable of dioxygen capture and subsequent O–O bond splitting. For this purpose, the two cationic sites that form the distant binuclear Fe^{2+} centres in six rings must face each other in parallel and axial configuration, and the Fe···Fe distance should be within a narrow range, from ∼7 to ∼8 Å.[308] However, the experimental confirmation of the involved face-to-face configuration of Fe–O species has not been definitive so far. Such active centres are capable of splitting dioxygen to produce, upon dissociation, a pair of ferryl species. The reaction is driven by the cooperative four-electron $2Fe^{2+} \rightarrow 2Fe^{4+}$ redox cycle, and its primary molecular steps, along with the corresponding energetic profiles, are shown (Fig. 31d1), taking the Fe/FER system as an example. The reaction pathway involves a top-on capture of O_2, followed by subsequent transformation of the η^1-O_2 into more stable η^2-O_2 species. The *trans* μ-η^1:η^1 O_2 transition state, located at −0.4 kcal mol^{-1} to separate reactants, is achieved by returning to the monodentate η^1-O_2 binding. The dissociation of the dioxygen moiety is energetically slightly favourable by −2.4 kcal mol^{-1} for the most stable side-on adduct. The activation energy of the O–O bond scission depends on the Fe···Fe distance for the iron cations accommodated in the β sites with the Al pairs placed in the *para*-position, preferably in FER, MOR, and BEA zeolites, with a distinct exception of LTA (where both rings are not parallel), see Fig. 31d2 and a suitable ref. 308.

4.3.2. Coordination and activation of NO. Although nitric oxide (NO) is thermodynamically prone to both decomposition and disproportionation, these processes do not proceed significantly without a catalyst. This is due to the considerable kinetic stability of the NO molecule, which arises primarily from a spin barrier. The latter, together with constraints imposed by orbital symmetry, present the most critical molecular obstructions that prevent efficient activation of NO along a straightforward route. Activation through the coordination of the NO molecule to the intrazeolite TMI centres imparts unique catalytic properties to the metal core and the nitrosyl ligand.

The properties and distinct chemical reactivity of the coordinated NO are often explained in terms of electron density transfer (ET), resulting in the withdrawal of a single electron from the 2π* orbital to produce a nitrosonium (electrophilic) $NO^{\delta+}$ species, or the addition of an electron to the 2π* orbital, forming a nitroside $NO^{\delta-}$ species of nucleophilic character.[14,315] Yet, using the Enemark–Feltham notation of the TMI nitrosyl adducts, $^{2S+1}\{TMI–NO\}^n$ (see Chapter 4.3), the direct attribution of a TMI–NO to nitrosonium ($NO^{\delta+}$) or nitroside ($NO^{\delta-}$) category can be circumvented. The other pathway to NO activation involves an oxygen transfer (OT), resulting in the oxidation of NO to NO_2. The occurrence of the elementary ET and OT events depends critically on the nature of the active site. The electron transfer is characteristic of the bare cations,[17,247] while oxygen transfer occurs in the case of the various mono or polynuclear oxo-cations.[316]

The epitomic NO^+ and NO^- species, which are expected to bind in linear and bent η^1-N mode, respectively. But typically observed adducts with the partial charge accumulated on the NO ligand ($NO^{\delta-}$), exemplified by ($\{^2CuNO\}^{11}$, $^2\{ZnNO\}^{11}$), are slightly bent with elongated and polarized N–O bonds. The $NO^{\delta+}$ containing adducts, such as ($^2\{NiNO\}^9$, $\{^3CoNO\}^8$), are also bent with the bonds shortened and polarized.[317,318] The NO_2^-/NO_3^- oxidation products, which play an essential role in some catalytic processes (*e.g.*, SCR of NO, oxidation of NH_3, selective oxidation reactions), are produced along mechanistically more intricate pathways involving the interaction of the activated (bound) NO with O_2 or *via* involvement of elusive HONO species produced upon the interaction of NO with the intrazeolite TMI–OH centres.[172]

The appearance of nitrosonium and nitroside, or other NO_x species can be deduced from the corresponding IR spectra, featured by characteristic position (blue- or red-shifted compared to the bare NO band) and the number of N–O bands.[319] For zeolitic systems, such simple discrimination of the nitrosonium *vs.* nitroside reactivity of NO^δ with δ close to +1 or −1, has been rarely observed, and situations with polarisation of the TMI–NO bond rather than formation of ionic adspecies *via* electron transfer are more common.[247,317,320,321]

Role of spin and metal electron configuration. The behaviour of the spin density of NO upon binding to TMI can be followed with EPR measurements of *in situ* NO adsorption. This procedure results in characteristic powder EPR spectra (Fig. 32a–e) attributed to the paramagnetic nitrosyl adducts. Depending on the investigated system (the number of unpaired 3d-electrons of the TMI core), the following processes can be distinguished:

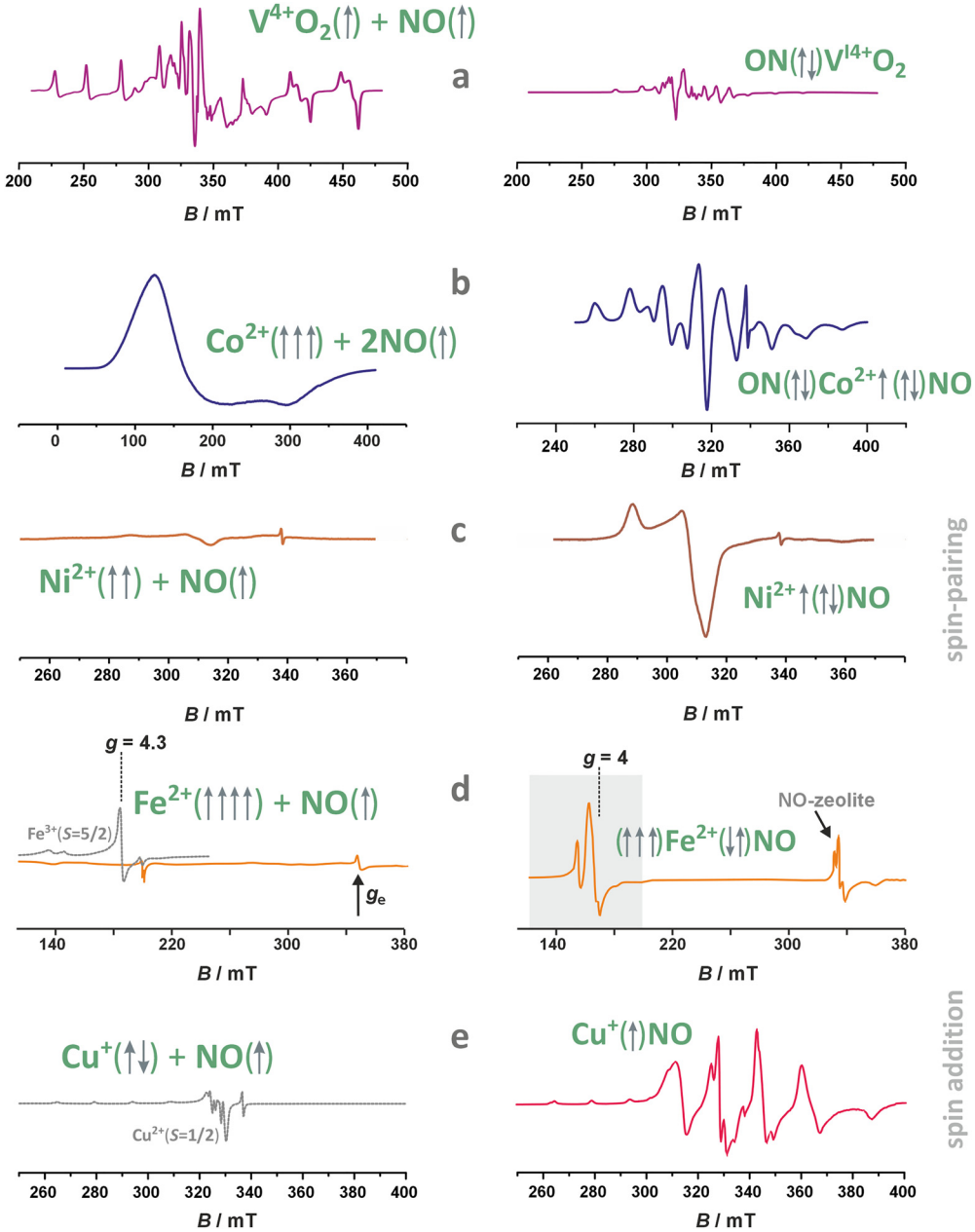

Fig. 32 Reactivity of TMI in zeolites toward NO monitored with the CW-EPR spectroscopy. NO adsorption on VO_2/SiBEA (a), Co^{2+}/ZSM-5 (b), Ni^{2+}/ZSM-5 (c), reduced Fe^{2+}ZSM-5 (d), reduced Cu^{+}/ZSM-5 (e) metallozeolites. The arrows schematically indicate the number of unpaired electrons involved in the TMI active centre and the resulting nitrosyl adducts. The dotted grey EPR spectra correspond to iron and copper in their parent oxidation states before autoreduction. Figure was based on data from ref. 247, 295, 316 and 322.

(1) spin pairing, (2) spin crossing, and (3) spin addition. The simple spin pairing was observed for VO_2 ($3d^1$) species (being indirectly deduced from disappearance of the EPR signal of VO_2),[295] high-spin $^4Co^{2+}$ ($3d^7$) centres (leading to the formation of $\{^2Co(NO)_2\}^9$ dinitrosyls upon pairing of two odd 3d electrons with two NO molecules),[17] and high-spin $^3Ni^{2+}$ ($3d^8$) cations (formation of the mononitrosyls $\{^2NiNO\}^9$ adducts).[247] The reaction of $^5Fe^{2+}$ ($3d^6$) with NO in ZSM-5 zeolite represents an example of spin pairing combined with spin crossing.[322–324] In contrast, the adsorption of NO onto reduced Cu^+ ($3d^{10}$) represents a simple spin addition process to the closed shell Cu^+ cation.[320] In all five cases, the formation of nitrosyl complex can be rationalized in terms of the spin processes occurring between the spin state of 3d TMI and that of NO ($^2\Pi_{1/2}$) radical ligand:

(1) $^2VO_2$/SiBEA + $NO_{(g)}$ ($^2\Pi_{1/2}$) → $^1\{ON\text{-}VO_2\}^2$/SiBEA;

(2) $^4Co^{2+}$/ZSM-5(BEA) + $2NO_{(g)}$ ($^2\Pi_{1/2}$) → $^2\{Co(NO)_2\}^9$/ZSM-5(BEA);

(3) $^3Ni^{2+}$/ZSM-5(BEA) + $NO_{(g)}$ ($^2\Pi_{1/2}$) → $^2\{NiNO\}^9$/ZSM-5(BEA);

(4) $^5Fe^{2+}$/ZSM-5 + $NO_{(g)}$ ($^2\Pi_{1/2}$) → $^3\{FeNO\}^7$/ZSM-5;

(5) $^1Cu^+$/ZSM-5 + $NO_{(g)}$ ($^2\Pi_{1/2}$) → $^2\{CuNO\}^{11}$/ZSM-5.

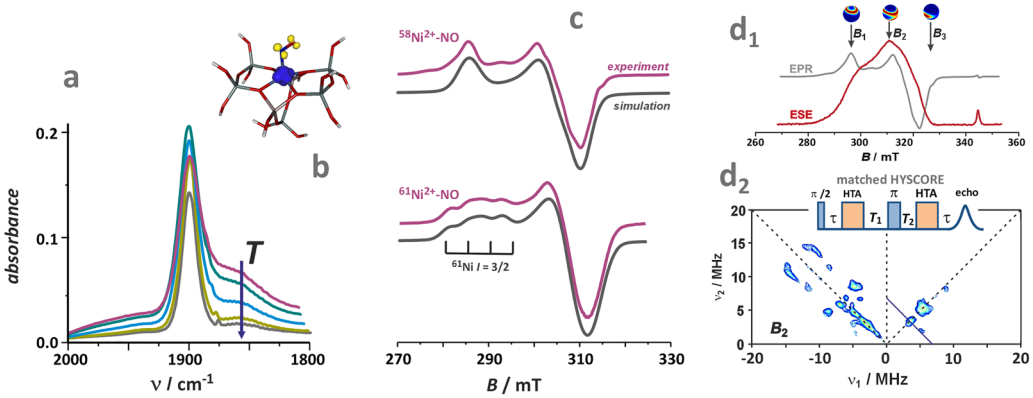

Fig. 33 Spectroscopic evidence of the formation of nitrosyl upon NO interaction with Ni^{2+}/ZSM-5. The IR spectra of NO adsorption at various temperatures (a), spin density contour of the $[NiNO]^{2+}$ adduct in ZSM-5 (b), CW-EPR spectra (77 K) of NO adsorption on Ni and isotopically enriched ^{61}Ni (I = 3/2) hosted in ZSM-5 zeolite (c), electron spin echo detected EPR signal (10 K), the arrows indicate observer positions (B_1, B_2, B_3) at which HYSCORE signals can be measured (d_1). HYSCORE spectrum due to the ^{14}N hyperfine interaction recorded at B_2 position with the matched pulse sequence (d_2). The figure was based on data from ref. 156 and 247.

In the case of the $^4Co^{2+}$ adducts with NO, analysis of the observed cobalt hyperfine splitting indicates that approximately 80% of the spin density ($\rho^{3d} \approx 80\%$) is localized on the metal centre. This suggests that the magnetic structure of the dinitrosyl intermediates can be represented as NO(↑↓)–↑Co^{2+}–(↓↑)NO, where the unpaired electron resides primarily on the cobalt ion. This adduct, however, undergoes interesting transformation upon thermal treatment, resulting in the reduction of the metal centre to zero-valent cobalt. The latter state was unambiguously confirmed by consecutive adsorption of CO and propene, resulting in EPR spectra characteristic of $3d^9$ electron configuration of the cobalt cation.[17]

Similarly, the g-tensor values of $Ni^{2+}NO$ adduct in ZSM-5 zeolite are characteristic of a metal-centred paramagnet with the $3d^9$ electron configuration.[3] This signal has been assigned to the adducts of the type $[Ni–NO]^{2+}$/ZSM-5 (S = 1/2, $3d^9$). A similar signal was reported earlier for surface adducts in the Ni–silica systems.[325] The $[Ni–NO]^{2+}$ notation does not reflect the actual redistribution of partial charges that occurs upon NO coordination to Ni^{2+}, and the corresponding shift of the $\nu_{N=O}$ IR band (1890–1898 cm^{-1}, Fig. 33a) concerning the 1874 cm^{-1} value of the physisorbed NO. The actual charge redistribution is closer to the $Ni^{(2-\delta)+}$–$NO^{\delta+}$ formulation. The relative position of the $NO\left(\pi^*_{2p}\right)^1$ donor level regarding the semi-occupied Ni $3d_{z^2}$ (σ donation channel) and the position of the occupied $3d_{xz}$ orbital in comparison to the empty level $\left(\pi^*_{2p}\right)^0$ (π back donation channel), dictate the extent of the actual ligand to metal charge transfer, where the coordinated NO molecule is partially oxidized to $NO^{\delta+}$. This is consistent with the experimentally observed blue shift in the NO stretching frequency in the IR spectrum.[247]

The EPR results also support such a molecular picture. The g-tensor parameters extracted from the CW-EPR spectrum of $\{^2NiNO\}^9$ adducts in ZSM-5 zeolite (Fig. 33c) are characteristic of a $3d^9$ electron configuration, which is supported by the presence of ^{61}Ni (I = 3/2) hyperfine splitting when an isotopically-enriched sample was used. At the same time, hyperfine splitting due to ^{14}N (I = 1) is not resolved due to an effective quenching of the spin density at the nitrogen nucleus resulting from the spin pairing ligation. The residual hyperfine structure can be unraveled using HYSCORE spectroscopy, a powerful method for characterizing paramagnetic species in porous materials.[95,116,117,156] Electron spin echo (Fig. 33d_1) and the HYSCORE spectrum for one selected orientation, corresponding to the maximum amplitude of the echo, is shown in Fig. 33d2 for the $\{^2NiNO\}^9$/ZSM-5 adduct. The characteristic correlation ridges in the so-called strong coupling regime correspond to the following ^{14}N hyperfine parameters A_{xx} = 14.0 MHz, A_{yy} = 9.0 MHz, A_{zz} = 6.0 MHz, implying that approximately 4% of the total spin density is localised on nitrogen.[156]

The above observations indicate that nitrosyl adducts are formed *via* a spin-pairing process, which in the case of Ni^{2+}/ZM-5 involves a one-electron $Ni^{2+}(3d^8)/Ni^+(3d^9)$ couple.[247] For the Co^{2+}/ZSM-5 (or BEA) system, adsorption of NO leads to the spontaneous formation of dinitrosyls, engaging a two-electron $Co^{2+}(3d^7)/Co^0(3d^9)$ couple.[316]

The IR and EPR evidence for the formation of paramagnetic $^2\{CuNO\}^{11}$ is shown in Fig. 34a and b. The bonding between the closed-shell Cu^+ and NO radical in the channels of ZSM-5 zeolite has been rationalized in terms of the spin addition mechanism and the s/d hybridization of the empty 4s and two occupied $3d_\sigma$ orbitals ($3d_{z^2}$ and $3d_{xz}$) of Cu, which interact with the $2\pi^*$ MO of NO.[320,321,326,327] The empty $3d_{z^2}$ + 4s acceptor state can overlap more efficiently with the in-plane $2\pi^*_x$ of NO. At the same time, the interaction of the NO lone pair is weaker as the latter is situated relatively low in the energy within the 3d manifold (see the MO interaction diagram in Fig. 34c). Such an interaction provides a pathway for the σ-type bond, producing the singly occupied molecular orbital (SOMO). The interaction of the occupied $3d_{yz}$ orbital with the remaining out-of-

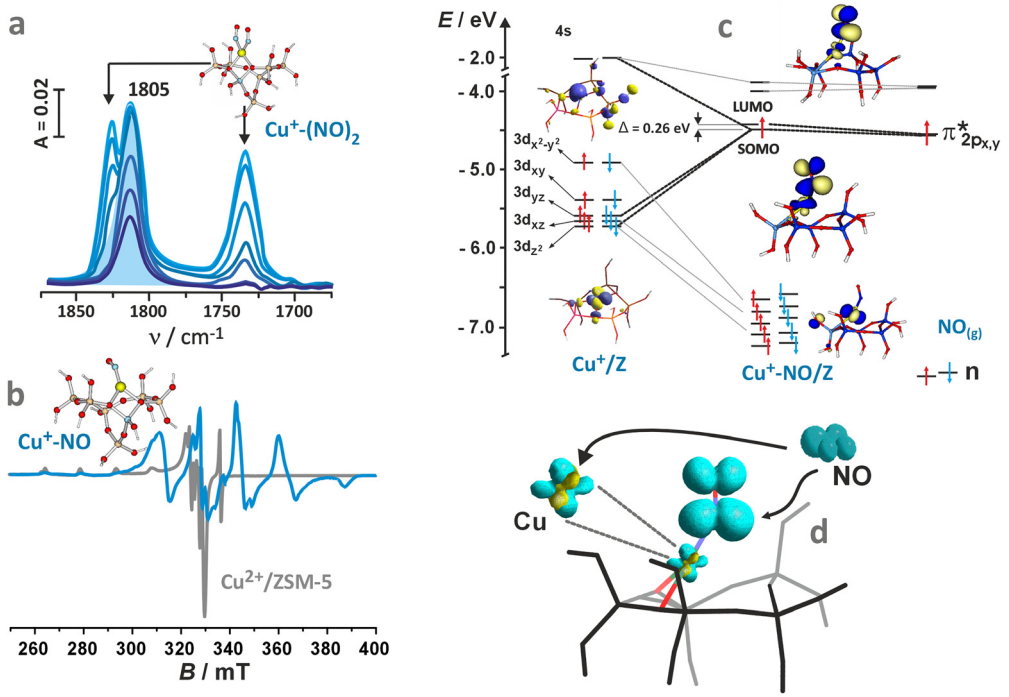

Fig. 34 Spectroscopic evidence of the nitrosyl adduct formation upon NO interaction with Cu^+/ZSM-5. IR spectra of NO adsorption with the highlighted mononitrosyl band at 1805 cm^{-1} (a), CW-EPR spectra of the parent Cu^{2+}/ZSM-5 zeolite and the adsorption complex, produced after thermal autoreduction of Cu^{2+}/ZSM-5 and subsequent NO adsorption (b), Kohn–Sham correlation diagram of the $\{^2CuNO\}^{11}$/ZSM-5 adduct (c), and the corresponding spin density contours of the mononitosyl species (d). Panels a and d adapted from ref. 345 with permission from Elsevier, Copyright 2007. Panel b adapted from ref. 172 under the terms of the CC BY 4.0 license, Copyright 2025, published by American Chemical Society. Panel c adapted from ref. 320 with permission from he American Chemical Society, Copyright 2003.

plane empty $2\pi_y^*$ gives rise to the lowest-unoccupied molecular orbital (LUMO). The local C_s symmetry allows for admixing of the Cu 4s state to the 3d manifold. The interaction with the $2\pi^*$ states of NO results in a charge and spin donation $\pi_x^* \rightarrow (3d_z^2 + 4s) + 3d_{xz}$, accompanied by a $3d_{yz} \rightarrow \pi_y^*$ back-donation. SOMO and LUMO are antibonding between Cu^+ and NO, exhibiting a mixed $2\pi^*$-3d character with a prevailing NO contribution. The redistribution of electronic charge within the Cu–NO unit leads to a partial oxidation of the copper centre and a concurrent reduction of the NO ligand, as evidenced by the red-shift of the N═O stretching vibration to 1805 cm^{-1}. In addition, such an orbital picture explains all characteristic features of the EPR spectrum of $\{^2CuNO\}^{11}$ adducts (Fig. 34b), *i.e.*, monoclinic symmetry, large hyperfine coupling constants ($^{63,65}Cu$, $I = 3/2$) due to involvement of Cu 4s in SOMO, and the ^{14}N ($I = 1$) hyperfine splitting that is typical of ligand-centred nitrosyls radical.[320]

Beyond the previously discussed $3d_{z^2} - \pi_x^*$ interaction, the primary factor driving the bending of the NO ligand is the enhanced orbital overlap between the π_x^* orbital of NO and the 4s orbital of the metal centre. This interaction becomes symmetry-allowed only in a bent geometry, making it inaccessible in the linear coordination mode. The spin density contour shows principal localization on the NO ligand with a sizable Cu contribution, and it is practically confined to the CuNO moiety (Fig. 34d). Thus, the copper nitrosyl in ZSM-5 is a ligand-centred $\{^2CuNO\}^{11}$ radical for spin classification purposes.

Charge flow during the TMI–NO bond formation and bonding mechanisms. The electronic density flows accompanying the TMI–NO bond formation can be elucidated and quantified using the NOCV method (see Chapter 4.1.1). Since NO is an open-shell ligand, the NOCV analysis should be performed in a spin-resolved (SR) fashion, *i.e.*, separately for the α (↑) and β (↓) spin densities. Moreover, the unpaired electrons on the NO and TMI–zeolite non-interacting fragments should be distributed and coupled consistently with the TMI–NO bond; this is necessary to avoid spurious intra-fragment charge flows that would blur the interpretation of the NOCV results.[328]

The SR-NOCV method has been applied to a series of increasingly complicated NO interactions with zeolitic TMI, starting from the simplest case of closed-shell Cu^+ cations,[329,330] through open-shell $3d^8$ Ni^{2+} (ref. 156) and $3d^9$ Cu^{2+},[330] up to the most complex $3d^7$ Co^{2+} active centres with NH_3 co-ligands[40,331] hosted in ZSM-5 zeolite. The SR-NOCV analysis of the NO binding to the Cu^+/Cu^{2+} sites[328–330] revealed the following most relevant electron-flow channels: (1) π^*-backdonation, (2) donation of an unpaired electron from NO π^*, (3) σ-donation from the nitrogen lone pair, (4) covalent Cu–NO contribution. They are illustrated in Fig. 35, using the SR-NOCV results for the representative $\{CuNO\}^{11}$, $\{CuNO\}^{10}$, and $^1\{Co(NH_3)_3(NO)\}^8$ species.

The channel (1), which represents backdonation from the doubly occupied Cu $3d_\perp$ to the empty $2\pi_\perp^*$ MO of NO, increases the population of the $2\pi^*$ (antibonding) orbital, leading to a

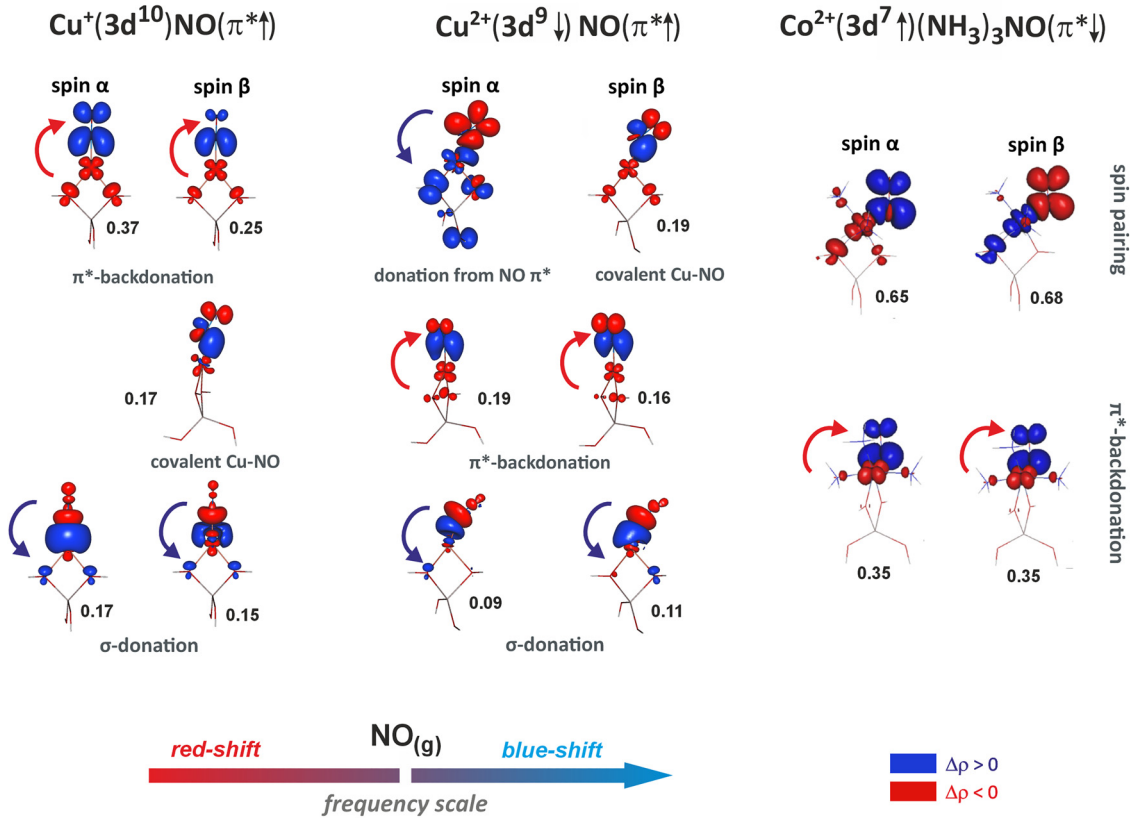

Fig. 35 Dominant SR-NOCV components of the differential density during the NO binding to intrazeolite Cu^{+}, Cu^{2+} cations and to $^{1}\{Co^{2+}(NH_3)_3\}$ complexes in ZSM-5, along with heuristic assignments of the electron flow channels and the corresponding NOCV eigenvalues. Contour values ±0.001 a.u. Adapted from ref. 40 and 330 with permissions from the Royal Chemical Society (Copyright 2016) and from the Canadian Science Publishing (Copyright 2013), respectively.

nitroside activation of the ligand ($NO^{\delta-}$). The channel (2), which represents the unpaired electron displacement from the initially singly occupied $2\pi_{\|}^{*}$ to the Cu–zeolite fragment, acts oppositely. The relative importance of these two channels is sensitive to the oxidation state of Cu and the embedding of zeolite. The 2π*-backdonation channel (1) is most efficient for the zeolitic Cu^{+} site, consistently with a pronounced red-shift of the NO stretching vibration for the intrazeolite $\{CuNO\}^{11}$ systems. The π*-backdonation is considerably diminished in the zeolitic Cu^{2+} site (*cf.* Fig. 34). In this case, this channel features strong polarization on NO and involves the electron density transfer from Cu $3d_{\perp}$ and nitric oxide O $2p_{\perp}$ to the bonding region, rather than straightforward π*-backdonation.[330] Moreover, in the $Cu^{2+}NO$ system, the effect of π*-backdonation is effectively cancelled by the opposite effect of the unpaired electron donation from the 2π* SOMO along the channel (2). The net outcome of this competition is the deactivation of NO, which is also reflected by the blue shift of the ν_{N-O} stretching frequency.[329,330] These results explain why the intrazeolite Cu^{2+} sites are inefficient in activating NO, although it binds this molecule more strongly than the intrazolite Cu^{+} centers.[330,332]

The remaining two electron density flow channels, shown in Fig. 35, are of minor importance for the NO activation and are relatively insensitive to the metal oxidation state and embedding.[328] The σ-donation channel (3) appears in all studied models, but hardly influences the strength of the NO bond, as the electron density is donated mainly from the nitrogen lone pair. The covalent Cu–NO channel (4) can be heuristically interpreted as a donation from the NO $2\pi_{\|}$ and Cu $3d_{\|}$ orbitals to the bonding region, accompanied by simultaneous intra-NO density redistribution. It may also be understood as the formation of a three-electron bond $\left(3d_{\|}\right)^{2}-\left(\pi_{\|}^{*}\right)^{1}$, followed by some $\pi_{\|}-\pi_{\|}^{*}$ mixing in NO. As this channel only exists in the β spin manifold, it contributes to the partial spin transfer from NO to Cu. Spin transfer is also connected with the channel (2), which only exists in the α spin manifold, and channel (1), which exists in both spin manifolds, but its α- and β-spin components are not balanced (compare eigenvalues of 0.37 and 0.25 for the $\{CuNO\}^{11}$ adduct in Fig. 35).

In summary, the discussed SR-NOCV results nicely corroborate the spin addition and backdonation mechanisms discussed above for the Cu–NO system, and the interpretation of the EPR experimental data. By showing competition between the two most relevant electron flow channels: (1) π*-backdonation and (2) donation of the 2π* unpaired electron, they rationalize the propensities of different Cu sites to activate NO. Such an insight can hardly be obtained from more popular descriptors, such as atomic charges and spin populations,

alone. In particular, the spin density on NO is not a direct indicator of its effective redox state, a conclusion that has also been pointed out in a broader context for other TMI–nitrosyl complexes.[50] The fractional charge of the ligated NO is a net result of the opposing electronic flows corresponding to donation and backdonation processes.

DFT studies, supplemented with SR-NOCV analyses, have also been used to elucidate the mechanism of NO bonding to zeolitic Co^{2+} sites in the presence of ammonia co-ligands.[40,331] The experimental studies of mononitrosyl species in Co^{2+}-exchanged MOR and FER zeolites demonstrate that the NO stretching frequency undergoes a blue shift, which changes to a considerable red shift upon NH_3 co-adsorption.[331] Following the experimental conditions, DFT calculations were conducted on simplified cluster models of the $\{CoNO\}^8$ species containing none, two, three, or five NH_3 co-ligands, which are embedded in a simple one-tetrahedron T1.[40,331] The construction of the more realistic zeolitic models is described elsewhere.[333,334]

The DFT modelling of the $(NH_3)_n\{CoNO\}^8$ adducts fully confirmed the electron-donating effect of NH_3 lone pairs, leading to enhanced Co 3d → 2π*-backdonation, and explaining the red-shift of the NO stretch in the $(NH_3)_n\{CoNO\}^8$ adducts. Interestingly, this electron flow channel turned out to be finely spin-state controlled, *i.e.*, highly more effective in the singlet than in the triplet spin state.[331] The relative energies of the two spin states are challenging to predict using the available approximate DFT methods, which is a typical problem for 3d-electron TMI complexes in various coordination environments.[53] Yet, the CCSD(T) and CASPT2 results show that the singlet and triplet spin states of the intrazeolite $\{CoNO\}^8$ species are close in energy, allowing them to coexist in equilibrium under experimental conditions.[40] The calculations also reveal that the most substantial red shift of the NO stretching occurs for the complex with three NH_3 co-ligands, rather than for the complex with five ligands. While being counterintuitive at first sight (ammonia is a stronger electron donor than zeolitic oxygen groups), this result can be rationalized by invoking the *trans* effect of the NH_3 ligand, present in the pentammine complexes. It leads to elongation of the Co–NO bond, and hereby to the reduction of the π*-backdonation effect in $[Co(NH_3)_5(NO)]^{2+}$ as compared with the $[Co(NH_3)_3(NO)]^{2+}$ zeolite adduct.[328] A similar pattern of complex competition between the binding of strong NH_3 co-ligands and preserving the covalent linkages to the zeolite framework, which is an electron-rich, but weaker ligand, has been observed for more realistic zeolite models.[334] It is not necessarily full ammonia saturation of the Co^{2+} site that leads to the highest extent of the NO activation.

According to the SR-NOCV analysis,[40] the Co–NO bond formation in the spin singlet $\{Co(NH_3)_3(NO)\}^8$ zeolitic species can be best characterized as a combination of (1) spin-pairing between $Co^{2+}(3d_{\parallel}, \uparrow)$ and NO $(2\pi^*_{\parallel}, \downarrow)$ with concomitant (2) π*-backdonation from Co $3d_{\perp}$ to NO $2\pi^*_{\perp}$ (Fig. 35). The spin pairing channel is consistent with the formation of a covalent σ Co–NO bond (having a significant biradical character – see below). The π*-backdonation channel, which activates the N–O bond, is found in both spin manifolds with the identical eigenvalues, and hence, it does not transmit the spin polarization.

The electronic structure of the discussed $^1[Co(NH_3)_3(NO)]^{2+}$ zeolite model (T1) has been described as unpolarized (closed-shell) singlet,[40] caused by the application of a pure density functional (BP86). In contrast, hybrid functionals can easily lead to a spin-polarized BS-DFT description, as seen for the intrazeolite $\{CuNO\}^{10}$ species discussed earlier. In general, both the existence of a BS solution[335] and the distribution of spin density[50,51] in the nitrosyl complexes are critically dependent on the choice of the exchange–correlation functional. The BS spin density, although helpful in visualizing the pattern of spin coupling accompanying TMI–NO bond formation, is not expected to accurately reproduce the physical spin density. It merely provides a means of simulating nondynamic correlation effects in the metal–ligand bond, within the limitations of the single-configurational DFT formalism.[50,336]

A more rigorous description of these effects can be obtained using the multiconfigurational wave function formalism, in which the principal electronic configuration (PEC) is mixed with other configurations, obtained by promoting electron pairs from the bonding to antibonding orbitals. In this way, the antibonding orbital (unoccupied in the PEC) gains fractional occupations, whereas the bonding orbital (doubly occupied in the PEC) reduces its effective occupation below two. Thus, the TMI–NO bond acquires a partial biradical character. In a sense, it is ''stretched'' or ''partially dissociated'' already in the equilibrium geometry due to non-optimal overlap between the metal and ligand orbitals.[337–339] This effect is most pronounced in first-row TMI due to the small size of their 3d valence orbitals. The ligand cannot approach close enough to achieve the optimum overlap with the 3d orbitals due to Pauli repulsion with the doubly occupied 3s3p outer-core orbitals, which are of approximately the same size as the 3d ones (see Pauli shield in (Fig. 17b)).[338] The NO ligand has doubly occupied 2π orbitals in a very similar space region as 2π* ones, giving rise to powerful Pauli repulsion.[339] These nondynamic correlation effects exacerbate problems associated with the non-innocent nature of NO, as they influence both the strength of the TMI–NO bond and the effective oxidation state of the NO ligand.

The discussed nondynamic correlation effects can be accounted for by using the CAS method with an active space containing the TMI 3d and NO 2π* orbitals as well as other relevant orbitals, *e.g.*, the additional shell of d orbitals and NO π orbitals, which are needed to achieve a balanced approximation of the electronic wave function in nitrosyl species.[40,50,337] The CAS calculations with 13–14 active orbitals have been performed for the intrazeolite $^{1,3}\{CoNO\}^8$ adducts with ammonia as co-ligands,[40] and for the $^2\{NiNO\}^9$ complex in ZSM-5 zeolite.[156] Based on these results, Fig. 36a shows the pairs of bonding and antibonding orbitals that describe the σ component of the TMI–NO bond.

The contributions of TMI and NO fragment orbitals to the bonding and antibonding orbitals are comparable,

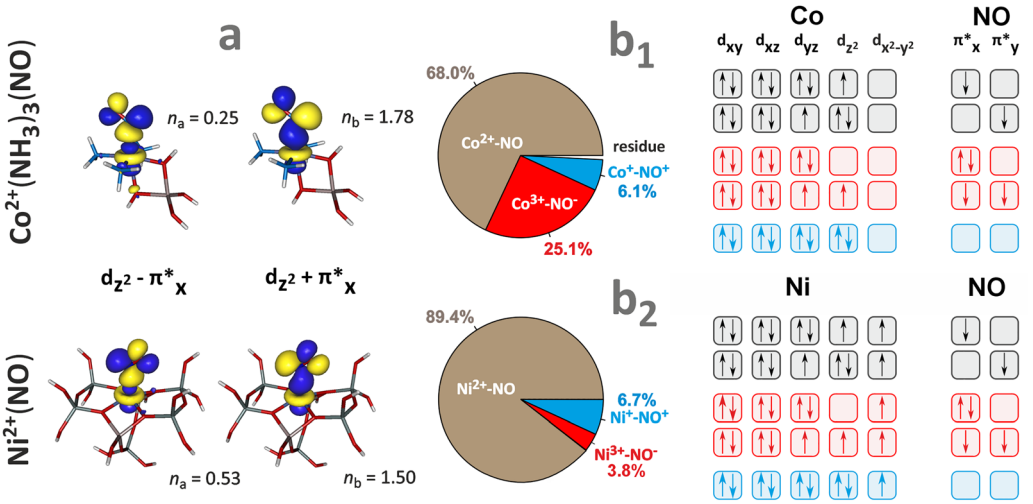

Fig. 36 CASSCF natural orbitals with bonding and antibonding character concerning the TMI–NO σ bond, and their fractional occupation numbers for zeolite cluster models hosting $(NH_3)_3\{Co(NO)\}^8$ and $\{NiNO\}^8$ adducts (a) based on results from. Contour values ±0.04 a.u. Breakdown of the contributions from the TMI–NO resonance structures resulting from VB analysis of the CAS wave functions for the $(NH_3)_3\{Co(NO)\}^8$ (b_1) and $\{NiNO\}^9$ (b_2) adducts into electronic configurations for the individual VB oxidation states. Figure was based on data from ref. 40 and 156 with panel b_1 adapted from ref. 328 under the terms of the CC BY license 4.0, Copyright 2021, published by MDPI.

demonstrating a highly covalent character of the σ-bonds, which is consistent with the spin pairing ligation mechanism.[156] The orbitals' fractional occupation numbers strongly deviate from the ideal integer values (*i.e.*, 2 for the bonding orbital, 0 for the antibonding orbital), indicating considerably reduced bond order, and hence a pronounced biradical character of these bonds. The effective bond order, $b = (n_b - n_a)/2$, amounts to 0.765 for the intrazeolite $\{CoNO\}^8$ complex and to 0.485 only for the $\{NiNO\}^8$/ZSM-5 complex. Thus, the σ-bond in the equilibrium geometry of Ni–NO exhibits a biradical character exceeding 50% (the biradical character is calculated as $(1 - b) \times 100\%$).

The spin density of the $\{NiNO\}^8$/ZSM-5 complex primarily originates from the SOMO, which is predominantly (95%) composed of the Ni $3d_{xy}$ orbital interacting with lone pairs of the zeolite oxygen atoms. Due to the spin coupling within the Ni–NO bond, the total spin population on Ni increases to +1.22, which is compensated by the negative spin population on NO (−0.17 on N, −0.10 on O) and residual positive spin population on the zeolite oxygens, according to Mulliken spin populations of the CAS wave function.[156] Only a minor part of the spin density is retained on the NO ligand (in agreement with the spin-pairing mechanism of ligation), which is consistent with the interpretation of the HYSCORE experimental results discussed above.

Further insight into the multiconfigurational electronic structure of TMI–NO bonds can be gained by analyzing the valence bond (VB) structure of the CAS wavefunction.[40,50] In this approach (VB-CAS), the active orbitals undergo a localization procedure, after which each active orbital can be assigned to either the TMI- or NO-fragment. The CAS wave function can be reinterpreted as a superposition of the VB resonance structures with a defined number of electrons assigned to the TMI fragment and the NO ligand (*i.e.*, definite oxidation states of these fragments). The VB-CAS method thus allows circumvention of the limitations of the Feltham–Enemark notation (see Chapter 4.3) by quantifying contributions from the resonance structures belonging to different oxidation states. The technique, initially developed for bioinorganic architectures,[50] has been subsequently applied to describe nitrosyl complexes in diverse coordination environments,[51,340,341] including intrazeolite TMI–NO adducts.[40,156] The VB-CAS method should be clearly distinguished from alternative approaches to assigning oxidation states in nitrosyl complexes, *e.g.*, based on the IUPAC rules (ionic approximation) and/or geometric arguments[342,343] and other types of orbital analyses.[344]

The contributions of the VB-CAS resonance structures for $\{Co(NH_3)_3NO\}^8$ are illustrated in Fig. $36b_1$,[40] and for the $\{NiNO\}^9$ complex in Fig. $36b_2$.[156] The most important individual electronic configurations for a given resonance form are also shown. For both analysed nitrosyl adducts, the CAS wave function is clearly dominated by the resonance form with neutral NO radical, which can be formulated as TMI^{2+}–$NO^{\bullet}$ (where TMI = Co or Ni). In the most important configurations of this type, the local spin on NO is antiferromagnetically coupled with the TMI spin. For example, in the $\{NiNO\}^9$ adduct, 87.3% of the CAS wave function is provided by the $Ni^{2+}(S_{Ni} = 1)NO^{\bullet}(S_{NO} = 1/2)$ resonance structure, with the critical single configuration $\left(d_{x^2-y^2}\right)^2\left(d_{xz}\right)^2\left(d_{yz}\right)^2\left(d_{xy}\right)^{\uparrow}\left(d_{z^2}\right)^{\uparrow}\left(\pi_x^*\right)^{\downarrow}\left(\pi_y^*\right)^0$ constituting 78.5% of the CAS wave function.[156] The large contribution of the TMI^{2+}–$NO^{\bullet}$ resonance form, particularly in the $\{NiNO\}^9$ complex, is thus consistent with the above-discussed considerable biradical character of the TMI–NO bonds, and corroborates lucidly the spin-pairing ligation mechanism. The shares of the essential ionic resonance structures, such as M^{2+}–NO^{-} or M^{+}–NO^{+}, are notably different in the two discussed

complexes, indicating partial nucleophilic character of $NO^{\delta-}$ in the case of $^{1}\{CoNO\}^{8}$ and partial electrophilic character of $NO^{\delta+}$ in $^{2}\{NiNO\}^{9}$. This is consistent with the positions of the NO stretching bands, which are either red-shifted or blue-shifted, in these two cases. Moreover, in the series of $\{CoNO\}^{8}$ adducts,[40] the relative shares of the Co^{3+}–NO^{-} or Co^{+}–NO^{+} resonance forms align well with changes of the N–O force constant and the stretching frequency, showing that predictions of the VB-CAS method generally correlate with other descriptors of the NO valence state. Concluding, the VB-CAS shares of the resonance structures appear to be more robust descriptors than the SR-NOCV eigenvalues when comparing complexes with different spin states or geometries.

Reactivity of the TMI–NO adducts with NO. The reactivity of nitrosyl adducts is closely related to how the NO molecule is coordinated, and to its electron configuration and spin state. For instance, the chemoselective capture of NO and the formation of mononitrosyl intermediates are pivotal prerequisites for its direct decomposition to N_2 and O_2 or its reduction into N_2 with the aid of hydrocarbons.[172,247,316] Since the formation of the N–N bond requires the proximity of two NO molecules, there are two possible pathways along which the adsorption of the second NO molecule can occur. These pathways have been distinguished based on the NO attachment locus (Fig. 37a) and can be termed inner-sphere and outer-sphere attacks. This mechanistic dichotomy determines the regioselective addition of NO to the mononitrosyl intermediate. The inner-sphere addition process leads to the formation of geminal dinitrosyl $^{2S+1}\{TMI–(NO)_2\}^{d+2}$ adducts, whereas the outer-sphere pathway results in a dimer bound to the metal centre $^{2S+1}\{TMI(N_2O_2)\}^{d+2}$.

The formation of dinitrosyl complexes in metallozeolite catalysts is confirmed, mostly by IR spectroscopy.[319] The disappearance of the band attributed to the N–O vibration of mononitrosyls and the simultaneous formation of two bands of the collective symmetric and antisymmetric vibrations of the $TMI(NO)_2$ species, provides direct evidence for the formation of dinitrosyl complexes at the expense of the parent mononitrosyl adducts.[319,345–347] Similarly, formation of N_2O_2 dimers, which are diagnostic of the outer-sphere mechanism, has also been observed by IR in the metallozeolites in the spectral range of 1420–1320 cm^{-1} corresponding to the N–N vibrations.[319]

Dinitrosyl complexes have often been postulated as intermediates of the NO disproportionation into N_2O and NO_2, catalysed by transition metal complexes in homogeneous[348,349] and zeolitic[350] systems. The two dinitrosyl conformations, namely attracto and repulso, are shown in Fig. 37b. According to the classification proposed by Richter and Legzdins,[351] the $3d^{5-10}$ transition metals prefer an attracto conformation. In this geometry, the bending of both NO groups results in a decrease in the oxygen–oxygen distance (“inward” bending). An “outward” bending, in turn, increases the distance between the oxygen atoms of both NO ligands, with a simultaneous reduction of the distance between the nitrogen atoms (repulso conformation). Such structures have been described in detail for copper(I) centres in zeolites,[346,347] and they differ in the respective symmetric and antisymmetric IR bands.[345]

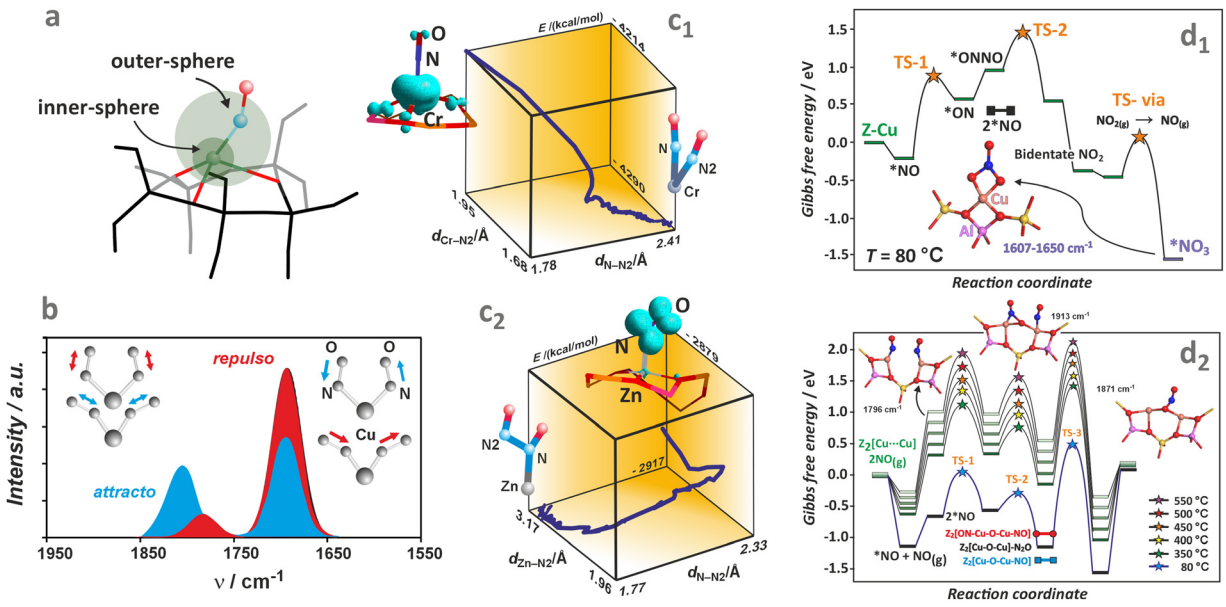

Fig. 37 The inner- and outer-sphere attack of the second NO molecule on intrazeolite nitrosyl complex (a). Comparison of DFT calculated IR dinitrosyl bands of $Cu^{+}(NO)_2$ species in the attracto and repulso conformations (b), based on data from ref. 345. DFT optimised pathways of the second NO molecule attachment to Cr^{+}–NO (c_1) and Zn^{2+}–NO (c_2) mononitrosyls, along with the respective spin density repartition that governs the inner- (Cr) or outer-sphere (Zn) direction of the NO attack. DFT-calculated free-energy diagrams at various temperatures for NO decomposition over a mononuclear Cu^{+} (d_1) and vicinal $Cu^{+}\cup Cu^{+}$ dimer (d_2) centres hosted in ZSM-5, adapted from ref. 350 with permission from Springer Nature, Copyright 2021.

The interaction pathway of the second NO molecule with a given mononitrosyl complex can be related to the spin repartition within this species. For the first-row paramagnetic TMI–NO/ZSM-5 adducts,[317] the spin density is confined almost entirely to the TMI–NO fragment, spreading on the zeolite backbone to a small extent only. Thus, the TMI–NO unit constitutes the magnetophore of the entire TMI–NO/ZSM-5 system (see Chapter 4.1).[321] Two examples of the spin density repartition in the $^{3}\{CrNO\}^{6}$ and $^{2}\{ZnNO\}^{11}$ magnetophores hosted in the ZSM-5 framework are shown in Fig. 37c_1 and c_2. They represent two extreme cases of metal-centered and ligand-centered metallo-radicals, respectively (see Fig. 18e).

The effect of the spin density distribution in TMI–NO on the attachment of the second NO molecule is illustrated by the reaction pathways shown in Fig. 37c_1 and c_2. For the $^{3}\{CrNO\}^{6}$ magnetophore, the ligation trajectory along which the interaction energy is minimized results in the formation of a dinitrosyl complex $^{2}\{Cr(NO)_2\}^{7}$ *via* an inner-sphere attack. A different scenario occurs for the $^{2}\{ZnNO\}^{11}$ magnetophore. Here, the binding of NO leads to the bond formation directly between the nitrogen atoms, as the incoming NO molecule is repelled from the first coordination sphere of the zinc centre. Therefore, a $^{3}\{ZnN_2O_2\}^{12}$ complex is formed along the outer-sphere mechanism. Thus, the outer- *vs.* inner-sphere dichotomy of NO coordination to the paramagnetic mononitrosyl intermediates is essentially controlled by the spin density distribution within the corresponding magnetophores. The inner-sphere attack, which occurs directly at the metal core, is expected for the metal-centered metallo-radicals. In contrast, for the ligand-centered metallo-radicals, the outer-sphere mechanism is preferred. The bent structure of the NO ligand with the associated accumulation of spin density on the nitrogen atom is particularly beneficial for directing the NO attack at the nitrosyl moiety.

The possible mechanisms of NO activation differ depending on the nuclearity of the active centres, as demonstrated for monomeric[345] or dimeric copper species[350] in zeolites. In the case of mononuclear copper centres, the spin density localisation on the ligand in the Cu–NO magnetophore suggests that the attack of the second NO on the copper nitrosyl intermediate is preferred *via* an outer-sphere pathway. It occurs with nearly zero activation energy and leads to the direct formation of the N–N bond *via* the N_2O_2 intermediate. The latter decomposes into N_2O, leaving behind highly reactive intrazeolite CuO/*z* species (its electronic structure is briefly discussed in Chapter 2.2). It can be brought to the initial state by interacting with the N_2O byproduct ($CuO/z + N_2O \rightarrow O_2 + N_2 + Cu/z$) or by reduction with auxiliary hydrocarbons (HC-SCR). However, the energy profiles of the reaction pathway (Fig. 37d_1) favour the dinitrosyl formation (inner-sphere) rather than the direct NO coupling (outer-sphere).[345] Two possible conformers of the dinitrosyl intermediates can be identified using IR spectroscopic signatures (the frequency difference between the symmetric (ν_{sym}) and antisymmetric (ν_{asym}) components, and the I_{sym}/I_{asym} intensity ratio).[345] Seemingly, only the relative intensities of the stretching vibrations are markedly altered upon changing the conformation, and the IR results confirm an attracto conformation of the copper dinitrosyls in ZSM-5 (see Fig. 37b). Although the attracto conformation brings both oxygen atoms closer to each other, the development of an O–O bond (for initiating direct NO decomposition into O_2 and N_2) is significantly impeded by the concomitant accumulation of the negative charge on these atoms when they approach. In the alternative repulso conformation, both nitrogen atoms are getting closer to each other. It is beneficial for the incipient N–N bond, and along this mechanistic variant, the NO decomposition takes place. As a result, for direct NO decomposition into N_2 and O_2, the attracto dinitrosyls are inert, and the repulso conformation favours the reaction initiated by the inner-sphere N–N bond formation. It requires, therefore, an initial transformation of the dinitrosyl intermediates from the attracto into the repulso conformation.[345,346] An energy diagram for this transformation is presented in Fig. 37d_1. As a result, the mechanistic cycle of the NO direct decomposition on the mononuclear centres of Cu accommodated in zeolite catalysts involves the following steps:

$$^{1}Cu^{+} + NO_{(g)} \rightarrow {}^{2}\{CuNO\}^{11} \rightarrow \textit{cis}\text{-}{}^{1}\{CuN_2O_2\}^{12} \rightarrow \textit{trans}\text{-}{}^{1}\{CuN_2O_2\}^{12} \rightarrow {}^{3}Cu^{2+}O^{-} + N_2O_{(g)}.$$

It can be accomplished by decomposition of the N_2O byproduct on the ensuing copper–oxo centres (see Chapter 4.3.3).[350,352] Such a mechanism of direct NO decomposition through the dimeric N_2O_2 intermediates is substantiated for CuZSM-5 zeolite by spectroscopic evidence.[319]

Another scenario of NO decomposition occurs over copper dimers and two vicinal single copper centers in ZSM-5 zeolite. The fraction of copper dimers and vicinal Cu centres increases with a decreasing Si/Al ratio and with a rise of the copper site density.[350,353,354] Such centres can interconvert from the vicinal $Cu^{+} \cup Cu^{+}$ into the dimer $(Cu–O–Cu)^{2+}$ species upon interaction with NO, and the corresponding energy profile is shown in Fig. 37d_2. The NO decomposition mechanism can be summarized in the following steps:

(1) capture of NO, $Cu^{+} \cup Cu^{+} + 2NO \rightarrow (ON)Cu^{+} \cup Cu^{+}(NO)$, the ensuing mononitrosyls are observed in IR spectra at 1813 cm^{-1},

(2) N–N bond formation with release of N_2O byproduct, $(ON)[Cu^{+} \cup Cu^{+}](NO) \rightarrow (Cu–O–Cu)^{2+} + N_2O$, formation of $(Cu–O–Cu)^{2+}$ is confirmed by the band at 1903 cm^{-1} observed upon subsequent NO adsorption $(Cu–O–Cu)^{2+} + 2NO \rightarrow (ON)[(Cu–O–Cu)^{2+}](NO)$,

(3) formation of dinitrogen, $Cu^{+} \cup Cu^{+} + N_2O \rightarrow (Cu–O–Cu)^{2+} + N_2$.

The latter step is discussed in more detail in Chapter 4.3.3.

Reactivity of TMI–NO with O_2 – examples for Cu–zeolites. Recent studies have explored the interaction of NO and O_2 with Cu centres of differing nuclearity, in both reduced and oxidized states, focusing on elucidation of the reactivity patterns and thermodynamic stability of intermediates under conditions that closely resemble those of actual SCO

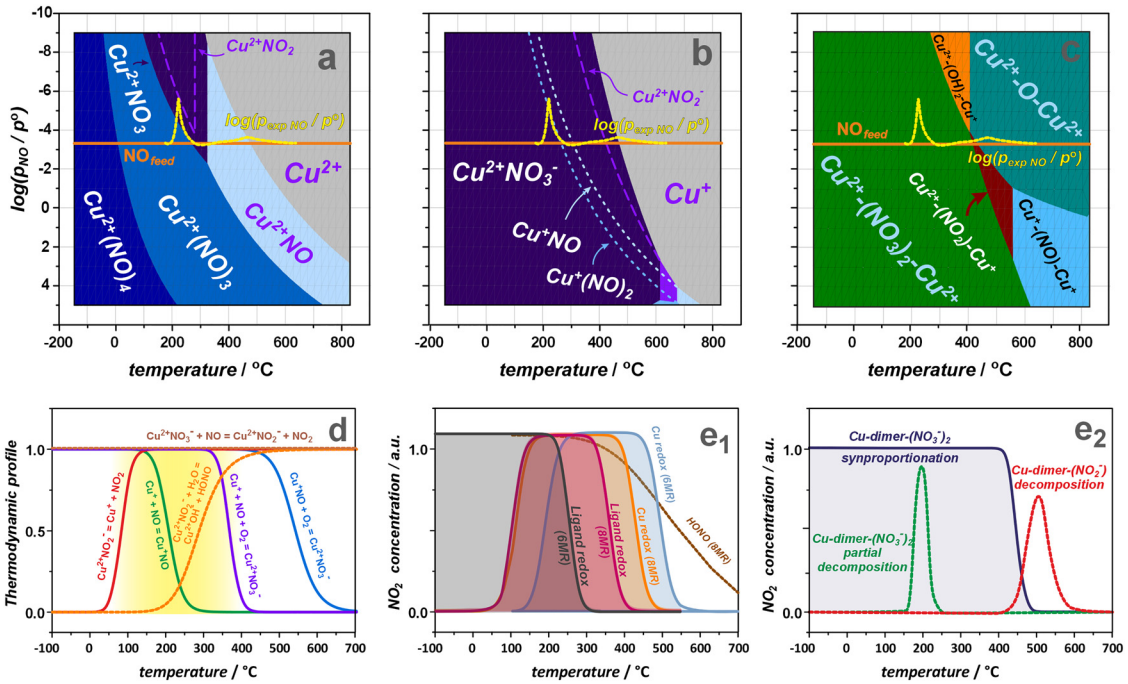

Fig. 38 Thermodynamic $\Delta G(p,T)$ diagrams for Cu^{2+} (a), Cu^{+} (b) cations, and dual copper centres Cu^{2+}–O^{2-}–Cu^{2+} (c) in CHA zeolite as a function of temperature (T) and partial pressure of NO (p_{NO}). Thermodynamic profiles for the NO oxidation reaction (NO_2 formation) on the isolated copper centres, according to the cationic metal-redox pathway (d). The calculated NO_2 production profiles based on the thermodynamic modelling for the isolated copper active centres (e_1) and copper dimers (e_2). Adapted from ref. 172 under the terms of the CC BY 4.0 license, Copyright 2025, published by the American Chemical Society.

and SCR processes. A typical reaction involving nitrosyls as intermediates is the reduction of NO to dinitrogen in the presence of O_2, using various reductants, such as hydrocarbons (HC-SCR) or ammonia (NH_3-SCR). Since early studies, the redox character of these reactions has been recognized, and Cu-containing zeolites, such as ZSM-5, CHA, have been identified as the most active catalysts.[355–360] Although there are several mechanistic proposals of the SCR reaction course,[33,277,361,362] their common point is the coexistence of the mutually coupled reduction half-cycle (RHC) and oxidation half-cycle (OHC).[214,228,300,363,364] The OHC is associated with the selective catalytic oxidation (SCO) of NO to NO_2 and to various charged (nitrates/nitrites) and protonated (HONO) NO_x species.[33,355–357,364] Spectroscopic IR data support the theoretical and thermodynamic predictions of the formation of Cu^{2+}–NO (1950–1880 cm^{-1}) and Cu^{+}–NO (1810–1800 cm^{-1}) intermediate species. The bands at 1620, 1595, and 1575 cm^{-1}, in turn, correspond to the symmetric stretching modes of bidentate NO_3^-, whereas the bands at 1500 and 1310 cm^{-1} come from the antisymmetric and symmetric modes of monodentate NO_3^- species,[214,365,366] overlapping with the antisymmetric and symmetric stretchings of the N-bonded nitrites (NO_2^-).[319] They are typically observed during the NO oxidation and SCR reactions in zeolites by *operando* IR.[278,367,368] The reactivity of NO and O_2 toward NO_2, NO_3^-/NO_2^- formation involves various copper species, such as bare Cu^{2+}/Cu^{+} and Cu^{2+}–OH^-, and dimeric $[Cu–O–Cu]^{2+}$, which can act as potential active centres for such reactions.[369]

A valuable thermodynamic insight into NO oxidation over CuSSZ-13 catalyst can be obtained from FPT modelling. The relative stability of the exemplary copper–NO_x^- species, formed in CHA zeolite after the reaction between NO and O_2, at various T and p_{NO} conditions is shown in Fig. 38, for the Cu^{2+}, Cu^{+}, and oxo $[Cu–O–Cu]^{2+}$ centers. In general, the oxidized isolated Cu^{2+} centres are unable to capture dioxygen, and the thermodynamic diagrams are dominated by copper(II)–nitrosyls and diverse NO_x adducts (x = 1–3) of a radical nature. Under the conditions similar to that of NO SCO, the stability regions of $Cu^{2+}NO_x$, bare Cu^{2+} and $Cu^{2+}NO$ species are shown in Fig. 38a. In the case of reduced Cu^{+} (Fig. 38b), which can be generated, *i.a.*, *via* reduction of Cu^{2+}–OH^- with NO producing HONO,[95,370] reaction with NO/O_2 and charge transfer lead to NO_3^- dominant anionic species. The complexes formed by the independent capture of NO and O_2 are unstable relative to nitrate and nitrite species. Under the experimental SCR/SCO conditions, nitrates decay at approximately 400 °C. For the dimeric active centres, the dinitrate Cu^{2+}–$(NO_3^-)_2$–Cu^{2+} adspecies dominate the experimental range of SCR/SCO. The simultaneous adsorption of water and NO is thermodynamically disfavoured, due to the lateral repulsion between H_2O and NO ligands. Notably, under the NO–SCO/SCR conditions, several metastable intermediates with comparable thermodynamic profiles can coexist and mutually interconvert. This dynamic equilibrium enhances the functional versatility of bridging copper centres, enabling them to participate in the stoichiometric transformation of nitrates,[33] promoting fast SCR through efficient NO_2 generation, for instance.[278,357]

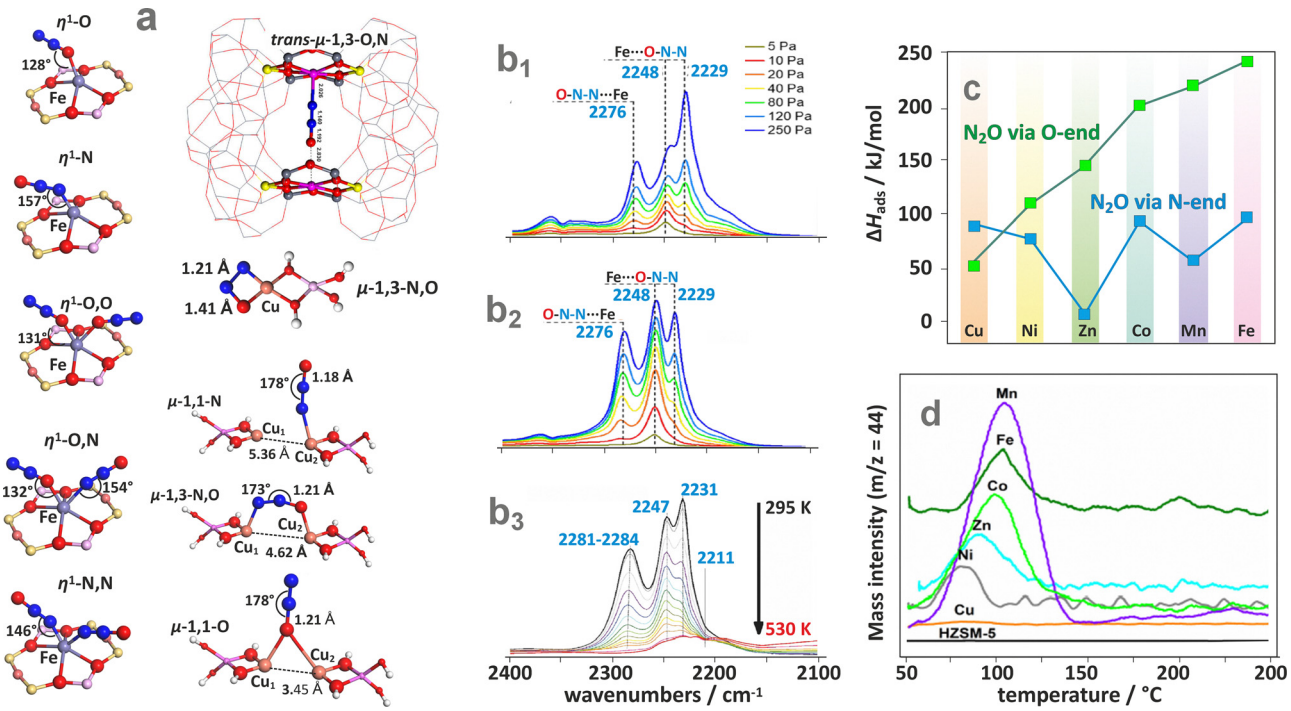

Fig. 39 Survey of the coordination modes of N_2O to single and dual TMI sites (a), based on data from ref. 20, 353, 371 and 376, with the middle structure adapted from ref. 90 with permission from Elsevier, Copyright 2010. Variable pressure (p_{N_2O} = 5–250 Pa) IR spectra of N_2O adsorbed at room temperature on Fe, Na-CHA (with Fe predominantly located in 6MR) (b_1), and Fe-CHA (with Fe predominantly located in 8MR) zeolites (b_2), and variable temperature adsorption of N_2O on the Fe/SSZ-13 catalyst followed by IR (b_3) adapted from ref. 377 under the terms of the CC BY 4.0 license, Copyright 2024, published by the American Chemical Society. Calculated adsorption energies for η^1-O and η^1-N binding of N_2O to various TMI hosted in the ZSM-5 zeolite (c) together with the corresponding experimental TPD-N_2O profiles (d).[373]

Recently, thermodynamic profiles have been constructed based on DFT/FPT calculations to unravel the course of NO–SCO elementary steps and underly driving forces under different experimental conditions.[172] Analysis of such profiles for the typical isolated Cu centres in SSZ-13 reveals the presence of three mechanistic routes of NO oxidation: (1) copper-redox pathway, (2) ligand-redox pathway, and (3) *via* HONO intermediates. In the case of dimeric Cu species, the NO SCO reaction can proceed (1) *via* direct NO_2 release (thermal decomposition of anionic NO_x^- adspecies) and (2) *via* formation of NO_2 due to the comproportionation of nitrates with the encaged NO. The corresponding concentration profiles of the involved adspecies and intermediates are shown in Fig. 38d and e.The predicted evolution of the NO_2 concentration with reaction temperature, along with the advanced mechanistic tenets, agrees well with the experimental results using isotopically labeled $N^{18}O$, $N^{16}O$, and $^{18}O_2$.[172]

4.3.3. Dissociative activation of N_2O. The catalytic chemistry of nitrous oxide is driven by technologies for abating anthropogenic N_2O emissions, and the use of N_2O as a unique oxidant that can provide atomic oxygen upon N_2O dissociation, brought about by its interaction with TMI centres.[18,20] Among the numerous efforts to understand the molecular routes of N_2O activation, those focused on metallozeolites with mono and dimeric iron[20,164] and copper as active centres[353] are particularly widespread and have led to notably detailed insights. Other notable examples of 3d TMI include Co,[371] Ni,[372] and, less frequently, Mn.[373]

Intrazeolite coordination of N_2O. The N_2O molecule is a relatively weak ligand acting as both a σ donor and a π acceptor.[374] It is attached most frequently in the top-on monodentate (η^1-O and η^1-N) way to single TMI cations (Fe, Co, Ni, Cu),[373] and in the *cis* μ-1,3-O,N, μ-1,1-O fashion on bridging M–O–M species.[353,375] Rather unique *trans* μ-1,3-O,N adducts attached to adjacent close-distant Fe cations are proposed in Fe/FER, based on DFT modelling.[90] In the case of $(N_2O)_2$TMI/Z adducts, η^1-O,O, η^1-O,N and η^1-N,N binding forms, as well as the bidentate η^2-O,N attachment of N_2O to single TMI have been reported,[376] see (Fig. 39a). Since the bis-N_2O adducts are observed only at high p_{N_2O} pressures and low temperatures, they are not relevant for catalytic considerations.

The variable pressure IR spectra of N_2O adsorption recorded at room temperature, shown in Fig. 39b1, indicate that for the Fe/6MR species hosted in the CHA matrix, the IR peak of the η^1-N mode dominates, whereas in the case of Fe/8MR the η^1-O (2229 cm^{-1}) and η^1-N (2276 cm^{-1}) adsorption modes exhibit IR signals of comparable intensities (Fig. 39b2).[377] This illustrates directly the influence of the zeolite ring size on the N_2O ligation by iron. The 2248 cm^{-1} band corresponds to Al···O–NN species. In the case of Fe/FER zeolites, the η^1-N binding is generally stronger than the η^1-O

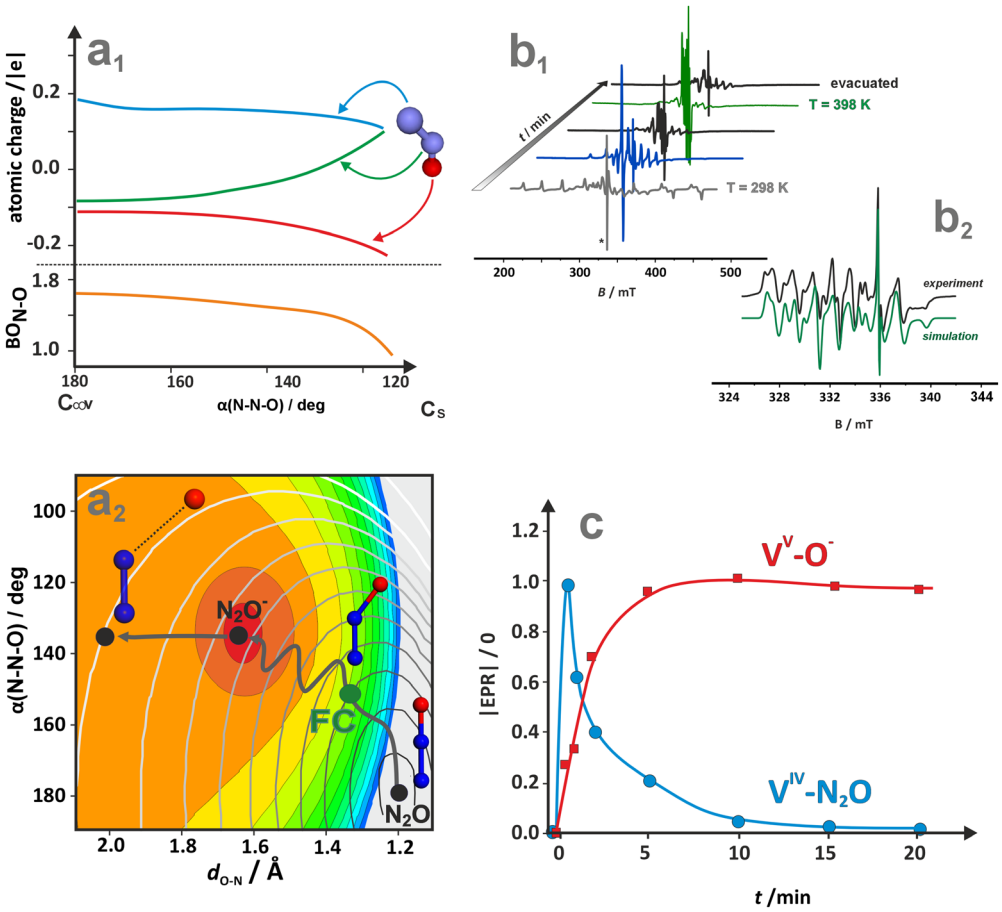

Fig. 40 Variation of the charge redistribution and the N–O bond order for the N_2O molecule upon bending (a_1), and overlay of the potential energy surfaces of N_2O (grey iso-energy lines) and N_2O^- (colour coded areas) with the schematic reaction pathway leading from linear N_2O molecule, through bent transition state at Frank–Condon (FC) locus into shallow minimum on the N_2O^- PES, prompting an eventual dissociation of the N_2O^- transient (a_2). Adapted from ref. 379 under the terms of the CC BY 4.0 license, Copyright 2024, published by the American Chemical Society. Evolution of the EPR spectra recorded during the reaction of N_2O with VO_2 centres entrapped in BEA zeolite (b_1), together with simulation of the EPR signal due to $[VO_2^+]$–$O^{\bullet -}$ species (b_2) (adapted from ref. 295 with permission from the Royal Society of Chemistry, Copyright 2016) together with the corresponding plot of gradual transformation of $[VO_2]$–N_2O into $[VO_2^+]$–$O^{\bullet -}$ *via* an electron transfer mechanism (c).

one, and significantly depends on the α or β locus, and the particular arrangement of Al atoms in the corresponding rings.[90] The temperature dependence of N_2O adsorption on Fe/SSZ-13 zeolite indicates that the beneficial η^1-O active mode persists till 530 K, whereas the spectator η^1-N one is completely depleted at this temperature (Fig. 39b3). The survey of the DFT-calculated N_2O adsorption energies for selected 3d TMI hosted in ZSM-5 catalysts, and the related N_2O-TPD profiles, are shown in Fig. 39c and d, respectively. The thermal stability of the N_2O-TMI adducts does not exceed 150 °C (520 K), and the position of the desorption peaks maxima (T_{max}) is linearly correlated with the calculated ΔH_{ads} values. The extent of metal-to-ligand charge transfer is the key factor controlling the adsorption strength.[373] However, alternatively to desorption, the ligated N_2O may react with the TMI centres, dissociating into N_2 and leaving the bound oxygen moiety behind (as discussed below).

General mechanistic considerations of N_2O activation. A characteristic feature of triatomic molecules like N_2O is that bending due to the ν_2 vibration (589 cm^{-1} in the gas phase) or upon interaction with the active sites (TMI) leads to its intrinsic preactivation. This is revealed by a significant buildup of negative charge in the oxygen moiety ($q_O = -0.2|e|$), and the merging of charge at both nitrogen atoms to the same value of $q_N = 0.1|e|$. An elongation of the NN–O bond (by ~0.3 Å) and a dramatic decrease in the NN–O bond order accompany such changes, making the bent N_2O molecule prone to oxygen release (Fig. 40a1). All these features play an important role in the N_2O activation process (Fig. 40a_2). Furthermore, since the ground state of $N_2O(^1\Sigma^+)$ is singlet, whereas the ground state of $O_2(^3\Sigma_g^-)$ is triplet, the decomposition of N_2O into N_2 and O_2 follows a nonadiabatic reaction coordinate with changing spin multiplicity.

The two generic mechanisms of N_2O activation are based on electron transfer (ET) and oxygen atom transfer (OT) scenarios.[317] However, in the case of metallozeolite catalysts, any of those occur in the exclusive form. Most N_2O dissociation reactions on metallozeolites are initiated by an electron density transfer from the TMI core to the N_2O ligand (cationic redox

pathway). The extent of the charge transfer, which assists in weakening the N–O bond and promoting transfer of the O-moiety to the TMI core, depends on its nature, location, and the type of zeolite framework. Alternatively, the O-species can also be accommodated on the μ-O^{2-} fragment of the bridging M–O–M centres, producing a peroxo ($O_2^{2-}(^1\Sigma_g^+)$) intermediate (defining anionic redox pathway).

Catalytic decomposition of nitrous oxide based on electron transfer (ET) can be formulated in terms of the classic three-step mechanism:

$$(1)\ N_2O(^1\Sigma^+) + e^- \rightarrow [N_2O^-]^* \rightarrow O^-(^2P) + N_2(^1\Sigma_g^+),$$

$$(2)\ O^-(^2P) + O^-(^2P) \rightarrow O_2(^3\Sigma_g^-) + 2e^-,$$

$$(3)\ O^-(^2P) + N_2O(^1\Sigma^+) \rightarrow O_2(^3\Sigma_g^-) + N_2(^1\Sigma_g^+) + e^-,$$

where the requisite electron provided by the donor $3d^n$ orbitals of the M^{p+}/z active site is accommodated on the antibonding $3\pi^*$ LUMO of N_2O. This mechanism involves the formation of a highly unstable N_2O^- transient, which imparts the necessary geometric and electronic rearrangements of the N_2O molecule, contributing to the inherent barriers of this process. To initiate the reaction, the intrazeolite TMI (i) provides orbitals of appropriate energy and symmetry for N_2O capture and subsequent accommodation of the resulting O^- intermediate; (ii) acts as a redox centre (allowing for electron shuttling); and (iii) as spin catalyst (facilitating nonadiabatic conversion of singlet $N_2O(^1\Sigma^+)$ reactant into triplet $O_2(^3\Sigma_g^-)$ product). The fact that the neutral N_2O is linear ($C_{\infty v}$), whereas the N_2O^- transient is bent (C_s), implies a need for significant internal reorganisation energy of the N_2O molecule to make ET feasible, according to the Franck–Condon principle (see the FC locus in Fig. 40a2).[378] Notably, upon bending, the adiabatic electron affinity of N_2O increases to 0.22 eV, favouring electron acceptance.[379] Since the potential energy surface of N_2O^- is relatively flat, this transient species immediately dissociates into N_2 and O^- moieties, because the FC locus is situated higher in energy than the N_2O^- dissociation barrier (Fig. 40a2). As a result, the NN–O bond breaking, which ET brings about, implies considerable bending of the N_2O molecule, which is a distinctive mechanistic feature of the dissociation process.

These considerations allow for the formulation of N_2O decomposition along the cationic redox mechanism for single M^{p+}/z centres in the following way:

$$(1)\ N_2O(^1\Sigma^+) + M^{p+}/z \rightarrow [OM]^{p+}/z + N_2(^1\Sigma_g^+),$$

$$(2)\ N_2O(^1\Sigma^+) + [OM]^{p+}/z \rightarrow O_2(^3\Sigma_g^-) + N_2(^1\Sigma_g^+) + M^{p+}/z,$$

$$(3)\ 2[OM]^{p+}/z \rightarrow O_2(^3\Sigma_g^-) + 2M^{p+}/z.$$

Since the specific charge transfer between the metal centres M and the ligated O-moieties depends on their actual nature, in these general equations only the overall charge "*p*+" of the involved species is explicitly indicated. For instance, the cationic redox mechanism may involve a single electron transfer producing radical oxyl species $O^{\bullet-}$/M, as in the case of $^2VO_2$/BEA, or consecutive two-electron transfer forming oxo-species (α-O), exemplified by $^5Fe^{II}$/BEA.[20]

The attack of the second N_2O molecule can be directed at the terminal oxygen or the metal centre, depending on the chemical characteristics of the accommodation sites imparted by their electronic structure and location in the zeolite matrix.[380] In the case of dimeric M–O–M species, the cation M centres or the bridging μ-O^{2-} centres may serve as a possible locus for lodging the O-moieties, forming a peroxo μ-O_2^{2-} species with a diagnostic band at near 867 cm^{-1}, typically observed by Raman spectroscopy.[381]

Using the N_2O decomposition on Fe/ZSM-5[380] as a straight example, the resultant mechanisms can be epitomised as:

$$N_2O(^1\Sigma^+) + [M\text{–}\mu\text{-}O^{2-}\text{–}M]^{p+}/z \rightarrow [O\text{–}M\text{–}O^{2-}\text{–}M]^{p+}/z + N_2(^1\Sigma_g^+),$$

$$[O\text{–}M\text{–}O^{2-}\text{–}M]^{p+}/z \rightarrow [M\text{–}\text{–}(\mu\text{-}O^{2-})_2\text{–}M]^{p+}/z,$$

$$N_2O(^1\Sigma^+) + [M\text{–}\text{–}(\mu\text{-}O^{2-})_2\text{–}M]^{p+}/z \rightarrow [O\text{–}M\text{–}\text{–}(\mu\text{-}O^{2-})_2\text{–}M]^{p+}/z + N_2(^1\Sigma_g^+),$$

$$[O\text{–}M\text{–}(\mu\text{-}O^{2-})_2\text{–}M]^{p+}/z \rightarrow [(O_2^{2-})M\text{–}\mu\text{-}O^{2-}\text{–}M]^{p+}/z \rightarrow [M\text{–}\mu\text{-}O^{2-}\text{–}M]^{p+}/z + O_2(^3\Sigma_g^-).$$

Actually, by involving both the metal and the bridging oxygen, it exhibits a mixed redox (cationic and anionic) character. The less common anionic redox alternative (attack on μ-O^{2-}) assumes the following sequence:

$$N_2O(^1\Sigma^+) + [M\text{–}(\mu\text{-}O^{2-})\text{–}M]^{p+}/z \rightarrow [M\text{–}(\mu\text{-}O_2^{2-})\text{–}M]^{p+}/z + N_2(^1\Sigma_g^+),$$

$$N_2O(^1\Sigma^+) + [M\text{–}(\mu\text{-}O_2^{2-})\text{–}M]^{p+}/z \rightarrow [M\text{–}(\mu\text{-}O^{2-})\text{–}M]^{p+}/z + O_2(^3\Sigma_g^-) + N_2(^1\Sigma_g^+),$$

suggested, *e.g.*, for the Cu–O–Cu in ZSM-5,[350] with possible O_2 evolution *via* the following step:

$$2[M\text{–}(\mu\text{-}O_2^{2-})\text{–}M]^{p+}/z \rightarrow 2[M\text{–}(\mu\text{-}O^{2-})\text{–}M]^{p+}/z + O_2(^3\Sigma_g^-).$$

Herein, the formal oxidation state of M remains essentially intact, whereas for the bridging O^{2-} moiety it changes from −2 to −1 due to the formation of μ-O_2^{2-} (peroxo) species. Additionally, depending on the N_2O coordination energy to the particular intrazeolite TMI and the reaction conditions, adsorption quasi-equilibria such as $N_2O + M^{p+}/z \leftrightarrow (N_2O\text{–}M)^{p+}/z$, $N_2O + [OM]^{p+}/z \leftrightarrow [OM\text{–}N_2O]^{p+}/z$ and $O_2 + M^{p+}/z \leftrightarrow (O_2\text{–}M)^{p+}/z$ have also been taken into account in the microkinetic analysis.[20,371,382,383]

Exemplary N_2O activation pathways on well-defined centres. Investigations documenting N_2O activation on metallozeolites induced by a distinct metal-to-ligand electron transfer (MLET) are hardly available in the literature. Nevertheless, a notable example is provided by the $VO_2(d^1)$ species encaged in the BEA zeolites interacting with N_2O.[295] The progress of the reaction $^2V^{4+}(=O)_2 + N_2O(^1\Sigma^+) \rightarrow {}^2[(O=)_2V^{5+}\text{–}O^{\bullet-}] + N_2(^1\Sigma_g^+)$ at room temperature followed by EPR is shown in Fig. 40b1, whereas the

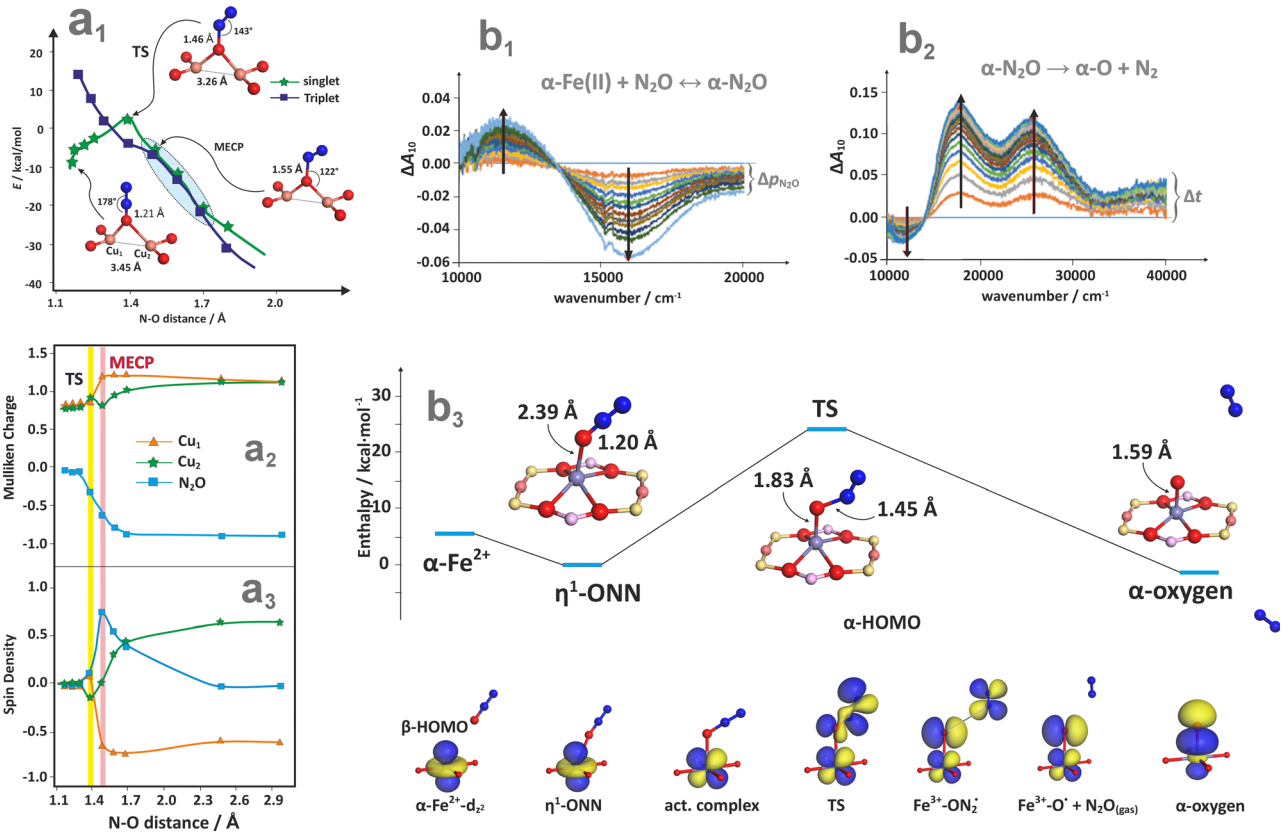

Fig. 41 N_2O decomposition over the bridging $Cu^+ \cup Cu^+$/ZSM-5 (a_1)–(a_3) and the single Fe^{2+}/*BEA (b_1)–(b_3) centres. Singlet and triplet potential energy surface for N_2O dissociation on the $Cu^+ \cup Cu^+$ centres (a_1), and the changes in the charge (a_2) and spin (a_3) densities along the O–N_2 reaction coordinate, adapted from ref. 353 with permission from the American Chemical Society, Copyright 2014. *Operando* UV-vis-NIR spectra of the Fe^{2+}/*BEA catalyst recorded during N_2O adsorption under variable p_{N_2O} pressures (0–0.05 atm) at 308 K (b_1). Gradual decomposition of the coordinated N_2O into $[FeO]^{2+}$ species and N_2 at 373 K in the time interval of 15 min (b_2), together with the corresponding energy profile accompanied by the associated molecular orbital structures of the key intermediates (b_3), adapted from ref. 20 with permission from Springer Nature, Copyright 2021.

EPR spectrum of the final $^2[(O{=})_2V^{5+}{-}O^{\bullet-}]$ product and its simulation are shown in Fig. 40b2. The obtained kinetic profiles of the reactant decay and the product formation (Fig. 40c) are entirely consistent with the MLET-induced dissociation of N_2O. A concerted capture of the resulting radical $O^{\bullet-}$ moiety by the $[(O{=})_2V^{5+}]^+$ core produces the $^2[(O{=})_2V^{5+}{-}O^{\bullet-}]$ species. The EPR parameters (g_{xx} = 2.0202, g_{yy} = 2.0173, g_{zz} = 2.0284 > g_e and A_{zz} = 1.65 mT, A_{yy} = 1.58 A_{zz} = 1.49 mT) are characteristic of the ligand-centred $O^{\bullet-}$ radical (manifested by the *g*-tensor features) attached electrostatically to the $(O{=})_2V^{5+}$ core (demonstrated by small superhyperfine values due to the coupling with ^{51}V, I = 7/2). This signal disappears (after 30 minutes) upon co-adsorption of CO or propene at ambient temperature, due to the highly reactive character of the $O^{\bullet-}$ radicals.

The mechanism of N_2O activation on cationic centres has been meticulously elaborated by DFT modelling, corroborated to some extent by spectroscopic studies, for the most widely investigated single Fe^{II}/z and $[FeO]^{2+}/z$ sites, and dimeric $Cu^+ \cup Cu^+$, $Fe^{2+} \cup Fe^{2+}$, Fe–O–Fe/*z* and Cu–O–Cu/*z* centres, accommodated in ZSM-5, BEA, CHA or FER zeolites.[20,164,353,380,384] The Co, Mn or Ni zeolites are less frequently examined.[385,386]

In particular, high activity of dimeric metal centres ($Cu^+ \cup Cu^+$) has been reported for Cu/ZSM-5 zeolites.[353] Among the bridging μ-1,1-O and μ-1,3-O,N, and terminal η^1-O binding modes of the N_2O molecule, only the μ-1,1-O attachment leads to the small activation energy (2 kcal mol^{-1}) that is compatible with the experimental value of 2.5 kcal mol^{-1}. The corresponding energy profile for the singlet and triplet PES indicates that the minimum energy crossing point (MECP) appears after the bent transition state (∠(ONN) = 143°) located on the singlet PES (Fig. 41a$_1$). In the MECP locus, the O–N_2 distance is elongated to ~1.55 Å, and the O–N–N angle decreased to 122°. Moreover, the associated charge and spin flows from both copper sites are distinctly uneven due to the slightly different local environments of the Cu ions (Fig. 41a$_2$ and a$_3$). The most significant changes in spin and charge transfer occur around the MCEP, but not at the TS point, which is a characteristic feature of the nonadiabatic character of N_2O dissociation, primarily driven by metal-to-ligand electron transfer.

In the case of intrazeolite iron, multiple spectroscopic studies (Mössbauer, VTVH-MCD, UV-vis, IR) corroborated by DFT modelling are available for the definite description of Fe^{2+}/z accommodated in the 6-member rings (β-6MR) present in

BEA, MFI, and FER, as high-spin square-planar ferrous species ($Fe^{2+}(d^6)$, with $S = 2$ and $D > 0$) that are particularly active in N_2O decomposition.[5] Such centres also appear in the 6MR sites of CHA, where the C_s-symmetric Fe^{2+} cations are less distorted from the square planar arrangement in comparison to C_2-symmetric Fe^{2+} centres in BEA.[147] They are collectively called α-Fe^{2+} species, and their structural deviations across different zeolites are reflected, among others, in the position of the diagnostic $3d_{z^2} \rightarrow 3d_{x^2-y^2}$ band appearing at 15 900 cm^{-1} in Fe/BEA, 15 200 cm^{-1} in Fe/ZSM-5, 16 100 cm^{-1} in Fe/FER, and 13 000 cm^{-1} in Fe/CHA.[135,147]

The remarkable reactivity of the α-Fe^{2+} centres to N_2O activation is realised by transferring formally two electrons from metal to ligand for complete N–O bond cleavage to produce $[Fe{=}O]^{2+}$ species (α-O) with concomitant N_2 release. At moderate temperatures (~150–250 °C), the reaction occurs quickly with an apparent activation energy of 9–13 kcal mol^{-1} for Fe/BEA,[20] Fe/ZSM-5, and Fe/FER catalysts.[5] This process can be followed quantitatively in the UV-vis-NIR *operando* set-up by observing the gradual transformation of the band at 15 900 cm^{-1} into 11 500 cm^{-1} with the isosbestic point at 13 500 cm^{-1}, which corresponds to the α-Fe^{2+} + N_2O → N_2O–α-Fe^{2+} process (Fig. 41b1). Subsequent transformation of the band at 11 500 cm^{-1} into the bands located at 16 900 cm^{-1} and 28 000 cm^{-1} (Fig. 41b2) is diagnostic of the N_2O dissociation (N_2O–Fe^{2+} → $[\alpha\text{-}Fe{=}O]^{2+}$ + N_2). The appearance of an isosbestic point at 14 000 cm^{-1} confirms this transformation univocally.[20]

The prime factors governing efficient N_2O reduction include the binding of N_2O to the active α-Fe^{2+} site in the η^1-O fashion. This promotes the cleavage of the N–O bond, accompanied by the requisite charge redistribution and the formation of a metal–oxo bond. It generates the driving force for the eventual O-atom transfer, without restraining the subsequent evolution of O_2 upon capture of the second N_2O molecule. A more detailed insight into the reaction coordinate for the oxygen release step on α-Fe/BEA (Fig. 41b3) reveals that this process occurs in two sequential MLET events, with a notable internal rearrangement of electrons within the 3d manifold of the iron core. Upon η^1-O attachment, an electron is transferred from the $3d_{z^2}$ orbital into the $3d_{yz}$ orbital, which enables an efficient π-back donation from the Fe^{2+} core into the $3\pi^*$ LUMO of the N_2O ligand.[20] The extent of this back-bonding is controlled, among others, by the presence or absence of an axial ligand. At the bent transition state (138°), located at 25 kcal mol^{-1}, the NN–O bond is elongated to 1.45 Å, whereas the Fe–ON_2 bond is contracted to 1.83 Å. The TS structure evolves into a highly unstable $Fe^{3+}(S = 5/2)\uparrow\downarrow N_2O^{\bullet-}$ ($S = 1/2$) species. Once the N–O bond is eventually cleaved, a transient Fe^{3+}–$O^{\bullet-}$ oxyl is formed with the LUMO composed mainly of the $2p_x$ orbital. A second electron transfer converts the oxyl species into the final oxo $[Fe{=}O]^{2+}$ units with $S = 2$ (Fig. 41b3).[20]

The complete energetic profiles of N_2O binding, activation and decomposition into elements on different active sites present in the exemplary Fe/ZSM-5 is shown in Fig. 42. They illustrate two mechanistic variants of this reaction for the iron cations, hosted in the β (Al atoms in the T4, T10 position, 4-fold coordination of Fe) and α (Al atoms in the T1, T7 positions, 5-fold coordination of Fe) positions, see Fig. 42a1 and a2, respectively.[380]

The energies of η^1-O adsorption of the N_2O ligand (−38 kJ mol^{-1} for α and −39 kJ mol^{-1} for β sites), the location of the bent transition states TS_1 (44 and 41 kJ mol^{-1}), and the

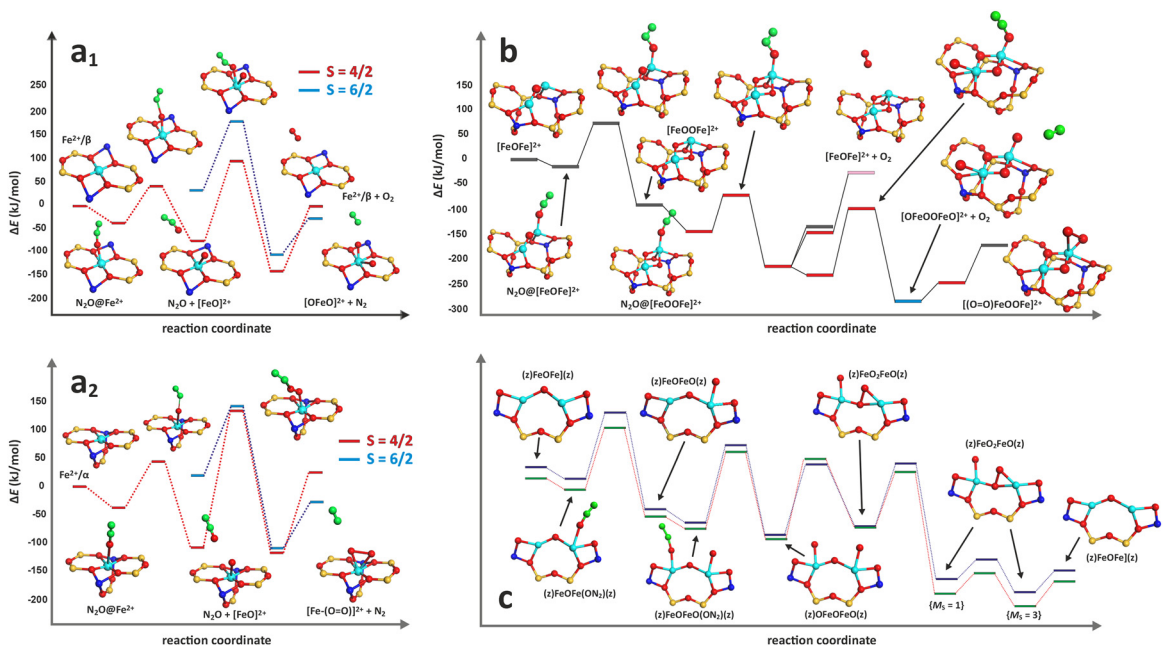

Fig. 42 Mechanistic variants of N_2O decomposition over single and bridging Fe–oxo. Energetic profiles for N_2O decomposition on Fe^{2+} cations hosted in the β (a_1) and α sites (a_2), and dimeric Fe–O–Fe centres (b) hosted in the ZSM-5 zeolite. The reaction energy diagram for the ferro (navy blue) – and antiferromagnetic (green) state of the dimeric iron active centres (c). The figure was based on data from ref. 164 and 380.

N_2O dissociation energies with concomitant formation of the $[FeO]^{2+}$ species (ΔE = −67 and −63 kJ mol^{-1}) are quite similar for both α and β sites Fig. 42a$_1$ and a$_2$. However, the reactivity of the resultant $[FeO]^{2+}$ units with N_2O, which closes the catalytic cycle by releasing O_2, evolves along different pathways.

In the case of β-sites, the N_2O attack is directed at the metal (Fe) centre with the activation barrier of 167 kJ mol^{-1} (TS_1) and d(Fe–ON$_2$) = 2.065 Å (Fig. 42a1). Upon dissociation of the ligated N_2O, the ensuing dioxo-iron intermediate is transformed into dioxygen, and the O_2 desorption barrier of 141 kJ mol^{-1} for S = 2 is decreased to 114 kJ mol^{-1} for S = 3. For α sites (Fig. 42a2), the N_2O attack is directed at the terminal oxo moiety, and the reaction is driven by the formation of an incipient O–O bond in the TS_2 state with a relatively high barrier of 243 kJ mol^{-1}. The ensuing η^2-O,O intermediate ($d_{(O-O)}$ = 1.345 Å) evolves next into gas phase O_2, restoring the Fe^{2+}/α active site. This uphill step costs 141 kJ mol^{-1} on the quintet (S = 2 + 0) potential energy surface, but is substantially decreased by 53 kJ mol^{-1} (α) for the septet (S = 2 + 1 = 3) PES, where oxygen is produced in its ground triplet state $O_2(^3\Sigma_g^-)$. The corresponding energy profile for S = 3 is marked in blue, indicating that only the last two steps are energetically favoured over the S = 2 pathway (Fig. 42a2).

These differences show that the local coordination environment around the Fe^{2+} cations and the PES spin multiplicity exhibit a considerable influence on the detailed mechanism and energetics of N_2O decomposition, modifying the rate constant *via* the transmission κ coefficient in the Eyring equation:

$$k(T) = \frac{k_B T}{h} \exp\left(\frac{-\Delta H^{\#}}{RT}\right) \times \kappa \times \exp\left(\frac{\Delta S^{\#}}{R}\right) \qquad (8)$$

The Landau–Zener transition probabilities P_{LZ} ($\kappa = 2P_{LZ} - P_{LZ}^2$) between the PES of different spin states, calculated for N_2O decomposition on both Fe^{II}/ZSM-5 and $[FeO]^+$/ZSM-5 sites, are larger than ∼0.05.[21] Such values indicate that without correcting the reaction rates of N_2O decomposition for changes in the spin multiplicity, the resultant inaccuracies are equivalent to the activation barrier of ∼4 kcal mol^{-1} at 700 K. The spin state exhibits substantial influence on the reaction energetics by modifying the electronic structure of the reactants, which is particularly important for attaining the ground triplet state of the O_2 product. Owing to the changes in the spin multiplicity, the reaction pathway becomes energetically more favourable.[380]

A remarkable mechanistic variant of this reaction has been reported for conceivably adjacent Fe centres hosted in the ferrierite matrix.[387] The unique short separation of the neighbouring face-to-face β-6MR sites (7.5 Å in FER *vs.* >9 Å in MFI and BEA), favoured by the suitable location of Al atoms (see Chapter 4.3.1), allows the adjacent α-Fe cations to act cooperatively for efficient N_2O activation by forming a *trans* μ-1,3-O,N bridge between both Fe(II) centres (Fe–NNO$\cdots$Fe → Fe + O–Fe + N_2). This finding has been attributed to explaining the superior activity of Fe/FER (∼3 times higher) in comparison to Fe/BEA and Fe/ZSM-5 at 230 °C,[90] revealing a distinct synergy between the framework topology and Al distribution. Accordingly, the calculated apparent barrier for the O-atom transfer for *trans* μ-1,3-O,N bridged intermediates (3–4 kcal mol^{-1}) is smaller for the η^1-O species (9–13 kcal mol^{-1}).

For N_2O decomposition on dimeric iron–oxo centres ([Fe–(μ-O^{2-})–Fe]$^{2+}$/ZSM-5), the minimum energy pathway after spin-state optimisation is shown in Fig. 42. Markedly, the reactivity of such species is dramatically higher in comparison to the isolated Fe^{2+} and $[FeO]^+$ active sites. It is characterised by the switch of the rate-determining step (RDS) from O_2 evolution at low temperatures (400–600 K) to N_2O dissociation at high temperatures (T > 600 K). The ferromagnetic *vs.* antiferromagnetic coupling within the [Fe–(μ-O^{2-})–Fe]$^{2+}$ centres exhibits a rather minor influence on the N_2O decomposition.[164] All the energy differences between the key mechanistic steps are below 5.5 kcal mol^{-1} (Fig. 42c). For molecular oxygen to desorb in its ground triplet state, the barrier for the PES crossing from the antiferromagnetic singlet to the antiferromagnetic triplet is equal to 7.9 kcal mol^{-1}, whereas for the ferromagnetic coupling it increases to 9.5 kcal mol^{-1}.

Survey of N_2O activation and decomposition on various metallozeolite catalysts. The overall reactivity trends in N_2O decomposition for the most commonly investigated Fe, Cu, Co, and Ni zeolites are summarised in Table 5. It is rather difficult to establish a definite universal order of the TMI activity variation since incoherent results have been reported. It is caused, most probably, by insufficient control over the speciation of the active sites, differences in the framework topology, and in the Si/Al and M/Al ratio (loading).

The effect of TMI nature and loading on N_2O reactivity is illustrated in Fig. 43a$_1$ for Fe, Co, and Cu/SSZ-13 zeolites.[371] The reaction rates (Fe ≫ Co > Cu) exhibit appreciably different responses to p_{N_2O} (see insert), with considerable deviation from the pseudo-first-order kinetics. The activation energies decrease in the order 141–148 kJ mol^{-1} (Co) > 111–113 kJ mol^{-1} (Cu) > 81–85 kJ mol^{-1} (Fe), whereas the preexponential factors for Fe (12.6–12.8 ([s kP]$^{-1}$) and Cu (11.8–12.87 [s kP]$^{-1}$) are quite similar, and significantly lower than that for Co (19.0–19.9 [s kP]$^{-1}$). On Co/SSZ-13, the N_2O decomposition occurs on the isolated Co cations, which tend to enhance the preexponential factor at the cost of a higher activation energy. For iron and copper, this process mainly occurs on dual-oxo

Table 5 Selected activity trends for N_2O decomposition observed for Fe-, Co- and Cu-exchanged SSZ-13, ZSM-5, BEA and MOR metallozeolite catalysts

Topology	Si/Al	M/Al	Activity order	Ref.
CHA (SSZ-13)	12	0.13–0.32	Fe ≫ Co > Cu	371
MFI (ZSM-5)	25	0.5	Cu ≈ Fe > Co	388
MFI (ZSM-5)	18	0.73–1.3	Cu ≫ Co > Fe	389
MFI (ZSM-5)	12.5	0.02–0.245	Fe > Co > Ni > Cu	372
BEA	15	0.11–0.21	Co > Fe > Cu	145
BEA	23–42	0.5–1	Cu > Co > Fe	385
MOR	9.2	0.64–0.80	Co > Fe ≫ Ni ∼ 0	386

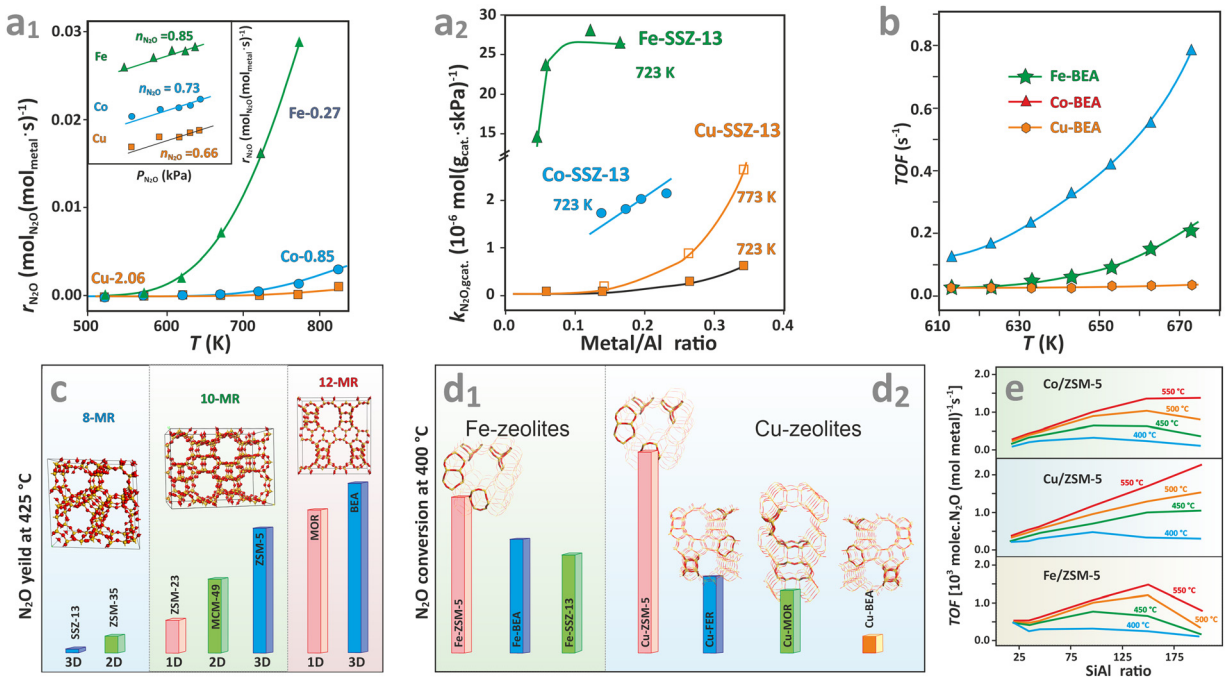

Fig. 43 Influence of the transition metal type (Co, Cu, Fe) hosted in CHA zeolites (a_1) and the M/Al ratio (a_2) on the N_2O decomposition performance, together with the apparent rate order (a_1, insert). The catalytic performance of Co, Cu, and Fe accommodated in BEA zeolites (b), the influence of the framework type (c) and (d_{1-2}), and the Si/Al ratio for Co/ZSM-5, Cu/ZSM-5, and Fe/ZSM-5 catalysts (e) on the deN_2O activity. Figure based on data from ref. 145, 371, 388, 390 and 391.

centres.[371] Thus, the rate constant for Co/SSZ-13 increases proportionally to the Co/Al ratio (Fig. 43a2). In the case of Fe/SSZ-13 catalysts, the rate constant increases till Fe/Al < 0.06 and then levels off, implying that only a fraction of the iron species is active in the N_2O decomposition. An exponential activity increase with the Cu/Al ratio suggests, in turn, that dimeric centres are responsible for deN_2O reactivity of Cu/SSZ-13, since statistically the number of pairs increases exponentially with copper loading. The same trend of the activity (Fe $\gg$ Co $>$ Cu) is also observed for BEA zeolites (Fig. 43b).[145] However, since the corresponding plots in Fig. 43a2 are derived from relatively small datasets, these conjectures warrant additional validation.

The influence of zeolite topology on N_2O decomposition over various Co/zeolites is illustrated in Fig. 43c, varying as Co/BEA $>$ Co/MOR $>$ Co/ZSM-5 $>$ Co/MCM-49 $>$ Co/ZSM-23 $>$ Co/ZSM-35 $>$ Co/SSZ-13.[392] In all cases, the active sites for this reaction are the isolated Co^{2+} cations. There is a consistent relationship between the self-diffusion coefficient of N_2O in different topological zeolites (established by computer simulation) and the N_2O conversion (apparently measured under diffusion limitation), revealing that the pore structure of the zeolites (size and dimensionality of the channels) affects the kinetics of the N_2O decomposition by influencing the N_2O diffusion within the zeolite pores. The three-dimensional pore structure and large pore size of Co/BEA appeared particularly beneficial among the investigated zeolites, leading to the N_2O conversion $X > 90\%$ at 400 °C. The worst activity of Co/SSZ-13 ($X < 10\%$) is attributed to the blocking of the small-sized pores due to the presence of segregated cobalt oxide entities, which are inactive. The significant influence of the framework topology on N_2O decomposition was also observed for Fe/Zeolites (Fig. 43d1). Yet the pore size effect is less pronounced in this case (Fe/ZSM-5 $>$ Fe/BEA $>$ FeSSZ-13).[390] The dramatic differences in the activity for the Fe/FER $\gg$ Fe/BEA $>$ Fe/ZSM-5, in turn, are explained by the presence of unique two face-to-face Fe(II) cations cooperating in the efficient activation of the N_2O molecule (discussed above). Notably, in the case of copper, the reactivity decreases as Cu/ZSM-5 $>$ Cu/FER $>$ Cu/MOR (Fig. 43d2),[391] implying that the effects of the zeolite framework and the nature of the encaged zeolites are of comparable relevance, and cannot be rigorously separated.

Another parameter that controls N_2O activation is the Si/Al ratio[388] and the distribution of Al atoms in the T sites of the zeolite framework.[377,384] The dependence of TOF values for N_2O decomposition on Co/ZSM-5, Cu/ZSM-5 and Fe/ZSM-5 catalysts with various Si/Al ratios at different temperatures for M/Al = 0.5[388] is shown in Fig. 43e. Generally, for all cations, the TOF values initially increase until Si/Al $\sim$ 100–150, and then tend to decline except for Cu/ZSM-5 at $T > 475$ °C. The drop of TOF for Si/Al > 150 is particularly pronounced in the case of the Fe/ZSM-5 catalyst.

The combined effects of structural heterogeneities in both the encapsulated TMI and the zeolite frameworks (including topology, Si/Al ratio, and Al distribution) on N_2O reactivity cannot be rigorously separated. Given the mutual interrelation

of these factors, their individual control is insufficient to establish universal reactivity trends for 3d metallozeolites as a function of a selected parameter. The inaccuracies are further emphasised by different conditions of the reaction, and variances resulting from distinct catalyst preparation methods (see Fig. 1).

Conclusions and outlook

After decades of extensive research on metallozeolites and the catalytic chemistry of small molecules, remarkable developments have been made on both fundamental and applied levels. The seemingly simple activation processes occurring in metal–ligand moieties can exhibit a complex nature that can be analyzed in detail by modern computational tools, such as NOCV-ETS, with orbital resolution. For a sensible elucidation of the bonding of non-innocent molecules to transition-metal ions, multireference methods, such as CASSCF or MP2, can provide an adequate treatment of the impact of static and dynamic correlation on the electronic and magnetic structure of the resulting intrazeolite adducts, in close relation to their reactivity. Nevertheless, it is rather difficult to establish definite, universal experimental TMI structure–reactivity trends, as incoherent results have often been reported. This is primarily caused by insufficient control over the speciation of the active sites, as well as by differences in the framework topology and the Si/Al and TMI/Al ratios among the investigated catalysts of nominally the same compositions. Therefore, there is still a need for further advances in the synthesis of metallozeolite materials with atomic precision, their site-specific characterisation, and complex mechanistic studies that benefit from the synergy between modern experimental and theoretical approaches. So far, most efforts have been focused on a few TMI compounds only, being limited essentially to the Cu, Fe, or Co triad, which exhibits the best catalytic performance in many critical catalytic processes, such as SCR, SCO, or C–H bond hydroxylation. However, a deep understanding of the principles of catalytic chemistry of TMI zeolite requires broadening the scope through more comprehensive studies across the periodic table to establish general patterns of bonding, activation, and reactivity, concerning the valence, coordination, and spin states of the encaged cations. These molecular foundations can provide rational tenets for classifying reactivity patterns, optimising existing structures, and predicting new multinuclear and heteronuclear active sites with enhanced reactivity. They may contain not only TMI but also auxiliary non-redox cations (*e.g.*, Ca or Ga) with electronegativities tuned to their purpose. The biocatalysis of small molecules can further inspire the constitution of such multinuclear centres. Additionally, the integration of novel zeolite synthesis and functionalization methods that reduce reliance on poorly controlled Al distribution and minimize unintended TMI speciation is crucial. Equally important is the development of new frameworks that promote deliberately designed supramolecular interactions with reactant molecules, intermediates, and transition states. This may facilitate essential future advancements in the application of metallozeolites in the catalytic chemistry of small molecules.

Further experimental progress can be achieved by applying, for example, phase-sensitive detection to enhance the signal-to-noise ratio and time resolution, particularly in *operando* catalytic studies of metallozeolites under working conditions.[393] Insights into the dynamical processes occurring in the cages and channels can be provided, in turn, by pulsed-laser excitations, synchronised with time-resolved spectroscopic detection of the resulting molecular changes on the scale from picoseconds to milliseconds.[394] Future research into speciation of active sites can also be inspired by recent advances in TEM imaging techniques, such as iDPC-STEM (integrated differential phase contrast STEM) or ptychography, which are capable of single-atom detection located in microporous channels, proving that TMI species can be directly visualised in beam-sensitive materials such as zeolites.[395,396]

Finally, many of the topics covered in this review are also relevant to the sister MOF materials functionalized by TMI.[397] Due to their unique hybrid structure, they provide even more versatile scaffolds for intentionally tuning the TMI properties, opening new areas of catalytic chemistry where progress is chiefly needed.

Conflicts of interest

There are no conflicts of interest to declare.

List of acronyms

n-MR	*n*-Member ring
ALMO	Absolutely localized molecular orbitals
BEA	Beta framework type code
BEEF-vdW	Bayesian error estimation functional with van der Waals
BS	Broken symmetry
CAS	Complete active space
CASPT2	Complete active space with second-order perturbation theory
CASSCF	Complete active space self-consistent field
CEC	Cation exchange capacity
CC	Coupled cluster
CCSD(T)	Coupled cluster with single, double, and perturbative triple excitations
CHA	Chabazite framework type code
COHP	Crystal orbital Hamiltonian population
CT	Charge transfer
CVD	Chemical vapour deposition
DFT	Density functional theory
EDE	Dispersion interactions
EDX	Energy-dispersive X-ray spectroscopy
ENDOR	Electron nuclear double resonance
EPR	Electron paramagnetic resonance
ESEEM	Electron spin echo envelope modulation

ET	Electron transfer
ETS-NOCV	Extended-transition-state natural orbitals for chemical valence
EXAFS	Extended X-ray absorption fine structure
FAU	Faujasite framework type code
FC	Franck–Condon
FPT	First principles thermodynamics
FTIR	Fourier transform infrared spectroscopy
HC	High coverage
HC-SCR	Hydrocarbon selective catalytic reduction
HF	Hartree–Fock
HOMO	Highest occupied molecular orbital
HSAB	Hard soft acid base
HYSCORE	HYperfine sublevel CORrElation spectroscopy
iDPC-STEM	(Integrated differential phase contrast STEM)
IEL	Inverse/inverted energy levels
IZA	International zeolite association
LC	Low coverage
LMCT	Ligand-to-metal charge transfer
LUMO	Lowest unoccupied molecular orbital
MAS-NMR	Magic angle spinning nuclear magnetic resonance
MD	Molecular dynamics
MEL	Mixed energy levels
MFI	MFI zeolite framework type code
ML	Machine learning
MLET	Metal-to-ligand electron transfer
MO	Molecular orbital
MOR	Mordenite framework type code
MP	Möeller–Plesset
CN	Coordination number of TMI *e.g.* Cu_{4c}
NEL	Normal energy levels
NOCV	Natural orbitals for chemical valence
OT	Oxygen transfer
PEC	Principal electronic configuration
PES	Potential energy surface
PL	Photoluminescence
rR	Resonance Raman spectroscopy
SCO	Selective catalytic oxidation
SCR	Selective catalytic reduction
SOC	Spin–orbit coupling
SOMO	Singly occupied molecular orbital
TMI	Transition metal ion
TPD	Temperature-programmed desorption
UV-Vis	Ultraviolet-visible spectroscopy
UV-Vis-NIR	Ultraviolet-visible-near infrared spectroscopy
VB	Valence band
VB-CAS	Valence bond complete active space
VTVH-MCD	Variable-temperature, variable-field magnetic circular dichroism
XAFS	X-ray absorption fine structure
XANES	X-ray absorption near edge structure
X-band CW-EPR	X-band continuous wave electron paramagnetic resonance
ZFS	Zero-field splitting

Data availability

No primary research results, software, or code have been included, and no new data were generated or analysed as part of this review. In a few cases, parts of the compound figures were based on the data available at: **https://ruj.uj.edu.pl/entities/publication/2c6d31d7-da08-466d-987d-fcaebbe5db6a**, **https://ruj.uj.edu.pl/entities/publication/8ae5ec29-e753-4aed-b1e5-1430e36cb24d**, **https://ruj.uj.edu.pl/entities/publication/d8b1269b-f698-4e80-9051-d96caf48fb52**.

Acknowledgements

The publication has been supported by the Faculty of Chemistry and the Priority Research Area (SciMat) under the Strategic Programme Excellence Initiative at Jagiellonian University.

References

1 J. Turkevich, J. Soria and Y. Ono, *J. Catal.*, 1972, **25**, 44–54.
2 K. Klier, R. Kellerman and P. J. Hutta, *J. Chem. Phys.*, 1974, **61**, 4224–4234.
3 E. Giamello, D. Murphy, G. Magnacca, C. Morterra, Y. Shioya, T. Nomura and M. Anpo, *J. Catal.*, 1992, **136**, 510–520.
4 W. Li, Y. Chai, G. Wu and L. Li, *J. Phys. Chem. Lett.*, 2022, **13**, 11419–11429.
5 B. E. R. Snyder, M. L. Bols, R. A. Schoonheydt, B. F. Sels and E. I. Solomon, *Chem. Rev.*, 2018, **118**, 2718–2768.
6 P. Vanelderen, J. Vancauwenbergh, B. F. Sels and R. A. Schoonheydt, *Coord. Chem. Rev.*, 2013, **257**, 483–494.
7 International Zeolite Association Home Page **https://iza-online.org/**.
8 K. Klier, *Langmuir*, 1988, **4**, 13–25.
9 W. Yan, S. Xi, Y. Du, M. K. Schreyer, S. X. Tan, Y. Liu and A. Borgna, *ChemCatChem*, 2018, **10**, 3078–3085.
10 J. A. Nasir, J. Guan, T. W. Keal, Y. Lu, A. A. Sokol and C. R. A. Catlow, *J. Catal.*, 2024, **438**, 115696.
11 B. Ipek, M. J. Wulfers, H. Kim, F. Göltl, I. Hermans, J. P. Smith, K. S. Booksh, C. M. Brown and R. F. Lobo, *ACS Catal.*, 2017, **7**, 4291–4303.
12 Y. Li and J. Yu, *Nat. Rev. Mater.*, 2021, **6**, 1156–1174.
13 M. Dusselier and M. E. Davis, *Chem. Rev.*, 2018, **118**, 5265–5329.
14 J. A. Nasir, A. M. Beale and C. R. A. Catlow, *Chem. Soc. Rev.*, 2024, **53**, 11657–11691.
15 C. Paolucci, J. R. Di Iorio, W. F. Schneider and R. Gounder, *Acc. Chem. Res.*, 2020, **53**, 1881–1892.
16 Y. Xu, X. Wang, M. Qin and Q. Li, *J. Environ. Chem. Eng.*, 2022, **10**, 107270.
17 P. Pietrzyk and Z. Sojka, *Chem. Commun.*, 2007, 1930–1932.
18 M. A. Newton, A. J. Knorpp, V. L. Sushkevich, D. Palagin and J. A. van Bokhoven, *Chem. Soc. Rev.*, 2020, **49**, 1449–1486.

19 B. E. R. Snyder, M. L. Bols, H. M. Rhoda, D. Plessers, R. A. Schoonheydt, B. F. Sels and E. I. Solomon, *Science*, 2021, **373**, 327–331.
20 M. L. Bols, B. E. R. Snyder, H. M. Rhoda, P. Cnudde, G. Fayad, R. A. Schoonheydt, V. Van Speybroeck, E. I. Solomon and B. F. Sels, *Nat. Catal.*, 2021, **4**, 332–340.
21 A. Heyden, B. Peters, A. T. Bell and F. J. Kiel, *J. Phys. Chem. B*, 2005, **109**, 1857–1873.
22 W. Loewenstein, *Am. Mineral.*, 1954, **39**, 92–96.
23 P. Sazama, K. Mlekodaj, J. Dedecek, V. Pashkova, E. Tabor, P. Klein, M. Urbanova, R. Karcz, S. R. Whittleton, H. M. Thomas, A. V. Fishchuk and S. Sklenak, *J. Phys. Chem. C*, 2019, **123**, 7968–7987.
24 S. Dzwigaj and M. Che, *J. Phys. Chem. B*, 2005, **109**, 22167–22174.
25 C. Lamberti, A. Zecchina, E. Groppo and S. Bordiga, *Chem. Soc. Rev.*, 2010, **39**, 4951–5001.
26 K. Tarach, J. Sobalska, A. Held, J. Dedecek, E. Tabor and K. Góra-Marek, *J. Phys. Chem. C*, 2024, **128**, 3759–3769.
27 K. Sun, F. Fan, H. Xia, Z. Feng, W.-X. Li and C. Li, *J. Phys. Chem. C*, 2008, **112**, 16036–16041.
28 S. Dźwigaj, M. Matsuoka, R. Franck, M. Anpo and M. Che, *J. Phys. Chem. B*, 1998, **102**, 6309–6312.
29 J. Chen, W. Huang, S. Bao, W. Zhang, T. Liang, S. Zheng, L. Yi, L. Guo and X. Wu, *RSC Adv.*, 2022, **12**, 27746–27765.
30 L. Čapek, V. Kreibich, J. Dědeček, T. Grygar, B. Wichterlová, Z. Sobalík, J. A. Martens, R. Brosius and V. Tokarová, *Microporous Mesoporous Mater.*, 2005, **80**, 279–289.
31 K. Góra-Marek, A. Glanowska and J. Datka, *Microporous Mesoporous Mater.*, 2012, **158**, 162–169.
32 K. Góra-Marek, B. Gil and J. Datka, *Appl. Catal., A*, 2009, **353**, 117–122.
33 M. Fedyna, B. Mozgawa, F. Zasada, K. Góra-Marek, J. Gryboś, W. Piskorz, C. Yin, Z. Zhao, P. Pietrzyk and Z. Sojka, *Appl. Catal., B*, 2023, **325**, 122309.
34 S. Zamani, M. Chiesa, V. Meynen, Y. Xiao, B. Prelot, J. Zajac, F. Verpoort, P. Cool and S. Van Doorslaer, *J. Phys. Chem. C*, 2010, **114**, 12966–12975.
35 D. Goldfarb and K. Zukerman, *Chem. Phys. Lett.*, 1990, **171**, 167–174.
36 D. Goldfarb, *Phys. Chem. Chem. Phys.*, 2006, **8**, 2325–2343.
37 V. Lagostina, E. Salvadori, M. Chiesa and E. Giamello, *J. Catal.*, 2020, **391**, 397–403.
38 S. Bordiga, E. Groppo, G. Agostini, J. A. van Bokhoven and C. Lamberti, *Chem. Rev.*, 2013, **113**, 1736–1850.
39 S. H. van Vreeswijk and B. M. Weckhuysen, *Nat. Sci. Rev.*, 2022, **9**, nwac047.
40 A. Stępniewski, M. Radoń, K. Góra-Marek and E. Broclawik, *Phys. Chem. Chem. Phys.*, 2016, **18**, 3716–3729.
41 W. Jeevapong, J. Sittiwong, M. Probst, B. Boekfa, C. Wattanakit, T. Maihom and J. Limtrakul, *J. Phys. Chem. C*, 2023, **127**, 8473–8481.
42 J. Klimeš and D. P. Tew, *J. Chem. Phys.*, 2019, **151**, 234108.
43 A. M. Teale, T. Helgaker, A. Savin, C. Adamo, B. Aradi, A. V. Arbuznikov, P. W. Ayers, E. J. Baerends, V. Barone, P. Calaminici, E. Cancès, E. A. Carter, P. K. Chattaraj, H. Chermette, I. Ciofini, T. D. Crawford, F. De Proft, J. F. Dobson, C. Draxl, T. Frauenheim, E. Fromager, P. Fuentealba, L. Gagliardi, G. Galli, J. Gao, P. Geerlings, N. Gidopoulos, P. M. W. Gill, P. Gori-Giorgi, A. Görling, T. Gould, S. Grimme, O. Gritsenko, H. J. A. Jensen, E. R. Johnson, R. O. Jones, M. Kaupp, A. M. Köster, L. Kronik, A. I. Krylov, S. Kvaal, A. Laestadius, M. Levy, M. Lewin, S. Liu, P.-F. Loos, N. T. Maitra, F. Neese, J. P. Perdew, K. Pernal, P. Pernot, P. Piecuch, E. Rebolini, L. Reining, P. Romaniello, A. Ruzsinszky, D. R. Salahub, M. Scheffler, P. Schwerdtfeger, V. N. Staroverov, J. Sun, E. Tellgren, D. J. Tozer, S. B. Trickey, C. A. Ullrich, A. Vela, G. Vignale, T. A. Wesolowski, X. Xu and W. Yang, *Phys. Chem. Chem. Phys.*, 2022, **24**, 28700–28781.
44 A. M. Teale, P. Verma and D. G. Truhlar, *Trends Chem.*, 2020, **2**, 302–318.
45 K. D. Vogiatzis, M. V. Polynski, J. K. Kirkland, J. Townsend, A. Hashemi, C. Liu and E. A. Pidko, *Chem. Rev.*, 2019, **119**, 2453–2523.
46 S. Svelle, C. Tuma, X. Rozanska, T. Kerber and J. Sauer, *J. Am. Chem. Soc.*, 2009, **131**, 816–825.
47 F. Berger, M. Rybicki and J. Sauer, *ACS Catal.*, 2023, **13**, 2011–2024.
48 K. Sillar, A. Hofmann and J. Sauer, *J. Am. Chem. Soc.*, 2009, **131**, 4143–4150.
49 M. Radoń and K. Pierloot, *J. Phys. Chem. A*, 2008, **112**, 11824–11832.
50 M. Radoń, E. Broclawik and K. Pierloot, *J. Phys. Chem. B*, 2010, **114**, 1518–1528.
51 Q. M. Phung, H. N. Nam and A. Ghosh, *Inorg. Chem.*, 2023, **62**, 20496–20505.
52 S. Vancoillie, H. Zhao, M. Radoń and K. Pierloot, *J. Chem. Theory Comput.*, 2010, **6**, 576–582.
53 M. Radoń, G. Drabik, M. Hodorowicz and J. Szklarzewicz, *Chem. Sci.*, 2024, **15**, 20189.
54 R. K. Carlson, S. O. Odoh, S. J. Tereniak, C. C. Lu and L. Gagliardi, *J. Chem. Theory Comput.*, 2015, **11**, 4093–4101.
55 D. A. Pantazis, *J. Chem. Theory Comput.*, 2019, **15**, 938–948.
56 Z. A. Alaithan, N. Harrison and G. Sastre, *J. Phys. Chem. C*, 2021, **125**, 19200–19208.
57 C. J. Heard, L. Grajciar and A. Erlebach, *Nanoscale*, 2024, **16**, 8108–8118.
58 A. J. Porter and A. J. O'Malley, *J. Phys. Chem. C*, 2021, **125**, 11567–11579.
59 V. Van Speybroeck, M. Bocus, P. Cnudde and L. Vanduyfhuys, *ACS Catal.*, 2023, **13**, 11455–11493.
60 G. Wang, C. Zhi, Y. Wang and Q. Wang, *Comput. Theor. Chem.*, 2023, **1227**, 114228.
61 D. J. Hutton, D. H. Lopez and F. Göltl, *React. Chem. Eng.*, 2024, **9**, 1685–1695.
62 M. P. Mitoraj, A. Michalak and T. Ziegler, *J. Chem. Theory Comput.*, 2009, **5**, 962–975.
63 P. Kozyra, M. Świętek, J. Datka and E. Brocławik, *J. Comput. Chem., Jpn.*, 2013, **12**, 30–37.
64 P. Pietrzyk, K. Podolska, T. Mazur and Z. Sojka, *J. Am. Chem. Soc.*, 2011, **133**, 19931–19943.

65 V. L. Deringer, A. L. Tchougreeff and R. Dronskowski, *J. Phys. Chem. A*, 2011, **115**, 5461–5466.
66 C. Liu, I. Tranca, R. A. van Santen, E. J. M. Hensen and E. A. Pidko, *J. Phys. Chem. C*, 2017, **121**, 23520–23530.
67 X. Li, H. Han, N. Evangelou, N. J. Wichrowski, P. Lu, W. Xu, S. J. Hwang, W. Zhao, C. Song, X. Guo, A. Bhan, I. G. Kevrekidis and M. Tsapatsis, *Nat. Commun.*, 2023, **14**, 3152.
68 S. Ma and Z. P. Liu, *Chem. Sci.*, 2022, **13**, 5055–5068.
69 D. Plessers, M. L. Bols, H. M. Rhoda, A. J. Heyer, E. I. Solomon, B. F. Sels and R. A. Schoonheydt, *Comprehensive Inorganic Chemistry III*, 3rd edn, 2023, pp. 148–164.
70 Q. Zhang, S. Gao and J. Yu, *Chem. Rev.*, 2023, **123**, 6039–6106.
71 N. Kosinov, C. Liu, E. J. M. Hensen and E. A. Pidko, *Chem. Mater.*, 2018, **30**, 3177–3198.
72 H. M. Rhoda, A. J. Heyer, B. E. R. Snyder, D. Plessers, M. L. Bols, R. A. Schoonheydt, B. F. Sels and E. I. Solomon, *Chem. Rev.*, 2022, **122**, 12207–12243.
73 Y. Wu, P. Deng, L. Liu, J. Zhang, H. Liu, X. Gao, F.-S. Xiao and L. Wang, *Chem. Soc. Rev.*, 2025, **54**, 4745–4762.
74 Y. Li, L. Li and J. Yu, *Chem*, 2017, **3**, 928–949.
75 J. Pérez-Ramírez, C. H. Christensen, K. Egeblad, C. H. Christensen and J. C. Groen, *Chem. Soc. Rev.*, 2008, **37**, 2530–2542.
76 C. Chizallet, C. Bouchy, K. Larmier and G. Pirngruber, *Chem. Rev.*, 2023, **123**, 6107–6196.
77 C. Cheng, P. Li, X. Yang and R. T. Yang, *Catal. Sci. Technol.*, 2016, **6**, 7561–7568.
78 E. Morra, G. Berlier, E. Borfecchia, S. Bordiga, P. Beato and M. Chiesa, *J. Phys. Chem. C*, 2017, **121**, 14238–14245.
79 K. A. Chalupka, W. K. Jozwiak, J. Rynkowski, W. Maniukiewicz, S. Casale and S. Dzwigaj, *Appl. Catal., B*, 2014, **146**, 227–236.
80 P. Pietrzyk, K. Podolska-Serafin, K. Góra-Marek, A. Krasowska and Z. Sojka, *Microporous Mesoporous Mater.*, 2020, **291**, 109692.
81 T. Yu, Y. Su, A. Wang, B. M. Weckhuysen and W. Luo, *ChemCatChem*, 2021, **13**, 2766–2770.
82 P. J. Smeets, J. S. Woertink, B. F. Sels, E. I. Solomon and R. A. Schoonheydt, *Inorg. Chem.*, 2010, **49**, 3573–3583.
83 B. Mozgawa, Copper active sites in chabazite–type zeolites in reactions of selective catalytic reduction of NOx with ammonia – insight into structure and reactivity using spectroscopic methods and DFT modelling, *PhD thesis*, Jagiellonian University, 2024.
84 J. E. Olszowka, M. Lemishka, K. Mlekodaj, P. Kubat, D. Rutkowska-Żbik, J. Dedecek and E. Tabor, *J. Phys. Chem. C*, 2021, **125**, 9060–9073.
85 Z. Sobalik, Z. Tvaruzkova and B. Wichterlova, *Microporous Mesoporous Mater.*, 1998, **25**, 225–228.
86 E. Broclawik, J. Datka, B. Gil and P. Kozyra, *Phys. Chem. Chem. Phys.*, 2000, **2**, 401–405.
87 M. Lemishka, J. Dedecek, K. Mlekodaj, Z. Sobalik, S. Sklenak and E. Tabor, *Pure Appl. Chem.*, 2019, **91**, 1721–1732.
88 Y. Jangjou, Q. Do, Y. Gu, L.-G. Lim, H. Sun, D. Wang, A. Kumar, J. Li, L. C. Grabow and W. S. Epling, *ACS Catal.*, 2018, **8**, 1325–1337.
89 B. Wichterlova, J. Dedecek and Z. Sobalik, Single Metal Ions in Host Zeolite Matrices: Structure-Activity-Selectivity-Relationships, in *Catalysis by Unique Metal Ion Structures in Solid Matrices*, ed. G. Centi, B. Wichterlova and A. T. Bell, 2001, pp. 31–53.
90 S. Sklenak, P. C. Andrikopoulos, B. Boekfa, B. Jansang, J. Nováková, L. Benco, T. Bucko, J. Hafner, J. Dedecek and Z. Sobalík, *J. Catal.*, 2010, **272**, 262–274.
91 P. J. Carl and S. C. Larsen, *J. Phys. Chem. B*, 2000, **104**, 6568–6575.
92 A. Godiksen, P. N. R. Vennestrøm, S. B. Rasmussen and S. Mossin, *Top. Catal.*, 2017, **60**, 13–29.
93 R. P. Vélez, U. Bentrup, W. Grünert and A. Brückner, *Top. Catal.*, 2017, **60**, 1641–1652.
94 Z. Sojka, *Catal. Rev.*, 1995, **37**, 461–512.
95 P. C. Bruzzese, E. Salvadori, S. Jäger, M. Hartman, B. Civalleri, A. Pöppl and M. Chiesa, *Nat. Commun.*, 2021, **12**, 4638.
96 V. Nagarajan, D. Rings, L. Moschkowitz, M. Hartmann and A. Pöppl, *Chem. Lett.*, 2005, **34**, 1614–1615.
97 E. Marceau, L. Bonneviot, S. Dzwigaj, J.-F. Lambert, C. Louis and X. Carrier, *J. Catal.*, 2021, **396**, 104–121.
98 J. A. Weil, J. R. Bolton and J. E. Wertz, *Electron Paramagnetic Resonance Elementary theory and Practical Applications*, Wiley, NY, 1994.
99 F. E. Mabbs and D. Collison, *Electron Resonance of d Transition Metal Compounds*, Elsevier, Amsterdam, 1992.
100 F. Giordanino, P. N. R. Vennestrøm, L. F. Lundegaard, F. N. Stappen, S. Mossin, P. Beato, S. Bordiga and C. Lamberti, *Dalton Trans.*, 2013, **42**, 12741–12761.
101 P. Rieger, *Coord. Chem. Rev.*, 1994, **135/136**, 203–286.
102 F. E. Mabbs and D. Collison, *Electron Resonance of d Transition Metal Compounds*, Elsevier, Amsterdam, 1992.
103 V. Ovchinnikov and V. N. Konstantinov, *J. Magn. Reson.*, 1979, **32**, 179.
104 J. C. Conesa and J. Soria, *J. Phys. Chem.*, 1978, **82**, 1575–1578.
105 A. Tuel, J. Diab, P. Gelin, M. Dufaux, J.-F. Dutel and Y. B. Taarit, *J. Mol. Catal.*, 1990, **63**, 95–102.
106 J. Peisach and W. E. Blumberg, *Arch. Biochem. Biophys.*, 1974, **165**, 691–708.
107 P. J. Carl and S. C. Larsen, *J. Catal.*, 1999, **182**, 208–218.
108 E. Morra, E. Giamello and M. Chiesa, *Chem. – Eur. J.*, 2014, **20**, 7381–7388.
109 A. Tuel, J. Diab, P. Gelin, M. Dufaux, J.-F. Dutel and Y. B. Taarit, *J. Mol. Catal.*, 1990, **63**, 95–102.
110 P. Pietrzyk, Z. Sojka, S. Dźwigaj and M. Che, *J. Am. Chem. Soc.*, 2007, **129**, 14174–14175.
111 B. M. Weckhuysen and R. A. Schoonheydt, *Stud. Surf. Sci. Catal.*, 1994, **84**, 965–972.
112 A. M. Volodin, G. M. Zhidomirov, K. A. Dubkov, E. J. M. Hensen and R. A. van Santen, *Catal. Today*, 2005, **110**, 247–254.

113 E.-M. El-Malki, D. Werst, P. E. Doan and W. M. H. Sachtler, *J. Phys. Chem. B*, 2000, **104**, 5924–5931.
114 K. Podolska-Serafin and P. Pietrzyk, *J. Mol. Struct.*, 2019, **1180**, 754–763.
115 E. Fernández, M. Moreno-González, M. Moliner, T. Blasco, M. Boronat and A. Corma, *Top. Catal.*, 2018, **61**, 810–832.
116 3w?>P. C. Bruzzese, E. Salvadori, B. Civalleri, S. Jäger, M. Hartmann, A. Pöppl and M. Chiesa, *J. Am. Chem. Soc.*, 2022, **144**, 13079–13083.
117 E. Morra, M. Signorile, E. Salvadori, S. Bordiga, E. Giamello and M. Chiesa, *Angew. Chem., Int. Ed.*, 2019, **58**, 12398–12403.
118 P. Rzepka, T. Huthwelker, J. Dědeček, E. Tabor, M. Bernauer, S. Sklenák, K. Mlekodaj and J. A. van Bokhoven, *Science*, 2025, **388**, 423–428.
119 J. Krzystek, A. Ozarowski and J. Telser, *Coord. Chem. Rev.*, 2006, **250**, 2308–2324.
120 B. M. Weckhuysen, A. A. Verberckmoes, M. G. Uytterhoeven, F. E. Mabbs, D. Collison, E. de Boer and R. A. Schoonheydt, *J. Phys. Chem. B*, 2000, **104**, 37–42.
121 A. Peng, M. C. Kung, M. O. Ross, B. M. Hofman and H. H. Kung, *Top. Catal.*, 2020, **63**, 1708–1716.
122 S. A. Bonke, T. Risse, A. Schnegg and A. Brückner, *Nat. Rev. Methods Primers*, 2021, **1**, 33.
123 R. Baran, L. Valentin and S. Dźwigaj, *Phys. Chem. Chem. Phys.*, 2016, **18**, 12050.
124 D. E. De Vos, B. M. Weckhuysen and T. Bein, *J. Am. Chem. Soc.*, 1996, **118**, 9615–9622.
125 J. Livage, *Materials*, 2010, **3**, 4175–4195.
126 J. Grand, S. N. Talapaneni, A. Vicente, C. Fernandez, E. Dib, H. A. Aleksandrov, G. N. Vayssilov, R. Retoux, P. Boullay, J. P. Gilson, V. Valtchev and S. Mintova, *Nat. Mater.*, 2017, **16**, 1010–1015.
127 D. Zhou, Y. Zhang, H. Zhu, D. Ma and X. Bao, *J. Phys. Chem. C*, 2007, **111**, 2081–2091.
128 S. Wannakao, B. Boekfa, P. Khongpracha, M. Probst and J. Limtrakul, *ChemPhysChem*, 2010, **11**, 3432–3438.
129 M. F. Fellah and I. Onal, *Phys. Chem. Chem. Phys.*, 2013, **15**, 13969–13997.
130 S. Dźwigaj, M. Matsuoka, M. Anpo and M. Che, *J. Phys. Chem. B*, 2000, **104**, 6012–6020.
131 B. E. R. Snyder, L. H. Böttger, M. L. Bols, J. J. Yan, H. M. Rhod, A. B. Jacobs, M. Y. Hu, J. Zhao, E. E. Alp, B. Hedman, K. O. Hodgson, R. A. Schoonheydt, B. F. Sels and E. I. Solomon, *Proc. Natl. Acad. Sci. U. S. A.*, 2018, **115**, 4565–4570.
132 J. B. Lim, S. H. Cha and S. B. Hong, *Appl. Catal., B*, 2019, **243**, 750–759.
133 M. H. Mahyuddin, Y. Shiota, A. Staykov and K. Yoshizawa, *Inorg. Chem.*, 2017, **56**, 10370–10380.
134 A. Oda, T. Ohkubo, T. Yumura, H. Kobayashi and Y. Kuroda, *Inorg. Chem.*, 2019, **58**, 327–338.
135 B. E. R. Snyder, P. Vanelderen, M. L. Bols, S. D. Hallaert, L. H. Böttger, L. Ungur, K. Pierloot, R. A. Schoonheydt, B. F. Sels and E. I. Solomon, *Nature*, 2016, **536**, 317–321.
136 S. Ye and F. Neese, *Proc. Natl. Acad. Sci. U. S. A.*, 2011, **108**, 1228–1233.
137 Y. Shimoyama and T. Kojima, *Inorg. Chem.*, 2019, **58**, 9517–9542.
138 F. Tielens and S. Dźwigaj, *Catal. Today*, 2010, **152**, 66–69.
139 M. Matsuoka, S. Higashimoto, H. Yamashita and M. Anpo, *Res. Chem. Intermed.*, 2000, **26**, 85–92.
140 M. Anpo, T.-H. Kim and M. Matsuoka, *Catal. Today*, 2009, **142**, 114–124.
141 S. Higashimoto, M. Matsuoka, H. Yamashita, M. Anpo, O. Kitao, H. Hidaka, M. Che and E. Giamello, *J. Phys. Chem. B*, 2000, **104**, 10288–10292.
142 H. S. Lacheen and E. Iglesia, *J. Phys. Chem. B*, 2006, **110**, 5462–5472.
143 M. Smoliło-Utrata, K. A. Tarach, K. Samson, M. Gackowski, E. Madej, J. Korecki, G. Mordarski, M. Śliwa, S. Jarczewski, J. Podobinski, P. Kuśtrowski, J. Datka, D. Rutkowska-Żbik and K. Góra-Marek, *Int. J. Mol. Sci.*, 2022, **23**, 5584.
144 M. H. Mahyuddin, A. Staykov, Y. Shiota and K. Yoshizawa, *ACS Catal.*, 2016, **6**, 8321–8331.
145 N. Liu, R. Zhang, B. Chen, Y. Li and Y. Li, *J. Catal.*, 2012, **294**, 99–112.
146 J. Gao, Y. Zheng, Y. Tang, J.-M. Jehng, R. Gryboś, J. Handzlik, I. E. Wachs and S. G. Podkolzin, *ACS Catal.*, 2015, **5**, 3078–3092.
147 M. L. Bols, S. D. Hallaert, B. E. R. Snyder, J. Devos, D. Plessers, H. M. Rhoda, M. Dusselier, R. A. Schoonheydt, K. Pierloot, E. I. Solomon and B. F. Sels, *J. Am. Chem. Soc.*, 2018, **140**, 12021–12032.
148 K. Mlekodaj, M. Lemishka, S. Sklenak, J. Dědeček and E. Tabor, *Chem. Commun.*, 2021, **57**, 3472–3475.
149 J. Wang, G. Li, X. Ju, H. Xia, F. Fan, J. Wang, Z. Feng and C. Li, *J. Catal.*, 2013, **301**, 77–82.
150 D. T. Bregante, L. N. Wilcox, C. Liu, C. Paolucci, R. Gounder and D. W. Flaherty, *ACS Catal.*, 2021, **11**, 11873–11884.
151 T. Ikuno, S. Grundner, A. Jentys, G. Li, E. Pidko, J. Fulton, M. Sanchez-Sanchez and J. A. Lercher, *J. Phys. Chem. C*, 2019, **123**, 8759–8769.
152 I. Kurzydym and I. Czekaj, *Molecules*, 2022, **27**, 300.
153 G. Wang, L. Huang, W. Chen, J. Zhou and A. Zheng, *Phys. Chem. Chem. Phys.*, 2018, **20**, 26522.
154 G. Li, E. A. Pidko, R. A. van Santen, C. Li and E. J. M. Hensen, *J. Phys. Chem. C*, 2013, **117**, 413–426.
155 M. H. Mahyuddin and K. Yoshizawa, *Catal. Sci. Technol.*, 2018, **8**, 5875–5885.
156 P. Pietrzyk, K. Góra-Marek, T. Mazur, B. Mozgawa, M. Radoń, M. Chiesa, Z. Zhao and Z. Sojka, *J. Catal.*, 2021, **394**, 206–219.
157 P. Pietrzyk, C. Dujardin, K. Góra-Marek, P. Granger and Z. Sojka, *Phys. Chem. Chem. Phys.*, 2012, **14**, 2203–2215.
158 D. W. Fickel and R. F. Lobo, *J. Phys. Chem. C*, 2010, **114**, 1633–1640.
159 A. R. Kulkarni, Z. J. Zhao, S. Siahrostami, J. K. Nørskov and F. Studt, *ACS Catal.*, 2016, **6**, 6531–6536.
160 G. D. Pirngruber, P. K. Roy and R. Prins, *Phys. Chem. Chem. Phys.*, 2006, **8**, 3939–3950.
161 A. J. Heyer, D. Plessers, J. Ma, B. E. R. Snyder, R. A. Schoonheydt, B. F. Sels and E. I. Solomon, *J. Am. Chem. Soc.*, 2024, **146**, 6061–6071.

162 L. Noodleman and E. J. Baerends, *J. Am. Chem. Soc.*, 1984, **106**, 2316–2327.
163 T. Soda, Y. Kitagawa, T. Onishi, Y. Takano, Y. Shigeta, H. Nagao, Y. Yoshioka and K. Yamaguchi, *Chem. Phys. Lett.*, 2000, **319**, 223–230.
164 N. Hansen, A. Heyden, A. T. Bell and F. J. Keil, *J. Phys. Chem. C*, 2007, **111**, 2092–2101, DOI: **10.1021/jp065574q**.
165 S. Li, Y. Wang, T. Wu and W. F. Schneider, *ACS Catal.*, 2018, **8**, 10119–10130.
166 G. Li and E. A. Pidko, *ChemCatChem*, 2019, **11**, 134–156.
167 C. Liu, G. Li, E. J. M. Hensen and E. A. Pidko, *ACS Catal.*, 2015, **5**, 7024–7033.
168 G. Li, E. A. Pidko, R. A. van Santen, C. Li and E. J. M. Hensen, *J. Phys. Chem. C*, 2013, **117**, 413–426.
169 L. Grajciar, C. J. Heard, A. A. Bondarenko, M. V. Polynski, J. Meeprasert, E. A. Pidko and P. Nachtigall, *Chem. Soc. Rev.*, 2018, **47**, 8307–8348.
170 K. Reuter and M. Scheffler, *Phys. Rev. B:Condens. Matter Mater. Phys.*, 2002, **65**, 035406.
171 K. Reuter and M. Scheffler, *Phys. Rev. Lett.*, 2003, **90**, 046103.
172 B. Mozgawa, F. Zasada, M. Fedyna, K. Góra-Marek, C. Yin, Z. Zhao, Z. Sojka and P. Pietrzyk, *ACS Catal.*, 2025, **15**(4), 2715–2734.
173 A. D. Becke, *J. Chem. Phys.*, 1993, **98**, 5648–5652.
174 C. Adamo and V. Barone, *J. Chem. Phys.*, 1999, **110**, 6158–6170.
175 S. Grimme, *Wiley Interdiscip. Rev.:Comput. Mol. Sci.*, 2011, **1**, 211–228.
176 K. E. Riley, M. Pitoňák, P. Jurečka and P. Hobza, *Chem. Rev.*, 2010, **110**, 5023–5063.
177 F. Göltl, A. Grüneis, T. Bučko and J. Hafner, *J. Chem. Phys.*, 2012, **137**, 114111.
178 T. Kerber, M. Sierka and J. Sauer, *J. Comput. Chem.*, 2008, **29**, 2088–2097.
179 L. Chen, T. V. W. Janssens and H. Grönbeck, *Phys. Chem. Chem. Phys.*, 2019, **21**, 10923–10930.
180 M. Fischer, *Z. Kristallogr. – Cryst. Mater.*, 2015, **230**, 325–336.
181 K. Stanciakova, J. N. Louwen, B. M. Weckhuysen, R. E. Bulo and F. Göltl, *J. Phys. Chem. C*, 2021, **125**, 20261–20274.
182 T. Hirano, in *MOPAC Manual*, ed. J. P. Stewart, 7th edn, 1993.
183 J. A. Greathouse, M. J. Paul, G. Xu and M. D. Powell, *Clays Clay Miner.*, 2023, **71**, 54–73.
184 G. Pireddu, F. G. Pazzona, P. Demontis and M. A. Załuska-Kotur, *J. Chem. Theory Comput.*, 2019, **15**, 6931–6943.
185 G. Piccini and J. Sauer, *J. Chem. Theory Comput.*, 2014, **10**, 2479–2487.
186 M. L. Bols, J. Devos, H. M. Rhoda, D. Plessers, E. I. Solomon, R. A. Schoonheydt, B. F. Sels and M. Dusselier, *J. Am. Chem. Soc.*, 2021, **143**, 16243–16255.
187 R. Zhang, E. Anderst, K. Groden and J.-S. McEwen, *Ind. Eng. Chem. Res.*, 2018, **57**, 13396–13405.
188 C. Paolucci, A. A. Parekh, I. Khurana, J. R. Di Iorio, H. Li, J. D. Albarracin Caballero, A. J. Shih, T. Anggara, W. N. Delgass, J. T. Miller, F. H. Ribeiro, R. Gounder and W. F. Schneider, *J. Am. Chem. Soc.*, 2016, **138**, 6028–6048.
189 R. Garten, W. Delgass and M. Boudart, *J. Catal.*, 1970, **18**, 90–107.
190 J. Pérez-Ramírez, G. Mul, F. Kapteijn, J. Moulijn, A. Overweg, A. Doménech, A. Ribera and I. Arends, *J. Catal.*, 2002, **207**, 113–126.
191 G. Li, P. Vassilev, M. Sanchez-Sanchez, J. A. Lercher, E. J. M. Hensen and E. A. Pidko, *J. Catal.*, 2016, **338**, 305–312.
192 E. A. Pidko, E. J. M. Hensen and R. A. van Santen, *Proc. R. Soc. London, Ser. A*, 2012, **468**, 2070–2086.
193 E. A. Pidko, E. J. M. Hensen, G. M. Zhidomirov and R. A. van Santen, *J. Catal.*, 2008, **255**, 139–143.
194 E. A. Pidko, R. A. van Santen and E. J. M. Hensen, *Phys. Chem. Chem. Phys.*, 2009, **11**, 2893–2902.
195 S. Wang, C. Li, C. Liu and W. Zhuang, *ChemCatChem*, 2025, **17**, e202401416.
196 S. A. Bates, A. A. Verma, C. Paolucci, A. A. Parekh, T. Anggara, A. Yezerets, W. F. Schneider, J. T. Miller, W. N. Delgass and F. H. Ribeiro, *J. Catal.*, 2014, **312**, 87–97.
197 B. R. Goodman, K. C. Hass, W. F. Schneider and J. B. Adams, *Catal. Lett.*, 2000, **68**, 85–93.
198 R. J. Deeth, *Phys. Chem. Chem. Phys.*, 2024, **26**, 18138–18148.
199 R. Zhang, N. Liu, Z. Lei and B. Chen, *Chem. Rev.*, 2016, **116**, 3658–3721.
200 V. Lyaskovskyy and B. de Bruin, *ACS Catal.*, 2012, **2**, 270–279.
201 M. Mitoraj and A. Michalak, *J. Mol. Model.*, 2007, **13**, 347–355.
202 A. Michalak, M. Mitoraj and T. Ziegler, *J. Phys. Chem. A*, 2008, **112**, 1933–1939.
203 P. Kozyra, E. Broclawik, M. P. Mitoraj and J. Datka, *J. Phys. Chem. C*, 2013, **117**, 7511–7518.
204 F. Sagan and M. P. Mitoraj, Non-covalent interactions in selected transition metal complexes. in *Transition Metals in Coordination Environments: Computational Chemistry and Catalysis Viewpoints*, ed. E. Broclawik, T. Borowski and M. Radoń, Springer International Publishing, Cham, Switzerland, 2019, pp. 65–89.
205 M. P. Mitoraj, F. Sagan, D. W. Szczepanik, J. H. de Lange, A. L. Ptaszek, D. M. E. van Niekerk and I. Cukrowski, *ChemPhysChem*, 2020, **21**, 494–502.
206 *Metal-Ligand Interactions: From Atoms, to Clusters, to Surfaces*, ed. D. R. Salahub and N. Russo, Springer, Dordrecht, 1990.
207 B. Zouchoune and A. Saiad, *Inorg. Chim. Acta*, 2018, **473**, 204–215.
208 Y. Jing, J. Liu, Z. Ye, J. Su, Y. Liu and Z. Ke, *Catal. Sci. Technol.*, 2021, **11**, 7189–7199.
209 Y. Gu, Q. Zhu, Z. Liu, C. Fu, J. Wu, Q. Zhu, Q. Jia and J. Ma, *J. Mater. Chem. A*, 2022, **10**, 14976–14988.
210 A. Delabie, K. Pierloot, M. H. Groothaert, B. M. Weckhuysen and R. A. Schoonheydt, *Microporous Mesoporous Mater.*, 2000, **37**, 209–222.

211 H. Petitjean, C. Chizallet and D. Berthomieu, *Ind. Eng. Chem. Res.*, 2018, **57**, 15982–15990.
212 P. Sazama, J. Moravkova, S. Sklenak, A. Vondrova, E. Tabor, G. Sadovska and R. Pilar, *ACS Catal.*, 2020, **10**, 3984–4002.
213 Y. Mao, H.-F. Wang and P. Hu, *Int. J. Quantum Chem.*, 2015, **115**, 618–630.
214 T. V. W. Janssens, H. Falsig, L. F. Lundegaard, P. N. R. Vennestrøm, S. B. Rasmussen, P. Georg Moses, F. Giordanino, E. Borfecchia, K. A. Lomachenko, C. Lamberti, S. Bordiga, A. Godiksen, S. Mossin and P. Beato, *ACS Catal.*, 2015, **5**, 2832–2845.
215 C.-Y. Sung, S. Al Hashimi, A. McCormick, M. Cococcioni and M. Tsapatsis, *Microporous Mesoporous Mater.*, 2013, **172**, 7–12.
216 R. Z. Khaliullin, A. T. Bell and M. Head-Gordon, *J. Chem. Phys.*, 2008, **128**, 184112.
217 R. Z. Khaliullin, E. A. Cobar, R. C. Lochan, A. T. Bell and M. Head-Gordon, *J. Phys. Chem. A*, 2007, **111**, 8753–8765.
218 A. Daouli, E. P. Hessou, H. Monnier, M.-A. Dziurla, A. Hasnaoui, G. Maurin and M. Badawi, *Phys. Chem. Chem. Phys.*, 2022, **24**, 15565–15578.
219 L. Benco and D. Tunega, *Phys. Chem. Miner.*, 2009, **36**, 281–290.
220 F. Gao, D. Mei, Y. Wang, J. Szanyi and C. H. Peden, *J. Am. Chem. Soc.*, 2017, **139**, 4935–4942.
221 L. N. Wilcox, S. H. Krishna, C. B. Jones and R. Gounder, *Catal. Sci. Technol.*, 2021, **11**, 7932–7942.
222 M. Colombo, G. Koltsakis, I. Nova and E. Tronconi, *Catal. Today*, 2012, **188**, 42–52.
223 F. Giordanino, E. Borfecchia, K. A. Lomachenko, A. Lazzarini, G. Agostini, E. Gallo, A. V. Soldatov, P. Beato, S. Bordiga and C. Lamberti, *J. Phys. Chem. Lett.*, 2014, **5**, 1552–1559.
224 I. Lezcano-Gonzalez, U. Deka, B. Arstad, A. Van Yperen-De Deyne, K. Hemelsoet, M. Waroquier, V. Van Speybroeck, B. M. Weckhuysen and A. M. Beale, *Phys. Chem. Chem. Phys.*, 2014, **16**, 1639–1650.
225 L. Chen, T. V. W. Janssens, M. Skoglundh and H. Grönbeck, *Top. Catal.*, 2019, **62**, 93–99.
226 K. Leistner, K. Xie, A. Kumar, K. Kamasamudram and L. Olsson, *Catal. Lett.*, 2017, **147**, 1882–1890.
227 B. Mozgawa, F. Zasada, M. Fedyna, K. Góra-Marek, E. Tabor, K. Mlekodaj, J. Dědeček, Z. Zhao, P. Pietrzyk and Z. Sojka, *Chem. Soc. Rev.*, 2021, **50**, 17159–17180.
228 C. Paolucci, I. Khurana, A. A. Parekh, S. Li, A. J. Shih, H. Li, J. R. Di Iorio, J. D. Albarracin-Caballero, A. Yezerets and J. T. Miller, *Science*, 2017, **357**, 898–903.
229 R. Millan, P. Cnudde, V. Van Speybroeck and M. Boronat, *JACS Au*, 2021, **1**, 1778–1787.
230 R. Millan, E. Bello-Jurado, M. Moliner, M. Boronat and R. Gomez-Bombarelli, *ACS Cent. Sci.*, 2023, **9**, 2044–2056.
231 Y. Fu, W. Ding, H. Lei, Y. Sun, J. Du, Y. Yu, U. Simon, P. Chen, Y. Shan, G. He and H. He, *J. Am. Chem. Soc.*, 2024, **146**, 11141–11151.
232 A. Martini, C. Negri, L. Bugarin, G. Deplano, R. K. Abasabadi, K. A. Lomachenko, T. V. W. Janssens, S. Bordiga, G. Berlier and E. Borfecchia, *J. Phys. Chem. Lett.*, 2022, **13**, 6164–6170.
233 A. Daouli, J. Rey, E. H. Lahrar, V. Valtchev, M. Badawi and R. Guillet-Nicolas, *Langmuir*, 2023, **39**, 15962–15973.
234 V. Zdravkova, M. Mihaylov and K. Hadjiivanov, *J. Phys. Chem. C*, 2012, **116**, 12706–12711.
235 A. Itadani, M. Tanaka, T. Mori, M. Nagao, H. Kobayashi and Y. Kuroda, *J. Phys. Chem. C*, 2007, **111**, 12011–12023.
236 G. Spoto, S. Bordiga, G. Ricchiardi, D. Scarano, A. Zecchina and F. Geobaldo, *J. Chem. Soc., Faraday Trans.*, 1995, **91**, 3285–3290.
237 Y. Kuroda, Y. Yoshikawa, S.-I. Konno, H. Hamano, H. Maeda, R. Kumashiro and M. Nagao, *J. Phys. Chem.*, 1995, **99**, 10621–10628.
238 J. Datka, P. Kozyra, E. Kukulska-Zając, M. Szutiak and N. Kumar, *Stud. Surf. Sci. Catal.*, 2004, **154B**, 1655–1660.
239 A. I. Serykh and M. D. Amiridis, *J. Phys. Chem. C*, 2007, **111**, 17020–17024.
240 S. Morpurgo, G. Moretti and M. Bossa, *Phys. Chem. Chem. Phys.*, 2007, **9**, 417–424.
241 V. Zdravkova, N. Drenchev, E. Ivanova, M. Mihaylov and K. Hadjiivanov, *J. Phys. Chem. C*, 2015, **119**, 15292–15302.
242 G. Frenking, I. Fernández, N. Holzmann, S. Pan, I. Krossing and M. Zhou, *JACS Au*, 2021, **1**, 623–645.
243 E. Mansoor, J. Van der Mynsbrugge, M. Head-Gordon and A. T. Bell, *Catal. Today*, 2018, **312**, 51–65.
244 G. Deplano, M. Signorile, C. Atzori, D. de Salusso, E. Borfecchia, V. Crocella and S. Bordiga, *Catal. Today*, 2024, **427**, 114403.
245 F. A. Cotton and G. Wilkinson, *Advanced Inorganic Chemistry*, Wiley, New York, 1980.
246 K. Podolska, Interaction of nickel ions in zeolites with small molecules: spectroscopic investigations and molecular modeling, *PhD thesis*, Jagiellonian University, 2011.
247 P. Pietrzyk, K. Podolska and Z. Sojka, *J. Phys. Chem. C*, 2011, **115**, 13008–13015.
248 P. Pietrzyk, T. Mazur, K. Podolska-Serafin, M. Chiesa and Z. Sojka, *J. Am. Chem. Soc.*, 2013, **135**, 15467–15478.
249 K. Hadjiivanov, H. Knozinger and M. Mihaylov, *J. Phys. Chem. B*, 2002, **106**, 2618–2624.
250 M. Mihaylov, O. Lagunov, E. Ivanova and K. Hadjiivanov, *Top. Catal.*, 2011, **54**, 308–317.
251 P. Pietrzyk, K. Podolska and Z. Sojka, *J. Phys. Chem. A*, 2008, **112**, 12208–12219.
252 L. Bonnevoit, D. Olivier and M. Che, *J. Mol. Catal.*, 1983, **21**, 415.
253 K. Dyrek and M. Che, *Chem. Rev.*, 1997, **97**, 305.
254 M. Che, *Stud. Surf. Sci. Catal.*, 1993, **75**, 31–68.
255 D. Oliver, M. Richard and M. Che, *Chem. Phys. Lett.*, 1978, **60**, 77–80.
256 K. I. Hadjiivanov and G. N. Vayssilov, *Adv. Catal.*, 2002, **47**, 307–511.
257 S. Bordiga, C. Lamberti, F. Bonino, A. Travert and F. Thibault-Starzyk, *Chem. Soc. Rev.*, 2015, **44**, 7262–7341.
258 X. Deng, D. Yang, W. Li, Y. Chai, G. Wu and L. Li, *Trends Chem.*, 2023, **5**, 892–905.
259 G. Busca, V. Lorenzelli and V. Sanchez-Escribano, *Chem. Mater.*, 1992, **4**, 595.

260 K. Góra-Marek, A. E. Palomares, A. Glanowska, K. Sadowska and J. Datka, *Microporous Mesoporous Mater.*, 2012, **162**, 175–180.
261 I. Malpartida, E. Ivanova, M. Mihaylov, K. Hadjiivanov, V. Blasin-Aubé, O. Marie and M. Daturi, *Catal. Today*, 2010, **149**, 295–303.
262 K. Góra-Marek, K. Brylewska, K. A. Tarach and M. Choi, *Dalton Trans.*, 2015, **44**, 8031–8040.
263 M. I. Shilina, T. N. Rostovshchikova, S. A. Nikolaev and O. V. Udalova, *Mater. Chem. Phys.*, 2019, **223**, 287–298.
264 S. M. Maier, A. Jentys, E. Metwalli, P. Müller-Buschbaum and J. A. Lercher, *J. Phys. Chem. Lett.*, 2011, **2**, 950–955.
265 E. Ivanova, M. Mihaylov, K. Hadjiivanov, V. Blasin-Aubé, O. Marie, A. Plesniar and M. Daturi, *Appl. Catal., B*, 2010, **93**, 325–338.
266 S. S. Goryashenko, Y. K. Park, D. S. Kim and S.-E. Park, *Res. Chem. Intermed.*, 1998, **24**, 933–951.
267 M. Saeidi and M. Hamidzadeh, *Res. Chem. Intermed.*, 2017, **43**, 2143–2157.
268 N. B. Younes, J. Martínez Ortigosa, O. Marie, T. Blasco and M. Mhamdi, *Res. Chem. Intermed.*, 2021, **47**, 2003–2028.
269 Y. Yokomichi, T. Yamabe, T. Kakumoto, O. Okada, H. Ishikawa, Y. Nakamura, H. Kimura and I. Yasuda, *Appl. Catal., B*, 2000, **28**, 1–12.
270 M. Anpo, M. Matsuoka, H. Mishima and H. Yamashita, *Res. Chem. Intermed.*, 1997, **23**, 197–217.
271 G. Brezicki, J. Zheng, C. Paolucci, R. Schlögl and R. J. Davis, *ACS Catal.*, 2021, **11**, 4973–4987.
272 W. Kaim and B. Schwederski, *Coord. Chem. Rev.*, 2010, **254**, 1580–1588.
273 P. Xiao, Y. Wang, Y. Lu, K. Nakamura, N. Ozawa, M. Kubo, H. Gies and T. Yokoi, *J. Am. Chem. Soc.*, 2024, **146**, 10014–10022.
274 M. J. Wulfers, S. Teketel, B. Ipek and R. F. Lobo, *Chem. Commun.*, 2015, **51**, 4447–4450.
275 A. R. Kulkarni, Z.-J. Zhao, S. Siahrostami, J. K. Nørskov and F. Studt, *Catal. Sci. Technol.*, 2018, **8**, 114–123.
276 A. A. Verma, S. A. Bates, T. Anggara, C. Paolucci, A. A. Parekh, K. Kamasamudram, A. Yezerets, J. T. Miller, W. N. Delgass, W. F. Schneider and F. H. Ribeiro, *J. Catal.*, 2014, **312**, 179–190.
277 M. Moreno-González, R. Millán, P. Concepción, T. Blasco and M. Boronat, *ACS Catal.*, 2019, **9**, 2725–2738.
278 C. Liu, G. Malta, H. Kubota, T. Toyao, Z. Maeno and K.-I. Shimizu, *J. Phys. Chem. C*, 2021, **125**, 21975–21987.
279 X. Guo, R. Zhang, Z. Di, B. Kang, H. Shen, Y. Wei, J. Jia and L. Zheng, *Appl. Catal., B*, 2024, **343**, 123519.
280 J. H. Enemark and R. D. Feltham, *Coord. Chem. Rev.*, 1974, **13**, 339–406.
281 W. Kaim and B. Schwederski, *Coord. Chem. Rev.*, 2010, **254**, 1580–1588.
282 C. J. Cramer, M. Włoch, P. Piecuch, C. Puzzarini and L. Gagliardi, *J. Phys. Chem. A*, 2006, **110**, 1991–2004.
283 P. Vanelderen, R. G. Hadt, P. J. Smeets, E. I. Solomon, R. A. Schoonheydt and B. F. Sels, *J. Catal.*, 2011, **284**, 157–164.
284 J. S. Woertink, P. J. Smeets, M. H. Groothaert, M. A. Vance, B. F. Sels, R. A. Schoonheydt and E. I. Solomon, *Proc. Natl. Acad. Sci. U. S. A.*, 2009, **106**, 18908–18913.
285 L. Vilella and F. Studt, *Eur. J. Inorg. Chem.*, 2016, 1514–1520.
286 A. Oda, Y. Mamenari, T. Ohkubo and Y. Kuroda, *J. Phys. Chem. C*, 2019, **123**, 17842–17854.
287 I. A. Pankin, A. Martini, K. A. Lomachenko, A. V. Soldatov, S. Bordiga and E. Borfecchia, *Catal. Today*, 2020, **345**, 125–135.
288 G. Yang, L. Zhou, X. Liu, X. Han and X. Bao, *Catal. Commun.*, 2007, **8**, 1981–1984.
289 C. J. Cramer and W. B. Tolman, *Acc. Chem. Res.*, 2007, **40**, 601–608.
290 K. Sobańska, A. Krasowska, T. Mazur, K. Podolska-Serafin, P. Pietrzyk and Z. Sojka, *Top. Catal.*, 2015, **58**, 796–810.
291 A. Oda, H. Torigoe, A. Itadani, T. Ohkubo, T. Yumura, H. Kobayashi and Y. Kuroda, *J. Am. Chem. Soc.*, 2013, **135**, 18481–18489.
292 R. F. Howe and J. H. Lunsford, *J. Am. Chem. Soc.*, 1975, **97**, 5156–5159.
293 A. Oda, T. Ohkubo, T. Yumura, H. Kobayashi and Y. Kuroda, *Angew. Chem., Int. Ed.*, 2017, **56**, 9715–9718.
294 A. Oda, J. Kumagai, K. Sawabe, T. Ohkubo, Y. Kuroda and A. Satsuma, *J. Phys. Chem. C*, 2021, **125**, 5136–5145.
295 P. Pietrzyk and K. Góra-Marek, *Phys. Chem. Chem. Phys.*, 2016, **18**, 9490–9496.
296 Z. Sojka, E. Giamello, M. Che, A. Zecchina and K. Dyrek, *J. Phys. Chem.*, 1988, **92**, 1541–1547.
297 A. Oda, T. Nanjo, T. Ohkubo and Y. Kuroda, *J. Phys. Chem. C*, 2020, **124**(21), 11544–11557.
298 S. Yao, E. Bill, C. Milsmann, K. Wieghardt and M. A. Driess, *Angew. Chem., Int. Ed.*, 2008, **47**, 7110–7113.
299 E. Kimura, R. Machida and M. Kodama, *J. Am. Chem. Soc.*, 1984, **106**, 5497–5505.
300 L. Chen, H. Falsig, T. V. W. Janssens and H. Grönbeck, *J. Catal.*, 2018, **358**, 179–186.
301 C. Negri, T. Selleri, E. Borfecchia, A. Martini, K. A. Lomachenko, T. V. W. Janssens, M. Cutini, S. Bordiga and G. Berlier, *J. Am. Chem. Soc.*, 2020, **142**, 15884–15896.
302 M. H. Mahyuddin, T. Tanaka, A. Staykov, Y. Shiota and K. Yoshizawa, *Inorg. Chem.*, 2018, **57**, 10146–10152.
303 H. Li, C. Paolucci, I. Khurana, L. N. Wilcox, F. Göltl, J. D. Albarracin-Caballero, A. J. Shih, F. H. Ribeiro, R. Gounder and W. F. Schneider, *Chem. Sci.*, 2019, **10**, 2373–2384.
304 K. Shimizu, R. Maruyama, T. Hatamachi and T. Kodama, *J. Phys. Chem. C*, 2007, **111**, 6440–6446.
305 A. B. Ene, M. Bauer, T. Archipova and E. Roduner, *Phys. Chem. Chem. Phys.*, 2010, **12**, 6520–6531.
306 T. Yumura, M. Takeuchi, H. Kobayashi and Y. Kuroda, *Inorg. Chem.*, 2009, **48**, 508–517.
307 A. Kornas, E. Tabor, D. K. Wierzbicki, J. E. Olszowka, R. Pilar, J. Dedecek, M. Śliwa, H. Jirglova, S. Sklenak, D. Rutkowska-Żbik and K. Mlekodaj, *Appl. Catal., B*, 2023, **336**, 122915.

308 E. Tabor, M. Lemishka, J. E. Olszowka, K. Mlekodaj, J. Dedecek, P. C. Andrikopoulosk and S. Sklenak, *ACS Catal.*, 2021, **11**, 2340–2355.
309 X. Yang, Z. Liu, B. Gao, Z. Chen, K. Yan, S. Wang, Y. Xia, Y. Zhang, L. Wang, X. Xu and Y. Tang, *ACS Catal.*, 2023, **13**, 15572–15580.
310 T. V. W. Janssens, E. Borfecchia, K. A. Lomachenko, H. Grönbeck and G. Berlier, *ChemCatChem*, 2024, **16**, e202400384.
311 P. J. Smeets, R. G. Hadt, J. S. Woertink, P. Vanelderen, R. A. Schoonheydt, B. F. Sels and E. I. Solomon, *J. Am. Chem. Soc.*, 2010, **132**, 14736–14738.
312 H. M. Rhoda, A. J. Heyer, B. E. R. Snyder, D. Plessers, M. L. Bols, R. A. Schoonheydt, B. F. Sels and E. I. Solomon, *Chem. Rev.*, 2022, **122**, 12207–12243.
313 C. Liu, H. Kubota, T. Toyao, Z. Maeno and K. Shimizu, *Catal. Sci. Technol.*, 2020, **10**, 3586–3593.
314 H. Lei, D. Chen, J.-Y. Yang, A. Khetan, J. Jiang, B. Peng, U. Simon, D. Ye and P. Chen, *Environ. Sci. Technol.*, 2023, **57**, 12465–12475.
315 I. Karamanis, A. Daouli, H. Monnier, M.-A. Dziurla, G. Maurin and M. Badawi, *Mol. Syst. Des. Eng.*, 2023, **8**, 1165–1181.
316 P. Pietrzyk, C. Dujardin, K. Góra-Marek, P. Granger and Z. Sojka, *Phys. Chem. Chem. Phys.*, 2012, **14**, 2203–2215–144.
317 P. Pietrzyk, F. Zasada, W. Piskorz, A. Kotarba and Z. Sojka, *Catal. Today*, 2007, **119**, 219–227.
318 Past and Present in DeNO$_x$ Catalysis: From Molecular Modeling to Chemical Engineering, in *Stud. Surf. Sci. Catal.*, ed. P. Granger and V. I. Parvulescu, 2007, vol. 171, pp. 27–65.
319 K. Hadjiivanov, *Catal. Rev.:Sci. Eng.*, 2000, **42**, 71–144.
320 P. Pietrzyk, W. Piskorz, Z. Sojka and E. Brocławik, *J. Phys. Chem. B*, 2003, **107**, 6105–6113.
321 P. Pietrzyk and Z. Sojka, *J. Phys. Chem. A*, 2005, **109**, 10571–10581.
322 A. M. Volodin, K. A. Dubkov and A. Lund, *Chem. Phys. Lett.*, 2001, **333**, 41–44.
323 R. Pérez Vélez, I. Ellmers, H. Huang, U. Bentrup, V. Schünemann, W. Grünert and A. Brückner, *J. Catal.*, 2014, **316**, 103–111.
324 S. Malykhin, A. Volodin and G. Zhidomirov, *Appl. Magn. Reson.*, 2008, **33**, 153–166.
325 Z. Sojka, P. Pietrzyk, G. Martra, M. Kermarec and M. Che, *Catal. Today*, 2006, **114**, 154–161.
326 C. W. Bauschlicher Jr., S. R. Langhoff and H. J. Partridge, *J. Chem. Phys.*, 1991, **94**, 2068–2072.
327 V. Umamaheswari, M. Hartmann and A. Pöppl, *J. Phys. Chem. B*, 2005, **109**, 1537–1546.
328 E. Brocławik, P. Kozyra, M. Mitoraj, M. Radoń and P. Rejmak, *Molecules*, 2021, **26**, 1511.
329 P. Kozyra, M. Radoń, J. Datka and E. Broclawik, *Struct. Chem.*, 2012, **23**, 1349–1356.
330 M. Radoń, P. Kozyra, A. Stępniewski, J. Datka and E. Broclawik, *Can. J. Chem.*, 2013, **91**, 538–543.
331 K. Góra-Marek, A. Stępniewski, M. Radoń and E. Brocławik, *Phys. Chem. Chem. Phys.*, 2014, **16**, 24089–24098.
332 F. Göltl and J. Hafner, *J. Chem. Phys.*, 2012, **136**, 064503.
333 P. Rejmak, E. Broclawik, K. Góra-Marek, M. Radoń and J. Datka, *J. Phys. Chem. C*, 2008, **112**, 17998–18010.
334 E. Broclawik, K. Góra-Marek, M. Radoń, M. Bucko and A. Stępniewski, *J. Mol. Model.*, 2017, **23**, 160.
335 M. Radoń, *Inorg. Chem.*, 2015, **54**, 5634–5645.
336 F. Neese, *J. Biol. Inorg. Chem.*, 2006, **11**, 702–711.
337 M. Radoń and E. Broclawik, Electronic properties of iron sites and their active forms in porphyrin-type architectures, in *Computational methods to study the structure and dynamics of biomolecules and biomolecular processes – from bioinformatics to molecular quantum mechanics*, ed. A. Liwo, Springer International Publishing, Cham, 2019, pp. 755–823.
338 M. Kaupp, *J. Comput. Chem.*, 2007, **28**, 320–325.
339 G. Monsch and P. Klüfers, *Angew. Chem., Int. Ed.*, 2019, **58**, 8566–8571.
340 N. C. Tomson, M. R. Crimmin, T. Petrenko, L. E. Rosebrugh, S. Sproules, W. C. Boyd, R. G. Bergman, S. DeBeer, F. D. Toste and K. Wieghardt, *J. Am. Chem. Soc.*, 2011, **133**, 18785–18801.
341 Q. M. Phung, H. N. Nam, V. Austen, T. Yanai and A. Ghosh, *Inorg. Chem.*, 2025, **64**, 1702–1710.
342 P. Karen, *Angew. Chem., Int. Ed.*, 2015, **54**, 4716–4726.
343 T. Ampßler, G. Monsch, J. Popp, T. Riggenmann, P. Salvador, D. Schröder and P. Klüfers, *Angew. Chem., Int. Ed.*, 2020, **59**, 12381–12386.
344 M. Gimferrer, J. Van der Mynsbrugge, A. T. Bell, P. Salvador and M. Head-Gordon, *Inorg. Chem.*, 2020, **59**, 15410–15420.
345 P. Pietrzyk, B. Gil and Z. Sojka, *Catal. Today*, 2007, **126**, 103–111.
346 A. Pulido and P. Nachtigall, *Phys. Chem. Chem. Phys.*, 2009, **11**, 1447–1458.
347 M. Radoń and E. Bocławik, *J. Phys. Chem. A*, 2011, **115**, 11761–11774.
348 R. Lin and P. J. Farmer, *J. Am. Chem. Soc.*, 2001, **123**, 1143–1150.
349 I. M. Wasser, S. de Vries, P. Moënne-Loccoz, I. Schröder and K. D. Karlin, *Chem. Rev.*, 2002, **102**, 1201–1234.
350 P. Xie, T. Pu, G. Aranovich, J. Guo, M. Donohue, A. Kulkarni and C. Wang, *Nat. Catal.*, 2021, **4**, 144–156.
351 G. B. Richter-Addo and P. Legzdins, *Metal Nitrosyls*, Oxford University Press, New York, 1992.
352 K. M. Farhan and P. K. Sajith, *Ind. Eng. Chem. Res.*, 2025, **64**, 5257–5268.
353 M.-L. Tsai, R. G. Hadt, P. Vanelderen, B. F. Sels, R. A. Schoonheydt and E. I. Solomon, *J. Am. Chem. Soc.*, 2014, **136**, 3522–3529.
354 A. Wijerathne, A. Sawyer, R. Daya and C. Paolucci, *J. Am. Chem. Soc. Au*, 2024, **4**, 197–215.
355 A. R. Fahami, T. Günter, D. E. Doronkin, M. Casapu, D. Zengel, T. H. Vuong, M. Simon, F. Breher, A. V. Kucherov, A. Brückner and J.-D. Grunwaldt, *React. Chem. Eng.*, 2019, **4**, 1000–1018.

356 L. Chen, T. V. W. Jansen, P. N. R. Vennestrom, J. Jansson, M. Skoglundh and H. A. Grönbeck, *ACS Catal.*, 2020, **10**, 5646–5656.
357 M. Bendrich, A. Scheuer, R. E. Hayes and M. Votsmeier, *Appl. Catal., B*, 2018, **222**, 76–87.
358 W. Hu, T. Selleri, F. Gramigni, E. Fenes, K. R. Rout, S. Liu, I. Nova, D. Chen, X. Gao and E. Tronconi, *Angew. Chem., Int. Ed.*, 2021, **60**, 7197–7204.
359 C. Liu, H. Kubota, T. Amada, K. Kon, T. Toyao, Z. Maeno, K. Ueda, J. Ohyama, A. Satsuma, T. Tanigawa, N. Tsunoji, T. Sano and K.-I. Shimizu, *ChemCatChem*, 2020, **12**, 3050–3059.
360 W. Hu, F. Gramigni, N. D. Nasello, N. Usberti, U. Iacobone, S. Liu, I. Nova, X. Gao and E. Tronconi, *ACS Catal.*, 2022, **12**, 5263–5274.
361 R. Daya, D. Trandal, U. Menon, D. J. Deka, W. P. Partridge and S. Y. Joshi, *ACS Catal.*, 2022, **12**, 6418–6433.
362 C. Liu, H. Kubota, T. Toyao, Z. Maeno and K.-I. Shimizu, *Catal. Sci. Technol.*, 2020, **10**, 3586–3593.
363 A. Oda, H. Shionoya, Y. Hotta, T. Takewaki, K. Sawabe and A. Satsuma, *ACS Catal.*, 2020, **10**, 12333–12339.
364 C. Paolucci, A. A. Verma, S. A. Bates, V. F. Kispersky, J. T. Miller, R. Gounder, W. N. Delgass, F. H. Ribeiro and W. F. Schneider, *Angew. Chem., Int. Ed.*, 2014, **53**, 11828–11833.
365 M. P. Ruggeri, I. Nova, E. Tronconi, J. A. Pihl, T. J. Toops and W. P. Partridge, *Appl. Catal., B*, 2015, **166–167**, 181–192.
366 H.-Y. Chen, M. Kollar, Z. Wei, F. Gao, Y. Wang, J. Szanyi and C. H. F. Peden, *Catal. Today*, 2019, **320**, 61–71.
367 Y. Zhang, Y. Peng, K. Li, S. Liu, J. Chen, J. Li, F. Gao and C. H. F. Peden, *ACS Catal.*, 2019, **9**, 6137–6145.
368 L. Negahdar, N. E. Omori, M. G. Quesne, M. D. Frogley, F. Cacho-Nerin, W. Jones, W. T. Price, R. A. Catlow and A. M. Beale, *ACS Catal.*, 2021, **11**, 13091–13101.
369 F. Gao, E. D. Walter, M. Kollar, Y. L. Wang, J. Szanyi and C. H. F. Peden, *J. Catal.*, 2014, **319**, 1–14.
370 C. Liu, S. Yasumura, T. Toyao, Z. Maeno and K.-I. Shimizu, *J. Phys. Chem. C*, 2022, **126**, 11594–11601.
371 F. Lin, T. Andana, Y. Wu, J. Szanyi, Y. Wanga and F. Gao, *J. Catal.*, 2021, **401**, 70–80.
372 G. He, B. Zhang, H. He, X. Chen and Y. Shan, *Sci. Total Environ.*, 2019, **673**, 266–271.
373 B. Zhang, G. He, Y. Shan and H. He, *Catal. Today*, 2019, **327**, 177–181.
374 W. B. Tolman, *Angew. Chem., Int. Ed.*, 2010, **49**, 1018–1024.
375 V. I. Avdeev and A. F. Bedilo, *Chem. Phys. Lett.*, 2018, **695**, 222–227.
376 D. Sengupta, J. B. Adams, W. F. Schneider and K. C. Hass, *Catal. Lett.*, 2001, **74**, 193–199.
377 P. Xiao, Y. Wang, Y. Lu, K. Nakamura, N. Ozawa, M. Kubo, H. Gies and T. Yokoi, *J. Am. Chem. Soc.*, 2024, **146**, 10014–10022.
378 Z. Sojka and M. Che, *J. Phys. Chem.*, 1996, **100**, 14776–14785.
379 L. Nowakowski, C. Hudy, F. Zasada, J. Gryboś, W. Piskorz, A. Wach, Y. Kayser, J. Szlachetko and Z. Sojka, *J. Am. Chem. Soc.*, 2024, **146**, 24450–24466.
380 G. Li, E. A. Pidko, I. A. W. Filot, R. A. van Santen, C. Li and E. J. M. Hensen, *J. Catal.*, 2013, **308**, 386–397.
381 H. Xia, K. Sun, K. Sun, Z. Feng, W. X. Li and C. Li, *J. Phys. Chem. C*, 2008, **112**, 9001–9005.
382 E. V. Kondratenko and J. Perez-Ramırez, *J. Phys. Chem. B*, 2006, **110**, 22586–22595.
383 C. Sang, B. H. Kim and C. R. F. Lund, *J. Phys. Chem. B*, 2005, **109**, 2295–2301.
384 Z. Sobalik, J. Novakova, J. Dedecek, N. K. Sathu, E. Tabor, P. Sazama, P. Stastny and B. Wichterlova, *Microporous Mesoporous Mater.*, 2011, **146**, 172–183.
385 Z. Piwowarska, E. Micek, M. Rutkowska and L. Chmielarz, *Microporous Mesoporous Mater.*, 2015, **209**, 54–65.
386 D. Pietrogiacomi, M. C. Campa, L. R. Carbone and M. Occhiuzzi, *Appl. Catal., B*, 2019, **240**, 19–29.
387 K. Jíša, J. Nováková, M. Schwarze, A. Vondrová, S. Sklenák and Z. Sobalik, *J. Catal.*, 2009, **262**, 27–34.
388 B. M. Abu-Zied, W. Schwieger and A. Unger, *Appl. Catal., B*, 2008, **84**, 277–288.
389 F. Kapteijn, G. Marban, J. Rodriguez-Mirasol and J. A. Moulijn, *J. Catal.*, 1997, **167**, 256–265.
390 A. Li, P. Wang, L. Zhang, H. Zhao, M. Jin and L. Lei, *Fuel*, 2024, **378**, 132888.
391 P. J. Smeets, M. H. Groothaert, R. M. van Teeffelen, H. Leeman, E. J. M. Hensen and R. A. Schoonheydt, *J. Catal.*, 2007, **245**, 358–368.
392 B. Kang, R. Zhang, M. Guo, X. Guo, Z. Di, Y. Wei and J. Jia, *Energy Fuels*, 2023, **37**, 18019–18029.
393 J. W. A. Fischer, F. Buttignol, A. Brenig, D. Klose, D. Ferri, V. Sushkevich, J. A. van Bokhoven and G. Jeschke, *Catal. Today*, 2024, **429**, 114503.
394 A. P. Hawkins, A. E. Edmeades, C. D. M. Hutchison, M. Towrie, R. F. Howe, G. M. Greetham and P. M. Donaldson, *Chem. Sci.*, 2024, **15**, 3453–3465.
395 K. Mitsuishi, K. Nakazawa, R. Sagawa, M. Shimizu, H. Matsumoto, H. Shima and T. Takewaki, *Sci. Rep.*, 2023, **13**, 316.
396 D. Liu, L. Liu, K. Wu, J. Zhou, Q. Cheng, J. Lv, T. Cao, D. Zhang, F. Lin and Y. Han, *J. Phys. Chem. C*, 2021, **125**, 18952–18960.
397 C. H. Hendon, A. J. Rieth, M. D. Korzyński and M. Dinca, *ACS Cent. Sci.*, 2017, **3**, 554–563.